Interactions of light with nanostructured materials

Evelin Csányi

The University of Sheffield
Department of Chemistry

A thesis submitted in partial fulfilment of the requirements for the degree of
Doctor of Philosophy

September 2023

Declaration

The work described in this thesis was undertaken at the University of Sheffield under the supervision of Professor Graham J. Leggett between October 2018 and September 2023, and at the Institute of Materials Research and Engineering, A*STAR, between October 2021 and September 2023 under the supervision of Dr Zhaogang Dong, and has not been submitted, either wholly or in part, for this or any other degree. All the work is the original work of the author, except where acknowledged.

Evelin Csányi

September 2023

Publications

1. Evelin Csányi, Yan Liu, Soroosh Daqiqeh Rezaei, Henry Yit Loong Lee, Febiana Tjiptoharsono, Zackaria Mahfoud, Sergey Gorelik, Xiaofei Zhao, Li Jun Lim, Di Zhu, Jing Wu, Kuan Eng Johnson Goh, Weibo Gao, Zhi-Kuang Tan, Graham Leggett, Cheng-Wei Qiu and Zhaogang Dong, Engineering and Controlling Perovskite Emissions via Optical Quasi-Bound-States-in-the-Continuum, *Adv. Funct. Mater*. **2023**, 2309539

2. Anna Lishchuk, Evelin Csányi, Brice Darroch, Chloe Wilson, Alexei Nabok and Graham J. Leggett, Active control of strong plasmon–exciton coupling in biomimetic pigment–polymer antenna complexes grown by surface-initiated polymerisation from gold nanostructures,*Chem. Sci.*, **2022**,13, 2405-2417

Acknowledgements

First, I would like to thank my dedicated supervisors. Prof Graham Leggett, thank you for all your support, guidance and encouragement over these years. Any challenge I faced you have always been there to support me. I am grateful for the opportunity to be a part of your research group, which helped me grow as a person and as a researcher.

Dr Zhaogang Dong, I would like to thank you for welcoming me into your research group. Your guidance helped me transition into a new research field. I am thankful for your mentorship and dedication to my growth and development during my academic journey.

I would also like to thank the A*STAR-Sheffield Research Attachment Program (ARAP) for providing the research studentship that made this work possible.

During this period, I had the privilege of collaborating with talented researchers who greatly contributed to the success of my projects. A huge thank you goes to Dr Deborah Hammond for measuring hundreds of XPS samples, the depth-profiling and help on analysis. I would also like to thank Dr Anna Lishchuk for providing the plasmonic gold arrays, the extinction measurements, dispersion plots, ellipsometry analysis and the modelling of the plasmon-exciton coupling energy. Dr Benjamin Bower and Dr Edwin Johnson for their help with the shipping of materials to Singapore. A special thank you goes to Dr Yan Liu for teaching me theoretical analysis and all her help during my attachment period. In addition, to the other great theoreticians, Dr Soroosh Daqiqeh Rezaei and Dr Qifeng Ruan for the FDTD data and multipolar decomposition. Dr Zhaogang Dong and Dr Febiana Tjiptoharsono are thanked for the nanofabrication of the Si nanostructures. Henry Yit Loong Lee for his help with the Cr evaporation and SEM imaging, and of course, for the banter. Dr Zhang Jun for getting me up to speed when I started at A*STAR. Thanks goes to Dr Zackaria Mahfoud for the TEM imaging sessions and to Dr Sergey Gorelik for the PL lifetime measurements. Thank you for our collaborators, Dr Xiaofei Zhao, Li Jun Lim and Prof Zhi-Kuang Tan who prepared and characterized the perovskite materials. Dr Dan Kai and Prof Xian Jun Loh for the synthesis and characterisation of the lignin-PEG polymer. Thanks to the NUS synchrotron team, Dr Xiao Chi and Dr Andrivo Rusydi for the UV range ellipsometry measurements. I would also like to extend my gratitude to all those who engaged in insightful discussions regarding the work.

To the members of the Prof Leggett and Dr Dong groups, I truly enjoyed working with you all! I also thank the UoS Chemistry Department and IMRE staff who were always helpful during my PhD, and the Masters students I supervised and worked along with.

I would like to thank my wonderful friends and all the people I had the pleasure of meeting along this journey. I could write an equally long document as this one on how much you have all enriched my life.

To Jasmin and Daz, I couldn't have asked for better friends. You stood by me, inspired me, and challenged me along this journey, which helped me grow as a person. I am grateful for all the love, support, jokes, tears, coffee and choc-almond waffles we shared. I extend my thanks to the rest of the close squad, Dan, Faizal and Teymour, who made this period of my life so memorable and fun. I don’t know what I would have done without you all! And of course, thanks to everyone from the A*STAR office and the friends I made in Singapore.

A huge thank you to Lili for her endless love and encouragement, even from 9500 km away. Ati, Dia and Robin, who all believed in me from day one. My friends, Csilla, Mike and Brad, whether in Notty house or in the chem dept corridors, our chats always made my day. I can’t wait to see you all again.

I also want to give a heartfelt thank you to Josh, who stood by me through the highs and lows, always being there for me. I couldn't have made it without you.

My thanks go to the ACE fam for all their support during my write-up months in Vietnam, and to the amazing people who were there with me to keep my spirits high during those hectic last weeks of the thesis writing. What a journey it’s been.

Lastly, I would like to thank my family for their unconditional love and support during this time, and for always believing in me. ♡

Abstract

This thesis explores the use of light-matter coupling to address key challenges in exciton transport in organic semiconductors, tuneable light-emission and UV plasmonic materials. Organic photovoltaics are promising candidates for solar energy capture; however, their performance is limited due short exciton diffusion lengths in organic semiconductors. To address this challenge, the design of biomimetic organic light-harvesting networks capable of strong plasmon-exciton coupling is explored. Pigment-polymer antenna complexes are formed by attachment of chlorophyll *a* (Chl) to poly(cysteine methacrylate) (PCysMA) scaffolds grown by surface-initiated atom-transfer radical polymerisation from brominated self-assembled monolayers. The organisation of Chl within the films is programmed by controlling the polymer grafting density and polymerisation time. The films are characterised using X-ray photoelectron spectroscopy (XPS) depth-profiling with giant gas cluster ions. For all grafting densities, Chl are distributed uniformly as a function of depth. However, the fraction of repeat units bound to Chl increases with decreasing grafting density. When synthesised from gold nanostructures, the plasmon-exciton coupling energies are correlated with the grafting density of the polymer layer, yielding plasmon-exciton coupling energies as high as 0.46 eV. Thus, it is demonstrated that plexcitonic complexes are promising templates for the design of biomimetic photonic materials with long-range energy transfer mechanisms. In the field of light-emission technologies, metal halide perovskite quantum dots (PQDs) have emerged as promising materials due to their exceptional photoluminescence (PL) properties. A wide range of applications could benefit from adjustable luminescence post-synthesis. In this work, an optical nanoantenna array is designed with polarization-controlled quasi-bound-states-in-the-continuum (q-BIC) resonances that can control and modify the perovskite PL wavelength. Si nanopillar arrays are fabricated using electron-beam lithography (EBL) that exhibit q-BIC resonances in the range of 690 nm to 804 nm under *y*-polarization, and from 638 nm to 696 nm under *x*-polarization. The energies of these resonances are tuned by variation of the nanostructure geometries. $FAPbI_3$ perovskites are deposited on the arrays using dip-coating and the optical properties are characterised using PL mapping measurements. A wavelength shift over a ~39 nm range was achieved, with additional spectral tuning enabled by the switching of the pump laser polarization. The design confers a 21-fold emission enhancement of the QDs. The research provides a path towards spectrally tailored quantum emitters. Lastly, interband plasmons (IBPs) are of interest as they enable plasmonic behaviour in non-plasmonic materials, such as semiconductors. IBPs arise from the electromagnetic excitation of bound electron oscillations, enabling plasmonic resonances into the deep ultraviolet (UV) range. Despite their significant potential, practical applications are limited due to their broad resonances. This thesis demonstrates the sharpening of the resonances of IBPs by more than one-order of magnitude via mode hybridization. Si nanodisk arrays are fabricated using EBL on top of a SiO_2 cavity. The optical response of the system is controlled by the geometrical design, which influences the interaction between the Si nanodisk plasmon resonances and the cavity modes. The experimental and simulated reflectance show a *Q*-factor enhancement from 1 to ~43. This high-*Q* resonance further increases light absorption of UV-absorbing lignin-modified polyethylene glycol films by 7.5-fold. Our findings could be applicable to other interband plasmonic materials and open up possibilities in applications requiring both narrow and broad band resonances, particularly in UV-specific areas.

Nomenclature

11-MUL	11-mercapto-1-undecanol
AFM	Atomic Force Microscopy
AGT	O6-alkylguanine-DNA-alkyltransferase
APTES	3-aminopropyltriethoxysilane
ARGET	Activators regenerated by electron transfer
ATP	Adenosine triphosphate
ATRP	Atom transfer radical polymerization
BChl *a*	Bacteriochlorophyll *a*
BFAST	Broadband fixed angle source technique
BIC	Bound-states-in-the-continuum
Chl	Chlorophyll *a*
CW	Continuous wave
CysMA	Cysteine methacrylate
DSSC	Dye-sensitized solar cell
DTBU	Bis[2-(2-bromoisobutyryloxy)undecyl] disulfide
EBL	Electron-beam lithography
ED	Electric dipole
EDC	Ethylcarbodiimide/N-hydroxysuccinimide
EM	Electromagnetic
EQ	Electric quadrupole
FA	Formamidinium
FDTD	Finite-difference time-domain
FEM	Finite-element method
FRET	Förster resonance energy transfer
FWHM	Full width at half maximum
GCIB	Gas cluster ion beam
HOMO	Highest occupied molecular orbital
HPLC	High Performance Liquid Chromatography
IBP	Interband plasmonic
ICP	Inductively-coupled plasma
IgG	Immunoglobulin G
IPA	Isopropyl alcohol
LC-MS	Liquid chromatography mass spectrometry
LCMS	Liquid chromatography-mass spectrometry
LED	Light-emitting diodes
LH1-2	Light-harvesting complex 1-2
LHC	Light-harvesting complexes
LHCI-II	Light-harvesting complex I-II
lignin-PEG	Lignin-polyethylene glycol
LSPR	Localized surface plasmon resonance
LUMO	Lowest unoccupied molecular orbitals

MA	Methylammonium
MD	Magnetic dipole
Me-PyPh *a*	Methyl pyropheophorbide a
MQ	Magnetic quadrupole
NHS	N-hydroxysuccinimide
NIR	Near-IR
NMR	Nuclear Magnetic Resonance
ODT	1-octadecanethiol
OEGMA	Hydroxy-terminated oligo(ethylene glycol) methacrylate
PBS	Phosphate buffered saline
PCE	Power conversion efficiency
PCysMA	Poly(cysteine methacrylate)
PE-CVD	Plasma-enhanced chemical vapour deposition
PL	Photoluminescence
PLQY	Photoluminescence quantum yield
PML	Perfectly matched layer
pOEGMA	Poly[oligo(ethylene glycol)methacrylate]
polyMPC	Poly(2-methacryloxoethyl-phosphorylcholine
polySB	Poly(sulfobetaine-methacrylate)
PQY	Photoluminescence quantum yields
PRET	Plasmonic resonant energy transfer
PV	Photovoltaic
PyPh *a*	Pyropheophorbide a
q-BIC	Quasi-bound-states-in-the-continuum
Q-factor	Quality factor
RC	Reaction centre
RGD	Arginine-glycine-aspartic acid
SAM	Self-assembled monolayer
SC-Zn-pyChl *a*	Succinimidyl zinc-pyrochlorophyllide *a*
SEM	Scanning electron microscopy
SI	Surface-initiated
SPP	Surface plasmon polaritons
SPR	Surface plasmon resonance
TEM	Transmission electron microscopy
UV	Ultraviolet
UV/vis	Ultraviolet/Visible
XPS	X-ray photoelectron spectroscopy
Zn-pyChl *a*	Zinc-pyrochlorophyllide *a*

Table of Contents

Chapter 1. Introduction

1.1 Control of light-matter interactions

Physicists have long sought to understand and to manipulate the interactions of light with matter. Albert Einstein's explanation of the photoelectric effect in 1905 marked a pivotal moment in understanding such interactions. In the 1920s, the development of quantum mechanics brought deeper understanding of light-matter interactions at the atomic and subatomic scales. Meanwhile, Max Planck's work on the quantization of energy and Louis de Broglie's concept of matter waves laid the foundation for quantum theory, which forms the basis of semiconductor physics.[1] These insights guided researchers to explore the behaviour of light and matter at the atomic and subatomic scales, which gained significant traction from the late 20th century onwards. This research laid the groundwork for engineering nanostructures that could exploit quantum effects to control light emission, absorption, and propagation.[2,3]

The design of nanostructures with dimensions comparable to or smaller than the wavelength of the incident light enabled the guidance and manipulation of light on surfaces. These confined electromagnetic (EM) waves can interact with organic and inorganic materials, nanoparticles, 0D to 3D crystals and more. Therefore, miniaturized devices that rely on such light-matter interactions became a reality, finding their use in a wide range of applications such as light-harvesting technologies, detectors, sensors, light-emitting devices, quantum computing, and encryption. [4–7]

This thesis explores the control of light-matter interactions via two key approaches: 1) The fabrication of nanostructures that support optical resonances with defined characteristics, such as spectral position, linewidth and sensitivity, and 2) the deposition and 3D arrangement of

organic and inorganic materials on such surfaces. It is shown that the strategic combination of these materials design elements provides a means to control light-matter coupling effects. This approach and the resulting optical phenomena are examined within different possible applications, such as solar energy capture, light-emitting devices and UV detectors.

First, the synthesis and characterisation of an artificial light-harvesting system is explored. Inspired by biological pigment-protein units, these systems offer extended exciton diffusion lifetimes – a key parameter in the design of efficient hybrid solar panels. The 3D arrangement of pigment molecules on surfaces is examined, combined with plasmonic materials. Next, the remarkable optical properties of perovskites are introduced. Different approaches are compared for tuning of the photoluminescence properties, involving the use of nanostructures and external stimuli. In particular, the advantages of the use of quasi-bound-states-in-the-continuum (q-BIC) are discussed. Lastly, it is demonstrated that semiconductors with strong interband transitions can offer plasmonic characteristics beyond the visible spectral region, addressing the limitations of conventional plasmonic materials. This capability proves valuable in the design of UV-specific sensor applications. While the quality of these resonances currently remains low, various design strategies are introduced to enhance the plasmonic behaviour of these materials.

The following introduction provides a detailed discussion of the background to each topic, the current state of the art, the remaining unsolved challenges and future outlook.

1.2 Alternate approaches to solar energy capture

In recent years, an immense amount of research has been directed towards improving existing solar energy capture technologies. The commercial photovoltaic (PV) market is currently dominated by devices based on silicon, which yield high efficiency and a long service life. However, despite the dominance of silicon-based PV, there has been a great deal of interest in developing organic and hybrid organic-inorganic materials as alternatives to silicon for solar capture technologies.[8–10] Organic semiconductors can be manufactured from earth-abundant elements in low energy processes. Moreover, they are lightweight and flexible.[11] In the drive towards net zero, and for applications in developing countries, these attributes are potentially important. However, these technologies possess significantly lower power conversion efficiencies (PCE) in comparison. This is because the excitation transfer in molecular materials occurs via incoherent energy transfer processes, leading to short exciton diffusion lengths. The exciton is an electrically neutral quasiparticle, which forms upon the excitation of an electron in the material. The absorption of a photon with sufficient energy leads to the promotion of an electron from a lower energy state to a higher energy state, leaving behind a positively charged electron hole. In semiconductors, the transition occurs between the valence and the conduction band, while molecular excitons are formed between the highest occupied molecular orbital (HOMO) and the lowest unoccupied molecular orbitals (LUMO). The electron-hole pair is Coulombically bound, and free excitons can diffuse within the material. In organic photovoltaics, the exciton must diffuse to a donor-acceptor interface within the cell, in order for the charges to separate and drive the generation of voltage and an electric current (Figure 1.1).

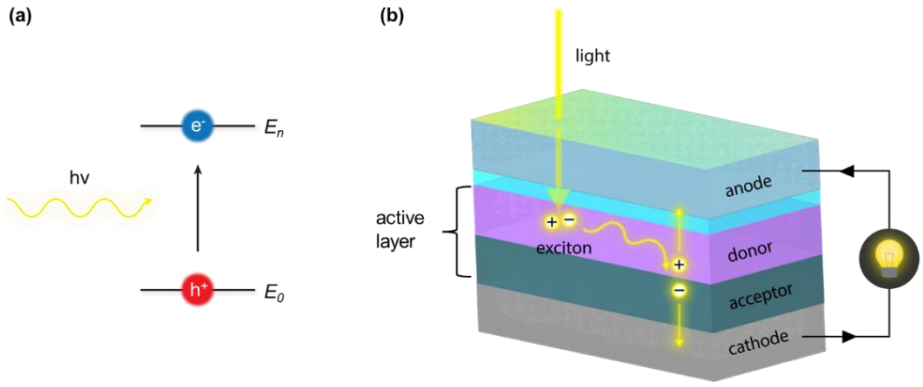

Figure 1.1. (a) Schematic representation of the generation of an exciton. The incoming light (with energy of hν, where h is Planck's constant and ν is the frequency) excites the material to promote the transition of an electron (e^-) from a lower energy state (E_0) to a higher one (E_n), leaving behind a positively charged electron hole (h^+). (b) Illustration of the exciton diffusion process towards the donor-acceptor interface within an organic solar panel.

For optimum performance, the excitons should have sufficiently long lifetimes, and therefore, long enough diffusion lengths to reach the interface without recombination, ideally in the matter of nanoseconds. The organic materials currently used are limited to short diffusion lengths, typically within the range of ca. 10 nm up to 50 nm.[12] Under such constraints, the improvement of these devices becomes problematic. One approach to overcome this challenge is to design multiple heterojunction devices, based on phase-separated copolymers consisting of nanometre-scale domains of donor and acceptor. While the efficiencies of these devices are approaching those of silicon PVs, the phase-separated structures are unstable and possess short commercial lifetimes.[13]

1.2.1 Light-harvesting in nature

Light-harvesting systems in nature are fuelled by highly efficient energy transfer processes. The excitation transport over long distances relies on electronic coherence between pigment molecules and short dephasing times. These properties make biological light-harvesting

complexes the ideal example for optimising artificial technologies that rely on the same processes. Therefore, it is important to first understand the principles that make efficient biological light-harvesting processes, such as photosynthesis.

Photosynthesis is a biological process in which energy from sunlight is converted into chemical energy. Nature has perfected its light-harvesting processes through years of evolution, providing energy to maintain Earth's biosphere and sustain life. Generally, this process is performed by a photosynthetic organism using the energy from sunlight to produce carbohydrate molecules and oxygen from water and carbon dioxide. Solar energy capture is carried out by pigment-protein complexes, known as light-harvesting complexes or antenna complexes, with the exception of green sulfur bacteria that uses chlorosomes for this purpose. Photons are absorbed by the pigments within the light-harvesting complexes to create excitons. By this mechanism, the collected energy is funnelled down an energy gradient by transferring the excitation from higher energy molecules to lower energy states. The energy eventually reaches a reaction centre where photo-induced charge separation drives the synthesis of adenosine triphosphate (ATP). These antenna systems are arranged in three-dimensional structures to minimize the number of energy transfer steps required to connect any two pigments in the array to reach a reaction centre (Figure 1.2).[14]

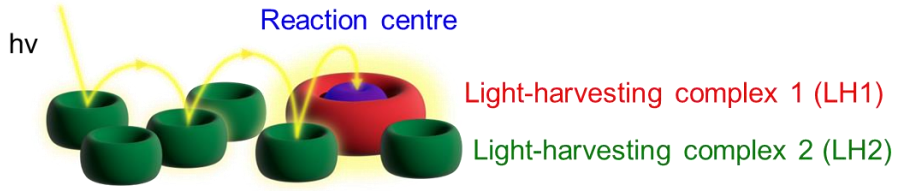

Figure 1.2. Illustration of the energy transfer mechanism found in light-harvesting organisms. The energy from light in transferred between light-harvesting complexes (green and red cylinders) towards a reaction centre (shown in blue).

The light-harvesting and energy transfer processes are carried out by similar mechanisms in most light-harvesting complexes, whether they are bacterial or plant-based. Importantly, all photosynthetic units contain large numbers of pigment molecules, which fulfil key photosynthetic roles. Such pigment molecules are typically chlorophylls or bacteriochlorophylls, but carotenoids and other cofactors such as quinones or iron sulfur centres can contribute to photosynthesis. These pigments are bound by photosynthetic proteins, where the concentration and the variety of pigment molecules ensure the efficient collection of available light at an appropriate spectrum.[14]

1.2.2 Chlorophyll *a*

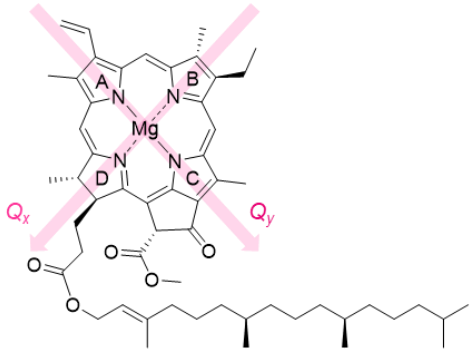

Figure 1.3. Structure of chlorophyll *a*, showing the pyrrole moieties labelled according to IUPAC.

Photosynthetic organisms rely on pigment molecules within their light-harvesting units to collect sunlight. A variety of pigment molecules is used in photosynthesis. Among these, chlorophylls and bacteriochlorophylls play particularly important roles in light-harvesting and energy transfer. It is believed that chlorophyll *a* and bacteriochlorophyll *a* were the first types of chlorophylls to be utilised in photosynthesis when life on Earth started.[15] However, a range of chlorophyll variants (*a*-*f*) is found in nature that differ in some of the functional groups present on the A and B rings of the chlorophyll structure (Figure 1.3). The *a* variant is the most common in green plants.[14]

Chlorophylls share most structural elements, such as the tetrapyrrole moiety with a reduced pyrrole ring, known as a chlorin ring, and the phytol chain, which is a long chain esterified terpenoid alcohol.[16] The planar chlorin ring contains a metal ion coordinated to the ring nitrogens, which provides the characteristic blue-green colour of the molecule. For chlorophyll *a*, the metal is a magnesium ion, which may be replaced by other coordination metals depending on the environment of the organism. The molecule has an almost square planar centre and width of ca. 10 Å on its side.[14] Another important aspect of the structure is its

isocyclic ring V (located next to ring C in Figure 1.3) which is susceptible to different chemical reactions. As the chlorin ring contains a delocalised π-system, it has an aromatic character that gives rise to optical properties that can be tuned by the chelating metal and the side chains of the chlorin ring.[17] While the molecule has a similar structure to porphyrins, it is the lack of symmetry of its electron cloud around the tetrapyrrole moiety that differentiates it from its aromatic counterparts, which can be observed directly from its absorption spectrum (Figure 1.4).

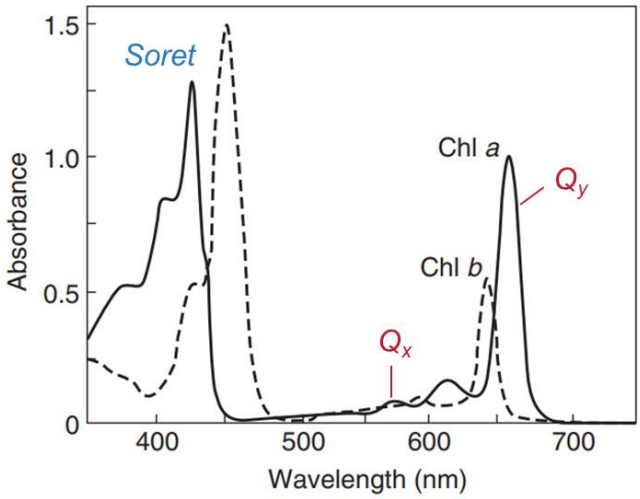

Figure 1.4. Absorption spectrum of chlorophyll a (Chl a, solid line) and chlorophyll b (Chl b, dashed line), as measured and presented by Lichtenthaler et al.[18]

The absorption spectrum of chlorophyll *a* can be interpreted by the Gouterman model, which is based on the four-orbital model derived for porphyrins.[19] The visible and near-ultraviolet absorption bands in the spectrum arise from electronic transitions. These are termed as the Q_y and Q_x transitions, referring to the *y*- and *x*-axis of the molecule, respectively. Following the IUPAC nomenclature, the *y*-axis goes through the nitrogens in pyrrole A and C, while the *x*-axis passes through the nitrogens in the B and D rings (shown in Figure 1.3). The origin of the asymmetry of the macrocycle comes from the reduced pyrrole ring D, therefore, the

delocalization of electrons does not stretch across the whole of the chlorin ring, resulting in the unique electronic transitions compared to porphyrins. The structural asymmetry means that electronic transitions that would be forbidden by the Laporte orbital selection rule, i.e. transitions between states that have the same parity with respect to an inversion centre in the molecule, become allowed. In addition, the electrons' spin remain the same during the transitions, obeying the spin selection rule. Thus, when the molecule is excited by light, a π to π* transition occurs. Absorption of light within the red spectral region populates the lowest excited state via the Q_y and Q_x electronic transitions, while absorption of blue light carries energy that can populate higher excited states, known as the Soret bands (Figure 1.5).

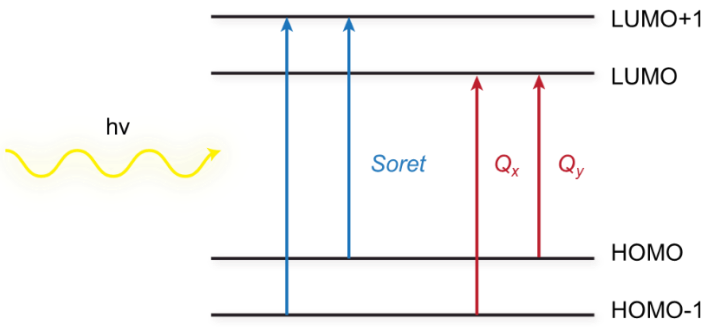

Figure 1.5. Representation of the relative energies of molecular orbitals of the chlorin ring showing the Q_x, Q_y and Soret electronic transitions.[14]

The higher excited state is relatively short lived and relaxes to the lowest excited state by dissipation of energy in the form of heat. Due to its longer lifetime, this state is involved in the electron transfer and energy storage processes in photosynthesis. An important consequence of these electronic transitions is the resulting polarization along the *x*- and *y*-axes of the molecule. Upon excitation, the transitions between the ground state and excited state gives rise to an oscillating electric dipole moment, caused by the movement of the electrons. The magnitude and direction of the dipole moment determine the polarization of the transition. Therefore, the

optical behaviour of the excited molecule can be described using a classical harmonic oscillator model, which is discussed in more detail later on.[14] Consequently, if incident plane polarized light has its electric vector parallel to the *y*-axis of the molecule (thus parallel to the polarization along the *y*-axis), a strong absorption can be observed due to the efficient interaction of light with π electrons through resonance. Similarly, a photon can be absorbed when the frequency of the transition dipole moment along the *x*-axis matches the frequency of the oscillating EM field. As photon absorption is the first step in photosynthesis, the optical properties and relative orientations of chromophores are important factors in the overall efficiency of light-harvesting and energy transfer steps.[20,21]

1.2.3 Structural and light-harvesting properties of LH2

Light-harvesting in nature is carried out by pigment-protein complexes. The simplest and best understood example of this can be found in purple bacteria, *Rhodopseudomonas acidophil*, which utilizes photosynthetic vesicles. The 3D structure of LH2 has been well researched and provides an understanding of the molecular mechanisms of photosynthesis. The vesicles contain a network of two different photosynthetic units embedded in the membrane, light-harvesting complex 1 (LH1) and light-harvesting complex 2 (LH2). Both units are made of *α* and *β* polypeptides derivatised with bacteriochlorophyll *a* (BChl *a*) and carotenoids, organised in rings in a simple and highly symmetrical fashion. The role of LH2 is to collect and transport energy from sunlight between the units untils it reaches LH1, which transfers this energy to the reaction centre.[22]

The structure of LH2 was investigated using high-resolution techniques, which revealed the arrangement of its protein units.[23,24] LH2 is made up of smaller subunits, each containing an α- and β-peptide, supporting three bacteriochlorophyll *a* molecules and one carotenoid molecule (Figure 1.6).

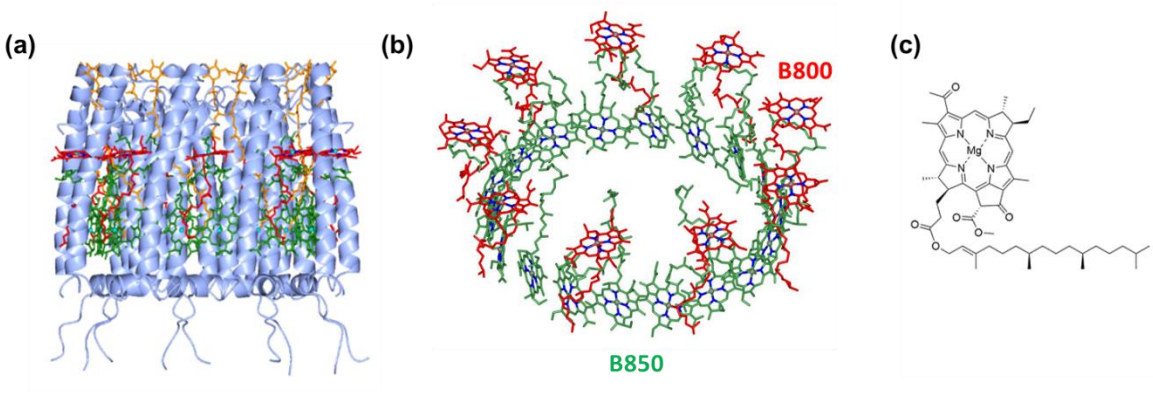

Figure 1.6. (a) Representation of the structure of LH2, showing the protein units, the bacteriochlorophylls (in red and green) and carotenoids (orange). (b) The arrangement of bacteriochlorophylls within the structure of LH2 and (c) the molecular structure of bacteriochlorophyll *a*, as illustrated by R. E. Blankenship.[14]

Nine units aggregate into a doughnut shaped structure with a diameter of 65 Å. There are two distinct chlorophyll environments in the complex. One of these is a ring of nine bacteriochlorophylls with the tetrapyrrole rings parallel to the plane of the membrane, held by metal-ligand interactions and hydrogen bonding. This ring has an absorption maximum at 800 nm and is therefore called the B800 ring. The Mg^{2+} ions are separated at ca. 21 Å from each other, resulting in a rather weak interaction between neighbouring chlorophylls. As energy transfer between pigment molecules is highly distance-dependent, the interaction between neighbouring pigments occurs *via* Förster resonance energy transfer (FRET), a non-radiative dipole-dipole interaction. Upon the absorption of sunlight, the energy is transferred via FRET to the second ring of chlorophylls. These can be found approximately 18 Å above this ring in the outer membrane, containing 18 chlorophyll molecules that are held perpendicular to the plane of the surface. These chlorophylls are bound in pairs by histidine residues at much closer proximity, ca. 9.5 Å, where van der Waals contact between the molecules allows their molecular orbitals to effectively overlap. The interaction shifts the absorption maximum of the pigments to a lower energy, 850 nm, and are therefore known as the B850 chlorophylls. The

close contact of the pigments allows coupling of the excitons, which essentially creates a delocalized system of π electrons where energy is shared coherently around the ring, with energy transfer rates at the femtosecond timescales.[25–27] In particular, the phytol chains have an important role in assisting pigment-pigment interactions. Freer et al. demonstrated that the chains of the three chlorophylls within each apoprotein unit are wrapped around each other, thus creating close van der Waals contact between the molecules. This orientation ensures efficient energy transfer by aligning the Q_x and Q_y transition dipoles.[28] Moreover, experimental results suggest that quantum coherence exists not only between the neighbouring pigments, but also between the B800 and B850 rings themselves, contributing to the highly efficient energy transfer processes observed in these biological systems.[29]

Taking inspiration from the organisation of biological light-harvesting systems, if similar structural principles could be applied in molecular photonic systems, it could help achieve efficient exciton transport between chromophores. Subsequently, combining the organic systems with appropriate functional layers can facilitate long-range energy transfer over the entire photovoltaic cell. To achieve this, it is important to select appropriate materials that can interact favourably with the organic molecules. In this regard, metals with plasmonic properties are an excellent choice due to their ability to interact and strongly couple with the excitonic states of the chromophores, resulting in the formation of long-lived excitons.[30]

1.2.4 Localized surface plasmon resonance

The free electrons at the surface of a metal oscillate about their mean positions. These oscillations are referred to as plasmons, and the frequency of oscillation is called the plasma frequency. In other words, a plasmon is a quantum of oscillation of the electron gas. The surface plasmons associated with metal nanoparticles typically have plasma frequencies corresponding

to the visible region of the electromagnetic spectrum; resonant coupling of these plasmons to incident light leads to the formation of localised modes called surface plasmon polaritons.

The optical properties of a metal can be described by the Drude model, which is based on free electrons moving against a fixed matrix of positive ion cores.[31] The model provides information about the optical response of the material in the form of the material's dielectric function (ε):

$$\varepsilon(\omega) = 1 - \frac{\omega_p^2}{\omega^2 + j\omega\gamma_d} \tag{1.1}$$

In which the plasma frequency is given by the term:

$$\omega_p^2 = \frac{ne^2}{\varepsilon_0 m} \tag{1.2}$$

where n is the refractive index of the material, ε_0 is the permittivity in vacuum, m is the effective optical mass, ω is the frequency and γ_d is the damping constant (referring to the relaxation time of the electron gas). Therefore, the complex dielectric function can be expressed using the real (ε_1) and imaginary (ε_2) components:

$$\varepsilon(\omega) = \varepsilon_1(\omega) + i\varepsilon_2(\omega) \tag{1.3}$$

$$\varepsilon_1 = n^2 - k^2 \tag{1.4}$$

$$\varepsilon_2 = 2nk \tag{1.5}$$

where n is the refractive index of the material and k is the extinction coefficient, which determines the optical absorption of the electromagnetic wave travelling through the medium – essentially quantifying the overall loss of light as it interacts with a material. In the Drude model, when the dielectric function passes through zero (zero-crossing photon energy), it signifies the collective oscillations of the electron cloud. Therefore, for a material to display

plasmonic behaviour, the real part of the complex dielectric function should be negative, and the imaginary part should be small. The photon energy at which this resonance condition is fulfilled is related to the ratio of the density (N) of free carriers (electrons) and the relative effective mass. Metals such as Au and Ag fulfil the resonance condition within the visible wavelength, thus giving rise to a strong absorption peak within this spectral region arising from the plasmon resonance. On the other hand, Al has a higher density of free electrons, and the real part of the complex dielectric function remains negative over a larger spectral range, which results in plasmonic behaviour at higher energies within the UV region.[32] For instance, Al/Al_2O_3 core-shell nanoparticles with diameters in the range of 12-25 nm display resonances at wavelengths as low as 215 nm within the deep UV region.[33]

The fields associated with surface plasmons are evanescent, thus the electromagnetic wave decays exponentially with distance from the surface. The decay length is ca. 20 nm into the metal and $\lambda/2n$ into the dielectric environment, where λ is the wavelength of the incoming light. If the incoming light wave has a wavelength that is equal to or smaller than the metal nanoparticle, the plasmon mode becomes bound and localized to the particle, creating localized surface plasmon resonances (LSPR, Figure 1.7).

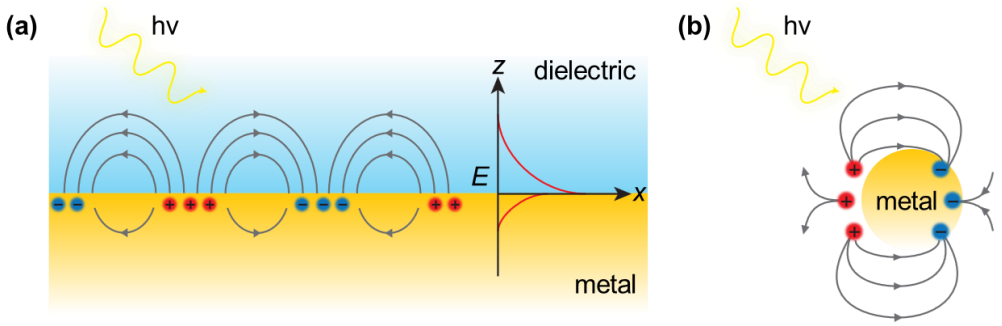

Figure 1.7. (a) Illustration of propagating surface plasmon polariton at the metal-dielectric interface, as well as a representation of the intensity of the electromagnetic wave (*E*) as a function of the distance from the interface. (b) Schematic of the localized surface plasmon resonance bound to a metal nanoparticle.

On the nanoparticles surface, the oscillation of the electron cloud creates positively and negatively charged regions. The opposite charges are bound by coulombic attraction which generates a restoring force with a characteristic frequency. Therefore, if the frequency of the incoming light matches the plasma frequency, the energy is coupled into the plasmon mode and becomes confined to the particle. In a classic example, this phenomenon is indicated by the red colour of colloidal solutions containing gold nanoparticles.[34] The behaviour of the resonant system can be quantified by its quality factor (*Q*-factor), which characterizes its ability to store energy and sustain oscillations at a specific frequency. In other words, it describes the capability of the system to confine energy and can be quantified by the following term:

$$Q = 2\pi \frac{e_s}{e_l} = \frac{f}{FWHM} \tag{1.6}$$

where e_s is the electromagnetic energy stored within the resonator and e_l is the energy lost per one radian of the cycle of oscillation. It can be related to the frequency (*f*) and the full width at half maximum (FWHM) of the resonance. High *Q*-factors allow for longer-lived plasmons, which in turn leads to more efficient and stronger interactions between plasmons and excitons.

Furthermore, plasmon resonances are highly sensitive to their surrounding environment. Therefore, high *Q*-factor resonances provide enhanced sensitivity to detect the changes near the metal surface, typically resulting in the shifting of the resonance absorption maximum, which forms the basis of various biosensing devices.[35]

1.2.5 Plasmonic solar cells

Plasmonic elements are incorporated into a wide range of nanotechnological devices. Their interesting optical properties enable applications in sensing, photovoltaics, catalysis, optics and more.[36,37] Notably, it was discovered that implementing such materials into light-harvesting devices can enhance the efficiency of photon to electron conversion.[38]

Ideally, the active layer in a bilayer solar cell would be ~100 nm. However, the exciton diffusion length in polymer semiconductors is typically a few tens of nanometres, thus the construction of an efficient bilayer cell is difficult.[39] Therefore, the active layer must be as thin as possible to optimise the charge separation and collection processes. At such low thicknesses, maximising the fraction of absorbed light becomes challenging. Alternatively, multiple heterojunction architectures have been introduced, however, the phase-separated structures suffer from stability problems.[40] To improve the performance of organic solar cells, the incorporation of plasmonic materials, such as metallic nanoparticles, into the active layer has been explored. The nanoparticles enable the scattering of incident light and lengthens the distance that photons travel inside the material, resulting in higher chances of light absorption within the active layer. Therefore, thinner active layers can be employed in the solar cell design (Figure 1.8).

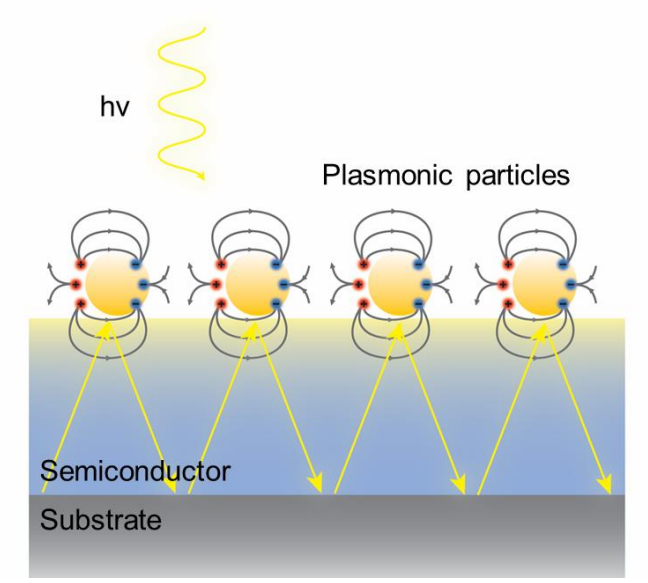

Figure 1.8. Schematic of the active layer of a plasmonic solar cell, where the plasmonic nanoparticles are deposited on the top of the semiconductor film.

The LSPR supported by nanoparticles on the anode can further enhance the PCE, by providing a means of energy transport *via* nonradiative plasmon resonant energy transfer (PRET) to nearby nanoparticles or to the semiconductor layer. This coupling effect results in the transfer of energy over long distances at an ultrafast timescale. Since the LSPR is an evanescent field, the energy can dissipate during the decay process to create hot carriers, which are electrons with sufficient energy to overcome the required energy barrier for the electron injection processes.[41] For example, dye-sensitized solar cells (DSSC) consist of a semiconductor material (typically titanium dioxide, TiO_2) coated with a photosensitive dye. The dye absorbs photons and generates electrons. When Dang et al. incorporated plasmonic multiple-core-shell structured oxide-metal-oxide nanoparticles into DSSCs, the PCE of the system increased from 8.3% to 10.8%.[42] Such improvements in the past have only been achieved by methods that focussed on creating panchromatic cells that cover the full-spectrum which typically required expensive and time-consuming manufacture processes. Similarly, in silicon-based solar cells, the PCE can be improved by ca. 30% by incorporation of plasmonic elements.[43] Needless to

say, these advanced methods have great potential and have already proved to be beneficial in the field of photovoltaic technologies.

1.2.6 Plasmon-exciton coupling

In classical physics, two harmonic oscillators are coupled when there is an exchange of energy between them. This can be observed when two pendulums are attached to and suspended from the same string, as shown on Figure 1.9.

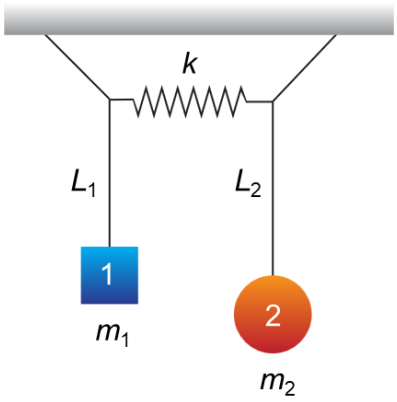

Figure 1.9. Representation of two pendulums of different masses (m_1, m_2) hanging from a string at distance L_1 and L_2, coupled by a spring (k). A simple model to show the behaviour of a coupled harmonic oscillator.

When the pendulums are of different shape and size, and are oscillating at different frequencies and amplitudes, the coupling effect eventually creates a hybrid mode of the two oscillators, with mixed characteristics of the original systems. In quantum theory, photonic modes can be treated as harmonic oscillators, with the energy E_n of an oscillator in the n^{th} quantum state being given by:

$$E_n = \left(n + \frac{1}{2}\right)\hbar\omega \qquad (1.7)$$

where $\hbar$ is the reduced Planck constant and n is an integer ≥ 0. In general, the coupling interaction can be classified into three regimes depending on the coupling strength between two quantum states. This is characterised by the Rabi frequency (Ω_n) and the coupling coefficient (g):

$$\Omega_n = \sqrt{4g^2(n_p + 1) + \frac{\Gamma^2}{4}} \tag{1.8}$$

where n_p is the photon energy. $\Gamma = \gamma_p - \gamma_0$, with γ_p being the decay rate of the plasmon mode and γ_0 is the decay rate of the exciton. The three coupling regimes are the following:

1) Weakly coupled plasmons and excitons, where the interaction is characterized by minimal energy shifts or hybridization between the two entities. Here, the wave functions of the coupling components are unperturbed and the plasmon and exciton energies remain largely distinct, resulting in separate peaks in absorption and emission spectra. These spectral features do not interact strongly with each other, and the system's optical properties predominantly reflect the individual behaviours of plasmons and excitons. However, the emission rate of the exciton may be modified due to the Purcell effect (see further details in Section 1.3.3).[44] In weakly coupled systems, $g \ll \frac{1}{2}(\gamma_p - \gamma_0)$.

2) Intermediate coupling, where constructive and destructive interferences give rise to mode splitting in the far-field optical spectrum. Here, g takes the value of $\frac{1}{2}(\gamma_p - \gamma_0) < g < \sqrt{\frac{1}{2}({\gamma_p}^2 - {\gamma_0}^2)}$. The splitting in the spectrum is often characterised by a Fano lineshape. Coherent energy transfer may be present between the two components is typically influenced by damping from one or more of the modes.[45]

3) In contrast, strong coupling leads to significant hybridization of the electronic states, forming new eigenstates of the system known as polaritons. In this regime, the absorption and emission spectra still exhibit two distinct peaks, but the separation between these peaks is notably larger than in weak coupling. The key feature of strong coupling is the observable splitting between polariton states (Rabi splitting), giving rise to lower and upper polariton branches in the absorption spectrum. For a strongly coupled system, $g > \sqrt{\frac{1}{2}({\gamma_p}^2 - {\gamma_0}^2)}$.[46] These polaritons display unique optical properties, including enhanced light-matter interactions.

Tsargorodska et al. discovered that attachment of light-harvesting (LH) complexes from purple bacteria attached to gold nanostructure arrays yielded a splitting in the plasmon band that was attributed to strong coupling between the plasmon mode and excitons in the chromophores in the LHCs (Figure 1.10).[47]

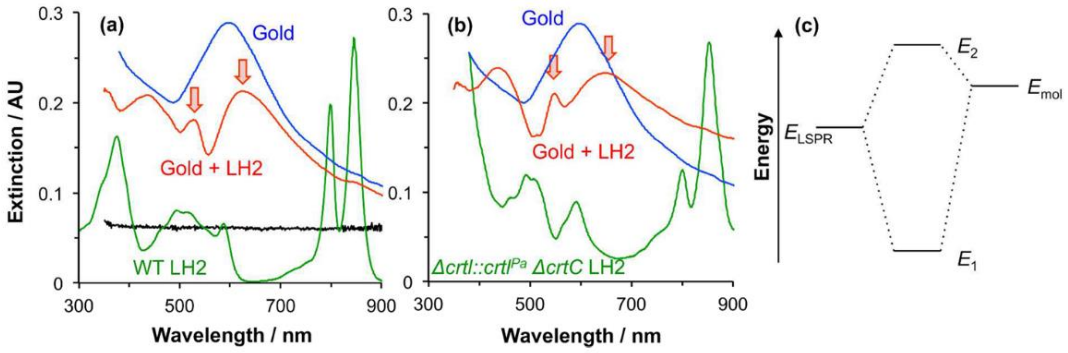

Figure 1.10. Extinction spectra demonstrating the strong plasmon-exciton coupling phenomenon. (a) Spectra of arrays of gold nanostructures before (blue) and after (red) attachment of wild type LH2 and (b) the mutant of LH2. The black line represents a monolayer of wild-type LH2 on glass. (c) Illustrative energy diagram of the hybridization of the LSPR and exciton states, which yields two new peaks with energies E_1 and E_2. The Figure was taken from the work of Tsargorodska et al.[47]

The experiments were repeated using maquette proteins that mimic biological complexes. It was found that although lower in intensity, the plasmon couples with the Q_x transition of chlorophyll *a*. This is because the transition dipole is perpendicular to the plane of the surface, aligning with the direction of the plasmon radiation. Within the strong coupling regime, the energy exchange between light and matter occurs at a rate that is faster than their individual decay rates, leading to coherent ultra-fast exchange of energy. The plasmon mode and exciton are hybridised to form two new "plexitonic" states, and the distance between the absorption maxima of the newly formed states is proportional to the strength of the coupling. The states possess energies that are different from the original oscillators. The scaled coupling energy of the system (E_c) can be estimated using the following expression:

$$E_c \approx \sqrt{\frac{\mu^2 E_{mol}^2}{\varepsilon_0 \varepsilon_b E_{LSPR}} \frac{N}{V_{LSPR}}} \tag{1.9}$$

Here, E_{mol} is the exciton energy and E_{LSPR} is the uncoupled LSPR energy. N is the number of dipoles located within the mode volume of the LSPR field, V_{LSPR}, μ is the transition dipole moment for the exciton dipole, ε_o is the permittivity of free space, ε_b is the relative permittivity medium. The expression demonstrates that the plasmon mode couples to an ensemble of excitons within the plasmon mode volume. Therefore, the density of chromophores within the plasmon mode influences the resulting coupling energy of the system. *I.e.,* a higher number of excitons within the mode volume can lead to larger coupling energies, and therefore stronger coupling. This correlation was demonstrated by Todisco et al. using cyanine dye molecules deposited onto arrays of plasmonic silver nanoparticles. The strength of the coupling was tuned by controlling the number of dipole molecules on the surface to achieve weak, strong and ultrastrong coupling regimes.[46]

The Jaynes-Cummings model is a useful tool for understanding coupled systems. The model describes the detuning (Θ) of the system, which refers to the energy difference between the exciton state and the LSPR state. It is defined as:

$$\Theta = \omega_p - \omega_0 \tag{1.10}$$

where ω_p is the plasmon frequency and ω_0 is the exciton frequency. By considering the coupling strength (Ω) which characterizes the interaction between these states, the frequencies of the coupled modes can be calculated using the following formula:[48]

$$\omega_{\pm} = (\omega_p - \omega_0)/2 \pm \sqrt{\Omega^2 + (\omega_p - \omega_0)^2} \tag{1.11}$$

Analysing the change in the energies of these coupled modes against system's detuning provides insights into the behaviour of the coupled system. In particular, the energy level diagram for the Jaynes-Cummings model can exhibit avoided crossings, where the energies of the coupled modes in the spectrum that would otherwise cross (*i.e.*, have the same energy) do not cross due to the strong coupling between the plasmon and exciton states (Figure 1.11).

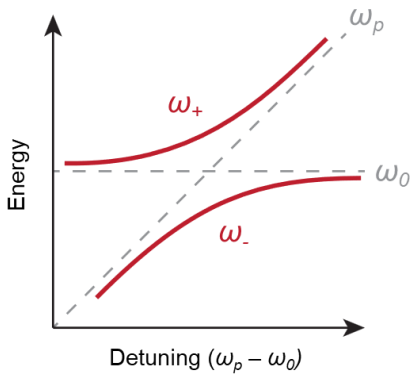

Figure 1.11. Representative plot of the energy levels of the coupled state in relation to the system's detuning, showing the avoided crossing phenomenon. The red lines represent the energy levels of the upper (ω_+) and lower (ω_-) energy coupled states, while the dashed lines shows to the energy of the uncoupled energy levels of the plasmon (ω_p) and exciton states (ω_0).

This avoided crossing depends on the coupling strength. At the avoided crossing point, the energy states of the coupled system are hybridized states, representing a mixing of the plasmon states and exciton states. Hence, the analysis of the energy levels of the coupled states against the detuning enables the determination of whether the system exhibits strong coupling.

Due to the ultrafast energy exchange between excitons and the plasmon mode, the strong coupling enables the transfer of energy between non-adjacent excitons. This phenomenon could potentially be exploited for the transportation of energy over long distances at ultrafast rates in light-harvesting devices. In particular, the energy of sunlight can could be guided on a surface while preventing most of the undesirable decoherence and charge-recombination processes that most solar energy devices suffer from.

1.2.7 Plexcitons in light-harvesting technologies

To achieve strong plasmon-exciton coupling in a protein monolayer, the minimum area dipole density required is ca. 10^{17} m^{-2} within the plasmon mode volume.[47] It can therefore be assumed that having a sufficient number of dipoles on plasmonically active surfaces will lead to a coupling interaction. Control over the coupling strength would allow fabrication of devices with precise characteristics. However, in existing technologies the maximum number of dipoles bound to the surface is currently subject to limitations, as most approaches attach chromophores in a 2D arrangement. Increasing the exciton density on the surface thus requires the deposition of multilayers of pigments. A common approach is to spin-coat the molecules onto the surface. For instance, chlorophyll *a* molecules were spin-coated onto nanostructured gold in plasmon-sensitized solar cells, leading to an enhancement of the PCE due to the formation of plexcitonic states from strong plasmon-exciton coupling.[49] In a similar experiment, an electrode composed of TiO_2 and nanostructured gold was coated with chlorophylls by dipping it in a solution for 12 hours. The presence of the plasmonic gold slowed charge-recombination processes and thus improved charge separation processes in the cell.[50] Chlorophyll can also be used in a combination with other biological dyes such as anthocyanin and betalain. When the mixture was bound to TiO_2 in dye sensitised solar cells, a PCE of 3.73% was achieved.[51] While these examples demonstrate the value of incorporating the principles of natural photosynthesis into artificial devices, it must be noted that in these examples the pigments are bound to the surface via physisorption. This offers a relatively weak attachment to the surface and little control over the arrangement of molecules. Furthermore, it is believed that physisorbed chlorophylls lie parallel to the plane of the surface, resulting in a weak interaction between neighbouring pigments and potential concentration quenching effects due to aggregation.

Instead, when chlorophylls are anchored with the use of a self-assembled monolayer (SAM), it allows efficient π-π stacking of the chlorin rings with the molecules oriented almost perpendicular to the surface. This leads to stronger interactions between pigment molecules, including more effective exciton coupling.[52]

1.2.8 Attachment of chromophores to solid surfaces

Molecules can be attached to a surface by either physisorption or chemisorption. Chemisorption offers the benefit of robust immobilisation because of the formation of strong specific interactions, such as covalent bonding, between the adsorbate and the substrate. One widely-used approach is to form a densely packed self-assembled monolayer (SAM), which covers the surface as an ultra-thin film. SAMs are isostructural with Langmuir-Blodgett films (*i.e.* they consist of close-packed, 2D crystalline assemblies of organic adsorbates. However, in contrast to Langmuir-Blodgett films, SAMs form spontaneously by adsorption from a dilute solution of the adsorbate in a suitable solvent, driven by strong specific interactions between the adsorbate head-group and the substrate combined with non-covalent interactions between the alkyl chains of the adsorbates (Figure 1.12).

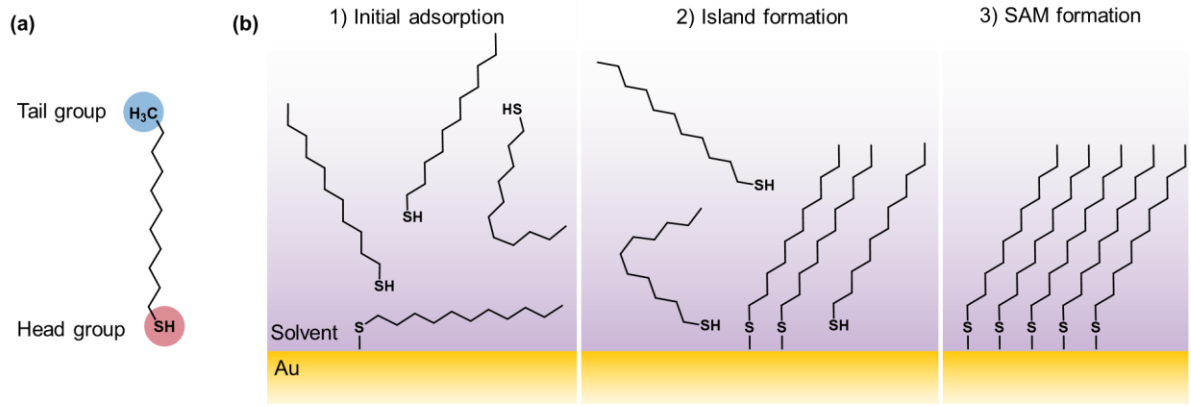

Figure 1.12. (a) Chemical structure of an alkylthiol molecule, 1-undecanethiol, showing the head group (thiol) and tail group (methyl) functionalities used in the SAM formation. (b) Representation of the formation of a SAM of alkylthiols from solution on gold. The steps involve the initial disordered adsorption to the surface, followed by formation of molecular islands of the molecules until an ordered SAM is eventually created.

Based on the choice of adsorbates, the SAM can act as an anchor to immobilise further moieties and build supramolecular systems from the bottom up on the surface while providing control over the position and orientation of each molecular building block. Thus, it is important to consider the functionality that forms the covalent bond with the surface (head group), the functional group on the opposite end of the molecule (tail group) and the backbone that connects the two. Therefore, selective attachment of molecules and higher order assemblies can be achieved by the use of an appropriate tail group, which provides the anchoring point on the surface.

In addition to their spatial organisation ability, the use of SAMs offers further advantages. SAMs are commonly employed to avoid the quenching effects of metal surfaces. The quenching effect results from the nonradiative dissipation of energy due to the energy transfer to the conduction electrons of the metal. This is commonly observed in fluorescence, and is distance-dependent, meaning that it becomes less pronounced as the distance between the metal

and the fluorophore increases. In the context of organic photovoltaics, the incorporation of a SAM serves as a spacing layer to prevent the quenching of the excited states of the materials. This is of particular importance in the design of organic photovoltaics, as the SAM can prevent undesired interferences with the energy transfer processes within the light-harvesting materials.

To design organic photovoltaics based on the principles of light-harvesting in nature, it is important to understand how such molecular systems perform their functions *in vitro*. Taking the example of LH complexes, in 2007 Kondo et al. constructed a model system to study the excitation energy transfer mechanism of the reaction centre (RC) containing LH1 complexes. Using SAMs of amino-terminated thiols with varying methylene chain lengths, the complexes were attached to gold electrodes in a 2D arrangement (Figure 1.13).[53]

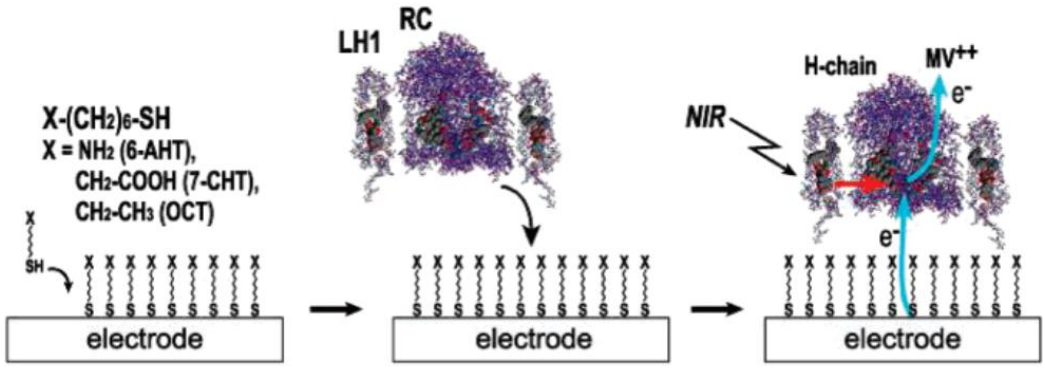

Figure 1.13. Illustration of the attachment of LH1-RC complexes to gold electrodes functionalized a SAM of amino-terminated thiols. The electron transfer pathway is indicated upon near-IR (NIR) irradiation. The figure was taken from the work of Kondo et al.[53]

The researchers found that the incorporation of the SAM prevents the denaturing of the proteins on the gold electrode, while providing sufficient electric contact between membrane protein and the electrode. Furthermore, the methylene chain length determined the overall efficiency of the electron transfer, where the maximum photoinduced photocurrent response was detected when the chain length was 6 carbon long. Using shorter SAMs, the excited states of the

chromophores are quenched by the metal, while longer SAMs act as an insulator, decreasing the photocurrent density. At the ideal distance, a photocurrent density of $5.1 \pm 0.5 \times 10^7$ A cm^{-2} Abs^{-1} was achieved, but only when the LH-RC complexes were well-organised on the surface. The discoveries highlighted the significance of the structural arrangement of the light-harvesting components, both in the vertical and lateral dimensions of the surface, to maximise photocurrent production. [54]

Applying these principles, scientists explored the construction of artificial light-harvesting systems based on biological architectures to generate photocurrent. Gold electrodes are typically functionalised with a monolayer of thiol-containing molecules, which form a strong covalent bond upon adsorption. However, there are various different methods to create SAMs on electrodes. For example, indium tin oxide electrodes can be functionalized with 3-aminopropyltrietoxysilane (APTES), which is highly effective at binding LH1 complexes *via* hydrogen bonding and electrostatic interactions.[55]

In DSSCs electrons are then injected into the semiconductor material, creating an electric current. In such cells, light absorption can be improved with the introduction of polymeric hole transporters; however, the electron transfer processes from the polymer to the metal oxides are often inefficient. A SAM of fullerene-based electron acceptors functionalized on mesoporous TiO_2 can help assist effective electron transfer and enhance photocurrent generation.[56] Similarly, Wang et al. showed that functionalising a mesoporous TiO_2 film with carboxy-chlorophyll derivatives can improve the PCE of $Cs_2AgBiBr_6$ double perovskite solar cells to 3.11%, with a 27% increase in short-circuit current density.[57]

Therefore, SAMs can provide a relatively simple means of surface functionalisation with high control over molecular functionalities, arrangement and orientation. However, for the design of plexciton-enhanced solar energy capture, these methods do not provide the means to increase

the number of dipoles vertically on the surface, as the system is confined to a monolayer of pigments.

1.2.9 Beyond the 2D architectures

The essential components of a biological light-harvesting complex are a protein scaffold and its complement of pigment molecules. The efficiency of the energy transfer steps is determined by the relative proximity and orientations of the pigment molecules to each other. In some complexes, such as LH2, which has a highly symmetrical structure, there appears to be spatial organisation of pigments, but in others, such as plant photosystem II (LHCII), spatial organisation is lacking. In all cases, the LHCs are formed in membranes, and the pigment molecules have an orientation relative to the membrane, but it is not, in fact, obvious whether this is necessary for their light-harvesting function. Another important aspect of LHCs is their pigment molecule density. For example, the plant-based LHCII contains a significantly higher density of dipoles than can be achieved in an organic solvent without unfavourable charge recombination processes.[58]

The construction of a covalently connected three-dimensional system would enable overcoming the limitations set by previous designs. In fact, Lishchuk et al. demonstrated that light-harvesting systems isolated from purple bacteria, spinach or artificially made photosynthetic protein complexes, which contain multilayered pigments held by a protein backbone, can all exhibit strong coupling with plasmonic gold surfaces.[59] However, from a technological perspective, the use of biological complexes in photovoltaics is impractical due to the sensitive nature of the proteins. Instead, the use of polymer architectures can fulfil the same functions as the protein backbones of LHCs.

1.2.10 Polymer brushes as molecular building blocks

Polymer brushes are thin films that consist of densely packed polymer chains covalently attached to a surface. The properties of the film depend on the selection of initiators, monomers and polymerisation process, allowing control over molecular composition, physical and chemical properties of the brush. The polymerization produces unique surface-tethered polymer architectures, suitable for a wide range of applications. The polymer chains are chemically bonded to the surface, with reduced degrees of freedom to adopt different conformations due to steric hindrance. This leads to dense networks of chains vertically stretched away from the surface, where the density of the brush depends on the concentration of anchoring sites.

There are two main synthesis routes to create brush films, the "grafting from" method, in which the polymer brush is grown directly from the surface and the "grafting to" method, where the polymer chains are prepared freely in a solution and are subsequently attached to a surface. The first method typically results in a higher density brush, while the latter approach offers a reduced density polymer film, prepared using a more complex fabrication process. For this reason, "grafting from" is often preferred over "grafting to", and the density of the brush is controlled by other means, discussed later in this chapter (Figure 1.14).

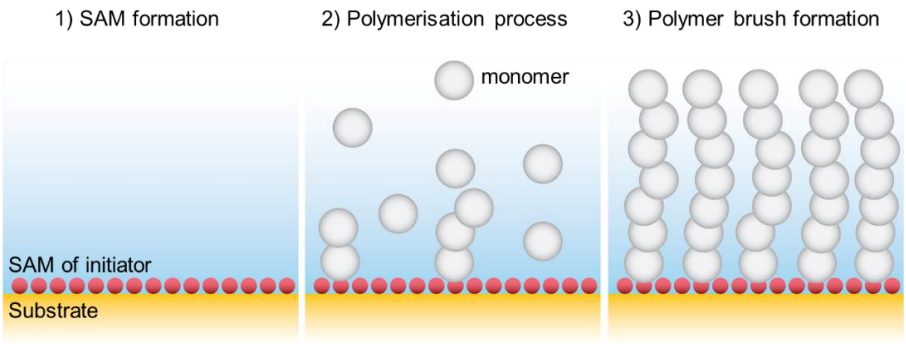

Figure 1.14. Illustration of the synthesis of surface-tethered polymer brushes using the "grafting from" method. The process involves forming a SAM of initiator molecules on the substarte, followed by the polymerisation process of choice to yield the formation of a polymer brush on the surface.

The first step in fabrication is the immobilization of an initiator to a solid surface. In surface-initiated atom transfer radical polymerisation (SI ATRP), the initiator is typically an alkyl halide bound to the surface. ATRP is a living radical polymerisation in which the initiator is transferred to the growing polymer chain end after each monomer addition cycle. It is important that the selected monomer can stabilise the propagating radical species; these commonly include styrenes, methacrylates, methacrylamides and acrylonitrile. A metal catalyst with two accessible oxidation states is required, typically a copper complex, which initiates the polymerisation *via* one-electron transfer to form the radical species of the initiator. A suitable catalyst provides fast initiation, which is detrimental to achieve narrow molecular weight distribution and ensure that all living chains propagate at a similar rate. This is a major advantage of ATRP, as it provides controlled chain growth with low polydispersity. However, due to the oxygen-sensitive nature of the catalyst, the reaction must be carried out under inert atmosphere to prevent oxidation processes converting the active Cu(I) species into Cu(II) and halting the reaction. To circumvent this, a variation of SI-ATRP may be carried out, known as "activators regenerated by electron transfer" (ARGET) ATRP (Scheme 1.1).[60]

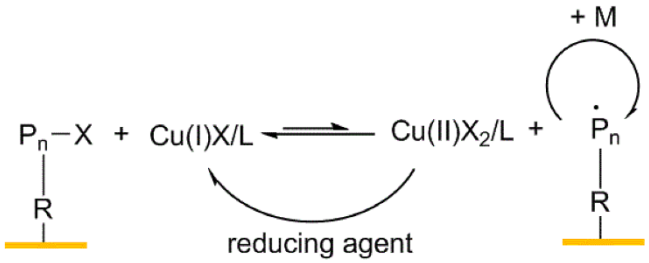

Scheme 1.1. Simplified mechanism of surface-initiated ARGET ATRP in which a reducing agent is employed to regenerate the catalyst. *M* denotes the monomer, P_n is the growing polymer chain, *X* is a halogen and *L* is a chelating agent.

The method includes the addition of a reducing agent in excess, *e.g.* ascorbic acid, to regenerate the active Cu(I) species in solution while also mopping up any dissolved oxygen in the reaction mixture.[60] This step significantly simplifies the polymerisation procedure, enabling the synthesis of polymer brushes with a wide range of functionalities without the need of inert conditions. Thus, complex systems may be created *via* relatively simple and cost-effective methods.

Based on the monomer of choice, different functionality and reactivity can be introduced to the brush. These thin films are therefore ideal for the specific binding and immobilisation of single molecules, enzymes or cells, enabling the building of functional organic layers and the characterisation of molecular functions and behaviour to different stimuli. For example, biologically inert poly(2-hydroxyethyl methacrylate) (pHEMA) brushes possess a pendant hydroxy functional group which can be modified to introduce biologically active functional groups. To create a cell-adhesive surface, arginine-glycine-aspartic acid (RGD) peptide units may be introduced. [61] This tripeptide is found in the cell-adhesion protein, fibronectin, which is involved in regulating cellular attachment where RGD units are bound to integrin membrane receptors. Using this approach, Tugulu et al. studied human umbilical vein endothelial cells by immobilizing them to pHEMA brushes.[62] The same researchers have derived a method to

functionalise the cell-resistant and antifouling poly[oligo(ethylene glycol)methacrylate] (pOEGMA) brushes with O6-alkylguanine-DNA-alkyltransferase (AGT) fusion proteins. This was achieved by first converting the pending alcohol groups into *p*-nitrophenyl chloroformate, then introducing a benzylguanine derivative that provides the binding sites for AGT proteins. This method was found to be selective of the AGT proteins only, and is useful in the study of AGT moieties with a protein of interest.[63]

One of the most widely used approaches for protein binding to surfaces is the use of carbodiimide crosslinking, otherwise known as the "EDC/NHS" coupling reaction, in which a carbodiimide and N-hydroxysuccinimide are used to convert a carboxylic acid to an active ester that can react with an amine to form an amide linkage. For example, pHEMA and pOEGMA brushes can be derivatised with the antibody immunoglobulin G (IgG), to which proteins can coordinate to.[64]

Given its compatibility with a wide range of monomers featuring diverse functionalities such as alcohols, carboxylic acids, and epoxy groups, SI ATRP opens up promising avenues for the modification and functionalization of polymer brushes.[65] Once an ideal attachment scheme is established between the monomer and guest molecules, another important factor to consider is the extent of functionalisation, *i.e.* the "yield" of the reaction. Brushes synthesized using the "grafted-from" method typically exhibit a tightly packed, dense structure, which can prevent the penetration of larger molecules into the brush. This results in a predominant attachment at the uppermost layers of the film. When the objective is to fully derivatise a polymer chain, as in the creation of light-harvesting networks with high pigment concentrations, it may be necessary to decrease the brush density, thereby achieving a more flexible and accessible molecular structure that reagents can diffuse into for binding.

1.2.11 Relationship between the grafting densities and properties of surface-grafted polymers

One approach to reduce the grafting density of surface-tethered polymers involves reducing the density of initiator sites on the surface by coadsorbing the initiator moiety with an inert adsorbate. Bao et al. employed this technique to create pHEMA brushes with varying film densities. Their findings demonstrated a direct correlation between reduced initiator density and the thickness of the polymer films.[66] This is expected, as polymer chains that have more spatial freedom around them can adopt a more relaxed conformation to collapse onto themselves (known as the "mushroom regime"), thus lowering their average height in dry conditions (Figure 1.15).

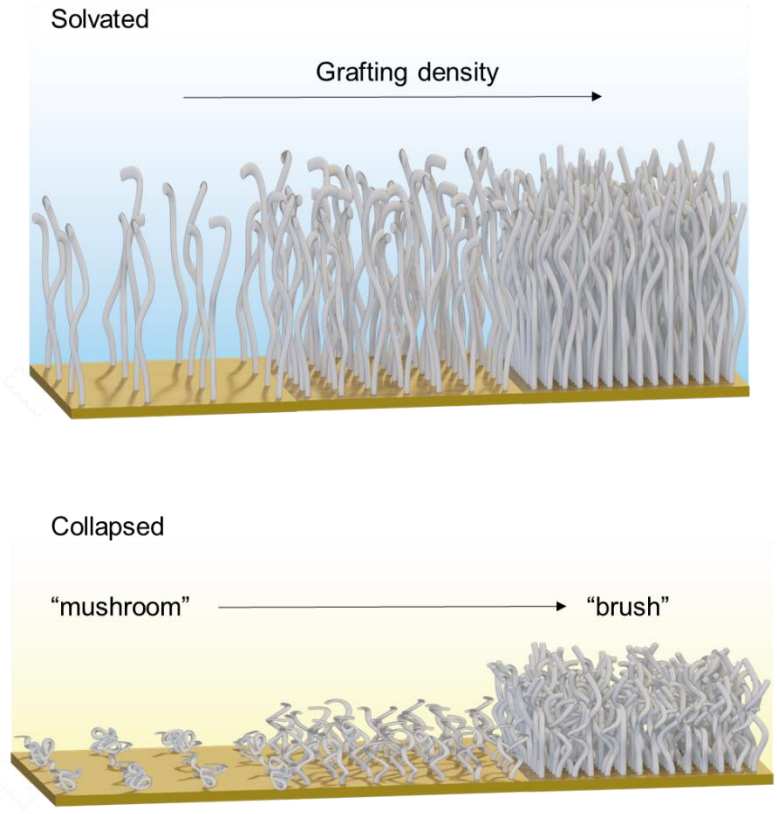

Figure 1.15. Illustration of the conformation of surface-grafted polymers as a function of the grafting density, in their solvated and collapsed forms.

The natural tendency of an isolated polymer chain on a surface is to collapse, forming a random coil which dimensions are defined by the radius of gyration. However, when polymer chains are grafted sufficiently closely to a surface, they experience steric repulsion, causing them to swell away from the surface ("brush regime").

The grafting density of the polymers influences the reactivity of the chains. When using smaller reagents in post-polymerisation modification, brushes can exhibit nearly quantitative attachment rates.[67,68] However, the attachment of bulkier reagents becomes problematic in dense polymer films. Hence, the creation of reduced density surface-grafted polymer films is particularly appealing for enabling subsequent post-synthesis functionalization.

Zapotoczny et al. used mixed SAMs, formed by coadsorbing p-tolytrimethoxysilane with p-(chloromethyl)phenyltrimethoxysilane onto silica, to vary the grafting density of 3-(trimethylsilyl-2-propynyl)methacrylate brushes.[69] By varying the ratio of the two adsorbates on the surface, the initiator density was controlled on the surface. Brushes were synthesised with high to low grafting densities, and subsequently reacted using copper-catalysed "click" chemistry with silicon phthalocyanine chromophores, containing two azide moieties. The attachment resulted in the linking of neighbouring polymer strands, where the highest density brushes experienced diffusion limited rates of the "click" reaction. Therefore, dense brushes possessed lower dye concentrations. In another study, researchers controlled the grafting density of hydroxy-terminated oligo(ethylene glycol) methacrylate (OEGMA) and methoxy-ended OEGMA films on silicon substrates by diluting the SAM with an inert silane. Subsequent attachment of azobenzene units revealed that the films with reduced density polymers exhibited a yield of 50%, whereas the brushes with the highest density only achieved a yield of 10%.[70] At sufficiently low grafting densities, it becomes possible to attach even larger materials to brushes at significantly high concentrations. For instance, 13 nm gold nanoparticles were

incorporated into poly(N,N-(dimethylamino ethyl) methacrylate) brushes. The initiator density was regulated using a combination of 2-bromo-2-methyl-N-(3-(triethoxysilyl)propyl)propenamide initiator and an inert silane. When the polymer chain density was high, ca. 0.5 nm^{-2}, the nanoparticles adhered primarily to the upper layer of the brush, resulting in relatively low particle concentrations. However, when the grafting density was reduced to ca. 0.26 nm^{-2}, the concentration of particles increased by twofold.[71]

Thus, the "grafting from" approach allows the fabrication of surface-tethered polymers. The use of mixed SAMs on the surface offers control over the grafting density and consequently, the reactivity of the polymer networks.

1.3 Metal halide perovskites in optoelectronic devices

A different approach to enhance the PCE of hybrid solar panels involves exploring alternative materials with exceptional light-absorbing characteristics. This exploration has led to the discovery of metal halide perovskites, which experienced a surge in popularity over the recent years owing to their outstanding optical properties.[72] The perovskite crystal structure was first derived from the mineral, $CaTiO_3$, which was discovered in 1839.[73] However, it wasn't until the past decade that researchers began to explore the properties of this crystal composition, after Miyasaka et al. demonstrated their potential as efficient absorbing materials for solar cells.[74] Since their emergence, perovskites have become a central focus in energy research, showing remarkable progress that resulted in highly competitive PCEs within solar cell technologies.[75] The rapid development paved the way to achieve photoluminescence quantum yields (PQY) exceeding 90%, strong optical absorption and low charge recombination rates with micrometre scale exciton diffusion lengths.[74,76–78] Consequently, the PCE of hybrid

organic/inorganic perovskite solar cells improved significantly from 3.8% to 22.1% in recent years.[79–82] Simultaneously, the photoluminescence (PL) properties of metal halide perovskites have attracted significant interest. The following sections explore the unique light-emitting properties of perovskites and their potential to revolutionize not only solar cell technologies but also the broader landscape of lighting, display technology, and sensor applications.

The emission characteristics of perovskites are strongly linked to their structural properties, such as chemical composition, crystal structure, and material dimensions, offering opportunities for precise tuning of the PL. More specifically, tailoring these properties allows for the modification of the material's band gap, defined as the energy difference between the valence band maximum and the conduction band minimum. The size of the band gap determines the optical properties of the material. Absorption of light leads to the formation of an exciton which subsequently relaxes via radiative decay, leading to the emission of a photon (Figure 1.16).

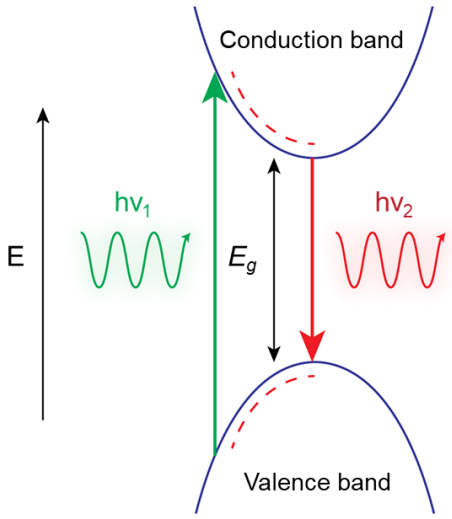

Figure 1.16. Energy level diagram of the photoluminescence process, involving the valence and conduction bands of a material. E_g refers to the energy of the band gap.

The wavelength of the emitted light is determined by the material's bandgap and the exciton binding energy. The latter refers to the energy required to separate an exciton into an electron and a hole. Highly efficient LEDs with remarkable colour purity have been developed with the use of perovskite materials, demonstrating a luminous intensity of 43 candela per ampere, which approaches the performance of commercially available phosphorescent organic LED lights.[83] Fine-tuning the bandgap serves as a versatile method to shape the material's optical properties. Notably, researchers have achieved a wide range of PL wavelengths across the visible and near-infrared spectral regions by simply adjusting the material's chemical composition, size, and structure.[84]

1.3.1. Perovskite structure and optical properties

Perovskites are crystalline materials characterized by the formula of ABX_3, where "A" is an organic or inorganic monovalent cation (*e.g.* Ca^{2+}, Sr^{2+}, Ba^{2+}, methylammonium (MA), formamidinium (FA)), "B" is a bivalent metal cation (*e.g.* Pb^{2+}, Cu^{2+}, Sn^{2+}, Co^{2+}, Ge^{2+}, Eu^{2+}) and "X" is typically a halogen (Cl^-, Br^-, I^-). The representative crystal structure is shown on Figure 1.17.

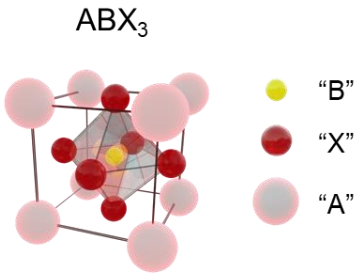

Figure 1.17. Cubic unit cell representation of the crystal structure of perovskites.

In order to assess the probability of perovskite structure formation during synthesis, the Goldschmidt tolerance factor (t_G) and the octahedral factor (μ_{oct}) should be taken into

consideration, which considers the ionic radii of the "A", "B" and "X" components. In the case of perovskites, the tolerance factor typically falls in the range of $0.8 \leq t_G \leq 1.0$.[85,86] Generally, for successful perovskite formation, the cations should be small enough to compensate for the larger ionic radii of the metals ($t_G \approx 1$). For instance, the combination of Pb^{2+} (1.19 Å) with I^- (2.20 Å) requires that the "A" component is limited to a maximum of 2.9 Å. This requirement is met by using small organic molecules consisting of less than three C-C or N-N bonds, such as "MA" or "FA".[87] The chemical composition of the perovskite structure plays an important role in tailoring its band gap. Besides the electronic properties of the constituent ions, variation of the "ABX_3" structure directly impacts bond lengths and angles within the crystal, subsequently influencing the overall perovskite lattice. For example, a larger ionic radius of the "A" cation leads to an expanded lattice, which decreases the band gap, leading to lower energy emissions.[88] On the other hand, the use of larger "X" cations typically leads to higher energy emissions, since the changing the cation causes a shift in the energy of valence and conduction bands relative to each other.[89]

Another approach to adjust the band gap and control the emitted wavelength of light involves manipulating the physical dimensions and structure of the perovskite crystals. By adjusting the organic and inorganic components, as well as the reaction conditions (*e.g.*, temperature and solvent system), 3D, 2D, 1D and 0D perovskites can be synthesised (Figure 1.18).

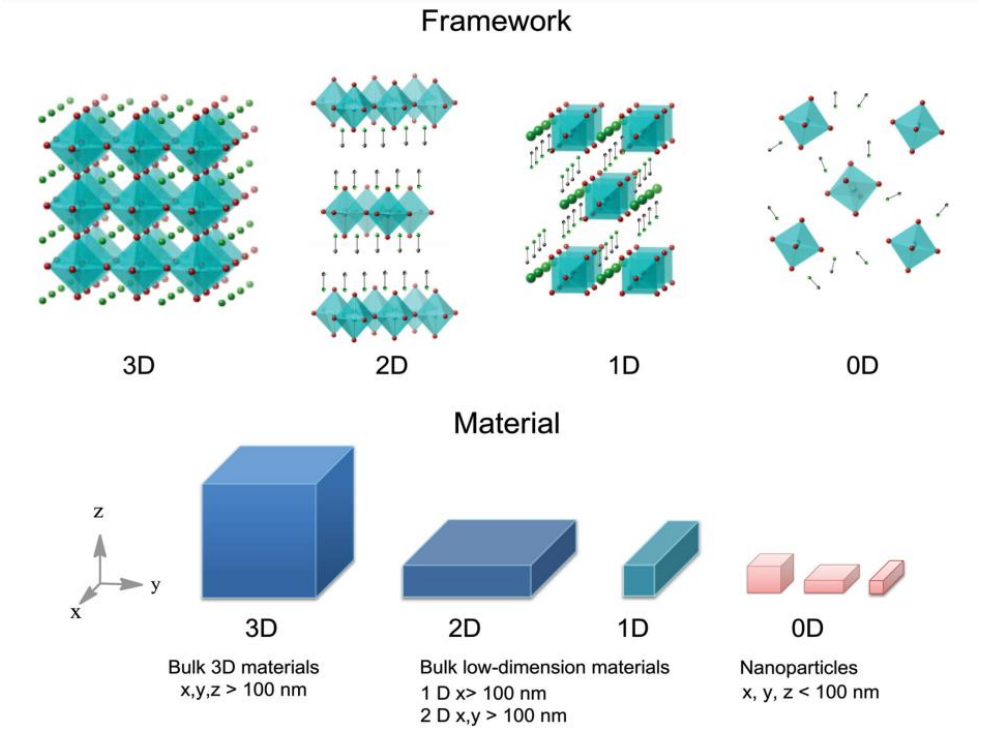

Figure 1.18. Schematic of the 3D, 2D, 1D, and 0D perovskite frameworks (top) and dimensionality of the materials (bottom). Figure was taken from the work of González-Carrero et al.[90]

Each morphology carries its set of advantages and disadvantages with respect to optoelectronic properties and stability. For example, the 3D perovskite structures, which are characterised by having multiple repeat units of the corner-sharing metal halide $[BX_6]^{4-}$ octahedra, are prone to degradation at ambient conditions.[87] On the other hand, low-dimensional perovskites with 2D structures, where the perovskites are one monolayer thick and extend across a 2D plane, exhibit increased resistance to moisture-induced degradation.[91] Additionally, they possess enhanced electron-hole Coulomb interactions forming tightly bound excitons within the energy range of 300-400 meV, which leads to high photoluminescence efficiencies.[92] Further reducing the particle size, the 2D sheets can be divided into perovskite wires and individual octahedra, creating 1D and 0D perovskite particles, respectively.[93] When the size of a perovskite nanoparticle decreases, the available energy levels for electrons and holes become quantized

due to the quantum confinement effect. In other words, the energy levels of electrons and holes become more discrete, leading to a smaller range of available energy transitions during recombination processes. Typically, smaller nanoparticles possess higher energy bandgaps in comparison to their higher-dimensional bulk counterparts.[94] In addition, 0D quantum dots exhibit narrower emission bandwidths and high exciton binding energies, while their unique structural properties lead to increased stability against moisture-induced degradation.[84] Leveraging the quantum confinement effect thus provides a versatile means to finely tune the material's optical and electrical properties.

1.3.2 Post-synthesis tuning of the photoluminescence

The ability to manipulate the band gap and consequently the PL properties of perovskites by altering their chemical composition, size, and particle shape has been extensively explored and established.[84] As discussed earlier, employing distinct particle sizes and morphologies presents advantages and disadvantages in terms of stability and optoelectronic characteristics. Therefore, in certain applications, preserving the intrinsic crystal properties, while selectively altering the PL characteristics, can offer advantages. In this regard, post-synthesis modification processes provide the opportunity to adjust the PL properties without altering the entire perovskite structure. However, to date, this remains a significant challenge.

One approach to adjust the PL properties after synthesis is to alter the material's chemical makeup via ion exchange.[95,96] Akkerman et al. demonstrated that the optical characteristics of colloidal $CsPbX_3$ nanoparticles could be tailored post-synthesis by exposure to Cl^-, I^-, or Br^- ions.[97] This method allows tuning of the nanoparticle emission across a wide spectral range from ca. 410 nm to 650 nm. The drawback of this is that the repeated ion displacement can introduce defects in the crystal structure, ultimately reducing the PL brightness and leading to bandwidth broadening. Alternative to the chemical exposure method, inducing distortions to

the perovskite lattice by applying external stimuli can also modify the PL emission wavelength. For example, in the case of $MAPbI_3$, the change in temperature from 12 K to 300 K induces a transition from tetragonal to orthorhombic phase around the temperature of 150 K. The transition is characterized by a shift in the emission wavelength from 780 nm to 750 nm.[98] Similarly, applying pressure to the crystals can lead to lattice distortions. In particular, anisotropic deformation of 2D phenylethylamine lead iodide ($(PEA)_2PbI_4$) perovskite can be achieved by subjecting the crystal sheets to high pressure.[99] Increasing the pressure from 0 GPa to 7.6 GPa results in a redshift from 521 nm to 602 nm. However, with increasing pressure, the PL intensity is gradually reduced, while the full width at half maximum (FWHM) of the PL peak broadens. Above 6.2 GPa, the changes to the PL properties become irreversible, while further above 7.6 GPa, the PL becomes fully quenched. Therefore, such methods may not be suitable for applications that require a stable PL brightness.

Alternative approaches to the above-mentioned external stimuli rely on the use strong electric or magnetic fields to modify the energy levels of perovskites, directly influencing the band gap of the materials. The valence band of metal halide perovskites is formed from s-like orbitals, while the conduction band has p-like orbital character, both originating from the Pb^{2+} orbitals. Within the electronic structure, there is a dark singlet state with total angular momentum of $J = 0$ and an optically active bright triplet state with $J = 1$.[100] When the perovskite adopts a tetragonal or orthorhombic phase, the degeneracy of the bright state is lifted. Therefore, upon excitation, the emission spectrum can show single, double, or triple bands depending on the phase and orientation of the crystal.[101] In the presence of a strong electric field, the degeneracy of the bright triplet state is broken, leading to the splitting of the energy levels, known as the Rashba effect (Figure 1.19).

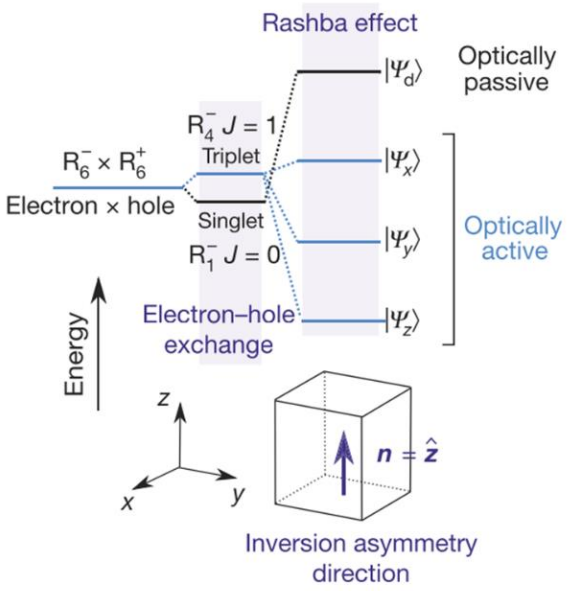

Figure 1.19. Fine structure of the band-edge exciton in $CsPbBr_3$, showing the splitting of the exction into three bright states and a dark state. The figure was taken from the work of Becker et al.[102]

In perovskites affected by the Rashba effect, the spin-dependent energy levels can lead to different optical transitions for electrons with different spin orientations, which can result in spin-dependent emission characteristics. This allows for the manipulation of energy band structures and, consequently, the PL properties of the material. For instance, $MAPbBr_3$ perovskites undergo a temperature-dependent PL band splitting under such conditions, with a maximum separation of the peaks of 28 nm at 300 K.[103] Similarly, the Stark effect, which refers to the splitting and shifting of spectral lines in the emission or absorption spectra in the presence of a weak electric field, can also modify the optical properties of the material. Li et al. observed a 2.6 nm shift in the PL wavelength of $CsPbI_3$ quantum dots as a result of this phenomenon.[104] Furthermore, the presence of an external magnetic field can lead to the modification of the PL properties *via* the Zeeman effect, enabling a shift in the emission energy and PL polarization state. However, the PL shift attributed to this method has remained modest. For example, when

subjecting $CsPbBr_3$ nanocrystals to magnetic fields from 0 T to 16 T, the emission wavelength shifts only by ca. 0.7 nm.[105] The PL peak shift achieved by various methods listed above was summarized in Table 1.1.

Method	Photoluminescence energy shift (meV)*	Conditions	Reference
Ion-exchange	133	Exposure to halide salts	95
Temperature	63	12 K to 160 K temperature change	98
Pressure	921	~2,900 atm to ~40,000 atm pressure change	106
Strain	2.6	Suspension over SiO_2 rings with biaxial strain	107
Magnetic field	30	0 T to 0.47 T change in magnetic field at 293 K	108
Rashba effect	110	Reflection and transmission geometry PL setup at 300 K	103
Zeeman effect	0.8	15 T magnetic field at 4.2 K	109
Stark shift	6.4	Use of co- and counter-circularly polarized pump−probe configuration	104

Table 1.1. Photoluminescence (PL) wavelength shift achieved by different methods outlined in the literature, including a brief note on the conditions at which the changes were observed. The values were extracted from the results provided in each work. *As some of these approached yield multiple PL bands due to a splitting phenomenon, we quote the emission wavelength shift of the second peak relative to the main PL peak position.

While a number of these methods can achieve considerable PL tuning and are effective to a certain extent, it is important to note that they can be destructive in nature and often require sophisticated equipment. Furthermore, they can induce irreversible changes and lead to the emergence of multiple emission bands. Consequently, these approaches may not be ideal for applications that require simpler setups and the generation of single, narrow emission peaks.

Given these limitations, there is a need to explore more effective and practical approaches for the post-synthesis PL tuning of perovskite materials.

1.3.3 The use of photonic structures to modify perovskite emissions

Photonic structures, including nanoantennas and cavity structures, emerged as powerful tools for tailoring and enhancing the optical properties of materials. As first proposed in the seminal work of Purcell in 1946, the emission properties of a material are strongly influenced by its surrounding electromagnetic environment.[110] Consequently, when an emitter is placed in the vicinity of such resonators, its absorption and emission properties undergo changes. In this context, photonic nanostructures provide a means to enhance the PL efficiency, control emission directionality and even manipulate the polarization state of emitted light of perovskite materials.[111]

The interaction between an emitter and a resonator is described by the Purcell effect, which refers to the weakly coupled interaction of a quantum emitter, such as an atom, molecule, or quantum dot, and a resonant mode (Figure 1.20).

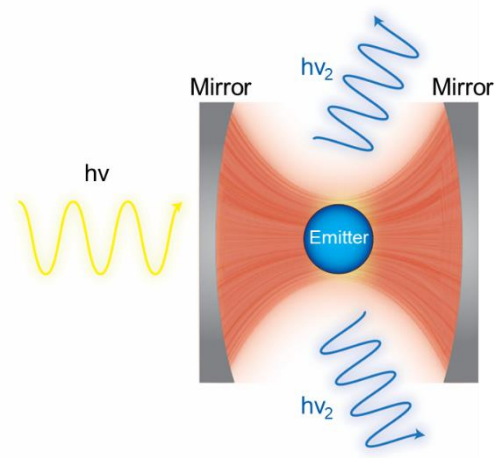

Figure 1.20. Representation of a quantum emitter in a resonant cavity, where Purcell coupling leads to an increased photon decay rate.

If the emitter is situated near or within an optical resonator, the emitter's interaction with the resonant cavity leads to modifications in its emission properties, primarily its spontaneous emission rate and the emitted photon's spectral characteristics. The presence of the resonant cavity modifies the local density of optical states of the emitter, essentially creating an environment with a higher probability of emitting photons. This leads to an increased rate of spontaneous emission, where the enhancement factor (also known as the Purcell factor, F_p) can be quantified by the following expression:[112,113]

$$F_p = \frac{3}{4\pi^2}\frac{Q}{V_{eff}}\left(\frac{\lambda}{n}\right)^3 \quad (1.12)$$

where Q is the quality factor of the resonance, V_{eff} is the effective mode volume, λ is the emission wavelength and n is the effective mode index.

Typically, to increase F_p, efforts are focussed on improving the Q-factor of a resonance or reducing the effective mode volume of the electromagnetic field. Optical cavities are excellent for this purpose as they are designed to confine and control light within small volumes. For instance, Fabry-Perot type cavities are constructed using two highly reflective mirrors that confine light to create standing electromagnetic fields within the cavity.[114] The mirrors employed can be thin metals or distributed stacked materials with multiple alternating dielectric and/or metal layers. For instance, alternating Ag and LiF layers can serve as a cavity to modify the emission wavelength of $CsPbBr_3$ nanocrystals. When placed upon the cavity, the perovskite emission wavelength can be shifted up to 8 nm, depending on the thickness of the mirror layer.[115] However, due to the quenching effect of the metal interface, this method leads to a 5-fold reduction of the PL intensity. In another study, it was shown by Liu et al. that when $CsPbBr_3$ nanocrystals are placed on top of 2.5 TiO_2/SiO_2 pairs, the directional forward emission

can be enhanced by 3-fold, while achieving a significant narrowing effect of the PL bandwidth.[116]

As the Purcell coupling modifies the spontaneous decay rate of an emitter, the effect can be directly observed by measuring the PL lifetime of the perovskite particles in the vicinity of the resonator. For instance, when $MAPbI_3$ thin films are deposited on stacked layers of Si_3N_4 and SiO_2, the spontaneous emission rate is reduced by 1.8-fold.[117] On the other hand, when using a Si_3N_4 photonic crystal nanocavity alone, $CsPbBr_3$ perovskite nanocrystals experience a 10-fold enhancement of the emission brightness, while the radiative lifetime of the emission is reduced by 2.9-fold.[118] In recent years, new designs have been developed based on these principles to further control and enhance the PL properties. For example, the PL brightness of $CsPbX_3$ QDs (where X = Cl, Br, I) can be significantly improved *via* the Purcell effect when coupled with a plasmonic Ag crystals and a polyvinylpyrrolidone spacer layer. This method enables a 3.5-fold enhancement in the total PL intensity.[119] The Purcell enhancement can also be achieved by depositing the material on a layer of SiO_2 photonic crystals with 200 nm diameter, which serves as an optical cavity and can modify the emission properties of perovskites. It was found that the PL of $CsPb(Br_{0.51}Cl_{0.49})_3$ perovskites can be enhanced by 6-fold compared to when coated on glass.[120]

Similar to optical cavities, nanostructures can also modify the PL properties of emitters.[121] Nanoantennas that support LSPR are popular for this reason, typically made of metals such as Ag, Au, Al or Cu. For example, Wu et al. reported that Er^{3+}-doped upconversion nanoparticles show an impressive 1.01×10^4 times enhancement of the PL intensity for red emission when sandwiched between a gold film and a layer of silver nanocubes (Figure 1.21).[122]

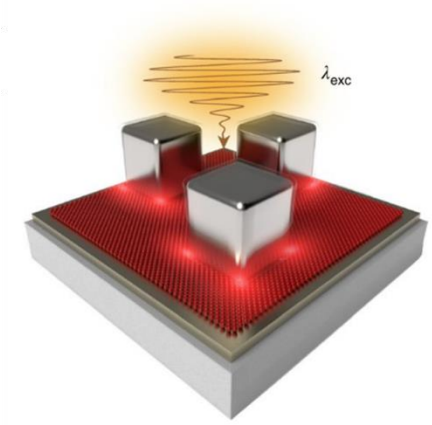

Figure 1.21. Illustration of a plasmonic cavity-coupled monolayer of upconversion nanoparticles (red spheres), sandwiched between a gold thin film and silver nanocubes. The figure was taken from the work of Wu et al.[122]

Here, the quenching effects from the metals are less pronounced, as the overall PL signal is dominated by the emission from the nanoparticles coupling to the gap plasmons, rather than the particles in contact with the metal interface. In general, the drawback of using metallic nanostructures is that its quenching effects should be mitigated. Such effects become detrimental to the PL brightness when the emitter is at distance less than 20 nm from the metal interface. Therefore, the incorporation of spacer layers is often required in these designs, which adds complexity to the fabrication of light-emission devices. Furthermore, conventional metal nanostructures support plasmonic resonances with relatively broad bandwidths, leading to lower *Q*-factors, which limits the maximum enhancement achievable by the Purcell effect. To address this, researchers in recent years focussed on the fabrication of nanostructures possessing optical modes with high *Q*-factors to couple with the excitonic state of emitters.

1.3.4 Bound-states-in-the-continuum (BIC)

Bound states are confined waves within a system. Examples of these include electrons in atoms, where the particles are confined due to potential energy wells. The bound states have discrete energy levels, which means that their energy is quantized. The states remain confined in the system (*i.e.* do not radiate out of the system), because their frequency is outside of the continuous spectral range of other propagating waves. Here, the spectral continuum refers to the range of energy levels in a system that are not quantized. Within the continuum, unbound radiative wave states – resonances – exist that "leak out" of the system. These are typically higher in energy, therefore, the bound states cannot interact with them, preventing their radiation into the far-field.

Bound-states-in-the-continuum (BICs) are unique in the sense that they defy these classical principles; they exist within the continuous spectrum of energy levels in the system yet remain perfectly confined (Figure 1.22).[123]

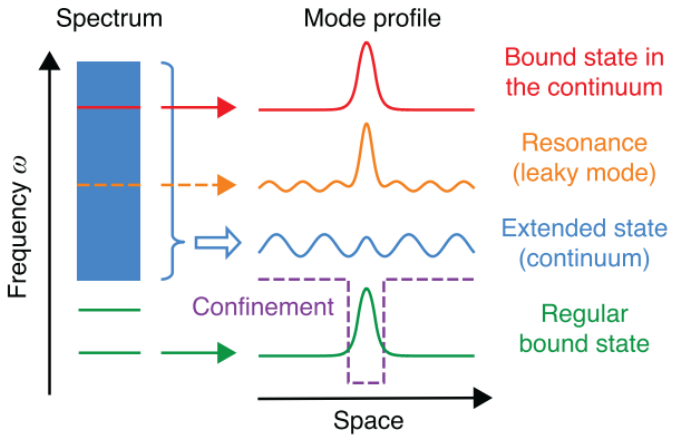

Figure 1.22. Illustration of the types of modes that can exist within a system. BICs lie inside the continuum but remain localized without radiation. The figure was created by Hsu et al.[123]

As BICs do not interact with the other existing states within the system, they cannot be excited by waves outside of the system coming from infinity and also cannot decay.[124] The consequence of this is that the *Q*-factor of BICs is theoretically infinite. When there is rotational symmetry or reflection in a particular system, symmetry-protected BICs arise, which remain localized as long as the symmetry of the system is protected. For example, extended photonic structures that are uniform or periodic in at least one dimension can possess such states. In such structures, the modes that belong in different symmetry classes are decoupled. Specifically, bound states can exist in one symmetry class coexisting with other symmetry class states that exhibit a continuous spectrum of modes, without any coupling between the two.[123] Here, the different symmetry classes are the even and odd modes. Even modes are wave patterns that exhibit symmetry under reflection about a particular centre point. On the other hand, odd modes are wave pattern which show anti-symmetry under reflection about a particular axis. In other words, rotation of the pattern about the axis would show an inverted wave pattern. For instance, cylindrical holes in a dielectric material that expand in the *x* and *y* directions have rotational symmetry around the *z*-axis (C_2). In this system, the even and odd modes with respect to the C_2 axis are decoupled, where the odd modes are radiative states and the even modes are bound to the system (Figure 1.23).[123,125]

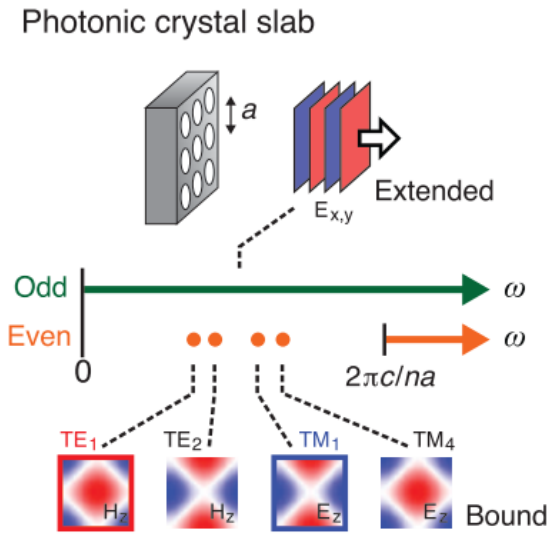

Figure 1.23. A photonic crystal with a hole array which has rotational symmetry around the *z*-axis (C_2). At normal incidence, even modes are bound states, while the odd modes propagate in the normal direction. The figure was taken from the work of Hsu et al.[123]

In order to access these high *Q* states, the modes must radiate out of the system. This can be achieved by breaking the symmetry of the system, which allows the BIC states to couple with the far-field and become resonances (Figure 1.24).

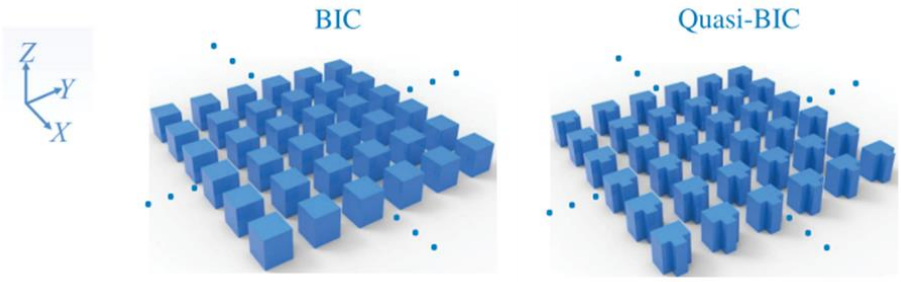

Figure 1.24. Example of the symmetry-breaking of the nanoarray geometry. While the symmetrical cube arrays possess BIC modes (left), introducing the asymmetrical element to its geometry leads to the formation of q-BIC modes (right). The figure was taken from the work of Liu et al.[126]

These resonances, known as quasi-BIC (q-BIC) states, mimic the characteristics of true BICs, while being optically accessible, which enables their use in various applications. They possess narrow linewidths and high *Q*-factors, making them particularly useful in sensing applications.

1.3.5 The use of q-BIC resonances to modify the optical properties of emitters

The use of q-BICs presents an alternative to plasmonic resonances for modifying the emission properties of an emitter. While plasmonic resonances have been extensively employed to enhance light-matter interactions, q-BICs offer several distinct advantages. One key advantage lies in their inherently narrow linewidths and ultrahigh *Q*-factors, leading to enhanced light-matter coupling and increased Purcell factors. Unlike plasmonic resonances, which often exhibit broad linewidths due to inherent losses in metals, q-BICs maintain exceptional coherence and spectral purity, facilitating a more precise control over resonance frequencies.[123] This property is critical for achieving efficient and selective enhancement of desired optical transitions. Additionally, q-BICs can be engineered within dielectric or photonic structures, avoiding the challenges associated with the fabrication complexity of metal-based plasmonics.

For instance, silicon can support q-BIC resonances.[127,128] Silicon's high refractive index and low absorption coefficients enable strong light confinement and manipulation within its nanostructures. By engineering periodic or structured silicon-based photonic systems, it is possible to create resonant modes that satisfy the conditions for q-BIC formation. For example, asymmetric holes in a square array possess q-BIC resonances, which can be used to increase the PL intensity of G-centres - a type of defect originating from substitutional carbon atoms in the lattice - of crystalline Si (c-Si) by 40 times.[129] Most notably, leveraging the asymmetrical structural design, the polarization of the emitted light could be controlled, showing linear polarization with directionality. These results are promising, as silicon's prevalence in microelectronics allows for the integration of q-BIC-enhanced processes into existing silicon-

based platforms. Other materials, such as monolithic hexagonal boron nitride, have also been explored to achieve q-BIC resonances. Cao et al. performed simulations which demonstrated that grating metasurfaces with broken in-plane inversion symmetry can realize an ultrahigh Purcell factor of 3.3×10^4, enhancing the spontaneous decay rate of single photon emitters.[130] Meanwhile, Zhen et al. studied periodic nanostructured cavities made of dielectric photonic crystals. When rhodamine 6G molecules are suspended near the cavity, the fluorescence signal was enhanced by 6300-fold due to the q-BIC resonant modes supported by the cavity.[131] Therefore, the use of q-BICs presents a promising tool to achieve high Purcell enhancement effects.

1.4 Interband transitions to realise plasmonic resonances outside the visible region

Silicon's significance goes beyond its ability to support q-BIC resonances.[132] The attributes of Si that enables it to support q-BIC resonances - its high refractive index, strong light confinement and compatibility with fabrication techniques - also position it as a candidate as a material with plasmonic character. Notably, silicon nanostructures exhibit interband transitions within the ultraviolet (UV) spectrum, giving rise to resonances with plasmonic behaviour.[133] This is particularly relevant for applications such as high-resolution imaging, advanced spectroscopy, and next-generation data storage, where the shorter UV wavelengths offer enhanced spatial resolution and sensitivity.[134]

1.4.1 Intraband vs interband plasmonics

In the earlier sections, plasmons were introduced as the collective oscillations of the electron cloud of metals. The phenomenon arises from the excitation by light, which induces intraband transitions within the conduction band from an occupied s-band to an empty s-band. However, in recent years, other materials have been identified as "plasmonic" that do not meet the conventional optical criteria required to observe such effects. As discussed in section *"1.2.4 Localized surface plasmon resonance"*, for metals, the coupling effect between light and the electron cloud can be modelled by the Drude expression.

While the Drude model provides an essential tool to describe the optical properties of metals, it starts to break down at frequencies where interband transitions between electronic bands can occur. For example, it does not fit the experimentally obtained data of Au beyond the visible region.[135] At these photon energies, transitions occur either from the valence d-band to a band at the Fermi surface, or the electron near the Fermi surface is excited to an empty conduction band. These transitions are known as the interband transitions (Figure 1.25).

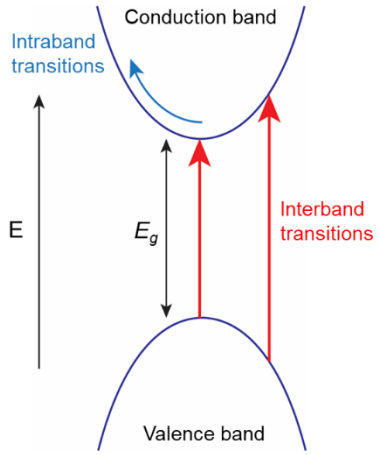

Figure 1.25. Illustrative energy level diagram demonstrating the intraband and interband and transitions between the valence and conduction bands of a material.

To describe the optical response of materials with interband transitions, the Drude-Lorentz model was introduced, where the Drude component accounts for the intraband effect and the Lorentz oscillator component takes into account the electronic interband transitions. The new complex dielectric function therefore becomes:[31]

$$\varepsilon(\omega) = 1 - \frac{\omega_p^2}{\omega^2 + j\omega\gamma_d} + \sum_{i=1}^{K} \frac{f_i\omega_i^2}{\omega_i^2 - \omega^2 - j\omega\gamma_i} \quad (1.13)$$

where K is the total number of higher-energy oscillators with the corresponding resonant frequency ω_j. $1/\gamma_i$ is the lifetime and f_j is the weighting coefficient. The use of this term allows the characterization of materials with plasmonic behaviour, where the resonances originate from interband transitions. The significance of this is that interband transitions can lie outside the visible region, giving rise to plasmonic resonances in the UV or near-IR regions in certain materials. In particular, it accurately describes the plasmonic behaviour of semiconductors such as Si.

1.4.2 UV plasmonic materials based on interband transitions

UV-based technologies are a widespread and established field, including water purification,[136] germicidal uses,[137] UV sensor integrated circuits,[138] air quality monitoring,[139] communication systems[140] and fluorescence detection.[141] Considering this, it is not surprising that an intense search has begun for materials that can push plasmonic resonances towards the UV region. Furthermore, the promise of using semiconductors for this job gathered much interest due to their adaptability to a number of applications.

As discussed earlier, Al has been explored as a UV plasmonic material. However, Al oxidizes rapidly in contact with air, and the plasmonic resonances are severely affected by the amount of Al_2O_3 within the structure.[142] To address this issue, interband plasmonic materials offer a

promising alternative solution. For instance, Pd and Pt have overlapping s- and d-bands at the Fermi energy, which gives rise to interband activity at a wide spectral range spanning from the UV to the NIR.[143] In addition, several p-block elements exhibit plasmonic behaviour originating from strong interband transitions. By fabricating nanostructures of these materials, one can realize a negative value of the real part and a small imaginary part of the complex dielectric function, thereby enabling plasmonic behaviour at the photon energy corresponding to interband transitions. For instance, Toudert et al. showed that for bismuth, the ε_2 spectrum exhibits a strong peak near 0.8 eV, attributed to interband transitions with a high oscillator strength.[144] This observation suggests that subwavelength Bi nanostructures can support plasmonic resonances outside the visible region. Indeed, Bi nanoparticles with a diameter of ~20 nm embedded in Al_2O_3 display a plasmon resonance around 400 nm in the UV region.[144]

Furthermore, Si, germanium (Ge), and amorphous arsenic (As) are semiconductors that feature strong interband transitions in the ultraviolet and visible regions. Si, in particular, is of interest due to its ease of surface deposition and patterning. Thin Si films with 60 nm thickness satisfy the resonance condition to support broadband SPPs down to 107 nm within the deep UV region.[145] Furthermore, cylindrical nanodisks and nanoholes of Si with diameters in the range of 50 – 170 nm possess localized plasmon resonances around 250 nm in the UV-C range (Figure 1.26).[133]

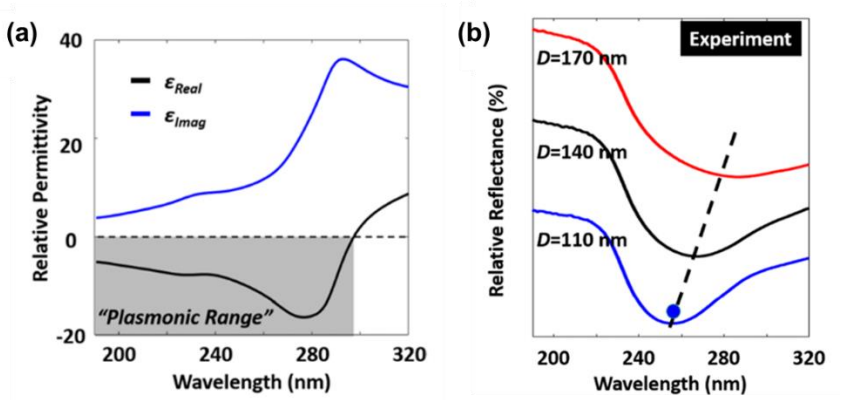

Figure 1.26. (a) Real (ε_{Real}) and imaginary (ε_{Imag}) parts of the complex dielectric function of Si within the UV range, showing that the negative ε_{Imag} leads to plasmonic behaviour. (b) Experimental reflectance spectra of Si nanodisks with diameters of 110 nm, 140 nm and170 nm, placed in a randomized order on the substrate. The spectra show the plasmon resonance dip within the UV region. The figure was taken from the work of Dong et al.[133]

Meanwhile, metasurfaces made of Si nanorods with 142 nm length and 32 nm width enable the manipulation of the phase of the scattered field for circularly polarized light within the wavelength range of 280 nm to 400 nm.[146] These unique properties of Si make it an excellent candidate for manipulating UV light.[147]

1.4.3 Improving the *Q*-factor of interband plasmonic materials

While interband plasmonic (IBP) materials hold significant promise, their plasmonic properties are still lacking compared to materials like Au and Ag, primarily due to the poor *Q*-factor of their resonances. Currently, the *Q*-factor of IPB materials remains low, not exceeding ~3, resulting in limited near-field enhancements.[134] For instance, the plasmon resonance of ~20 nm diameter Bi nanoparticles exhibit a *Q*-factor of only 1.[144] Similarly, the UV plasmonic Si nanostructures also possess a low quality resonance of 1.[133] This leads to broadband plasmon resonances - a drawback for applications such as optical sensors and photodetectors, where higher *Q*-factors are crucial for improved device performance.[148,149]

The low *Q*-factor in IPB materials can primarily be attributed to their high Ohmic losses, associated with the conversion of plasmon energy into heat that dissipates into the material.[150] In general, the width of plasmon bands is determined by damping effects, involving radiative and nonradiative processes. Radiative decay typically originates from particle plasmons transforming into photons through coupling between different optical excitations. Other damping effects, such as scattering, propagation, and inherent losses exists also contribute to the linewidth broadening. Additionally, surface roughness, limitations in fabrication methods, and the presence of other materials impact the Q-factor.[151] Therefore, to improve the quality of resonances, these loss mechanisms must be addressed.

Firstly, optimizing the nanostructure design is crucial. Selecting nanofabrication methods that produce precise nanostructures with minimal surface roughness and high geometrical accuracy is essential. Electron beam lithography is therefore a popular choice; it involves the use of a focused beam of electrons to expose a resist material, which is subsequently developed to create the desired pattern with sub-10 nm resolution.[152] Further enhancements can be achieved through annealing to reduce grain boundaries, increase surface smoothness, and improve material crystallinity.[153] The nanoparticle size can also be considered to control the plasmon band linewidth. Particles that are much smaller than the wavelength of the incoming light experience a displacement in the nanoparticle's charge distribution from its equilibrium position, which leads to a dipole moment oscillation. This dipolar resonance is the most fundamental type of plasmonic resonance. However, if the particle size is increased, higher-order modes can be accommodated, including quadrupole, octupole, and other higher-order multipoles (Figure 1.27).

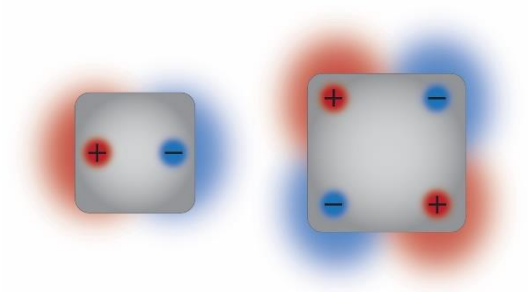

Figure 1.27. Illustration of the charge distribution of a nanoparticle supporting a dipole mode (left) and another particle possessing a quadrupole mode (right).

These modes involve more complex charge distributions, leading to resonances at different frequencies compared to the dipole modes. For instance, quadrupole modes feature charge distributions with two pairs of opposite charges along different axes, resulting in more complex field patterns. Multipole modes can be dark modes (subradiant), due to the opposing charges cancelling one another. Therefore, they are characterized by their minimized interaction with external electromagnetic fields - with reduced radiative damping effects - leading to minimal scattering and radiation.[154] The reduced far-field scattering results in intense near-field effects, amplifying interactions with neighbouring materials. Their interaction with radiative modes (bright modes, superradiant) gives rise to hybridized properties and distinct resonant features, where the linewidth of the overall resonance can be significantly reduced.

Another approach to improve the *Q*-factor of plasmon resonances involves the use of dielectric cavities. A dielectric layer placed between a mirror and the nanostructured material can effectively confine energy from incident light, giving rise to cavity resonances. For example, nanodisks fabricated from Al typically exhibit plasmonic resonances with a *Q*-factor in the range of 2-4. Zhu et al. demonstrated that a significant reduction in radiation damping be achieved by fabricating the Al nanodisk array on top of fused silica, where far-field coherent interactions improved the *Q*-factor to 27.[155] Additionally, researchers reported an ultrahigh sensitivity cavity-coupled plasmonic device using the combination of Au nanorods with a

Fabry-Perot cavity of a resonant dielectric photonic crystal slab. The interaction between the broad Fabry-Perot cavity resonance and the plasmonic resonance of the Au nanorods lead to a hybridization effect, resulting in a *Q*-factor of 435 and an ultrastrong near-field effect in the visible region.[156]

Zhang et al. presented a highly efficient room temperature UV surface plasmon polariton (SPP) nanolaser, operating at 370 nm, with a remarkably low threshold of approximately 3.5 MW cm^{-2}.[157] This threshold is nearly 1,000 times lower compared to previous room temperature visible plasmonic nanolasers. The performance of the nanolaser is attributed to the presence of a high-*Q* cavity, originating from the efficient coupling between photonic and plasmonic modes. The device structure comprised of a triangular GaN nanowire deposited on an Al film, separated by a thin SiO_2 cavity layer to reduce the Ohmic losses.

A different method to enhance the Q-factor involves the coupling interaction between wide and narrow resonances to achieve electromagnetically induced transparency (EIT).[158] This phenomenon originates from a quantum interference effect within a three-level quantum system, typically involving gas phase atoms. The system comprises a ground state $|1\rangle$, a metastable state $|2\rangle$, and an excited state $|3\rangle$. Transitions from $|1\rangle$ to $|3\rangle$ and $|2\rangle$ to $|3\rangle$ are dipole allowed, while $|1\rangle$ to $|2\rangle$ is dipole forbidden. A control field couples to states $|2\rangle$ and $|3\rangle$, while a probe field couples into state $|1\rangle$.[159]

In the absence of the control field, the probe field is absorbed via the $|1\rangle$ to $|3\rangle$ transition. However, when the control field is activated, the interaction induces destructive interference between the absorption and emission pathways. This interference results in a narrow frequency window around the probe field, making it “transparent”. Consequently, the probe field can propagate through the medium without significant absorption. [160]

As previously mentioned, systems can exhibit dark and bright modes, with bright (radiative) modes having a large scattering cross section and low *Q*-factors, such as plasmonic modes. In contrast, dark modes possess high *Q*-factors because they do not radiate via far-field coupling. Dark modes, which can act as a metastable level, can interact with a dipole-allowed transition to the ground state and an additional energy level upon pumping. If combined with microcavity systems, the coupling between the cavity modes corresponds to the control field, while input from the first cavity mode corresponds to the probe field.[159] Thus, the coupling between the narrow mode with a broad mode of a resonator produces a sharp EIT spectrum is with a high *Q*-factor.[151] For example, metamaterials comprising of a design based on a nanoring and a nanorod can realise a resonance with a 60% transmittance and a Q-factor of 97.[161]

In summary, the low *Q*-factors observed in IPB materials limits their potential in the field of nanoplasmonics. Although researchers have made substantial progress in enhancing the *Q*-factor of plasmonic materials using surface design, achieving high quality UV plasmonic resonances remain challenging. Nevertheless, these advancements represent significant steps towards realizing high-*Q* resonances in IPB materials, thus opening the path towards their UV applications.

1.5 Aims

The aim of this thesis is to examine three different approaches to the control of light-matter interactions that offer promise for solving key challenges in solar energy capture, tuneable light-emission and UV plasmonic materials. In particular, the work addresses the following challenges identified in the preceding review of the literature.

1) The performance of organic photovoltaics is limited by the short exciton diffusion lengths in organic semiconductors, which results from the dominance of incoherent excitation transfer mechanisms. It is hypothesized that the development of new molecular materials that embody coherent excitation transfer mechanisms could transform the performance of molecular semiconductors. One way to achieve such coherent excitation transfer is to incorporate strong light-matter coupling. In the strong coupling regime, the coherent ultrafast exchange of energy among the ensembles of emitters emerges from the underpinning physics. However, the design rules of such materials are currently lacking.

To address this, **Chapter 3** describes the synthesis of biomimetic organic light-harvesting networks, inspired by photosynthetic light-harvesting complexes capable of strong plasmon-exciton coupling. In nature, pigment-protein antenna complexes regulate interconnected networks of energy transfers. Taking inspiration from these biological systems, artificial pigment-polymer complexes are created in which poly(cysteine methacrylate) (PCysMA) scaffolds grown from gold nanostructures by surface-initiated polymerisation are decorated with Chl. To control the properties of plasmon-exciton coupling, the excitons must be organised in 3D. This is achieved by control of the grafting density, degree of polymerisation and coupling chemistry. The resulting polymers are analysed as a function of depth using X-

ray photoelectron spectroscopy (XPS) depth profiling with a giant gas cluster source, with the coupling chemistry characterised in detail.

2) Perovskites exhibit remarkable light emission characteristics. However, there is limited potential to control the properties of a particular material via post-synthetic methods; thus, adjusting the emission wavelength of the material to suit a specific application is challenging. In this chapter, a different approach is explored that is based on the incorporation of photonic nanostructures. It is hoped that this will provide a method for the synergistic control of the emission properties in devices. Although such approaches have been attempted previously, the maximum spectral shift reported to date has been modest, with a quenching of the PL brightness.

In **Chapter 4**, a new approach to the post-synthesis PL tuning of perovskite materials is explored. The coupling of q-BIC resonances to the perovskite exciton states via the Purcell effect enables the homogeneous tuning of the emission wavelength. Si nanostructures which support optical q-BIC resonances are fabricated via electron beam lithography and the perovskite nanoparticles are deposited onto the nanostructures by dip-coating. Analysis of the Purcell effect is carried out using both theoretical and experimental methods. The emission wavelength shift is tuned by adjusting the geometrical parameters of the Si nanostructures, as well as the polarization state of the incident laser light. Thus, the work aims to introduce an alternate approach to tuning the emission without the need for extreme conditions.

3) The incorporation of plasmonic elements in devices can greatly improve their performance. While conventional plasmonic materials are widely employed for this purpose, their plasmonic resonances are limited to the visible spectral region. However, a diverse range of UV-specific applications would benefit from plasmonic elements. IBP materials have the potential to address the demand for UV-plasmonic technologies. Nevertheless, they exhibit large intrinsic

losses, resulting in low *Q*-factors for their plasmonic resonances, which limits their practical applications.

Chapter 5 demonstrates an approach to overcome this challenge by exploring a nanoantenna design to improve the *Q*-factor of IBP resonances in the UV region. Using lithographically designed Si nanostructures fabricated on top of a photonic SiO_2 cavity, the interaction between the LSPR and the photonic cavity modes is investigated. The extent of hybridisation between the modes is controlled by varying the cavity thickness, disk height, diameter and the pitch. To examine the sensitivity of the high-*Q* resonance to its local environment, a UV-absorbing lignin-polyethylene glycol (lignin-PEG) co-polymer film is deposited over the plasmonic array, and the resulting optical properties are characterised using experimental and simulated reflectance measurements.

These three chapters aim to demonstrate that the optical properties of molecular films can be programmed via the integration and synergistic design of nanostructured photonic elements. It is hoped that such strategies may provide flexible new routes to the design and construction of photonic devices for applications in solar energy capture, optoelectronics, sensors and many other fields.

Chapter 2. Methods

2.1 Analytical and characterisation methods

2.1.1 Nuclear Magnetic Resonance (NMR) spectroscopy

The ^{1}H NMR spectra was obtained using Bruker Avance and Avance III HD NMR spectrometers, operated at a frequency of 400 MHz. The samples were dissolved in ca. 5 mL solvent in milligram quantities and filtered prior to the measurement. The ^{1}H NMR results can be found in the experimental sections of the following chapters.

2.1.2 High Performance Liquid Chromatography (HPLC)

Liquid chromatography mass spectrometry (LC-MS) analysis was carried out with a Waters LCT classic time-of-flight (ToF) liquid-chromatography mass spectrometer at the Sheffield Department of Chemistry Chromatography Service. Milligram-scale samples were dissolved in ca. 2 mL dichloromethane prior to the analysis.

2.1.3 Reflectance spectroscopy

Reflectance measurements were carried out using a polarized broadband light source on a CRAIC UV-VIS-NIR micro-spectrophotometer. The measurements were calibrated using a NISR calibration sample (CRAIC Technologies) to record the absolute reflectance and operated with an integration time of 100 ms with an average of 50 measurements per spectrum. Measurement conditions specific to each study are outlined in *Chapter 4* and *Chapter 5*.

2.1.3 Ultraviolet-visible spectroscopy

Compounds dissolved in the appropriate solvents and the spectra were measured using a 2 mL quartz cuvette with a 1 cm path length. Measurements in dry conditions were recorded by attachment of the sample to a custom-made holder. The sample faced the incident light source laying upright, with a pinhole positioned above the sampling area of interest. The analysis was carried out using an Agilent Technologies Cary 50 spectrophotometer in the spectral range of 350 - 800 nm or with a Cary 5000 spectrophotometer, in a spectral range of 350 - 850 nm.

2.1.4 Photoluminescence (PL) and PL lifetime measurements

The PL measurements were carried out in ambient conditions. The mapping was conducted on a WITec Alpha 300 S Scanning Near-field Optical Microscope in confocal microscopy mode. A linearly polarized 532 nm CW laser with a power of 50 µW was focused on the sample through a 50× objective with a NA of 0.6. An integration time of 0.05-0.10 second was used. The time-resolved PL was collected on a Picoquant Microtime 200 TCSPC system coupled with an Olympus microscope in confocal configuration, with a 20× objective lens. The data was recorded and fitted with Picosharp software. A pulsed laser of 640 nm, with pulse duration of 70 *p*s was used to excite the sample, and the repetition rate was set to 40 MHz, with an average power of 1 µW. To collect the spectrally integrated PL (660-800 nm range), a Si single photon avalanche photodiode (APD) was used. The instrument response function (IRF) was obtained using the scattered excitation light from the sample, from which the instrument response time was determined (~240 *p*s). The PL spectra and PLQE were obtained by photo-exciting the samples in an integrating sphere, using a Spectra-Physics 405 nm (100 mW, CW) diode laser, and measuring the absorption and photoluminescence using a calibrated Ocean Optics Flame-T and Flame-NIR spectrometer.

2.1.5 Scanning electron microscopy (SEM) and transmission electron microscopy (TEM)

Prior to the SEM imaging, the samples were coated with 2 nm Cr to reduce the charging. The metal was deposited using electron beam evaporation (Denton Explorer E-beam Evaporator), at a deposition rate of 1 Å/s and a pressure of 4×10^{-6} Torr. SEM imaging (Elionix, ESM-9000) was carried out using an electron acceleration voltage of 5 kV. The TEM imaging was performed using FEI Titan equipped with a Gatan OneView camera, and was carried out at 200 kV.

2.1.6 Contact angle goniometry

The contact angle of deionised water was measured using a Rame-Hart 100-00 goniometer on the sample surfaces. The volume of a 2 µL droplet was used, which was deposited on the sample slide by raising the sample stage towards the droplet, after which the stage was lowered. The contact angle was measured 5 s after the deposition, three times on each side of the droplet.

2.1.7 Spectroscopic ellipsometry

Ellipsometry is a non-destructive surface characterization technique for the determination of the thickness, composition, refractive index, and other optical characteristics of thin films and layered structures. The characterization is based on the change in the polarization of light after interaction with the sample surface.[162]

The sample is illuminated with a continuous beam of linearly polarised light at an angle, typically 60-75 º with respect to the sample surface, and the reflected beam is directed into an analyser and detector. Upon reflection, the polarization state of the light wave becomes elliptical. This change in the polarization state is measured and expressed in terms of the

amplitude ratio, psi (Ψ), and the phase difference, delta (Δ) of the incoming light wave, and are analysed as a function of wavelength (Figure 2.1).[163]

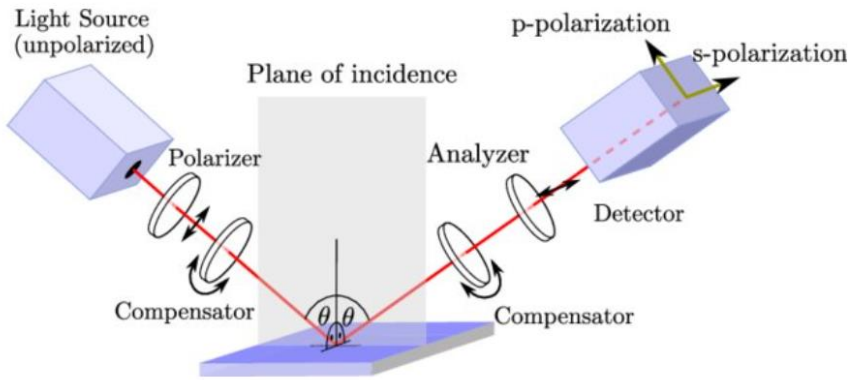

Figure 2.1. Experimental setup for spectroscopic ellipsometry measurements, as illustrated by Negara et al.[163]

The detected signal in itself does not provide information about the sample properties but can be used to construct a computational model which enables the deconstruction of the signal into the optical properties of the sample.[162] To analyse the change in the polarization state that occurs during reflection, the incident and reflected light is decomposed into two components, *p*-polarized light, characterized by its electric field vector oscillating parallel to the plane of incidence, and *s*-polarized light, with its electric field vector perpendicular to the plane of incidence. The elliptical polarization arises from the superposition of these two linearly polarized waves. Upon reflection, the amplitudes of the *p* and *s* components become altered, here denoted as r_p and r_s. The ratio of these two amplitudes is the complex reflectance ratio (ρ), and it holds information about both Ψ and Δ, as described by the following relationship:[164]

$$\rho = \frac{r_p}{r_s} = \tan \Psi \cdot e^{i\Delta} \qquad (2.1)$$

The properties of the light beam also depend on the angle of incidence, which, in turn, provides information about the refractive index (n) of the medium, as governed by Snell's law:

$$n_1 \sin\theta_2 = n_2 \sin\theta_2 \tag{2.2}$$

Here, n_1 is the refractive index of the medium that the incident wave travels through, and n_2 corresponds to the refractive index of the sample being analyzed. θ_1 is the angle of the incident light, and θ_2 is the angle of refraction.

When light enters into a new medium, its speed is altered (c'), and its ratio with the speed of light in a vacuum (c) provides the material's refractive index:

$$n = \frac{c}{c'} \tag{2.3}$$

When light propagates within absorbing materials, the refractive index alone cannot adequately describe its behaviour. It is therefore necessary to introduce the complex refractive index (N), which involves incorporating the material's extinction coefficient (k) in the following manner:

$$N = n - ik \tag{2.4}$$

Using this equation, the sample's relative permittivity can be determined, also known as the complex dielectric constant (ε) of the material. It consists of real (ε_1) and imaginary parts (ε_2), as introduced in *Chapter 1*, and it is related to N by the following expression:

$$\varepsilon = \varepsilon_1 - i\varepsilon_2 = N^2 \tag{2.5}$$

Thus, measuring Ψ and Δ yields important insights into the optical properties of the sample. By constructing an appropriate computational model for the experimental data, the sample can be characterized, extracting information about its film thickness, composition, and surface

roughness and optical constants. In addition, important parameters such as the sample's reflectance and transmittance can be derived.

2.1.7.1 Experimental procedure

The experimental measurements were carried out using a J. A. Wollam Co. Inc M-2000TM-V variable angle ellipsometer. The data in *Chapter 3* was collected at an incidence angle of 70 º over a spectral range of 371 - 1600 nm or using an Alpha-SE ellipsometer operating at 370 - 1000 nm at an angle of 75 º. The data presented in *Chapter 5* was carried out using 50 º, 60 º and 70 º incident angles across the 190 nm to 320 nm spectral region. The modelling of the experimental data was performed using CompleteEASE software 5.14.

2.1.8 X-ray Photoelectron Spectroscopy (XPS)

XPS is an analytical technique which provides quantitative and elemental analysis of the composition of materials. The measurement is performed by irradiating a sample with X-rays, which causes the emission of electrons from the core shells of the atoms. These emitted electrons are then analysed to determine their kinetic energy and, consequently, the elemental composition of the material and chemical state of the atoms within the sample.

In the experimental setup, the sample is mounted in an ultrahigh vacuum chamber ($< 10^{-7}$ Pa). The X-rays are generated by a beam of electrons directed at an anode, which generates a focused beam of X-rays with a specific energy depending on the source material, typically Mg *K*α (1253.6 eV) or Al *K*α (1486.6 eV)). The X-rays are focussed on the sample surface at a known angle to the surface normal and penetrate the solid in 1-10 µm on the target area of the substrate. When the X-rays collide with the sample, core electrons are ejected from the atoms near the surface due to the photoelectric effect. If the X-ray provides sufficient energy, it can overcome the binding energy of the electron in the atom and can be ejected from the Fermi

energy level into the vacuum as a photoelectron. The electrons that escape the sample surface are then collected into an electron energy analyser and the electron detector (Figure 2.2).

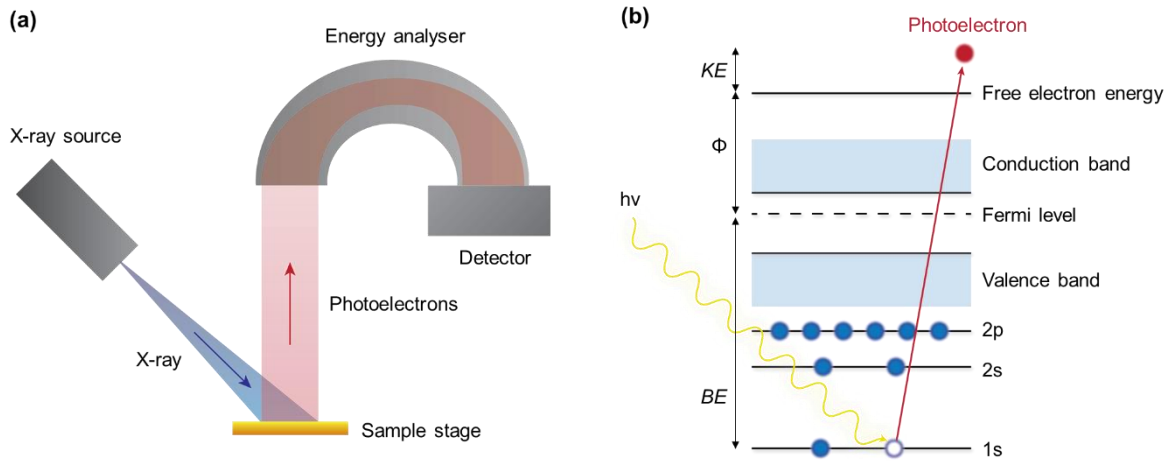

Figure 2.2. (a) Schematic illustration of the experimental setup of XPS. (b) Energy level diagram displaying the process of the photoemission effect, where the incident X-ray causes the emission of a photoelectron from the 1s orbital of an atom. *BE*, *KE* and Φ refers to the binding energy, kinetic energy and work function, respectively.

When the emitted electrons reach the detector, their kinetic energy (*KE*) is measured, which allows the determination of the binding energy (*BE*) of the atomic orbital from which the electron is ejected. This can be calculated using the following expression:

$$BE = E_p - (KE - \Phi) \tag{2.6}$$

Where E_p is the photon energy of X-ray photons and Φ is the work function, a correction factor for the instrument which correlates to the minimum energy required to eject an electron from beyond the Fermi energy. During the analysis, the work function and photon energy are known values, therefore, the binding energy can be determined. The electrons ejected from different atomic orbitals (s, p, d, etc.) have different binding energies, characteristic to their chemical bonding state and local environment. The analysis provides a spectrum with the measure of

signal intensity against binding energies, giving rise to peaks corresponding to their originating chemical bonding environments. The peak intensity (I) is described by:

$$I = J\rho\sigma K_c\lambda_a \tag{2.7}$$

Where J is the photon flux, ρ is the atomic concentration, σ is the emission cross-section and K_c accounts for the proportion of electrons transmitted as a function of kinetic energy (the transmission function), the detector efficiency and the effect of stray magnetic fields on the transmission of low-energy electrons. λ_a is the attenuation length, which refers to the distance that an emitted photoelectron can travel through a material before losing a significant amount of its energy. Typically, the attenuation length limits the sampling depth to ~10 nm of the surface of an organic thin film. Because of this, conventional XPS measurements are limited to only the top layers of the surface.

2.1.8.1 XPS depth profiling

Analysis of the composition of thin films with a thickness larger than 10 nm is limited using conventional XPS measurements due to the short sampling depth of the method. A solution to this is to use depth profiling, a specialized XPS technique used to analyse the chemical composition and elemental distribution of a material as a function of depth.[165] In this configuration, layers of the sample surface are etched by an ion beam, followed by the sampling of the material (Figure 2.3).

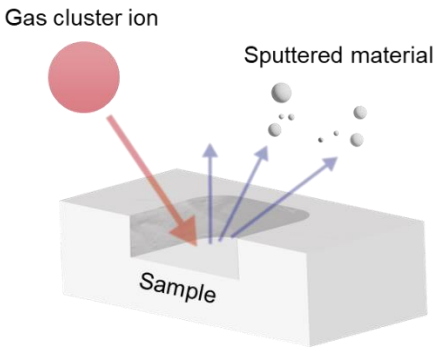

Figure 2.3. Illustration of the etching of the surface layer of a material using a gas cluster ion beam.

In sputter depth profiling, a high-energy ion beam is rastered across the sample surface. Using a gas cluster ion beam (GCIB) depth profiling setup, the primary component is the ion source. High-purity gas is introduced to the ion gun via a gas inlet. The choice of gas depends on the specific experimental requirements and the nature of the sample under investigation. For example, noble gases are commonly employed due to their interness. Furthermore, the size of the ion clusters is considered. Smaller ions can be more damaging to the surface, while larger gas clusters, such as Ar_{1000}^{+} or C_{60}^{+} are more suitable for sensitive materials, which require a gentle etching process.[166] Within the ion source, the gas undergoes an expansion process, leading to adiabatic cooling. This cooling induces the formation of gas clusters as the individual gas atoms combine, held together by van der Waals forces (Figure 2.4).[167]

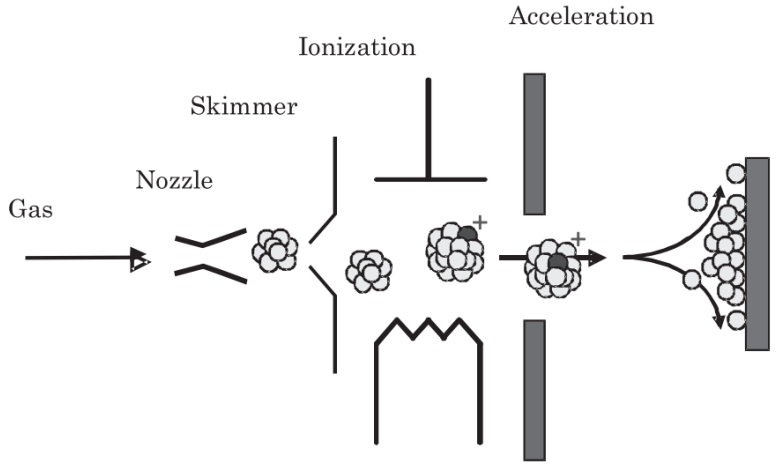

Figure 2.4. Schematic of the generation of a gas cluster ion beam, as illustrated by Yamada et al.[167]

To form the gas cluster ions, electrons are introduced into the expansion chamber. The electrons collide with the gas atoms within the clusters, resulting in ionization. Using an accelerator, these ions bombard the material and sputter away surface layers. When a layer is removed, the beam is blanked and XPS measurements are taken to analyse the composition and chemical states of the newly exposed surface. This process can be repeated multiple times to assemble a depth profile that shows the variation of chemical composition as a function of depth.

2.1.8.1.1 Experimental measurements

XPS measurements were collected using a Kratos Axis Supra spectrometer (Kratos Analytical, Manchester, UK). The source used was a monochromatized Al Kα X-ray source using an emission current of 15 mA, operating at 225 W and a base pressure of 10^{-8} – 10^{-10} mbar. The analysis area was 700 µm × 300 µm. High-resolution and survey scans were acquired with pass energies of 40 eV and 160 eV, with a resolution of 0.10 eV and 1.0 eV, respectively. The peak fitting was carried out using the CasaXPS software. The peak positions were calibrated to the

main hydrocarbon C1s signal, which was set to 285 eV. The conditions of depth-profiling measurements were adjusted depending on the sampled material. Further details can be found in *Chapter 3*.

2.1.9 Atomic Force Microscopy (AFM)

Atomic force microscopy (AFM) is a nanoscale imaging and characterization technique. It enables the characterisation of surfaces with nm resolution, providing information on the topography and the mechanical properties of materials. This information is derived by the analysis of the interaction between a probe tip supported by a cantilever and the sample surface (Figure 2.5).[168]

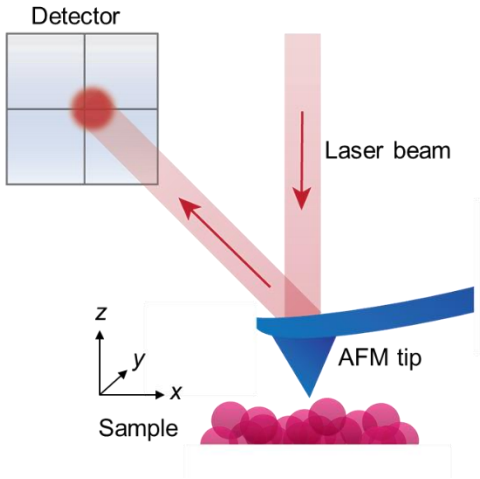

Figure 2.5. Schematic the AFM measurement, showing the probe tip of the cantilever near the sample surface.

During the measurement process, a laser beam is focussed on the top of the cantilever, which is reflected onto a photodetector. When the AFM tip is brought into close proximity to the surface, the atomic forces between the tip and sample can lead to the deflection of the cantilever. As the cantilever moves away from its original position, the reflected laser beam is

monitored on the detector, which provides information about the mechanical properties of the surface. The interaction force between the tip and sample is described by Hooke's law:

$$F = -k_c z \tag{2.8}$$

where F is the force exerted on the cantilever, k_c is the cantilever's spring constant and z is the cantilever deflection from its equilibrium position. To construct an image of the surface, the sample stage is moved in the x- and y- plane and the interaction force is measured as a function of position. This interaction between two atoms can be described by the Lennard-Jones potential (V_{LJ}):[168]

$$V_{LJ}(r) = 4\varepsilon_d \left[\left(\frac{\sigma_d}{r}\right)^{12} - \left(\frac{\sigma_d}{r}\right)^{6}\right] \tag{2.9}$$

where r is the distance between two particles (here, the atom of the tip of the AFM probe and the surface atoms or molecules), ε_d is the potential well depth and σ_d is the distance between particles at which the potential energy is zero. The expression provides the potential energy curve in terms of attractive and repulsive forces as a function of the separation distance between the tip and the sample surface (Figure 2.6).

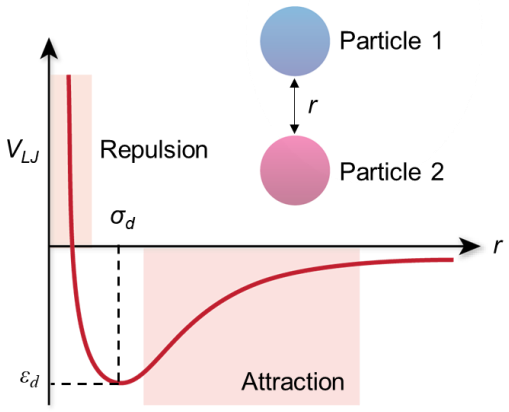

Figure 2.6. Representation of the Lennard-Jones potential curve for neutral two particles as they approach each other.

When the tip approaches the surface, the attractive forces cause a downward deflection of the tip. However, when the tip is very close to the surface, mechanical instabilities cause it to jump into mechanical contact. As the load is increased further, the tip experiences a repulsive force, and the cantilever is deflected away from the surface. Rastering the tip across the surface, the *z*-position of the cantilever is continuously adjusted by a feedback system according to the changes in the cantilever's oscillation amplitude, in order to keep it at a constant value. Therefore, the analysis of the variation in the *z*-position provides topological information of the surface.

AFM measurements can be carried out in two operating methods, tapping-mode and contact-mode. In contact mode, the tip remains in constant mechanical contact with the surface and the repulsive force acting at the tip-sample contact is measured. Through the application of an external load, the tip is pushed into the surface material and a constant force between the tip and the sample is maintained by adjusting the height of the cantilever. The deflection of the tip is measured as it is scanned across the surface. A variety of modifications of contact mode enable the measurement of the adhesion and stiffness properties of the sample, and forces related to chemical interactions, including electrostatic forces and chemical bonding forces.

In tapping mode AFM, the tip oscillates near the sample surface at its resonance frequency. The tip makes intermittent contact with the sample, leading to the dissipation of energy. By controlling the oscillation amplitude, it is possible to move between light tapping (oscillation amplitude close to the free oscillation amplitude) and heavy tapping (amplitude set point below the free amplitude). Because the probe only strikes the sample intermittently in tapping mode, less energy is dissipated in the contact than is the case in contact mode, and the risk of sample damage during imaging is greatly reduced, although not completely eliminated.

2.1.9.1 Experimental measurements

Atomic Force Microscopy (AFM) measurements were carried out in air using a NanoScope Multimode V microscope (Bruker, Germany). Images were obtained in tapping mode with OTESPA-R3 tapping probes (Bruker, Germany, resonance frequency of ca. 300 kHz and a nominal tip radius of 7 nm). The measurements were analysed with the Bruker NanoScope Analysis (v.1.5) software.

2.1.10 Theoretical analysis using finite-difference time-domain (FDTD)

The optical characteristics of nanostructured surfaces were examined using theoretical techniques. The simulations were performed using the three-dimensional finite-difference time-domain (3D FDTD) method.

To simulate the electromagnetic properties of a material, FDTD relies on solving Maxwell's equations, which describe how electric and magnetic fields interact and propagate through space. The algorithm was first proposed in 1966 by the applied mathematician, Kane Yee, and has been perfected since to enable the calculation of reflectance, transmission, diffraction, interference, and absorption of materials.[169] Using a simulation software, a model is constructed based on the parameters of the nanostructure of interest. This involves defined geometrical properties and the use of specific optical constants for each material employed in the model. In addition, electromagnetic sources and detectors can be employed that can inject and monitor radiation, respectively. Within the model, the spatial area of interest is selected, which divides the space into grid cells with finite dimensions. For each cell, the software calculates the electric and magnetic field values by solving Maxwell's equations. The simulation progresses in discrete time steps, continuously updating the electric and magnetic

field values at each grid cell. Therefore, the modelling allows the determination of the field evolution as a function of time.[170]

To obtain mode distributions and far-field spectra, FDTD simulations were carried out using Ansys Lumerical FDTD Solutions R2.4 software. Detailed outline of the simulation procedures can be found in *Chapter 4* and *Chapter 5*.

2.2 Surface fabrication techniques

2.2.1 Fabrication of gold slides

Microscope coverslip glass slides (22 mm × 50mm, #1.5 thickness, obtained from Menzel-Gläser, Germany) were used as substrates for chromium and gold deposition. The thermal evaporation was carried out using a diffusion pumped Edwards 306 thermal evaporator with a bell jar evaporation chamber and a piezoelectric film-thickness monitor, and the metals were deposited from a gold wire (99.997% trace metals basis, Goodfellow Advanced Materials, UK) and chromium chips (99.5% trace metals basis, Sigma-Aldrich). The glass slides were placed ca. 12 cm above the current-driven evaporation sources. The gold wire was evaporated from a tungsten cup boat, while the chromium chips were evaporated from a tungsten coiled wire boat. The evaporation chamber was roughed out to a pressure of 10^{-1} mbar via a rotary pump, after which the diffusion pump was engaged for high vacuum. When the pressure of at least 10^{-6} mbar had been reached, the current was supplied to the boat to achieve a deposition rate of 0.1 nm/s. Further details can be found in *Chapter 3*.

2.2.2 Photolithography

Photolithography is the process of creating patterns on a substrate by light exposure of a photoresist coating. The light is focused on the sample surface through a mask, which contains the desired pattern. When exposed, the photoresist undergoes a chemical change to harden or decompose, depending on whether a positive or negative photoresist is used. Positive resists become more soluble in the developer solution when exposed, while negative resists harden and cannot be removed during the development process. Subsequent to the exposure process, the sample is developed and etched to remove the material under the areas of the decomposed resist to yield the patterned surface (Figure 2.7).[171]

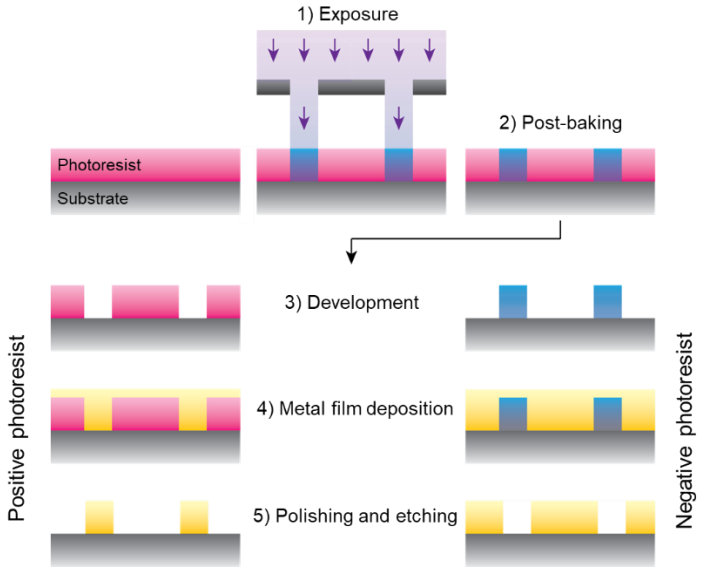

Figure 2.7. A typical photolithography and metal deposition process, adapted based on the illustration of Museau et al.[172]

The resolution limit of the technique is primarily dictated by the wavelength of the light used (λ). The minimum feature size (CD) that can be printed is calculated using the following expression:

$$CD = k_1 \frac{\lambda}{NA} \tag{2.10}$$

where k_1 is a coefficient that accounts for process-related factors and *NA* is the numerical aperture of the objective used. Therefore, to achieve higher resolution, the use of low wavelength light sources is preferred. In particular, the resolution limit using UV light is ca. 100 nm, while deep-UV light enables the fabrication of features of ca. 50 nm in dimension.[171] While this surface patterning technique provides a versatile and reliable fabrication of nanopatterned substrates, proximity effects that originate from the diffraction or scattering of light passing through the mask can lead to badly resolved or distorted patterns. An alternative method, interferometric lithography, operates on a similar principle but eliminates the need for a photomask. In this technique, a sample with a thin film coating is exposed to UV light, and patterns are created by the interference of two interacting light waves.

2.2.3 Interferometric lithography

A typical experimental setup of interferometric lithography consists of the use of a continuous wave UV laser, with its laser beam split into two beams that are guided to interact on the sample surface from different incident angles.[173] When the laser beams are irradiated on the sample surface, the constructive and destructive interference of the two laser beams selectively exposes the photoresist according to the phase difference of the two interacting beams. The nanostructures are created by carefully tuning both waves to obtain the desired interference pattern on the surface. After the exposure, the sample undergoes a development process specific to the photoresist used.

This method enables the creation of patterns over a large area with significantly enhanced resolution and accuracy, below the diffraction limit of the light source. In the work discussed in *Chapter 3,* a Lloyd's mirror was employed to obtain interferometric patterns of gold, which eliminates the need of a second laser beam.[174] Additionally, instead of the conventional method

of spin-coating a photoresist, a self-assembled monolayer (SAM) of thiol molecules bonded to gold were used as a resist, which form a highly ordered dense thin film of molecules on the surface. In the exposed areas, the alkanethiolates are photooxidised into sulfonates that are weakly physisorbed on the surface and are therefore easily removed. The subsequent etching process can then remove the material under the exposed areas to reveal the pattern.

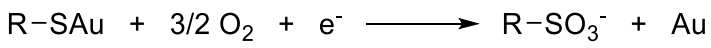

Scheme 2.1. Photooxidation process of the Au-S bond.

The experimental setup consists of a 244 nm laser beam directed onto a Lloyd's mirror interferometer. The sample is mounted on one side of the interferometer and the mirror is positioned at a tilted angle of 2θ, as shown in Figure 2.8.[175]

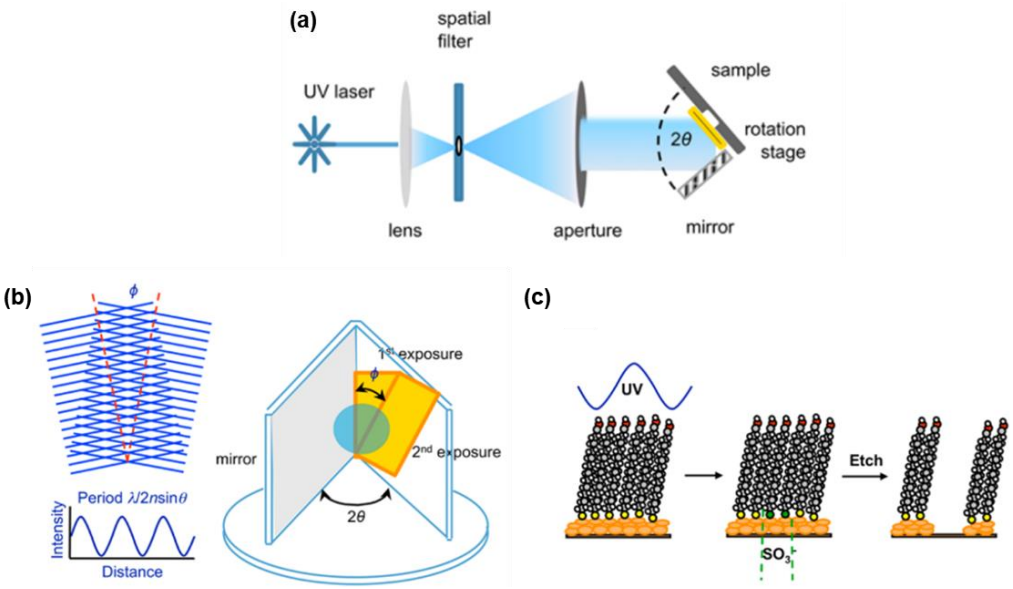

Figure 2.8. (a) Schematic illustration of the Lloyd's mirror interferometric lithography setup used for the fabrication of gold nanostructures. (b) Diagrams demonstrating the fabrication of the patterns by two exposures, with the sample rotated by an angle of φ between the exposures. (c) The photooxidation of the SAM on the gold surface exposed to the UV light, followed by the etching process to remove the exposed areas. The figure was taken from the work of Tsargorodska et al.[175]

The incident laser beam illuminates the interferometer, exposing the sample to both the direct laser beam and its reflection from the mirror. This interaction results in the formation of parallel lines, with the pitch (*p*) between two adjacent lines determined by the following equation:

$$p = \frac{\lambda}{2nsin\theta} \tag{2.11}$$

Where λ is the wavelength of light, n is the refractive index of the medium and θ is the angle between the sample plane and the mirror. Multiple exposures enable the creation of intricate periodic patterns. For instance, rotating the sample by an angle of φ around its in-plane axis allows the creation of period nanodot arrays, as outlined in the following experimental procedure.

2.2.3.1 Experimental process

The patterning was carried out using a Lloyd's mirror two-beam interferometer. A Coherent Innova 300C frequency-doubled argon-ion laser (Coherent, UK) was used to generate UV light (244 nm). The beam was passed through a focusing objective, 10 µm pinhole, then a spatial filter and expanded to irradiate a region ca. 0.8 cm^2 in size. The angle between the mirror and the sample in the interferometer was varied between 20 ± 2.5º and 30 ± 2.5º. The etching of the photopatterned monolayers was carried out by immersion in a solution of 2 mM cysteamine with 8% V/V of ammonia in ethanol. After etching, the samples were rinsed with ethanol, dried with nitrogen and annealed in a chamber furnace (Carbolite, UK) at 525 ± 3°C for 120 min with a heating rate of 7 °C min^{-1}. Further details of the fabrication process are outlined in *Chapter 3*.

2.2.4 Micropatterning of surface-grafted polymers

Micropatterned polymer brushes were prepared using a photolithographic process. Briefly, a SAM of thiols formed on gold surfaces is exposed to a UV laser through a copper mesh grid mask. The oxidized thiols are then washed off the surface and replaced by a SAM of the ATRP initiator. After the SAM formation, polymer brushes are grown form the initiator-covered regions (Figure 2.9).

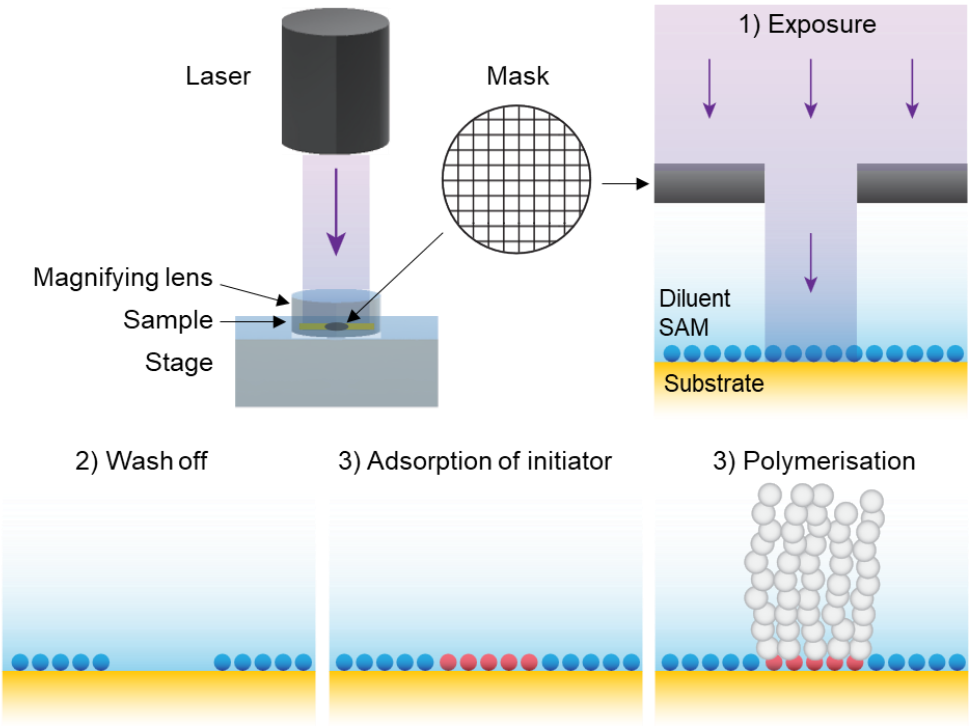

Figure 2.9. Illustration of the micropatterning process. A sample is prepared with a "diluent" molecule SAM, followed by the exposure to UV light through a mesh grid. The photo-oxidised molecules are then removed by a solvent wash. Following, the sample is immersed in a solution of the initiator-containing thiols to form a SAMs on the exposed surface, from which the polymerisation can be initiated.

2.2.4.1 Experimental procedures

The exposure was carried out using a Coherent Innova 300 C frequency-doubled argon ion laser (λ = 244 nm) through a copper mesh grid with a mesh of 2000, which was held in place by a quartz disk. The experimental process is outlined in detail in *Chapter 3*.

2.2.5 Electron-beam lithography (EBL)

Electron-beam lithography (EBL) is a nanofabrication technique that allows the precise fabrication of nanostructures on a substrate using a focused electron beam.

A resist is deposited onto the substrate by spin-cpating. The resist serves as a mask to protect or expose specific areas of the substrate during the electron exposure. A positive or negative type resist can be used, depending on the sample requirements. After coating with the resist, the sample is loaded into a sample holder with thin conducting layers above or below the resist, in order to reduce any charging effects. The holder is then transferred into the high vacuum EBL chamber, where the patterning takes place. The electrons are emitted from an electron gun, often using a field-emission electron source. These electrons are focused into a fine beam using electromagnetic lenses to be scanned across the sample surface in a predetermined pattern. The scanning is controlled using a computer software, which allows the creation of complex patterns by defining the desired geometries on the surface, designing the scan path and specifying exposure parameters such as beam current and exposure time. In particular, the exposure dose, which depends on the beam current and exposure time, needs to be controlled to prevent overexposure or underexposure of the resist.

After the electron beam exposure has been completed, the sample is subjected to a controlled baking process to stabilize the resist material and remove any remaining solvent, after which it is gradually cooled to room temperature. Subsequently, the resist is developed by immersion

in an appropriate solvent to selectively remove the areas where the resist remained soluble. These are the exposed areas of positive resists and the unexposed areas of negative resist types. Rinsing the sample thus yields the desired surface pattern.

2.2.5.1 Fabrication procedures

The samples were spin-coated (5k round-per-minute (rpm)) with 2% hydrogen silsesquioxane (HSQ, Dow Corning XR-1541 E-beam resist), after which the lithography process was carried out immediately. Using electron beam lithography (EBL, Elionix ELS-7000), the patterns were written with an electron acceleration voltage of 100 keV, a beam current of 500 pA, and the exposure dose depending on the desired pattern characteristics. To develop the sample, it was immersed in a solution of NaOH/NaCl (1% wt./4% wt. in de-ionized water) for 60 seconds and deionized water for another 60 seconds, followed by rinsing with acetone, isopropyl alcohol (IPA) and drying with nitrogen.[176] Details of the sample fabrication specific to each study are outlined in *Chapter 4* and *Chapter 5*.

Chapter 3. Chlorophyll Binding to Poly(cysteine methacrylate) Scaffolds in Pigment-Polymer Antenna Complexes studied by Depth-Profiling X-Ray Photoelectron Spectroscopy

3.1 Introduction

Light-harvesting complexes (LHCs) organise pigment molecules (chlorophylls and carotenoids) with exquisite precision within photosynthetic membranes in plants and bacteria.[14] There has been intense interest in the design of biomimetic materials that are inspired by these pigment-protein complexes for applications in solar energy capture,[177–180] artificial photosynthesis,[181–183] photonic device fabrication[184,185] and other areas.[186,187] Recently, a new approach to the design of biomimetic light-harvesting structures was described, in which *pigment-polymer* antenna complexes, formed by the covalent attachment of chlorophylls (Chl) to surface-grafted polymer scaffolds grown by atom-transfer radical polymerisation (ATRP) from gold nanostructures, are coupled to localised surface plasmon resonances (LSPRs) to yield *plexcitonic antenna complexes*.[48] In these systems, strong light-matter coupling leads to the formation of macroscopically-extended excited states, in which an ensemble of excitons exchanges energy coherently with a confined optical mode. Concentrations of Chl were achieved in plexcitonic antenna complexes that were ~3× higher than those found in plant antenna complexes, and plasmon-exciton coupling energies up to 0.4 eV were achieved, ~2× larger than those determined for similar systems based on biological LHCs.

Thus, plexcitonic antenna complexes are promising templates for the design of novel kinds of biomimetic photonic materials. However, to realise this goal, it is desirable to achieve a high

degree of programmability, so that materials can be designed that display bespoke optical properties. In the strong coupling regime, the coupling energy E_C is proportional to $\sqrt{N}$, where N is the number of excitons within the plasmon mode volume. Moreover, the field strength of the plasmon mode decays with distance, being greatest near to the gold surface. Thus, to achieve programmability of optical properties, it is necessary to be able to control the organisation of excitons (Chl) within the polymer scaffold. Chl are bulky, with a molecular mass ~ 2× that of the PCysMA repeat unit; thus penetration of Chl into the polymer scaffold is expected to be sterically hindered, and strongly dependent on the polymer grafting density, and the task of controlling the distribution of Chl within the scaffold is challenging.

The distribution of the pigments within polymer brushes can be controlled via covalent attachment to the monomer units, which prevents aggregation and loss of the chromophores, while aiding their solvation.[188,189] One approach to achieve this is by synthesising and polymerising dye-containing monomer units. However, this poses challenges due to potential back-biting and cross-linking processes, which hinder the polymerisation mechanism and rate.[190] Moreover, many common dye molecules act as radical traps, thus inhibiting radical polymerisation mechanisms. Alternatively, molecules can be coupled to pre-formed polymer chains using various chemical procedures, including carboxylic acid activation with carbodiimide and succinimide chemistry,[191,192] triazines and alkyne-azine cycloadditions,[193,194] or thiol-ene coupling.[195–197] When smaller molecules are involved, the degree of functionalisation is typically high (>70%).[196] For instance, 4-(trifluoromethyl)benzylamine can be readily attached to brushed containing succinimidyl group-activated carbonate monomers.[198] However, bulkier molecules are subject to significant steric constrains, and their diffusion into the polymer network depends significantly on the density of the brush

film.[64,68,199] Consequently, low attachment rates and inhomogeneous distribution within the films are commonly observed.

In plexcitonic antenna complexes, the scaffold is a surface-grafted poly(amino acid methacrylate), poly(cysteine methacrylate), PCysMA, grown by atom-transfer radical polymerisation (ATRP) from initiators at the surface of gold nanostructures. This enables the grafting of uniform films with high controllability of the polymer thickness.[200] Chl are covalently coupled to pendant amine groups via active ester linkers. The goal of this study is to determine the extent to which the organisation of Chl (and hence, excitons) can be programmed in 3D by regulating the polymerisation time and grafting density of the surface-grafted polymers. We use depth-profiling by X-ray photoelectron spectroscopy (XPS) combined with sputtering by Ar_{3000}^+ and Ar_{2000}^+ gas clusters to characterise the distribution of Chl in the surface-grafted film as a function of the degree of polymerisation and grafting density.

Conventional XPS depth-profiling approaches are impeded by the limited sampling depth (for angle-resolved measurements[201]) and the high rate of ion beam damage (in conventional depth-profiling using argon ion beams[202,203]). In recent years, however, there has been interest in the application of gas cluster sources to the analysis of polymeric materials. In contrast to conventional Ar^+ sources, which yield a high rate of degradation in polymer systems, giant gas cluster ion sources (GCIS) offer controllable, low rates of erosion, thus opening the way to accurate in-depth analysis.[202,204,205] In particular, gas cluster sources offer the possibility for chemical state analysis with depth,[206–208] whereas older approaches tended to yield largely compositional analyses.[209–213]

In this chapter the utility of Ar_{3000}^+ and Ar_{2000}^+ clusters for the characterisation of Chl binding to PCysMA scaffolds is examined. In addition, the plasmon-exciton coupling of the plexcitonic complexes grown from nanostructured gold is analysed using extinction measurements. It is shown that XPS depth-profiling facilitates sensitive, quantitative analysis of Chl binding as a function of depth, degree of polymerisation and surface grafting density. These findings demonstrate that the grafting density of the polymer films can be controlled by co-adsorption of initiator-terminated disulfides and inert thiol molecules. Chemical state analysis enables quantitative measurement of the fraction of cationic nitrogens in pendant amine groups as a function of depth, revealing a charge gradient through the film. In contrast, chemical state analysis indicates that there is a uniform distribution of the pigment molecules throughout the films, while the overall concentration of Chl within the polymer is dependent on the polymer grafting density. The extinction spectra of the plexcitonic complexes formed by growing Chl-functionalised scaffolds from gold nanostructures is measured. It is demonstrated that the plasmon-exciton coupling is readily controlled by manipulation of the architecture of the plexcitonic complexes, and that the XPS depth-profiling data are correlated with plasmon-exciton coupling energies, determined by modelling of the strong coupling. This study of biomimetic pigment-polymer antenna complexes opens up exciting possibilities in the design of applications that require organic networks with tailored optical properties, such as solar energy capture,[40,214–216] catalysis[217,218] and advanced photonic devices.[219–222]

3.2 Experimental

3.2.1 Materials

Acetone-d6 (≥ 99%), ammonia solution (35%), deuterium oxide (99.9%), methanol (HPLC grade, 99.99%), sulfuric acid (≥95%), sodium hydroxide (≥ 97%), dichloromethane (HPLC grade, 99.8) and dimethylformamide (99%) were obtained from Fisher Scientific (Loughborough, UK). Ethanol (HPLC grade, ≥99.8%), acetone (HPLC grade, 99.8%), Diethyl ether (HPLC grade, ≥ 99.8%) and n-hexane (HPLC grade, ≥97) were obtained from Honeywell Research Chemicals (Loughborough, UK). Acetic acid (≥ 99.7) petroleum ether (40-60°C HPLC grade) and ethyl acetate (99.5%) were obtained from Sigma-Aldrich, Poole, UK. Chloroform-D (99.8%), hydrochloric acid (35%) and hydrogen peroxide (30%) and tetrahydrofuran (99.7%) were obtained from VWR chemicals (Lutterworth, UK).

11-mercapto-1-undecanol (97%), 2,2'-Bipyridyl (≥ 99%), 2,4,6-Trimethylpyridine (99%), 2-Bromoisobutyrylbromide (98%), 3-(Acryloyloxy)-2-hydroxypropyl methacrylate (≥ 70%), 3-Aminopropyltriethoxysilane (99%), 4-(dimethylamino)pyridinium 4-toluenesulfonate (98%), Bis[2-(2-bromoisobutyryloxy)undecyl]disulphide (97%), Copper (II) chloride (99%), cysteamine hydrochloride (≥ 98%), L-Ascorbic acid (reagent grade, ≥ 98%), L-Cysteine, 3-(acryloyloxy)-2-hydroxypropyl methacrylate, lithium hydroxide monohydrate (≥ 98%), dimethylphenyl phosphine (99%), N-(3-Dimethylaminopropyl)-N'-ethylcarbodiimide hydrochloride (crystalline), N-Hydroxysuccinimde (98%), oxalyl chloride (99%), paraffin oil (puriss), phosphate buffered saline (tablets), triethylamine (≥ 99.5%) and zinc acetate dihydrate (99.999%) were obtained from Sigma-Andrich, UK. Spinach leaves (500 g) were procured from a local supermarket retailer. Silica gel (40-63 μm particle size), sand (acid-washed) was obtained from VWR chemicals (Lutterworth, UK). Magnesium sulfate (anhydrous, ≥ 70%),

sodium chloride (≥ 99.5%), sodium dodecyl sulphate (micropellets), sodium hydrogen carbonate (≥ 99%), sodium hydroxide (≥ 97%) was purchased from Fisher Scientific (Loughborough, UK. Argon gas (ISO 14175-I1-Ar, Pureshield) was purchased from BOC (UK).

Chromium chips (99.5% trace metals basis) were obtained from Sigma-Aldrich. Gold wire (99.997% trace metals basis) was obtained from Goodfellow Advanced Materials (UK). Microscope coverslip glass slides (22 mm × 50mm, #1.5 thickness) were purchased from Menzel-Gläser (Germany) The AFM tapping probes (OTESPA-R3 model, resonance frequency of ca. 300 kHz and a nominal tip radius of 7 nm) were obtained from Bruker (Germany). Copper mesh grids (mesh 2000, 3.05 mm) were purchased from Agar Scientific (Essex, UK).

Deionized water was created by filtering water with an Elga Purelab Option DV35 water filtration system, measured to a conductivity rating of 15 mΩ.cm.

3.2.2 Methods

3.2.2.1 Characterization of the synthesised materials

The ^{1}H NMR spectra was obtained using Bruker Avance and Avance III HD NMR spectrometers, operated at a frequency of 400 MHz. Liquid chromatography mass spectrometry (LC-MS) analysis was carried out with a Waters LCT classic time-of-flight (ToF) liquid-chromatography mass spectrometer at the Sheffield Department of Chemistry Chromatography Service.

3.2.2.2 Cleaning of glassware and substrates

Prior to their use, microscope coverslip slides and glassware were cleaned by immersion in piranha solution (a mixture of 30% hydrogen peroxide and 70% concentrated sulfuric acid). Once cooled to room temperature, the glassware was rinsed with copious amounts of deionised water and sonicated for 10 – 15 min, after which it was placed in an oven (ca. 90 ºC) to dry.

3.2.2.3 Fabrication of gold slides

Microscope coverslip glass were used as substrates for chromium and gold deposition. The thermal evaporation was carried out using a diffusion pumped Edwards 306 thermal evaporator with a bell jar evaporation chamber and a piezoelectric film-thickness monitor, and the metals were deposited from a gold wire and chromium chips. The gold wire was evaporated from a tungsten cup boat, while the chromium chips were evaporated from a tungsten coiled wire boat. The evaporation chamber was roughed out to a pressure of 10^{-1} mbar via a rotary pump, after which the diffusion pump was engaged for high vacuum. When the pressure of at least 10^{-6} mbar had been reached, the current was supplied to the boat to achieve a deposition rate of 0.1 nm/s to create a chromium adhesive layer with a thickness of 5 – 7 nm and a gold layer with a thickness of 20 – 25 nm. After the required thickness was reached, the current was lowered slowly and the Cr/Au coated coverslip slides were left to cool for at least 30 min.

3.2.2.4 Fabrication of gold nanostructure arrays

The gold nanostructures were fabricated by Dr Anna Lishchuk using interference lithography, as outlined in the following reference article.[174] Gold slides were functionalised with a SAM of 1-octadecanethiol (ODT) by immersion in a 1 mM solution of ODT in degassed ethanol for 18 h. Following, the slides were rinsed with ethanol and dried with nitrogen, after which they were immediately photopatterned by interferometric lithography. The patterning was carried

out using a Lloyd's mirror two-beam interferometer. A Coherent Innova 300C frequency-doubled argon-ion laser (Coherent, UK) was used to generate UV light (244 nm). The beam was passed through a focusing objective, 10 μm pinhole, then a spatial filter and expanded to irradiate a region ca. 0.8 cm^2 in size. The angle between the mirror and the sample in the interferometer was varied between 20 ± 2.5º and 30 ± 2.5º. A dose of 35 – 40 J cm^{-2} was used to expose the SAM functionalized gold surfaces. Parallel lines of gold nanostructures were created by a single exposure. Patterns of gold nanodots were achieved by a second exposure after the rotation of the sample on the stage by different angles. The second exposure was carried out at a dose 15 – 20% lower than the first one to avoid overexposure.

The etching of the photopatterned ODT monolayers was carried out by immersion in a solution of 2 mM cysteamine with 8% V/V of ammonia in ethanol. After etching, the samples were rinsed with ethanol, dried with nitrogen and annealed in a chamber furnace (Carbolite, UK) at 525 ± 3°C for 120 min with a heating rate of 7 °C min^{-1}.

3.2.2.5 Preparation of micropatterned PCysMA brushes

Substrates with Cr/Au were functionalised with 11-mercapto-1-undecanol by immersion in a 2 mM ethanolic solution, as outlined in the *Formation of mixed self-assembled monolayers* in Chapter 3. After the 24 h incubation period, the slide was removed, rinsed with ethanol and dried with nitrogen. Subsequently, the sample was exposed to a Coherent Innova 300 C frequency-doubled argon ion laser (λ = 244 nm) through a copper mesh grid with a mesh of 2000, which was held in place by a quartz disk. The samples were exposed using a dose of 62 J cm^{-2} to photooxidise the alkanethiolates in microscale patterns. The samples were then rinsed with ethanol and moved into 2 mM ethanolic solutions either DTBU or the mixed solutions of DTBU and 11-MUL for 2 hours. When ready, the samples were removed from the solution,

rinsed with ethanol and dried with nitrogen, after which the PCysMA brushes were grown from the samples as outlined in section *"3.2.2.17 Synthesis of PCysMA brushes"*. Following, the thickness of the polymer layers was determined using tapping-mode AFM measurements.

3.2.2.6 Optical characterization

Spectroscopic ellipsometry was carried out on an Alpha-SE ellipsometer (J. A. Woollam Co., Lincoln, NE), using a He-Ne laser with an excitation of $\lambda = 633$ nm. The data was recorded at an incident angle (Φ) of 70º. During the data fitting process, the dry polymer films were fitted using a refractive index (n) of 1.50.[223] Ultraviolet-visible spectroscopy analysis was carried out using an Agilent Technologies Cary 50 spectrophotometer in the spectral range of 350 - 800 nm. The gold plasmonic arrays prepared with interferometric lithography were measured with a Cary 5000 spectrophotometer, in a spectral range of 350 - 850 nm.

3.2.2.7 Contact angle goniometry

The contact angle of deionised water was measured using a Rame-Hart 100-00 goniometer on the sample surfaces, using a droplet of a 2 µL. The contact angle was measured 5 s after the deposition, three times on each side of the droplet.

3.2.2.8 XPS measurements and depth-profiling procedures

XPS measurements were collected using a Kratos Axis Supra spectrometer (Kratos Analytical, Manchester, UK). The source used was a monochromatized Al Kα X-ray source using an emission current of 15 mA, operating at 225 W and a base pressure of 10^{-8} – 10^{-10} mbar. The analysis area was 700 µm × 300 µm. High-resolution and survey scans were acquired with pass energies of 40 eV and 160 eV, with a resolution of 0.10 eV and 1.0 eV, respectively. The

conditions of depth-profiling measurements were as follows. For fully dense brush films, the measurements were carried out by etching of the material using a Ar_{3000}^+ cluster source and energy of 10 keV, which was rastered across a 2 mm × 2 mm region. After the etching process, high resolution spectra were collected over a 110 µm × 110 µm sampling area in the centre of the crater with a resolution of 0.2 eV, using a 40 eV pass energy and ion beam current of 7.3 nA. The etching time was 60 s per etching cycle. For the films with a grafting density of $\chi_{Br(Au)} = 0.47 \pm 0.11$, the etching time was 15 s per cycle, while for polymers with $\chi_{Br(Au)} = 0.39 \pm 0.07$, a time of 10 s was used. The depth-profiling of the lowest density films of $\chi_{Br(Au)} = 0.26 \pm 0.05$ were collected by etching with an Ar_{2000}^+ cluster source and energy of 5 keV. The ion beam current was 6.3 nA and an etching time of 5 s was selected. The peak fitting was carried out using the CasaXPS software. The peak positions were calibrated to the main hydrocarbon C1s signal, which was set to 285 eV.

3.2.2.9 AFM measurements

Micropatterned pCysMA brushes were prepared as outlined in *"3.2.2.5 Preparation of micropatterned PCysMA brushes"* after which the samples were transferred to the microscopy setup to be measured in ambient conditions. The measurements were carried out in air using a NanoScope Multimode V microscope (Bruker, Germany). Images were obtained in tapping mode with OTESPA-R3 tapping probes (Bruker, Germany, resonance frequency of ca. 300 kHz and a nominal tip radius of 7 nm). The measurements were analysed with the Bruker NanoScope Analysis (v.1.5) software.

3.2.2.10 Synthesis of cysteine methacrylate (CysMA)

The monomer was prepared following the method of Alswieleh et al.[2] L-Cysteine (7.54 g, 62.23 mmol) was dissolved in 100 mL of deionised water, and 3-(acryloyloxy)-2-hydroxypropyl methacrylate (13 mL, 14.86 g, 69.36 mmol) was added slowly to the stirred aqueous solution. Afterwards, dimethylphenyl phosphine (20 μL, 1.94 μg, 1.41 x 10^{-8} mol) was added as a catalyst to initiate the reaction. The cloudy solution was then stirred at room temperature for 2 h, after which time the solution became colourless. Once complete, the product was washed with ethyl acetate (2 x 100 mL) followed by dichloromethane (3 x 100 mL). The water was then removed by rotary evaporation at 55 – 60°C to produce a white solid. After collection, the solid was then dried under reduced pressure for 48 h, with analysis confirming the CysMA monomer as a white, crystalline solid (16.175 g, 48.12 mmol, 77%). The resulting CysMA monomer was stored in a desiccator at room temperature. ^{1}H NMR (400 MHz, D_2O) δ (ppm)=1.86 (s, 3H), 2.60–3.15 (m, 6H), 3.74 (m, 1H), 3.84 (m, 1H), 4.08–4.43 (m, 4H), 5.67 (s, 1H), 6.09 (1H); ^{13}C NMR (400 MHz, D_2O) δ (ppm) = 17.37, 26.41, 32.18, 33.95, 53.61, 65.27, 65.34, 66.90, 127.18, 135.66, 168.72, 172.75, 174.14; TOF MS LD^+: expected = 335.37 g·mol^{-1}, observed = 336.0 [$(M+H)^+$, M=$C_{13}H_{21}NO_7S$]; HPLC (30 min, 10% Acetonitrile in water (0.1% trifluoroacetic acid), detection = 225 nm) = 22.8 min, 90.0%.

3.2.2.11 Extraction of pheophytin *a*

Spinach leaves (500 g) were prepared by cutting the stems and mid-veins from the leaves and discarding them, followed by washing with deionised water. These were then dried on paper towel and then frozen for 16 h at -20°C. This matter was then macerated in 6 instalments by placing the leaves in a blender with acetone (250 mL) and stirring on a pulse setting for several min until a dark green slurry was obtained. The extract was then filtered by standard vacuum filtration to separate the dark green liquid from the leftover pulp. The acetone and the remaining

water were then removed by rotary evaporation to give a dark green substance. This was extracted from the remaining water first using petroleum ether 40-60°C followed by washing with 60% aqueous methanol. The resulting organic layer was dried over magnesium sulfate, filtered and the solvent removed, leaving a green solid.

To simplify the separation process, all the chlorophylls present in this initial mixture were reduced to their non-metallated pheophytin variants. Here, the solid was dissolved in glacial acetic acid (25 mL) and stirred for 3 h at room temperature. The solution was then neutralised to pH 7 with careful addition of saturated aqueous sodium hydrogen carbonate solution. A brown precipitate was formed in the solution. This precipitate was then extracted from the water layer using dichloromethane and the combined organic layer washed with water before drying and solvent removal as before. The resulting brown solid was then purified by column chromatography (silica, 6:3:2 n- hexane: ethanol: acetone) to give pheophytin *a* as a black solid (235 mg, 0.288 mmol). R_f =0.33 (6:3:1 hexane: ethanol: acetone); LC-TOF-MS ES+, obs. *m/z* = 872 (17.191 min), calc. = 871.22 [$(M + H)^+$, M=$C_{55}H_{74}N_4O_5$]. ^{1}H NMR (400 MHz, $CDCl_3$) δ (ppm) = 0.09, -1.60 (br s, 1H, NH), 0.69-0.97 (m, pythyl CH-CH_3) 0.96-1.41 (m, pythyl CH_2), (m, pythyl vinyl, 2H) 1.82 (d, *J* = 6.29, 3H), 1.90 (m, 3H), 2.08 (m, 3H), 2.19, 2.36 (m, 2H), 2.50, 2.64 (m, 2H), 2.83 (br t, *J* = 5.39, 2H), 3.26 (s, 3H, methyl), 3.42 (s, 3H, methyl), 3.71 (br s, 3H, methyl), 3.71 (br s, 2H, CH_2-CH_3) 3.90 (s, 3H, $COOCH_3$), 4.23 (br d, *J* = 7.71 Hz, 1H) 4.31 (m, 2H, pythyl CH_2), 4.46 (m, 1H HC-CH_3), 4.50 (m, 3H, CH_3) 5.15 (m, 1H, pythyl vinyl), 5.14, 5.38 (m, multiple H, aggregation), 6.18 (d, *J* = 9.16, 1H, vinyl), 6.22 (s, 1H, C*H*-$COOCH_3$), 6.31 (d, *J* = 19.21 Hz, 1H, vinyl, cis), 8.02 (dd, *J* = 11.28, *J* = 5.97, 1H, vinyl, trans) 8.58 (s, 1 H, ring δ-H), 8.85 (s, 1H, ring α-H), 9.40 (s, 1H, ring β-H).

3.2.2.12 Methyl pyropheophorbide *a* (Me-PyPh *a*)

Extracted pheophytin *a* (312 mg, 0.358 mmol) was dissolved in pure 2,4,6-collidine (20 mL) and the vessel backfilled with an argon atmosphere. This solution was then stirred at 130 °C with a reflux condenser under argon for 16 h. Once complete, the collidine was removed using a high-vacuum rotary evaporator (70-80 °C, 1-4 mbar) to give a brown solid. This solid was then immediately dissolved in an ice-cold sulfuric acid solution (50% in deionised water, 50 mL) and stirred at room temperature under argon for 3 h. The mixture was then poured into 1 L of ice water and the pH of the solution was adjusted to 5 using an aqueous solution of sodium hydroxide. The solution was left to stir for 4 h, allowing to precipitate. The precipitated black solid was collected by vacuum filtration, washed with ice cold water and then dissolved in dichloromethane (100 mL) to collect. The organic solution was washed with water (3 x 100 mL) and once with 10% aqueous sodium bicarbonate (100 mL), followed by drying with magnesium sulfate and solvent removal as before. The resulting solid was then purified by column chromatography (silica, 6:3:2 n-hexane: ethanol: acetone) to give a brown solid (108 mg, 0.197 mmol, 55%): R_f = 0.48; LC-TOF-MS ES+, obs.=549 (14.006 min), calc.=548.69 [$(M)^+$, M = $C_{34}H_{36}N_4O_3$]. ^{1}H NMR (400 MHz, $CDCl_3$) δ (ppm) = 0.13, -0.71 (br s, 2H, NH) 0.85-0.96 (m, aggregation), 1.19-1.39 (m, aggregation), 1.47 (s, 3H), 1.70 (t, *J* = 7.66 Hz, 3H), 1.89 (d, *J* = 5.77, 3H), 2.06 (m, 3H), 2.19, 2.33 (m, 2H), 2.59, 2.73 (m, 2H), 2.84 (br t, *J* = 5.95 Hz, 2H), 3.22 (s, 3H), 3.42 (s, 3H), 3.65 (s, $COOCH_3$, 3H), 3.66 (s, 3H), 3.67 (s, 2H), 3.70 (s, 3H), 4.31 (br d, *J* = 7.16 Hz, 1H), 4.51 (dd, *J* = 7.16 Hz, 1H), 5.21 (dd, *J* = 19.62 Hz, J = 42.55 Hz, 2H), 5.38 (m, multiple H, aggregation), 6.18 (d, *J* = 11.57 Hz, 1H, vinyl), 6.29 (d, *J* = 17.90, 1H, vinyl), 7.02 (s, 1H, cis), 7.99, (dd, *J* = 6.10 Hz, *J* = 11.45 Hz, 1H, vinyl, trans), 8.59 (s, 1H, ring δ-H), 9.37 (s, 1H, ring α-H), 9.48 (s, 1H, ring β-H).

3.2.2.13 Pyropheophorbide *a* (PyPh *a*)

Me-PyPh *a* (102 mg, 0.186 mmol) was dissolved in tetrahydrofuran (25 mL) to which aqueous lithium hydroxide monohydrate (3 M, 10 mL) was added. This mixture was stirred under argon at room temperature for 18 h. Once complete, the solution was neutralised with addition of 3 M aqueous hydrochloric acid dropwise until pH 7 was reached according to universal indicator paper. The organic layer was then extracted with dichloromethane (3 x 50 mL), washed with water (3 x 100 mL) followed by brine (100 mL), then dried with magnesium sulfate, filtered and evaporated as before. This resulted in a black solid (71 mg, 0.138 mmol, 74%): TOF-MS ES+, obs. = 535.1, calc. = 534.66 [$(M + H)^+$, M = $C_{33}H_{34}N_4O_3$]. ^{1}H NMR (400 MHz, $CDCl_3$) δ (ppm) = 0.12, -1.73 (br s, 1H, NH), 0.89 (br dd, *J* = 6.61 Hz, 2H), 1.24 (d, *J* = 6.15 Hz, 3H), 1.25-1.39 (m, aggregation), 1.65 (t, *J* = 7.68 Hz, 3H), 1.83 (d, J = 7.09 Hz, 3H), 2.24, 2.36 (m, 2H), 2.65 (m, 2H), 3.15 (s, 3H), 3.38 (s, 3H), 3.06 (s, 3H), 3.59 (s, 3H), 4.06 (q, *J* = 6.15 Hz, 1H), 4.29 (br d, J = 9.22 Hz, 1H), 4.48 (br dd, *J* = 6.66, *J* = 7.43 Hz, 1H) 5.18 (q, *J* = 19.84 Hz, J = 41.50 Hz, 2H), 6.13 (d, *J* = 11.46 Hz, 1H, vinyl), 6.24 (d, *J* = 18.09 Hz, 1H, vinyl, cis), 7.91 (dd, *J* = 6.26 Hz, J = 11.46 Hz, 1H, vinyl, trans), 8.54 (s, 1H, ring δ-H), 9.26 (s, 1H, ring α-H), 9.36 (s, 1H, ring β-H).

3.2.2.14 Zinc-pyrochlorophyllide *a* (Zn-pyChl)

PyPh *a* (71 mg, 0.138 mmol) was dissolved in dichloromethane (35 mL) and saturated zinc acetate dihydrate in methanol (4 mL) was added to this. The solution was then refluxed at 35 °C under argon for 40 min, after which the solution was observed to changed colour form dark brown to dark green. The organic layer was then extracted with ethanol (40 mL) followed by washing with water (3 x 50 mL). Drying with magnesium sulfate, filtration and solvent removal were then carried out as before to give a blue-green solid (66 mg, 0.110 mmol, 80%). TOF MS

LD+: expected = 695.097 g mol^{-1}, observed = 693.5 [$(M–2H)^+$, M = $C_{37}H_{35}N_5O_5Zn$]. ^{1}H NMR (400 MHz, $CDCl_3$) δ (ppm) = 0.09 (s ??), 0.88 (br t, *J* = 7.46 Hz, 3H, methyl), 1.00 (t, *J* = 7.59 Hz, 3H), 1.05-1.48 (m, multiple H, aggregation), 1.53 (q, *J* = 6.70 Hz, 3H), 1.79 (d, *J* = 28.31 Hz, 3H, methyl), 2.05 (m, 2H, CH_2-CH_2-COOH), 2.32 (m, 2H, CH_2-CH_2-COOH), 2.83 (t, *J* = 5.68 Hz, 2H, CH_2-CH_3), 3.17 (s, 3H, methyl), 3.34 (s, 3H, methyl), 3.68 (s, 3H, methyl), 3.95 (d, *J* = 7.10, 2H), 5.17 (br m, 1H), 5.37 (br m, 1H), 5.77 (dd, *J* =6.68 Hz, *J* = 10.96 Hz, 2H, vinyl), 6.39 (*J* =6.85 Hz, *J* = 10.57 Hz, 2H, vinyl), 7.00 (d, *J* = 7.23 Hz, 1H, vinyl, cis), 8.01 (m, 1H, vinyl, trans), 8.47 (br s, 1H, ring δ-H, 1H), 9.35 (br s, 1H, ring α-H), 9.55 (br s, 1H, ring β-H); TOF-MS ES+, obs. = 597.2, calc. = 598.024 [$(M – H)^+$, M = $C_{33}H_{32}N_4O_3Zn$]; IR (CH_2Cl_2 solvent, cm^{-1}) = 3500–2400 (broad band, O-H stretch), 3010 (sp^2 C-H stretch), 2926, 2858 (sp^3 C-H stretch), 1711 (C=O stretch), 1460 (aromatic C=C stretch), 1375 (C-O stretch); UV/Vis (dimethylformamide, nm) = 430 (Soret), 573 (Q_x), 656 (Q_y); HPLC (21 min, 75% Acetonitrile in water (0.1% trifluoracetic acid), detection=254 nm) = 12.4 min, 96.8%.

3.2.2.15 Succinimidyl zinc-pyrochlorophyllide *a* (SC-Zn-pyChl)

Zn-pyChl (10 mg, 1.67 × 10^{-5} mol) was mixed with 4-(dimethylamino)pyridinium 4-toluenesulfonate (5 mg, 1.7 × 10^{-5} mol), N-hydroxysuccinimde (20 mg, 0.174 mmol) and crystalline N-(3-dimethylaminopropyl)-N'-ethylcarbodiimide hydrochloride (22 mg, 0.115 mmol), followed by evacuation and backfilling with argon. The mixture was then dissolved in dry dichloromethane (36 mL) under an argon atmosphere, and the resulting solution was then stirred for 16 h at room temperature under argon. Once complete, the solution was diluted with dichloromethane (50 mL) and washed with water (2 x 50 mL) and once more with saturated brine solution (50 mL). The organic layer was then dried with magnesium sulfate, filtered and evaporated as before to give a green solid (11 mg, 1.58 × 10^{-5} mol, 95%). ^{1}H NMR (400 MHz,

$CDCl_3$) δ (ppm) = 0.09 (s ??), 0.88 (br q, J = 2.65 Hz, J = 6.68 Hz, 3H, methyl), 0.99 (t, J = 7.52 Hz, 3H), 1.05-1.48 (m, multiple H, aggregation), 1.53 (q, J = 6.6 Hz, J = 6.89 Hz, 3H), 1.65 (d, J = 16.07 Hz, 3H, methyl), 2.03 (m, 2H, CH_2-CH_2-COOH), 2.32 (m, 2H, CH_2-CH_2-COOH), 2.85 (d, J = 21.23 Hz, 2H, CH_2-CH_3), 3.17 (s, 3H, methyl), 3.26 (s, 3H, methyl), 3.68 (s, 3H, methyl), 3.86 (d, J = 6.82, 2H), 5.17 (br m, 1H), 5.32 (s, 4H, succinimidyl H), 5.37 (br m, 1H), 5.76 (dd, J =6.73 Hz, J = 11.06 Hz, 2H, vinyl), 6.13 (m, multiple H, aggregation), 6.39 (J =6.80 Hz, J = 10.48 Hz, 2H, vinyl), 7.01 (d, J = 7.33 Hz, 1H, vinyl, cis), 7.98 (q, J = 6.18 Hz, J = 11.48 Hz, 1H, vinyl, trans), 8.46 (s, 1H, ring δ-H, 1H), 9.24 (s, 1H, ring α-H), 9.41 (s, 1H, ring β-H); TOF MS LD+: expected = 695.097 g mol^{-1}, observed = 693.5 [$(M–2H)^+$, M = $C3_7H_{35}N_5O_5Zn$]; FTIR (solid state, cm^{-1}) 3352 (N-H stretch), 3189 (sp^2 C-H stretch), 2959, 2921 (sharp, sp^2 C-H stretch), 2851 (sharp, sp^3 C-H stretch), 2274 (N=C=O stretch), 1779 (sharp, C=O stretch), 1729 (sharp, C=O stretch, amide), 1661 (C=C stretch), 1535 (N-O stretch), 1375 (C-O stretch), 1200 (sharp, C-O/C-N stretch); UV/Vis (dimethylformamide, nm) = 431 (Soret), 573 (Q_x), 658 (Q_y).

3.2.2.16 Formation of mixed self-assembled monolayers

The Cr/Au-coated microscope coverslips were first cut, then rinsed with ethanol and dried using nitrogen. Ethanol was degassed with nitrogen for 1 h before preparing ethanolic solutions with varying molar ratios of bis[2-(2-bromoisobutyryloxy)undecyl] disulfide (DTBU, the ATRP initiator) and 11-mercapto-1-undecanol (11-MUL) to achieve a total concentration of 2 mM. To create single component monolayers, the same procedures were followed using the appropriate adsorbate at a concentration of 2 mM. Subsequently, the slides were immersed in the solution for 24 h at 4 ºC. When needed, the slides were rinsed with ethanol and dried using nitrogen.

3.2.2.17 Synthesis of PCysMA brushes

For the polymerization process, solutions containing the following components were prepared: CysMA (750 mg, 2.231 mmol, dissolved in 4 mL H_2O at 0.56 M concentration), Copper(II) chloride ($CuCl_2$) (14.6 mg, 0.109 mmol, dissolved in 5 mL H_2O), 2,2'-Bipyridyl (38.8 mg, 0.248 mmol, dissolved in 5 mL ethanol), and L-ascorbic acid (100 mg, 0.568 mmol, dissolved in 10 mL H_2O at 56.8 mM concentration). The $CuCl_2$ and 2,2'-bipy solution were combined to create a vivid blue $Cu(bipy)_2Cl_2$ complex solution (10 mL, with [$CuCl_2$] = 10.9 mM and [2,2'-bipy] = 24.8 mM). The L-ascorbic acid solution (0.18 mL, 1.02×10^{-5} mol) was added to the CysMA solution first, followed by the Cu/bipy solution (0.35 mL, containing $n_{(Cu)} = 3.82 \times 10^{-6}$ mol). The resulting solution was mixed gently, then left undisturbed for 7 – 10 min. Once the solution turned brown, the samples with self-assembled monolayers were immersed in the solution for different time intervals to achieve the desired polymer thickness. When ready, the sample was removed from the solution then washed thoroughly with deionized water and ethanol, after which it was stored in ethanol at 4°C until further use.

3.2.2.18 Attachment of succinimydyl zinc-pyrochlorophyllide *a* to PCysMA brushes

The as synthesised N-Hydroxy succinimidyl ester derivative of chlorophyll (*Chl*) was dissolved in a 1:3 mixture of DMF: phosphate buffered saline (pH 8, 10 mM) at a concentration of 1 mM. Once dissolved, PCysMA samples were immersed in the chlorophyll solution and functionalisation allowed to occur for 16 - 18 h. Once complete, the samples were washed with DMF followed by deionised water. This same procedure was used for both continuous gold substrates and plasmonic arrays of gold nanostructures. Samples were stored in ethanol in a fridge at the temperature of 4 °C until required.

3.2.2.19 Attachment of Chl to a SAM of 11-MUL

Zn-pyrochlorophyllide *a* (6 mg) was dissolved in anhydrous dichloromethane (10 mL) under argon atmosphere. Oxalyl chloride (5 mL) was added to the solution and stirred at room temperature for 2 hours, followed by the removal of solvent under reduced pressure to give a Zn-pyrochlorophyllide *a* acyl chloride as a green solid, which was used immediately for the coupling reactions. The SAMs were prepared by immersing substrates with gold were in a 2 mM solution of 11-mercapto-1-undecanol in degassed ethanol for 48 hours. The slides were then washed with ethanol, dried with nitrogen and were immersed in a freshly prepared solution of 3 mM Zn-pyropheophrobide *a* acyl chloride in anhydrous dichloromethane for 18 hours at -4 °C. The slides were then washed with dichloromethane, followed by washing with degassed ethanol and drying with nitrogen. The surfaces were analysed using X-ray photoelectron spectroscopy.

3.2.2.19 Attachment of Chl to pCysMA grown from glass

The clean glass samples were immersed in the solution mixture of 2% of 3-aminopropyltriethoxysilane (APTES) and 98% of ethanol for 30 min. The slides were then rinsed with ethanol and dried using nitrogen gas. Subsequently, the slides were placed in clean glass vials on a hotplate at 120 °C for 30 min. The top of the vials was covered with Al foil to avoid light exposure. Following the annealing process, the samples were immersed in a mixture of 0.37 mL 2-bromoisobutyrylbromide, 0.41 mL triethylamine and to 60 mL of dichloromethane. After the immersion for 30 min at room temperature, the slides were rinsed with dichloromethane, ethanol and dried using nitrogen gas. The polymerisation process and Chl attachment was then carried out according to the procedures outlined in *"3.2.2.17 Synthesis of pCysMA brushes"* and *"3.2.2.18 Attachment of succinimydyl zinc-pyrochlorophyllide a to PCysMA brushes*."

3.3 Results and discussion

Biological light-harvesting antennas regulate exciton molecules spatially via a network of proteins. The careful arrangement of the various pigment molecules is vital for the efficient transport of energy within the photosynthetic system. A biomimetic antenna should therefore follow a similar model, whereby loss is mitigated through "architectural" means. This is achieved in pigment-polymer complexes by using a polymer brush film to fulfil the role played by the protein scaffold in light-harvesting proteins. Figure 3.1 shows the method used to synthesise surface grafted pigment-polymer antenna complexes, as described in detail by Lishchuk et al.[48]. First, a poly(cysteine methacrylate) (PCysMA) scaffold is grown by surface-initiated activators regenerated by electron transfer atom transfer radical polymerisation (SI ARGET ATRP) from a self-assembled monolayer (SAM) containing bromine-terminated alkylthiolates. Second, a derivative of a zinc chlorophyllide functionalised with a linker terminating in an N-hydroxy succinimidyl ester group is coupled to amine groups on the scaffold. The aim of the work in this chapter was to discover how to achieve high concentrations in polymer films, distributed uniformly through the surface-grafted polymer layer.

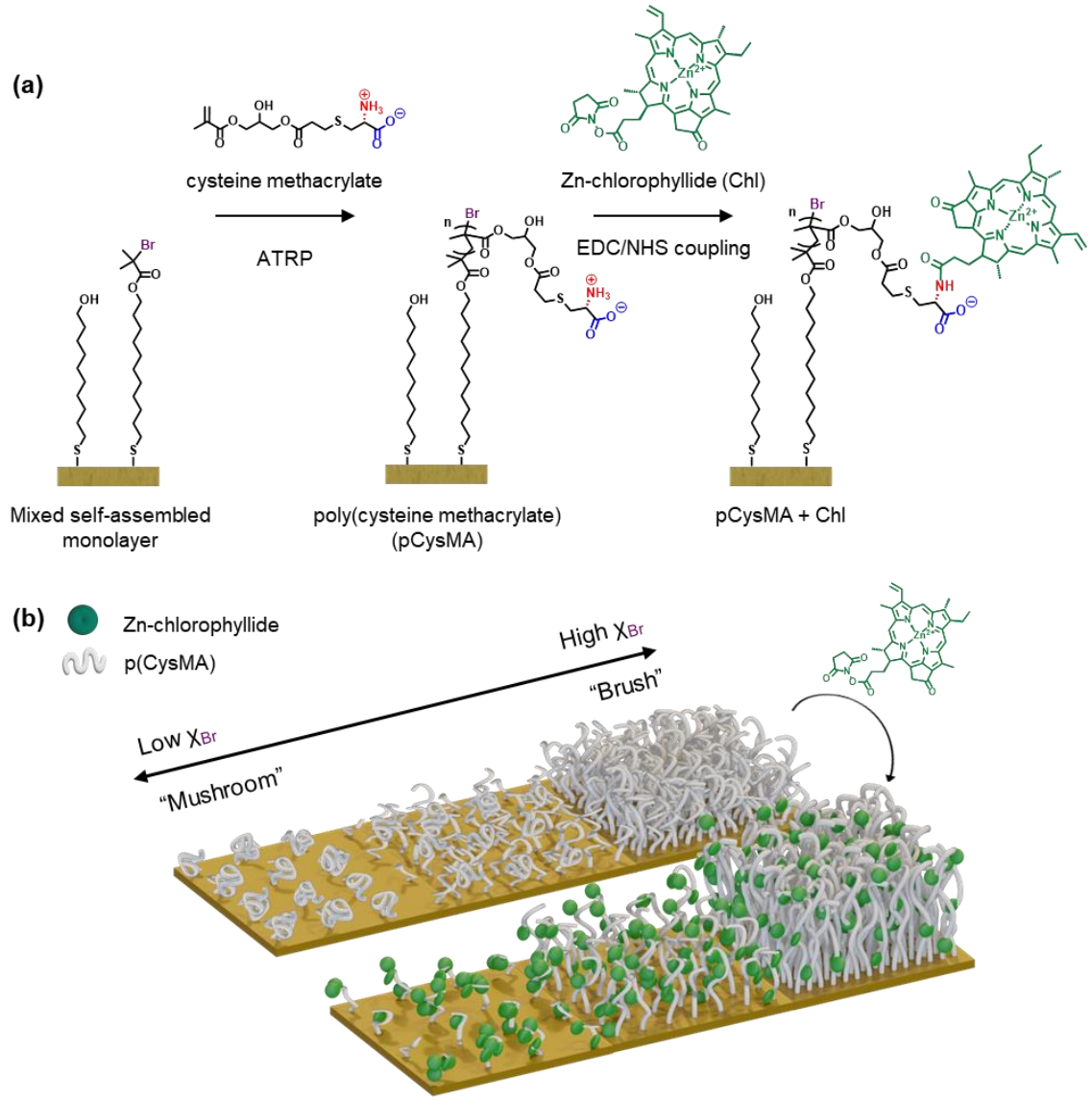

Figure 3.1. Synthesis of pigment-polymer antenna complexes. (a) Reaction scheme demonstrating the formation of a mixed self-assembled monolayer using 11-mercapto-1-undecanol (11-MUL) and bis[2-(2-bromoisobutyryloxy)undecyl] disulfide (DTBU, initiator molecule), followed by surface-initiated ATRP to grow CysMA, and subsequent functionalisation with the active ester modified chlorophyll *via* ethylcarbodiimide/N-hydroxysuccinimide (EDC/NHS) coupling. (b) Illustration of pCysMA films grown from varying initiator molar fractions (χ_{Br}) on gold, depicting the consequent conformation changes. The networks are derivatised with *Chl* which concentration and distribution along the chains are regulated by the grafting density of the polymer.

3.3.1 Characterisation of Initiator-Functionalised SAMs

It was hypothesised that the density of chlorophyllides within the surface-grafted polymer film could be controlled by regulating (a) the grafting density and (b) the polymerisation time *t* of the surface-grafted polymers. To control the grafting density of surface-tethered polymers, bis[2-(2-bromoisobutyryloxy)undecyl] disulfide (DTBU) was co-adsorbed with mercaptoundecanol (11-MUL) from solutions containing various ratios of the two adsorbates to form mixed SAMs on gold. DTBU is a symmetrical disulfide and dissociates on adsorption onto the gold surface to yield two bromine-terminated alkylthiolates, while 11-MUL acts as an inert diluent. After adsorption onto gold, the molecules form thiolates of similar chain lengths. The molar concentration of the initiator sites in the SAM was regulated by changing the ratio of the concentrations of the two adsorbates in the solution from which the SAM was formed.

Previous studies of mixed SAMs have indicated that there is a competition between kinetics and thermodynamics during monolayer formation,[224–228] with the consequence that the composition of a mixed SAM typically differs slightly from the composition of the solution form which it is formed. Thus, the compositions of the mixed SAMs used in this study were characterised by XPS. Representative high-resolution spectra are shown in Figure 3.2. Detailed information, including the peak positions, full widths at half maximum (FWHM), the fitting parameters, peak areas and % atomic compositions can be found in Table A1.1-A1.5.

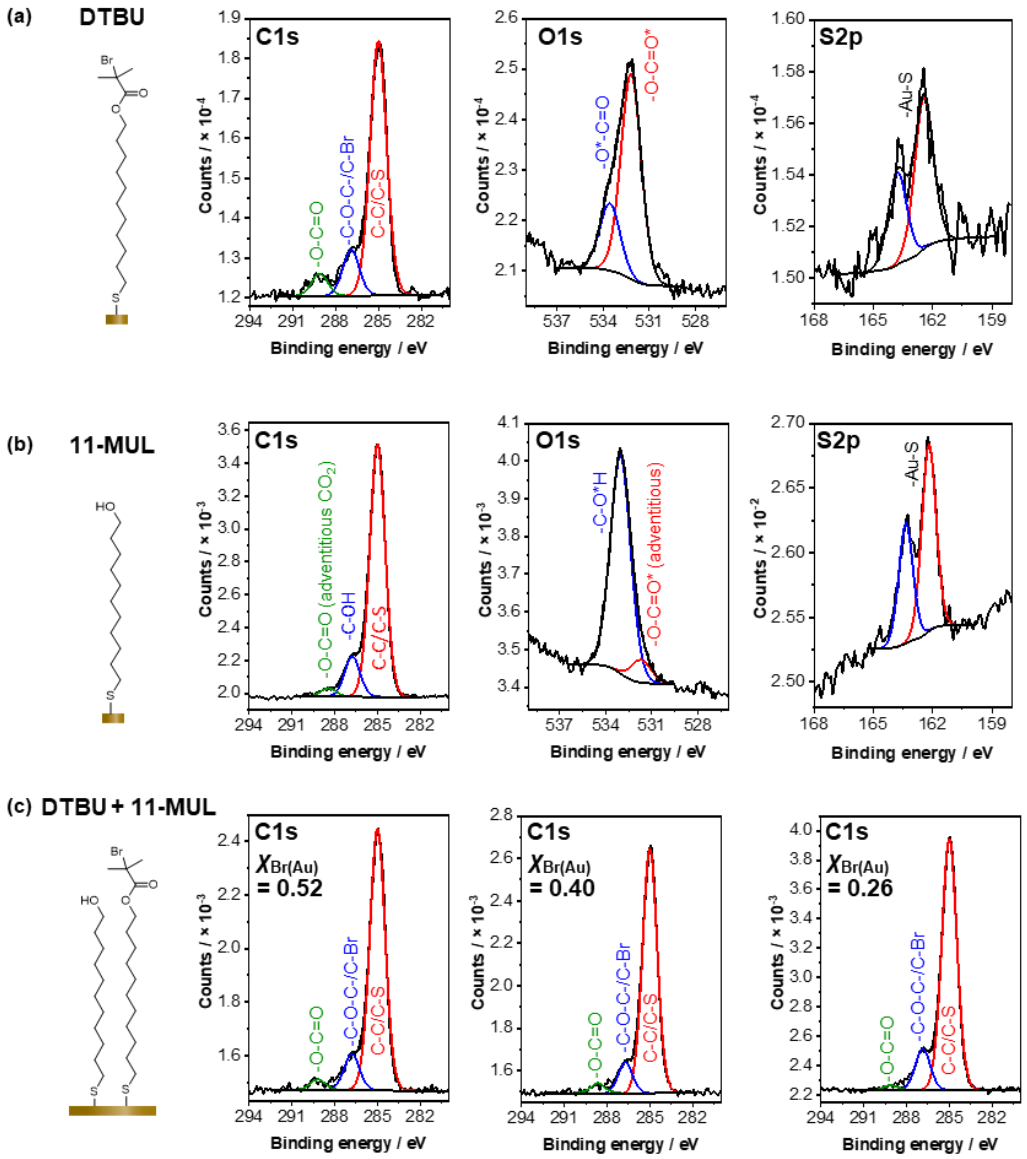

Figure 3.2. High-resolution C1s, O1s and S2p XPS spectra of self-assembled monolayers (SAMs) using (a) bis[2-(2-bromoisobutyryloxy)undecyl] disulfide (DTBU, initiator molecule), (b) 11-mercapto-1-undecanol (11-MUL) and (c) representative C1s spectra of mixed SAMs of the two, with calculated surface molar ratios of the Br-containing initiator sites of $\chi_{Br(Au)}$ = 0.52, 0.40 and 0.26. The chemical structures of the surface-tethered molecules are shown on the left.

Carbon-halogen bonds are susceptible to photolysis under extended X-ray exposure[229] and, moreover, the Br3d peaks observed for the SAMs studied here were noisy. Thus, quantitative analyses of the initiator-containing SAMs were performed using high resolution C1s spectra

rather than the Br3d data. As shown in Figure 3.2(a), the C1s spectrum of DTBU SAM exhibits a peak at 289.1 eV, corresponding to the carbonyl group carbon (C=O), a peak corresponding to the C-O and C-Br environment at 286.7 eV, and the C-C/C-S peak at 285 eV. The C1s spectrum of an 11-MUL SAM exhibits a small feature at 286.9 eV, due to the carbon atom adjacent to the hydroxyl group, in addition to the C-C/C-S peak at 285 eV. Since the carbonyl functional group is present only in DTBU, the mole fraction of the adsorbed initiator site ($\chi_{\mathrm{Br(Au)}}$) within the film can be derived from the C1s peak area ratios according to the following equation:

$$\chi_{\mathrm{Br(Au)}} = \frac{\chi_{\mathrm{Br(sol)}} \times A_{exp}}{A_{calc}} \tag{3.1}$$

where $\chi_{\mathrm{Br(sol)}}$ is the mole fraction of initiator sites in the solution, A_{exp} is the experimentally determined ratio of the fitted peak areas corresponding to the C1s carbonyl group and the C-C/C-S pea and A_{calc} is the calculated ratio of the functional groups in the SAM, assuming that the surface composition reflects that of the solution composition. Using this method, Figure 3.3(a) shows the calculated mole fraction of bromine-terminated adsorbates in the SAM ($\chi_{\mathrm{Br(Au)}}$) as a function of the mole fraction of brominated alkyl chains in solution ($\chi_{\mathrm{Br(sol)}}$), assuming that one mole of DTBU molecules is equivalent to two moles of brominated alkyl chains.

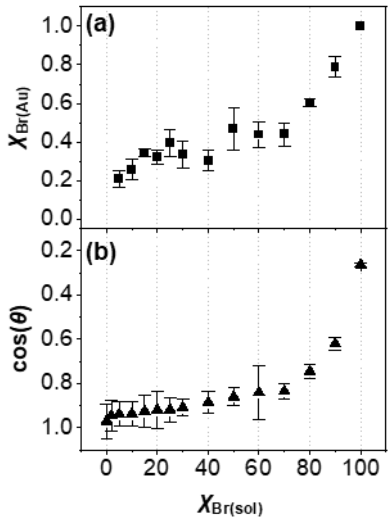

Figure 3.3. Influence of grafting density on kinetics of growth of PCysMA brushes. (a) Dependence of the mole fraction of initiator-functionalised adsorbates on the gold surface ($\chi_{Br(Au)}$) on the mole fraction of brominated chains in solution ($\chi_{Br(sol)}$), determined from XPS analysis. (b) Variation in the cosine of the contact angle of a deionised water droplet on mixed SAMs formed from varying DTBU:11-MUL ratios in solution.

A non-linear relationship was observed between $\chi_{Br(sol)}$ and $\chi_{Br(Au)}$. At low values of $\chi_{Br(sol)}$, the mole fraction of brominated chains in the SAM is greater than that in the solution from which it is formed; however, when the mole fraction of brominated chains in solution is increased above 0.5, the surface becomes enriched in the diluent molecules. These observations are supported by contact angle measurements (Figure 3.3(b)). The water contact angle of a DTBU SAM is 75 ± 2º, and for an 11-MUL SAM it is 14 ± 2º. At small values of $\chi_{Br(sol)}$, $\cos\theta$ increases slowly, reflecting enrichment of the SAM in brominated chains, but it increases rapidly above $\chi_{Br(sol)} = 0.6$, as the surface becomes enriched in 11-MUL instead.

These data are explained by the differences in the adsorbates used. The brominated adsorbate, DTBU, is a dialkyldisulfide in the solution phase, and contains a bulky Br at its tail, while 11-

MUL is an alkylthiol. At small values of $\chi_{Br(sol)}$, each disulfide initially adsorbs to occupy two surface sites; if the rates of diffusion of the two adsorbates are similar, then the surface will be enriched in the brominated chains because each collision between a disulfide and the gold surface leads to the formation of two gold thiolates. However, as the value of $\chi_{Br(sol)}$ becomes large, the comparative bulk of the disulfides begins to hinder their approach to the surface at higher fractional coverages, whereas the smaller 11-MUL molecules adsorb faster at higher coverages, thus enjoying a small competitive advantage.

3.3.2 Dependence of polymerisation kinetics on grafting density

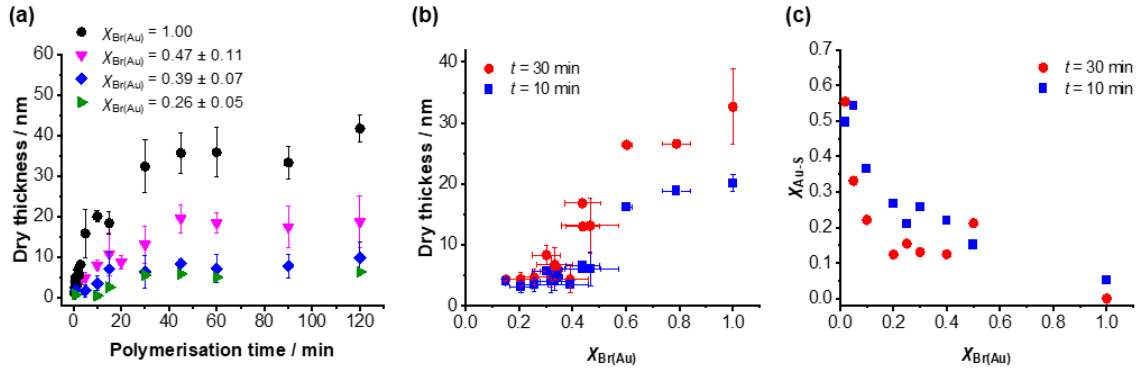

Figure 3.4. (a) Dry thicknesses of pCysMA films grown from SAMs formed from solutions with $\chi_{Br(Au)}$ = 1.00, 0.47 ± 0.11, 0.39 ± 0.07 and 0.26 ± 0.05 at a range of polymerisation times. (b) Dry pCysMA brush thicknesses prepared using 10 min and 30 min polymerisation times as a function of $\chi_{Br(Au)}$, determined by spectroscopic ellipsometry. (c) Fraction of Au-S bonding in the high-resolution S2p XPS spectrum for pCysMA films grown for 10 min and 30 min from SAMs with varying mole fractions of brominated chains.

The growth kinetics of PCysMA films formed by ARGET-ATRP were determined as a function of the mole fraction of bromine-terminated adsorbates in the SAM ($\chi_{Br(Au)}$). Figure 3.4(a) shows the dry thickness of pCysMA grown from $\chi_{Br(Au)}$ = 1.00, 0.47 ± 0.11, 0.39 ± 0.07 and 0.26 ± 0.05 as a function of the polymerisation time *t*. For all grafting densities, the general behaviour is similar: the thickness increases rapidly at first, with the rate of growth

slowing after ~ 10 min, to reach a limiting dry thickness after ~ 45 min. This suggests that the radicals at the polymer chain ends become terminated at comparable rates across the range of grafting densities studied here. At t = 45 min, the thickness of a fully dense brush is 36 ± 5 nm, decreasing to 20 ± 3 nm for $\chi_{Br(Au)}$ = 0.47 ± 0.11 after the same reaction time. For $\chi_{Br(Au)}$ = 0.39 ± 0.07 and 0.26 ± 0.05 the film thicknesses were 8.5 ± 1 nm and 5.9 nm, respectively. These observations are consistent with expectations based on our understanding of the relationship between polymer conformation and grafting density.[230,231] At high initiator densities, steric repulsion inhibits collapse of surface grafted polymers; however, as the grafting density is reduced, steric repulsion decreases until eventually it is lost completely, and the surface-grafted chains collapse to adopt a mushroom conformation.

To further examine the relationship between initiator concentration and film growth, we measured the dry thicknesses of pCysMA films prepared with polymerisation times of 10 min and 30 min (Figure 3.4(b)). For all grafting densities, the higher polymerisation time yielded thicker films, due to the longer chain lengths. At the highest initiator density ($\chi_{Br(Au)}$ = 1.0), pCysMA had a dry thickness of 20 ± 1 nm at t = 10 min and 32 ± 6 nm at t = 30 min. In these fully dense brush films, steric repulsion between the neighbouring polymer strands forces them to stretch away from the surface. However, as the initiator density is reduced to $\chi_{Br(Au)}$ = 0.30 ± 0.05, the thickness decreases monotonically due to the progressive reduction in steric repulsion. At $\chi_{Br(Au)}$ < 0.30 ± 0.05, a change in behaviour is observed: as the grafting density is reduced below this value, the thickness varies more gradually as a function of the initiator density. This change in behaviour is attributed to the transition to a mushroom confirmation in the surface-grafted polymers.[232,233] The heights of the mushrooms, and therefore the corresponding film thickness, are determined by the radius of gyration of the

surface-grafted chains. The transition in conformation from "brush" to "mushroom" is likely around the point of $\chi_{Br(Au)} = 0.30 \pm 0.05$, where the slope of the gradient changes significantly.

These changes in film thickness as a function of grafting density are correlated with changes in the S2p XPS spectrum. The binding energy of the $S2p_{3/2}$ peak for sulfur in thioether linkages in PCysMA is 163.6 eV,[234] while for thiolate sulfur atoms in the SAM it is 162.0 eV.[235] Inelastic scattering of photoelectrons means that the photoelectron signal from the underlying monolayer is attenuated by the polymer film. Thus, when the polymer film is thicker than the XPS sampling depth, the contribution to the S2p peak from gold thiolates is lost. Typically, the XPS sampling depth is estimated to be ~10 nm for molecular materials.[236] Figure 3.4(c) shows the variation in the ratio of the two contributions to the S2p peak as a function of grafting density for polymerisation times of 10 min and 30 min. As expected, the contribution to the S2p peak from thiolate sulfur for a given grafting density is larger for t = 10 min than for t = 30 min. The S-Au contribution decreases with increasing grafting density, consistent with the data in Figure 3.4(b). The S-Au contribution is undetectable for a 33 nm thick fully dense brush,[38] as expected. For a fully dense brush of 20 nm thickness (t = 10 min), the thiolate contribution to the S2p signal is small, but not zero. This indicates that the XPS signal is attenuated more gradually by these surface grafted polymers, which have lower densities than some other molecular materials, for example SAMs, for which the XPS signal is attenuated more rapidly. As the grafting density is reduced, the relative contribution of the thiolate sulfur to the S2p signal increases, such that at the lowest grafting initiator density used here ($\chi_{Br(Au)} = 0.21 \pm 0.04$) the thiolate signal for t = 10 min is ~ 10 × that for a fully-dense brush.

3.3.3 Depth-profiling of pCysMA brushes

The composition of surface-grafted polymer films was analysed as a function of depth using XPS in combination with a giant gas cluster ion source (GCIS). Bombardment of the surface-grafted polymer causes sputtering (removal) of material from the film, but when a GCIS is used for depth-profiling, a low energy density is achieved in the profiled region, leading to a low sputtering rate combined with minimal modification of the chemical structure of the analysed area. For polymer films with $\chi_{Br(Au)} = 1.00$, 0.47 ± 0.11 and 0.39 ± 0.07, an Ar_{3000}^{+} cluster source was selected and raster-scanned across a 2 mm × 2 mm region. Lower density films, such as $\chi_{Br(Au)} = 0.26 \pm 0.05$, were etched using Ar_{2000}^{+} clusters. Each etch cycle was followed by collection of high resolution and survey spectra over a 110 µm × 110 µm sampling area in the centre of the crater. To estimate the polymer film thickness after each etching cycle, a calibration plot was created by measuring the Au4f:C1s peak area ratios for a series of brush films with known thicknesses (Figure A1.1). The natural logarithm of $Au4f_{7/2}$:C1s peak area ratio extracted from the high-resolution narrow spectra was plotted as a function of the polymer dry brush thickness determined by spectroscopic ellipsometry. The data was fitted with a straight line, which enables the calculation of the thickness based on Au4f:C1s peak area ratios alone. Therefore, provided that the $Au4f_{7/2}$ signal can be detected, the linear relationship plot allows the estimation of the brush thickness based on the XPS depth-profile data.

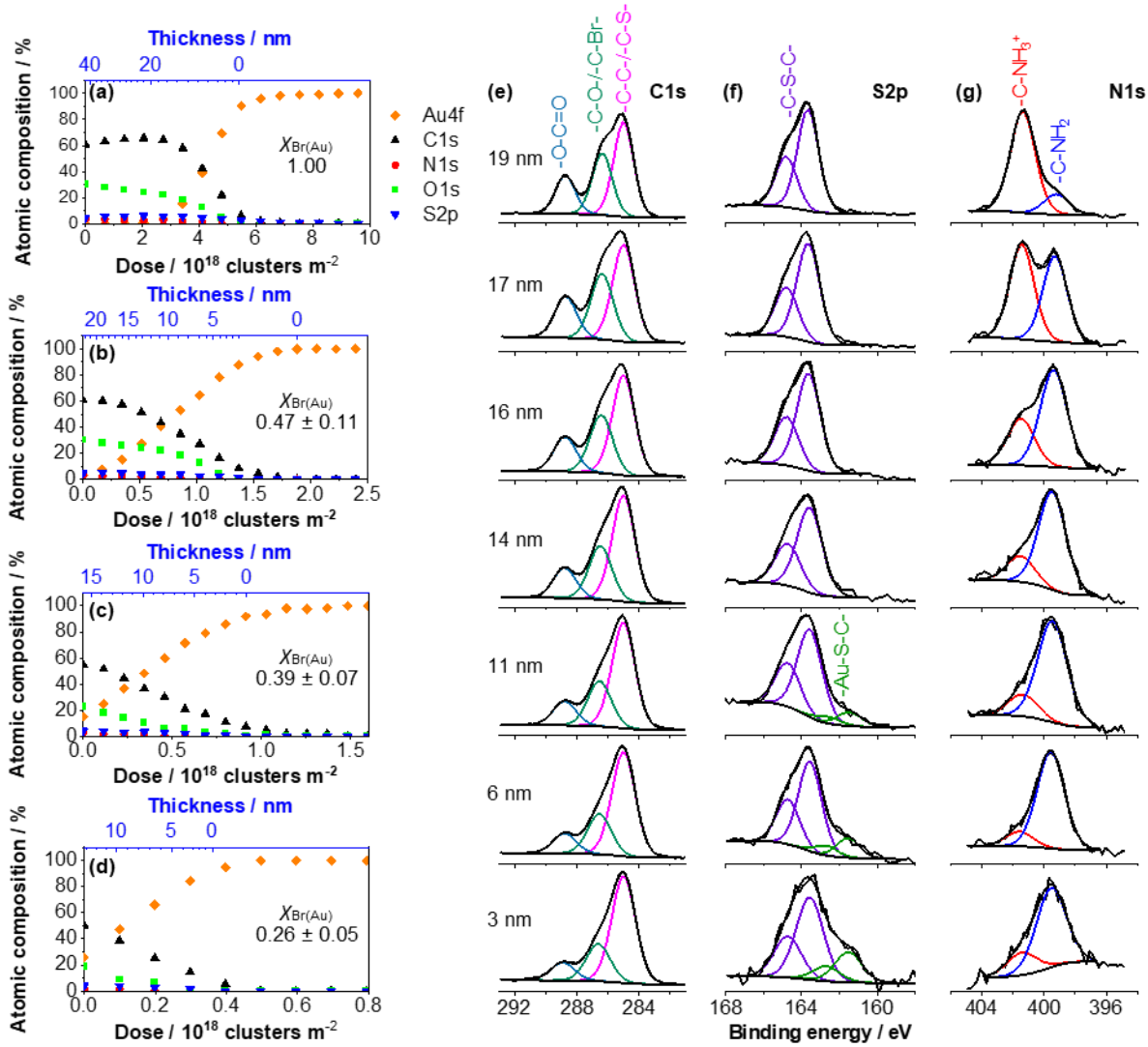

Figure 3.5. Characterisation of pCysMA brush films. Atomic composition changes as a function of depth for pCysMA films (t = 60 min) with grafting densities of (a) $\chi_{Br(Au)}$ = 1.00, (b) $\chi_{Br(Au)}$ = 0.47 ± 0.11, (c) 0.39 ± 0.07 and (d) 0.26 ± 0.05. The dose corresponds to the number of ion clusters per surface area during the etching process. High resolution (e) C1s, (f) N1s and (g) S2p spectra of a full density pCysMA brush (t = 60 min) after etched down to different thicknesses.

Figure 3.5(a) shows the change in composition as a function of dose for fully-dense pCysMA brushes ($\chi_{Br(Au)}$ = 1.00 and t = 60 min, dry thickness 42 nm). Up to a dose of 3×10^{18} clusters m^{-2}, the N, C and S concentrations remain approximately constant, although

the O1s signal declines very slightly in intensity. During this initial period, the upper part of the brush is being sputtered, and the polymer film is thicker than the XPS sampling depth. Thus, gold is not detectable. For doses larger than 3×10^{18} clusters m^{-2}, the polymer film is thin enough for gold to be detectable. As the dose increases from 3 to 6×10^{18} clusters m^{-2}, the areas of the C1s, N1s, O1s and S2p peaks decline to zero, while the intensity of the Au4f peak increases, reaching a limiting value at a dose of 8×10^{18} ions clusters m^{-2}, corresponding to complete removal of the polymer film.

Figure 3.5(b)-(d) shows elemental compositional depth profiles for reduced density brushes $\chi_{Br(Au)} = 0.47 \pm 0.11$ and for brushes $\chi_{Br(Au)} = 0.39 \pm 0.07$ and 0.26 ± 0.05, with thicknesses 22 nm, 16 nm and 13 nm, respectively. As expected, the dose at which the C1s and Au4f curves cross decreases as the grafting density is reduced. For fully dense brushes, the Au4f peak is not detected at first, being observed only after a dose of $\sim 0.7 \times 10^{18}$ m^{-2}. However, for the mushrooms (c,d), the Au4f peak is detected in the spectra of unmodified films and continues to increase in intensity throughout the depth profile. The complete removal of the films is achieved after doses of $\sim 1.9 \times 10^{18}$, 1.5×10^{18} and 0.5×10^{18} clusters m^{-2} for films with $\chi_{Br(Au)} = 0.47$, 0.39 and 0.26, respectively.

High-resolution XPS spectra collected after each etching cycle reveal the changes in the polymer chemistry as a function of depth. Figure 3.5(e)-(g) show the evolution of the C1s, S2p and N1s spectra as a function of the etched-down thickness for fully-dense brushes. The largest peak in the C1s spectrum appears at 285 eV, corresponding to the C-C and C-S bonding environments. Peaks are also observed at 286.4 eV and 288.4 eV, the former corresponding to carbon atoms single bonded to oxygen and the latter corresponding to carboxylate carbon atoms. As the thickness of the film decreases from 19 nm to 3 nm, there is a gradual reduction

in the areas of the features at 286.4 eV and 288.4 eV, and a relative increase in the size of the peak at 285 eV. This is attributed to the relative increase in the contribution from the close-packed hydrocarbon chains in the underlying SAM as the polymer film thickness decreases. There are ~ 5 thiolates nm^{-2}, whereas the grafting density of the brush is estimated to be ~0.5 chains nm^{-2}.[232,237] Thus, once the SAM lies within the XPS sampling depth, it contributes significantly to the feature at 285.0 eV.

The S2p spectrum for a fully-dense brush film exhibits a doublet, with the largest of the two peaks appearing at 163.8 eV. This doublet corresponds to the thioether $S2p_{1/2}$ and $S2p_{3/2}$ peaks, with the $S2p_{3/2}$ peak having the higher binding energy. However, when the film thickness is reduced to 11 nm, a second doublet appears, with the $S2p_{3/2}$ peak being observed at 162.3 eV. At this thickness, the sampled depth includes a portion of the initiator layer, and 162.3 eV corresponds to the binding energy of the thiolate $S2p_{3/2}$ peak.

The N1s spectrum of fully dense brushes exhibits two features, a dominant peak at 401 eV attributed to protonated amine, and a smaller peak at 399.2 eV corresponding to neutral amine groups. The ratio of the protonated and neutral amine groups was ca. 8:2, consistent with previous reports.[223,238] However, significant changes were observed in the magnitude of this ratio as a function of depth. After removal of only 2 nm of the brush film, the areas of the peaks attributed to protonated and deprotonated amines were nearly equal, and after removal of the top 5 nm of the brush, the neutral amine peak was the larger of the two, with a protonated:neutral amine peak area ratio of 2:8. This ratio remained unchanged when the thickness of the film was reduced further. These data suggest that while the amino acid pendant groups are largely charged in the top 2 nm of polymer, the charge density is much smaller throughout the majority of the polymer brush film.

Similar behaviour was observed in reduced density polymer films, although the top layers of these films exhibited lower charge densities than the full density brushes. For example, analysis of polymers grown from $\chi_{Br(Au)} = 0.47 \pm 0.11$ and 0.39 ± 0.07 showed $-NH_3^+$ and $-NH_2$ group ratios of ca. 6 : 4 before etching. An explanation for this increased charge density in the interfacial region is suggested by the work of Tolba and Xia, who modelled the interactions between water and poly(sulfobetaine-methacrylate) (polySB) and poly(2-methacryloxoethyl-phosphorylcholine) (polyMPC).[239] They found that the increase in water content close to the polymer/water interface led to more charge being transferred to the adsorbed water molecules from these zwitterionic polymers. It is likely that bound water remains largely intact even after transfer to the XPS instrument for analysis, with the consequence that the modified charge density is largely (or at least partially) preserved during analysis. Because the degree of solvation is expected to be reduced for collapsed mushroom structures, it is expected that charge transfer in the interfacial region will be less effective for PCysMA films grown at small grafting densities, consistent with the observations made here using XPS depth-profiling.

3.3.4 Control of chlorophyll binding through variation of grafting density

By varying the grafting density of the surface-grafted polymers, the kinetics of the reaction between chlorophyll and polymer chains may be controlled to achieve densely packed chlorophyll networks that mimic light-harvesting pigment-protein complexes. Chl was extracted from spinach and modified to obtain the chlorophyllide with a carboxylic acid linker group. Before addition to pCysMA, the carboxylic acid group was converted into an NHS group and used via EDC/NHS coupling to the amines of CysMA (Scheme 3.1).

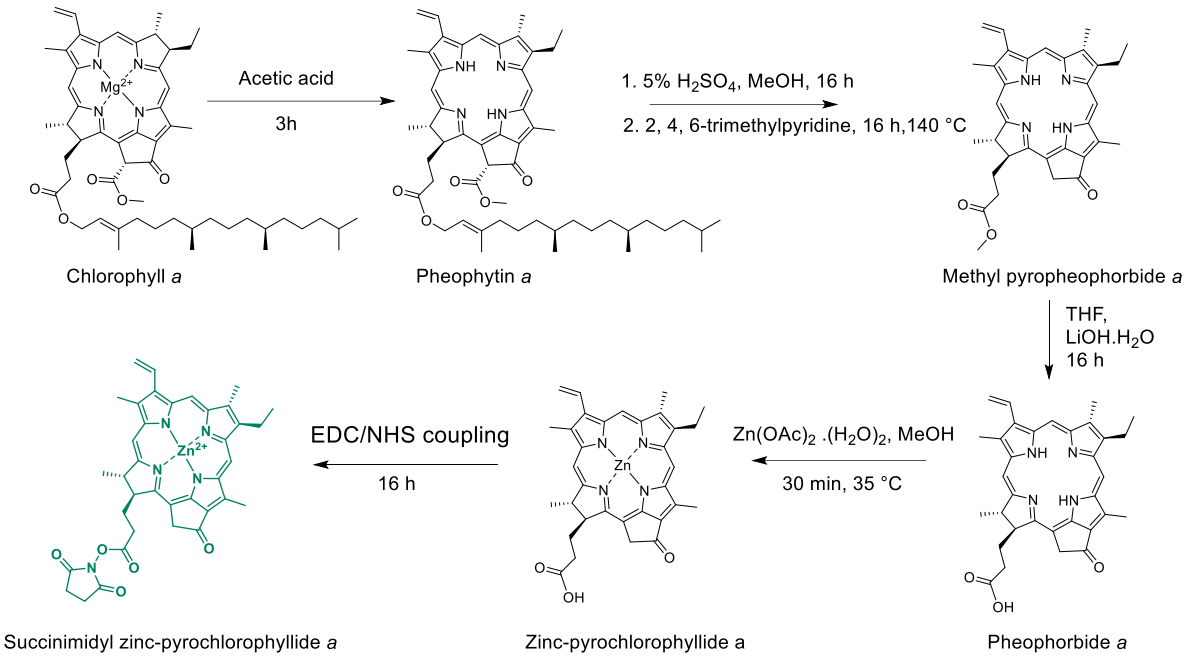

Scheme 3.1. Reaction scheme outlining the conversion of chlorophyll *a* into succinimidyl zinc-pyrochlorophyllide *a*.

The activated molecule was used immediately by dissolving the dry product in the 1:3 DMF:phosphate buffered saline (PBS, pH 8) solvent system, which was for incubating the substrates with pCysMA films for 42 hours at 4 ºC. The kinetics and the extent of chlorophyll binding to pCysMA was investigated by analysis of N1s and S2p high-resolution spectra, before and after the coupling reaction. Reference spectra to aid identifying the key bonding environments in Chl are shown in Figure 3.6, including a drop-cast film of the active ester-modified chlorophyll on gold and the chlorophyll functionalised SAM of 11-MUL. The XPS fitting details can be found in Table A1.6-A1.7.

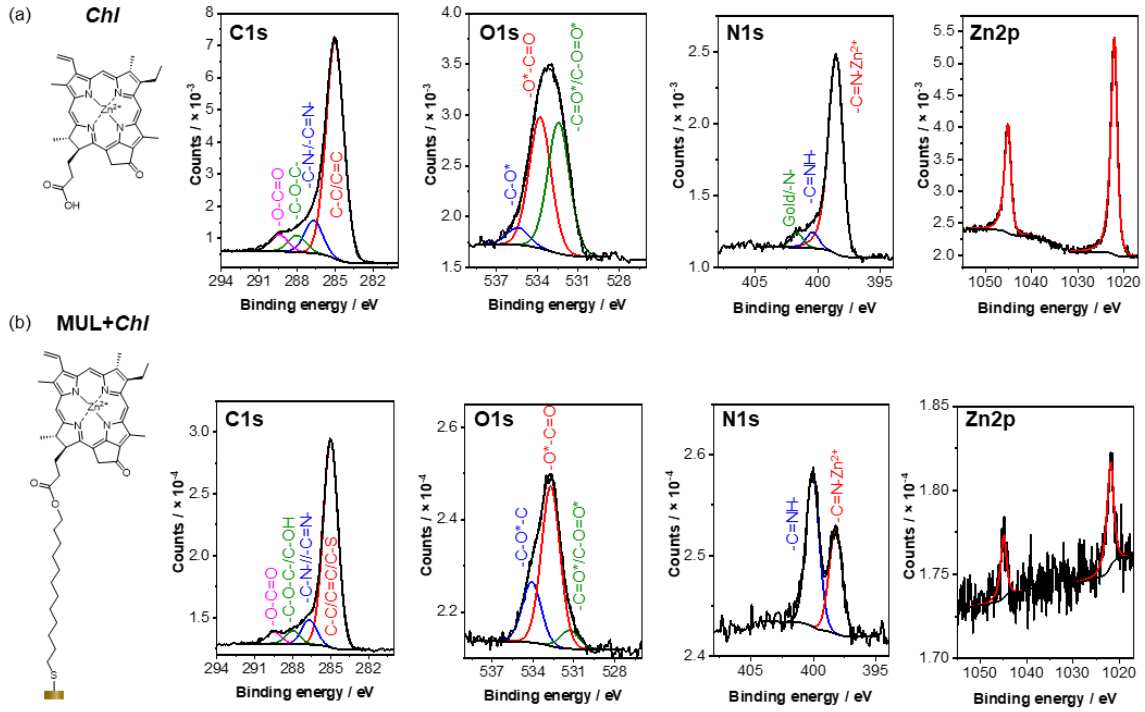

Figure 3.6. High resolution C1s, O1s, N1s and Zn2p XPS spectra of (a) drop-casted Zinc-pyrochlorophyllide *a* (*Chl*) on a gold slide and (b) *Chl* functionalised SAM of 11-MUL on gold.

The high resolution N1s spectra for both reference sample shows prominent peaks at ~398.5 eV, which corresponds to the nitrogens that are part of the delocalized chlorin ring and donate electron density to Zn^{2+}. Meanwhile, the peak at ~400.1 eV originates from the Chl molecules that lost the central Zn^{2+} ion.[240] The overall contribution of this peak significantly larger for the Chl functionalised SAM, indicating that the reaction conditions may lead to partial demetallation of the pigment. In addition, the drop-casted Chl sample contains an additional peak at 401.7 eV, associated with the interaction of the chlorin ring nitrogens with the gold surface.[241]

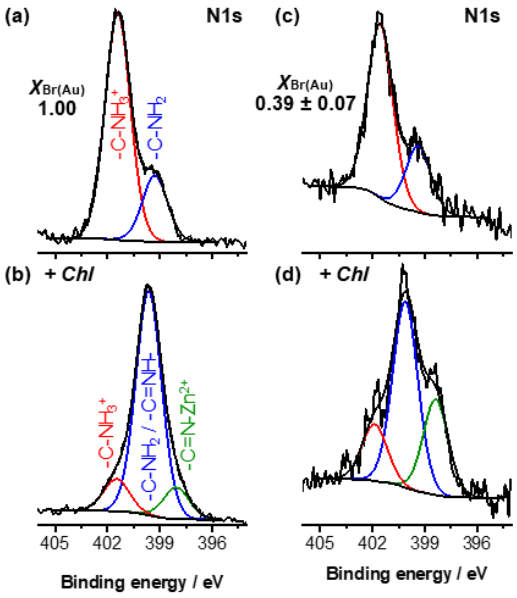

Figure 3.7. Characterisation chlorophyll binding to pCysMA brushes of various grafting densities. (a,b) High-resolution N1s XPS spectra of full density ($\chi_{Br(Au)}$ = 1.00) surface-grafted polymers with 30 min polymerisation time before (a) and after (b) reaction with Chl. (c,d) High-resolution N1s spectra of reduced density ($\chi_{Br(Au)}$ = 0.39 ± 0.07) surface-grafted polymers with the same polymerisation time (c) before and after (d) reaction with Chl.

Figure 3.7(a)-(d) shows the change in the N1s spectrum after binding chlorophyll to full density ($\chi_{Br(Au)}$ = 1.00, t = 30 min) and reduced density ($\chi_{Br(Au)}$ = 0.39 ± 0.07, t = 30 min) pCysMA films. Before the addition of Chl, the N1s spectrum of the full-density brush displayed peaks at 401.6 eV ($-NH_3^+$) and 399.5 eV ($-NH_2$) in an 8:2 ratio, consistent with data in Figure 3.5(g). Following attachment of Chl, the $-NH_3^+$ peak is greatly reduced in intensity, while the $-NH_2$ peak is now the largest in the spectrum. A new peak is observed at 398.1 eV, corresponding to the nitrogens in the tetrapyrrole ring in Chl that are coordinated to the positively charged Zn^{2+} ion at the centre of the macrocycle. The observation of this peak confirms the presence of Chl within the polymer brush.

The attachment of the pigment occurs via the formation of an amide bond between a pendant amine on the polymer and the Chl. This is indicated by the drop in $-NH_3^+$ peak intensity compared to the other N1s bonding environments, since some of the $-NH_3^+$ groups are converted into the more electron dense amides. This is consistent with the increase in the intensity of the peak at 399.5 eV after reaction. Additionally, the fraction of charged nitrogens may be reduced during the reaction because of the use of mildly basic conditions (pH 8).

To estimate the Chl to monomer ratio in the films, the N1s and S2p peak area ratios were compared before and after the coupling reaction. Poly(cysteine methacrylate) (PCysMA) contains one sulfur and one nitrogen atom per repeat unit. After the attachment of a *Chl* molecule, the repeat unit gains an additional four nitrogen atoms (Figure 3.8).

Monomer unit: **1 S + 1 N**

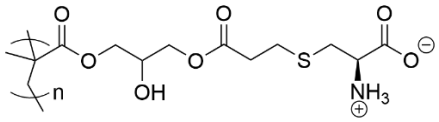

Monomer + Chl unit: **1 S + 5 N**

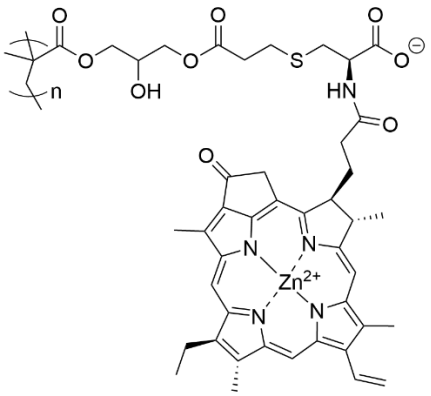

Figure 3.8. Chemical structure of the monomer unit, CysMA (top) and the Chl-functionalised monomer unit (bottom). The number of sulfur (S) and nitrogen (N) atoms is indicated.

Since the S concentration on the surface remains unchanged after the Chl attachment, the ratio of the N/S peak areas before $\left(\frac{N}{S}\right)_{PCysMA}$ and after $\left(\frac{N}{S}\right)_{Chl}$ the Chl addition, determined from the high-resolution XPS spectra, can be used to account for the excess N within the brush after the coupling reaction. Note that as each *Chl* contains four nitrogens, the result must be divided by four. Therefore, we can use the following equation to estimate the *Chl*:monomer molar fraction within the :

$$\frac{Chl}{monomer} = \left(\frac{\left(\frac{N}{S}\right)_{Chl}}{\left(\frac{N}{S}\right)_{PCysMA}} - 1 \right) / 4 \qquad (3.2)$$

For this sample, the molar fraction of Chl to monomer was found to be 0.24, equivalent to one Chl for every 4.2 monomer units. However, when the grafting density of pCysMA is reduced to $\chi_{Br(Au)} = 0.32 \pm 0.04$, the films can accommodate larger amounts of Chl in the film due to the decreased steric hindrance of the chains. The calculated Chl:monomer molar fraction was 0.39 for this film, 1.6 times higher than that of the fully dense polymer, and equivalent to one chlorophyll for every 2.6 monomer units. This increase in the concentration of Chl in the film is reflected in the substantial increase in the area of the N1s peak at 398.4 eV (tetrapyrrole N coordinated to Zn^{2+}).

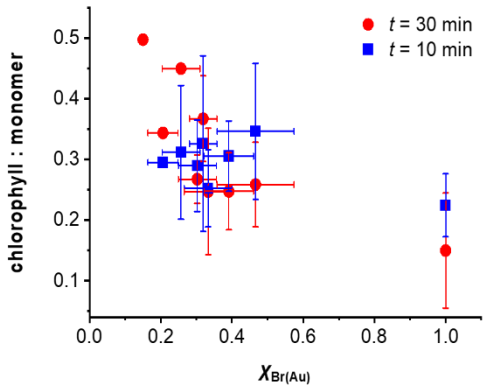

Figure 3.9. The Chl:monomer ratio within the polymer films as a function of $\chi_{Br(Au)}$, calculated from XPS data.

Figure 3.9 shows how the Chl:monomer ratio calculated from the N1s:S2p peak area ratio varies with the grafting density. While there is some significant scatter in the data (probably because the S2p peak and the N1s peak are both noisy), the Chl:monomer ratio decreases with increasing grafting density, as expected. Within experimental error, there appears to be little difference in the Chl:monomer ratio for films grown with the same grafting density and different polymerisation times (10 and 30 min). Furthermore, addition of Chl to the brush structure led to a significant increase in the thickness of the polymer film, consistent with the expectations, given the high molar mass of the Chl relative to that of the polymer repeat unit. Analysis of the film height before and after addition of the pigment was carried out using tapping mode atomic force microscopy (AFM) of micropatterned surface-grafted pCysMA films (Figure 3.10)

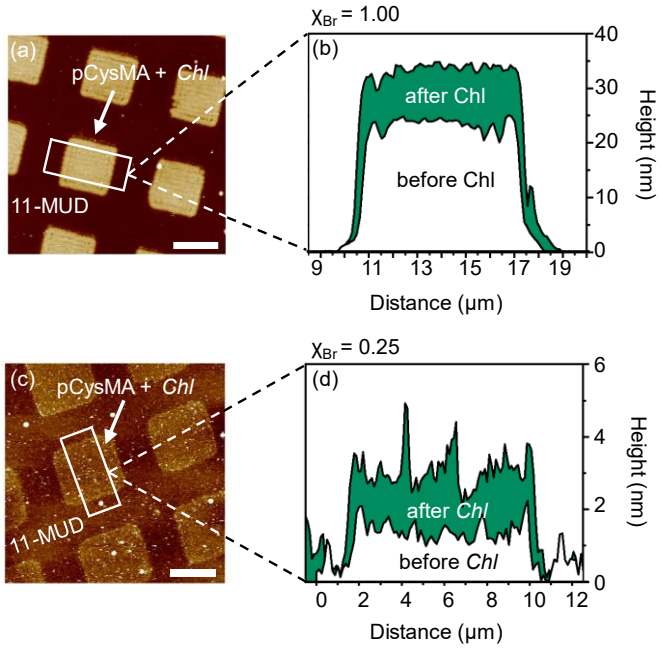

Figure 3.10. (a) AFM tapping mode image of a dry micropatterned full density polymer brush (*t* = 30 min) after attachment of *Chl*. The bright squares contain the pCysMA brush film while the dark regions are covered with monolayer of 11-mercaptoundecanol (11-MUL). The dashed line corresponds to the averaged area cross section of the square shown in (b) for a brush film before and after chlorophyll binding. (c) Shows the image of a dry micropatterned reduced density brush ($\chi_{Br(Au)}$ = 0.39 ± 0.07) with *t* = 30 min after the *Chl* coupling. The dashed line shows the cross section presented in (d), which depicts the height change before and after the attachment reaction.

Briefly, a SAM of 11-MUL was exposed to a UV laser through a copper mesh grid, leading to photo-oxidation of the adsorbates in the exposed areas.[242] The oxidised thiols were then replaced by immersion of the patterned substrate in a solution of the initiator solution, leading to displacement of the sulfonates by the brominated adsorbate. Subsequently, brush films were grown for 30 min from the square patterns.[223,243] The resulting pCysMA squares were analysed by tapping mode AFM before and after the Chl reaction. The fully dense brush film showed a thickness of ca. 23 nm before the functionalisation. After the Chl binding, a 30% increase in height was observed, attributed to the covalent coupling of Chl to the polymer scaffold. When

$\chi_{Br(Au)}$ = 0.39 ± 0.07, the film grown for 30 min had a thickness of ca. 1.5 nm. The relatively low thickness is likely due to the small elastic moduli of surface tethered polymers, which are easily compressed by the AFM tip during the imaging process. Attachment of the pigment, however, doubles the thickness to 3 nm, based on the cross-section analysis. The doubling of the reduced density polymer film thickness indicates a higher Chl:monomer ratio compared to the fully dense brush, which increases only by ca. 1/3 of its original height.

3.3.5 Depth-profiling of Chlorophyll-Functionalised pCysMA brushes

The data in Figure 3.10 demonstrate that the amount of Chl bound to the polymer scaffold varies with the grafting density: in fully dense brushes, steric hinderance limits the derivatisation of PCysMA by Chl, but as the grafting density is reduced, this steric hinderance is reduced, leading to a progressive increase in the amount of Chl bound to the scaffold. However, these data do not provide insight into the vertical distribution of Chl relative to this surface. To examine the vertical distribution of Chl, XPS depth-profiling was carried out using Ar_{3000}^{+} and Ar_{2000}^{+} as outlined before on PCysMA films prepared using $\chi_{Br(Au)}$ = 1.00, 0.47 ± 0.11, 0.39 ± 0.07 and 0.26 ± 0.05, with t = 60 min (Figure 3.11).

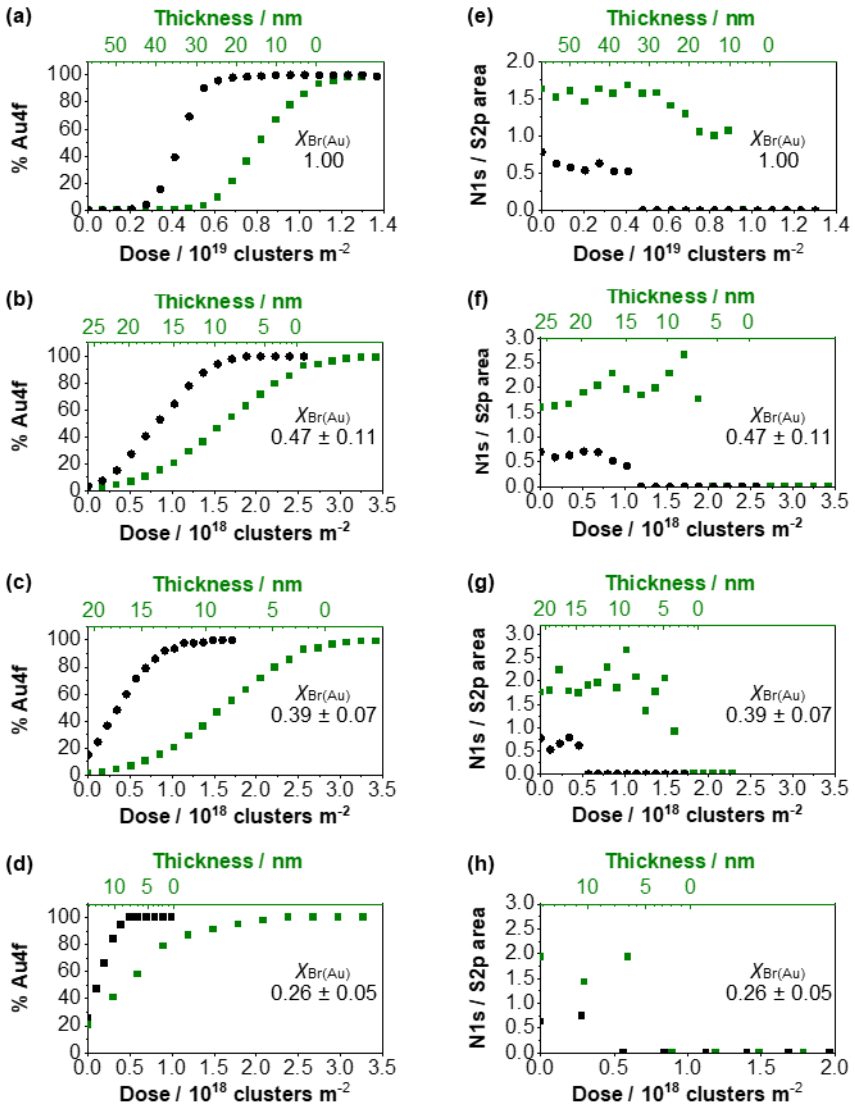

Figure 3.11. Depth-profiling analysis of pCysMA films before and after Chl attachment. (a) N1s/S2p peak areas of a fully dense brush $\chi_{Br(Au)}$ = 1.00, and reduced density brushes (b) $\chi_{Br(Au)}$ = 0.47 ± 0.11, (c) 0.39 ± 0.07 and (d) 0.26 ± 0.05, at t = 60 min polymerisation time before (black dots) and after (green squares) the Chl coupling reaction. The thickness was estimated by averaging the difference in brush height between the consecutive etching cycles and calculated by the calibration plot outlined in the main text. (d-e) Comparison of the N1s/S2p peak areas of the same surface-grafted polymers before and after the Chl attachment.

Figure 3.11(a)-(d) show depth profiles acquired by measuring the intensity of the Au4f peak as a function of depth. For fully-dense films, Au remains undetectable until ~10 nm has been removed from the film. After this, the Au4f peak grows in intensity (black circles), reaching a limiting value after ~ 40 nm have been removed from the film. However, after attachment of Chl to fully dense brushes, the Au4f remains undetectable until ~ 20 nm has been removed from the film. As the film is sputtered, the Au4f intensity increases, reaching a limiting value after ~ 65 nm has been removed from the film. The change is attributed to the increase in layer thickness due to *Chl* binding. Analysis of the $\chi_{Br(Au)} = 1.00$ brush shows that the Au4f signal reaches a stable value after a dose of 0.8×10^{19} clusters m^{-2}, indicating that the entire film has been removed. After addition of *Chl*, the removal of the entire film requires a dose of 1.4×10^{19} clusters m^{-2}, which is a 2-times smaller sputtering rate compared to the as-prepared polymer.

For the lowest density film, $\chi_{Br(Au)} = 0.26 \pm 0.05$ a dose of 0.5×10^{18} clusters m^{-2} was required for complete removal of pCysMA. However, when Chl is attached, a significantly larger dose, 2.4×10^{18} clusters mm^{-2}, is required to remove the entire layer. Thus, the etching rate was 3.4 times slower, indicating that a substantial amount of additional material has been deposited on the brush films. The dry thickness was estimated after each etching cycles using the calibration plot outlined in Figure A1.1. The estimated dry thickness increased by 25% of the fully dense film, 18% of the $\chi_{Br(Au)} = 0.47 \pm 0.11$ film, 31% and 8.3% for the $\chi_{Br(Au)} = 0.39 \pm 0.07$ and 0.26 ± 0.05, respectively.

The N1s and S2p peaks exhibit poorer signal-to-noise ratios than the Au4f peak. Nevertheless, they provide a convenient means to measure the distribution of the pigment within the dry film (Figure 3.11(e)-(h)). Analysis of film prior to etching yields N/S ratios that are consistent with the results obtained using conventional XPS measurements discussed above. Sampling of clean

films prepared with $\chi_{Br(Au)}$ = 1.00, 0.47 ± 0.11, 0.39 ± 0.07 and 0.26 ± 0.05 showed N/S ratios of 0.78, 0.70, 0.77 and 0.63, respectively. After the coupling reaction, these ratios increased to 1.62, 1.60, 1.75 and 1.93, respectively. Thus, the N/S ratio increases after incubation with the Chl as the grafting density decreases, consistent with the conclusion that Chl binds more extensively to the reduced density polymers.

The Chl functionalised fully dense brush had an estimated thickness of 57 nm. The upper half of the brush shows a nearly constant N/S ratio, indicating a homogeneous distribution. After sputtering had reduced the film thickness to 28 nm, the N/S ratio began to decrease as the interface was approached, reaching a value of 1.1, after which it dropped rapidly as the film was sputtered completely. Thus, we conclude that even for the fully-dense brush with considerable steric hindrance, Chl is able to penetrate and bind fully along the chains, with only a small decrease in the concentration towards the bottom. This is an interesting finding as reports on post-polymerisation modification of polymer brushes that involve smaller reagents than Chl showed predominant localisation on the top of the films.[244,245]

When the grafting density of pCysMA is reduced, the N/S ratio changes comparatively little until the interface is approached for each polymer. Therefore, the results suggests that Chl penetrates all brushes, where the amount of bound Chl reflects the kinetics of the reaction. XPS depth-profiling therefore reveals the hidden nature of the Chl-pCysMA binding, which is undetected by conventional means. Therefore, interpretation based on traditional XPS sampling can provide an inaccurate account of Chl within the polymer volume. In particular, it overestimates the number of pigment molecules in the fully dense brush and underestimates the amount in reduced density films. Using an average of the N/S values from the depth-profiles against the unetched N/S ratio of the clean brush, the Chl:monomer ratios were calculated. It was found that overall, the fully dense films exhibited a Chl:monomer ratio of 0.20, meanwhile,

$\chi_{Br(Au)}$ = 0.47 ± 0.11, 0.39 ± 0.07 and 0.26 ± 0.05 films showed a ratio of 0.45, 0.38 and 0.78, respectively.

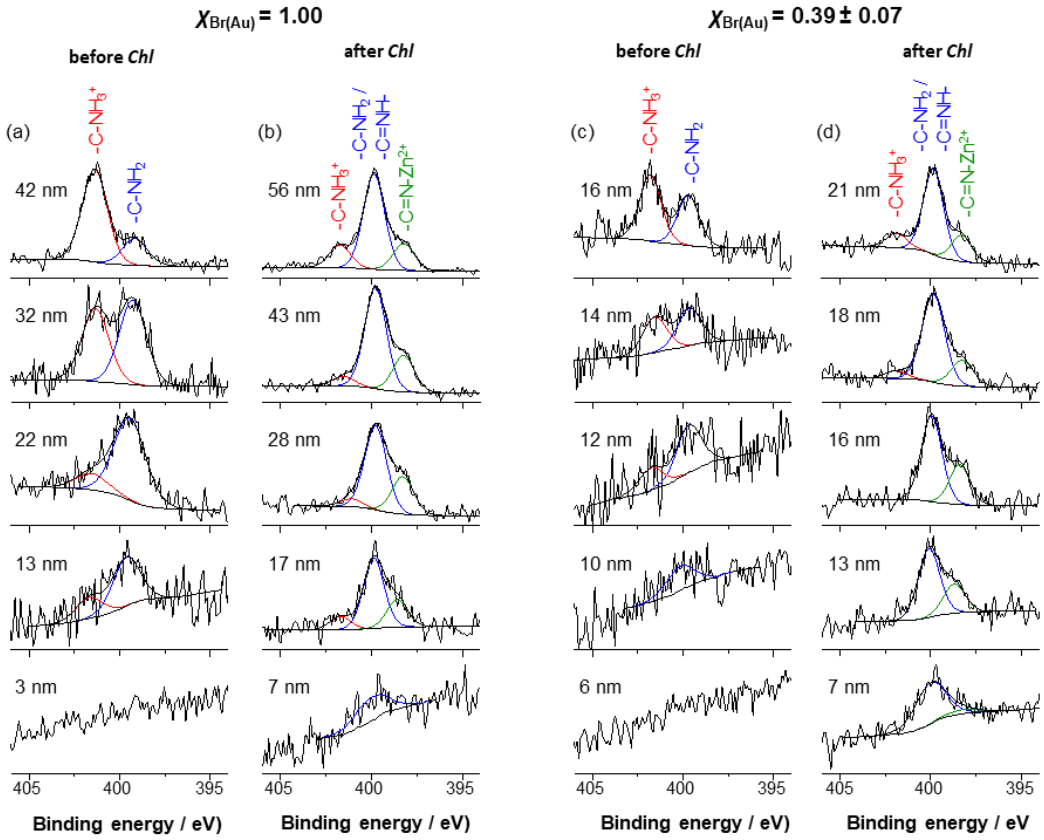

Figure 3.12. Representative N1s high-resolution spectra of selected depth-profiles. (a) Fully dense pCysMA after a number of sputtering cycles. The thickness in the inset corresponds to the estimated thickness of the film after each etching cycle. (b) Shows the depth-profiling of the same brush after addition of Chl. (c) PCysMA brush prepared with $\chi_{Br(Au)}$ = 0.39 ± 0.07 before and (d) after Chl functionalisation.

Examination of N1s high-resolution spectra as a function of depth reinforced these conclusions (Figure 3.12). As discussed above, Chl-binding is indicated by a decrease in the $-NH_3^+$ peak area and the appearance of a new low binding energy attributed to nitrogens in the chloring ring that are coordinated to Zn^{2+}. A notable difference between the fully dense and reduced density films is that while the $-NH_3^+$ peak intensity decreases in both while approaching the

middle of the film, it remains present in the dense brush but disappears in the reduced density film. Additionally, the chlorin ring nitrogen peak was observed throughout the whole of the layer from top to the bottom. In both cases, the relative intensity of the peak increases towards the middle of the materials, however, the ratio was slightly higher in reduced density brushes. The findings are in good agreement with the conclusions drawn by the analysis of the N/S peak ratios. The Chl concentration gradient observed in the reduced grafting density pCysMA may be the consequence of the charge gradient of the zwitterionic brush. Neutral amine groups are better nucleophiles and were found to be predominant towards the bottom of the film. The active ester containing pigments can readily bind to these sites over the charged functional groups. Moreover, the chlorin ring is coordinating a Zn^{2+} ion, which positive charge density may be repelled by the charged amines on film. While fully dense brushes pose significant steric hindrance, those with reduced chain density can allow Chl to diffuse into the layer and localise preferentially within its more neutral segments.

3.3.6 Plasmon-exciton coupling

To investigate the plasmon-exciton coupling behaviour of the Chl-derivatised surface-grafted polymer films, substrates with plasmonic gold nanostructures were prepared using interferometric lithography.[174] Polymers were functionalised with Chl as described earlier, and their extinction spectra were measured in dry conditions. Representative spectra of polymers with $\chi_{Br(Au)} = 1.00$ and $\chi_{Br(Au)} = 0.15$ and $t = 30$ min before and after the attachment of Chl is shown in Figure 3.13.

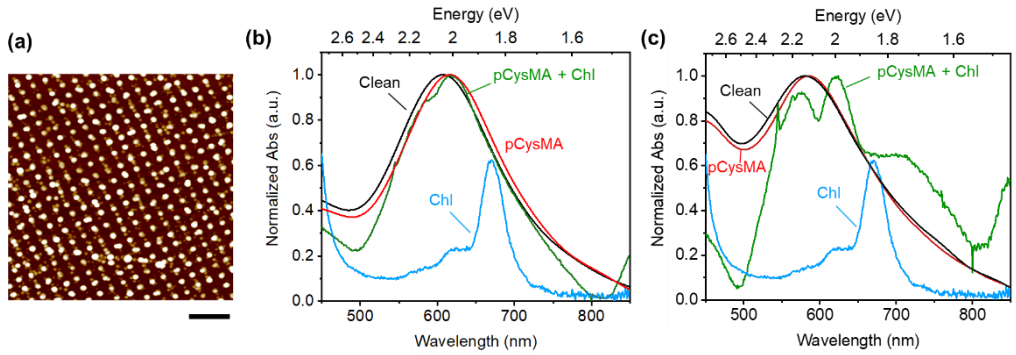

Figure 3.13. (a) Tapping AFM image of a gold nanoarray prepared using interferometric lithography. The scale bar corresponds to 1 µm. Normalised extinction spectra for nanostructure arrays when clean (red) and with pCysMA before (black) and after (green) the attachment of Chl, using a surface initiator density of (b) $\chi_{Br(Au)}$ = 1.00 and (c) $\chi_{Br(Au)}$ = 0.15, and polymerisation time of 30 min. The blue spectrum corresponds to Chl-functionalised pCysMA grown on a glass slide, using a polymerisation time of 30 min.

Polymerization on the nanostructured gold arrays resulted in a small redshift in the plasmon band wavelength, shifting from 608 nm to 615 nm for the dense brush, and from 580 nm to 585 nm for the reduced density polymer film. Upon the attachment of Chl to the full density brush, the spectrum exhibited a small splitting in the plasmon band. The calculated scaled coupling energy was 0.14 eV, indicating a weak coupling between the plasmon and exciton states. Details on the modelling and calculation of the coupling energy can be found in the Supporting Information of the following research article.[48]

In contrast, the reduced density films showed a significant change in the spectra. A pronounced splitting of the plasmon peak was observed, with a calculated scaled coupling energy of 0.38 eV, which is within the strong coupling regime. The increase in the coupling strength is attributed to the higher concentration of excitons within the plasmon mode volume. Importantly, a clear correlation between the grafting density of the polymer films and the scaled coupling energy of the system was found. Polymer films were grown from the plasmonic arrays

with surface initiator densities of $\chi_{Br(Au)}$ = 1.00, 0.47, 0.15 and 0.10, using polymerisation times of 1.5 min, 4 min, 10 min and 30 min (Figure 3.14).

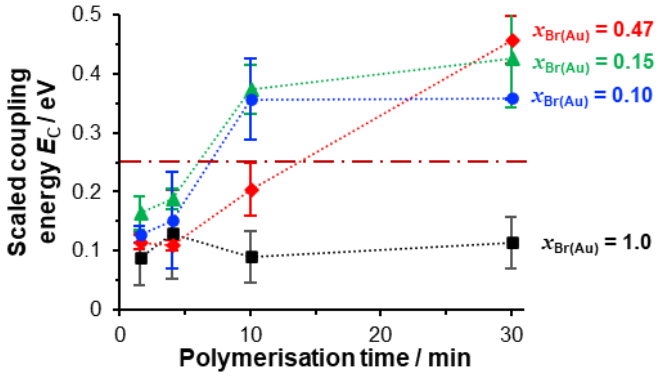

Figure 3.14. The scaled coupling energy E_C as a function of the polymerisation time for surface initiator densities of $\chi_{Br(Au)}$ = 1.0 (squares), 0.47 ± 0.11 (diamonds), 0.15 (triangles) and 0.10 (circles). The dashed line corresponds to the threshold for strong plasmon-exciton coupling of 0.25 eV.

For full density brushes, the change in polymerization time, and thus the height of the brush films, showed no impact on the scaled coupling energy, which remained at ca. 0.1 eV for the arrays. These findings imply that the exciton density within the plasmon mode volume remains relatively constant as the polymer height is varied. When the grafting density is reduced, the short polymerisation times of 1.5 min and 4 min resulted in weak coupling at all grafting densities. However, increasing the polymerisation time to 30 min, the coupling energies increased significantly from ~0.10 eV to the range of 0.35-0.45 eV for these lower-density films. Notably, the $\chi_{Br(Au)}$ = 0.47 polymers exhibited the highest coupling energies, reaching 0.46 ± 0.4 eV at 30 minutes of polymerization times. The findings suggest that at short polymerisation times the reduced density films are too short, resulting in a limited number of excitons on the surface. Increasing the polymer height provides a higher number of pigment binding sites on the surface, thus, the attachment of Chl results in larger concentrations of

pigment molecules within the plasmon mode volume. The lower density films can therefore accommodate a greater number of Chl molecules compared to the densely packed brushes, leading to higher coupling energies. Notably, the coupling energies achieved with the polymer-antenna complexes were higher than those observed when using LH2 complexes on plasmonic gold arrays.[47]

The coupled system can be characterized using the Jaynes-Cummings model, which describes the detuning (Δ) of the system in relation to the coupling strength (Ω). To calculate the energies of the coupled states, Eqn. 1.11 was used:

$$\omega_{\pm} = (\omega_p - \omega_0)/2 \pm \sqrt{\Omega^2 + (\omega_p - \omega_0)^2} \qquad (1.11)$$

where ω_p is the plasmon frequency and ω_0 is the exciton frequency. The change in the energies of these coupled modes against system's detuning was plotted for 84 different nanostructured arrays with Chl-functionalised pCysMA brushes, prepared using $\chi_{Br(Au)}$ = 1.00, 0.47, 0.15 and 0.10, with polymerisation times of 10 min and 30 min (Figure 3.15).

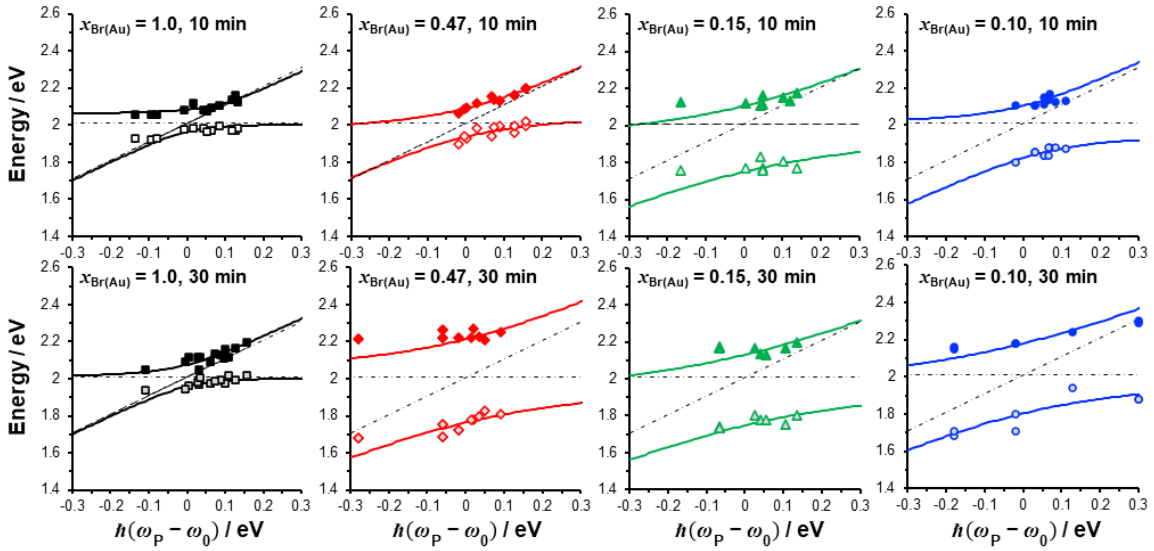

Figure 3.15. The energies of the coupled modes against the detuning parameter of Chl-functionalised pCysMA films using $\chi_{Br(Au)}$ = 1.0, 0.47 , 0.15 and 0.10, with 10 min (top row) and 30 min (bottom row) polymerisation times. The dashed lines correspond to the energies of the exciton and plasmon states and the solid lines are fitted to the upper and lower plexciton states.

An avoided crossing was observed on all of the plots prepared, indicating that each grafting density and polymerization time led to the coupling of the plasmon and exciton states. However, there was a significant difference in the separation of the energy curves for fully dense and reduced density brushes. At the crossing point of $\omega_p = \omega_0$, indicated by the dashed lines, the energy difference of the coupled states corresponds to the Rabi energy.

As anticipated from the calculated scaled coupling energies, the energy separation for fully dense brushes remained small at both polymerization times, suggesting weak coupling. For brushes with a reduced grafting density of $\chi_{Br(Au)}$ = 0.47 and 10 min polymerization time, a similar behaviour was observed. However, increasing the polymerization time to 30 min led to an increased energy difference, consistent with strong coupling. Notably, the lowest grafting density films that exhibit a mushroom conformation on the surface ($\chi_{Br(Au)}$ = 0.15 and 0.10), a

significant Rabi splitting was observed at both polymerisation times, indicative of strong coupling. These findings are consistent with the XPS studies, which revealed that reduced density polymer films contain higher concentrations of pigment molecules. Therefore, the modulation of surface grafting density provides control over the coupling strength in these systems, as evidenced by the observed variations in the spectra.

3.4 Conclusions

The use of mixed self-assembled monolayers provides a simple and effective way to control the initiator concentration ($\chi_{Br(Au)}$) on gold surfaces. Using surface-initiated ATRP, zwitterionic pCysMA brushes with controllable grafting densities and thicknesses were synthesised as scaffolds to organise pigment molecules in a 3D arrangement. To create pigment-polymer antenna complexes, the surface-grafted polymers were derivatised with an active ester modified Chl. The chemical state analysis of the systems was carried out using conventional XPS characterisation. Additionally, characterisation as a function of depth was achieved using Ar_{3000}^{+} and Ar_{2000}^{+} gas cluster sputtering that enabled the removal of thin layers of material without chemically altering the films. Conventional XPS sampling demonstrate a correlation between the surface grafting density and the extent of functionalisation, showing increased binding of Chl to films with $\chi_{Br(Au)} < 0.39 \pm 0.07$. XPS depth-profiling revealed the Chl concentration along the film thickness. In particular, the Chl concentration decreases as a function of depth for fully dense brushes but remains broadly constant in reduced density films. This may be due to preferential binding towards the neutral regions of the in clean pCysMA films. Therefore, XPS depth profiling provides a more accurate quantification of the extent of Chl functionalisation within the volume of the film. While dense brushes have a Chl:monomer

ratio of about 0.20 in the film volume, reduced density films can accommodate as high as 4 times more Chl due to the reduced steric constraints. The density of Chl on the surface can therefore be regulated by variation of the surface grafting density and layer thickness. The surface-tethered polymers provide controllable platforms for the organisation of pigments in a 3D arrangement. The synthesis of the surface-grafted pCysMA films on plasmonic nanostructured gold surfaces showed that the LSPR states can strongly couple with the exciton states of Chl. The coupling energy correlates with the grafting density of the polymer films, due to the variation of the Chl concentrations within the plasmon mode volume. At the ideal grafting densities, scaled coupling energies as high as 0.46 eV were observed. Therefore, these systems can offer the ability to control the coupling energy via the adjustment of the polymer grafting density.

Chapter 4. Engineering and Controlling Perovskite Emissions via Optical Quasi-Bound-States-in-the-Continuum

4.1 Introduction

Metal halide perovskites are fast emerging as the next-generation semiconductor materials.[246–250] The explosion of interest in these materials has been driven by their outstanding photoluminescence quantum yield (PLQY) of > 90%, high charge carrier mobility, micrometre scale exciton diffusion lengths and low-cost synthesis.[251–253] Furthermore, by tailoring the chemical composition, size or shape of perovskite nanoparticles, materials with bandgaps that span a wide spectral range, from ultraviolet to near-infrared (NIR) regions can be produced.[84,254] However, the nature of such bottom-up methods inevitably leads to some degree of non-uniformity in the particle morphology, which can result in line broadening and inconsistent emission wavelengths due to the quantum confinement effect.[255] Furthermore, after the synthesis of the perovskite material is completed, its luminescence properties are fixed and cannot be fine-tuned *in situ*. Such drawbacks are detrimental in applications that require the refined tuning of emissions at specific wavelengths, such as light-emitting diodes (LEDs),[76,256–258] photodetectors[259–261] single-photon sources[262] and lasers.[263,264]

Recognizing these challenges, post-synthesis engineering of the perovskite emission properties has gained attention recently. For example, adjustment of the photoluminescence (PL) wavelength has been achieved via ion exchange,[95–97] lattice distortions or phase transitions induced by applying external stimuli such as changes in temperature,[98] pressure[99,106] or strain.[107] Some of these methods allow a PL shift over a broad range; for example, up to ~760 nm (~921 meV) under an extremely high pressure of ~40,000 atmosphere.[106] However,

it is typically accompanied by significant broadening of full-width-at-half-maximum (FWHM), intensity quenching and requires a sophisticated setup which is impractical for many applications. Alternatively, leveraging the Rashba,[103,265] Zeeman[105] or Stark effects[104] under DC magnetic field or circularly polarized pumping enables the breaking and detection of the triplet state to manipulate their radiative channels, where a PL shift of ~6.6 nm (~30 meV)[108] can manifest. Nevertheless, these approaches often yield multiple emission with bands, rendering them unsuitable for devices that require a single emission peak.

An alternate approach is to use lithographically-defined photonic antennas to modulate the emission properties of these materials.[128,266–272] By coupling the optical modes of an antenna system to the excitonic states of emitters, the optical response of perovskites can be tailored to achieve unique effects, such as enhanced luminescence,[116,273] optical encoding,[272,274] polarization tuning[275,276] and highly tunable emission chirality.[277,278] However, despite these advancements and the attraction of such an approach, the maximum spectral shift reported to date is only 8 nm (~20 meV) *via* coupling to a microcavity, at the expense of a ~5-fold reduction of the PL intensity.[115] One potential approach to address these challenges is the use of quasi-bound-states-in-the-continuum (q-BIC) modes derived from bound-states-in-the-continuum modes (BICs), which are wave solutions found within a radiative continuum but entirely isolated from it.[126] While true BICs remain optically inaccessible,[279] the q-BIC mode could be designed to couple with the radiative continuum via symmetry-breaking characteristics, making them accessible from far-field radiation for their use in practical devices. Compared to other resonant modes, q-BICs possess high quality factors (*Q*-factors), strong field confinement and minimal radiation losses, which allows the resonances to effectively couple with the excitonic states of emitters, offering a more efficient approach for engineering the emission properties in perovskite materials.

In this chapter, the design of an optical nanoantenna array with polarization-controlled q-BIC resonances is explored. The array was designed to be capable of controlling the PL emission of formamidinium lead iodide ($FAPbI_3$) perovskite quantum dots (QDs), leading to a shift of ~39 nm. The aim of the work was to modify the radiative decay channel of the QDs was *via* the Purcell effect. Because $F_p \propto Q/V_{eff}$, where F_p is the Purcell factor, Q is the Q-factor of the resonance and V_{eff} is the effective mode volume, the use of q-BIC resonances with relatively high Q-factors and compact mode volumes is expected to enable realisation of a high F_p.[280,281] The coupling was accomplished by the use of top-down lithography to engineer the optical resonances of nanoantennas, without affecting the QDs' physical or chemical properties. Consequently, a homogeneous tuning of the perovskite emission wavelength was demonstrated over a wide bandwidth of ~39 nm (~82 meV). Furthermore, the antenna array allows for the switching of the PL wavelength by varying the polarization state of the incident laser. Besides tunability, a PL enhancement of ~21-fold and narrowing of the linewidth was realized. These results provide a non-destructive approach to fine-tune the emission wavelength, saturation and brightness of the perovskite emission at ambient conditions. Incorporation of this design concept could expand the range of applications of perovskites and create new opportunities in the fields of tunable optoelectronics, lighting and display, lasing, and spectrally tailored single-photon emitters.[282–287]

4.2 Experimental

4.2.1 Materials

$FAPbI_3$ perovskite particles were provided by collaborators.[10] Acetone (HPLC grade, 99.8%), 2-Propanol (HPLC grade, ≥ 99.9%), toluene (anhydrous, 99.8%) were obtained from Sigma-Aldrich. Sodium hydroxide (≥ 97%) and sodium chloride (≥ 99.5%) were purchased from Fisher Scientific.

Hydrogen silsesquioxane (XR-1541 E-beam resist) was purchased from Dow Corning, Silicon wafers (Test Grade, (100), P14723) were obtained from PI-KEM Ltd. Si substrates with 300 nm SiO2 were purchased from Silicon Valley Microelectronics, Inc. Chromium chips (99.5% trace metals basis) were obtained from Sigma-Aldrich.

4.2.2 Methods

4.2.2.1 Fabrication of the q-BIC nanoantenna arrays

360-nm-thick amorphous silicon (a-Si) was deposited on top of Si substrates with 300 nm SiO_2 overlayer, using plasma-enhanced chemical vapor deposition (PE-CVD, Oxford Instruments Plasmalab System 100). The process was carried out using SiH_4 at a flow rate of 45 sccm and Ar at 30 sccm. The temperature was set at 250 ºC with a pressure of 8.0 mTorr, a RF power of 50 watts and inductively-coupled plasma (ICP) power of 3000 watts. When ready, the sample was spin-coated (5k round-per-minute (rpm)) with 2% hydrogen silsesquioxane (HSQ), after which the lithography process was carried out immediately. Using electron beam lithography (EBL, Elionix ELS-7000), the patterns were written with an electron acceleration voltage of 100 keV, a beam current of 500 pA, and the exposure dose of 8,960 – 20,480 μC/cm^2 to achieve elliptical shapes with lengths ranging from 215 nm to 254 nm and widths ranging from 69 to

103 nm. To develop the sample, it was immersed in a solution of NaOH/NaCl (1% wt./4% wt. in de-ionized water) for 60 seconds and deionized water for another 60 seconds, followed by rinsing with acetone, isopropyl alcohol (IPA) and drying with nitrogen.[176] Finally, to create the nanopatterns, the sample was etched by inductively-coupled-plasma (ICP, Oxford Instruments Plasmalab System 100) using Cl_2 at a flow rate of 22 sccm. The ICP and RF power were 300 watts and 100 watts, respectively, under 5 mTorr and a temperature of 10 ^{o} C.

4.2.2.2 Preparation and coating of formamidinium lead iodide quantum dots ($FAPbI_3$ QD)

The details of the $FAPbI_3$ QD synthesis can be found in the work by Xue J. et al.[10] The synthesized $FAPbI_3$ solution was centrifuged at 6k rpm for 10 min. The supernatant was separated, and the centrifugation cycle was repeated 3 times. The supernatant was then filtered using a microfilter with a 0.2 μm pore size and diluted 1:2 with toluene to yield the final solution for dip-coating. To deposit the $FAPbI_3$ QDs, the q-BIC arrays were first oxygen plasma treated by exposure to inductively-coupled plasma (ICP, Oxford Plasmalab System 80). A pressure of 10 mTorr, a 100 watts DC power and 500 watts coil power was used during the process with an O_2 flow rate of 50 sccm at room temperature. Immediately after, the sample was dip-coated in the $FAPbI_3$ QD solution at a speed of 0.8 mm min^{-1} in a nitrogen filled glove box, at room temperature. The samples were stored in the dark in nitrogen atmosphere at room temperature until further use.

4.2.2.3 Spectroscopic characterization

Reflectance measurements were carried out using a polarized broadband light source on a CRAIC UV-VIS-NIR micro-spectrophotometer equipped with a ×5 objective lens and a numerical aperture of 0.12. The measurements were calibrated using a NISR calibration sample

(CRAIC Technologies) to record the absolute reflectance and operated with an integration time of 100 ms with an average of 50 measurements per spectrum. To obtain the angle-resolved reflectance measurements, back-focal-plane (BFP) spectroscopy was carried out with an Andor SR-303i spectrograph and inverted optical microscope (Nikon Ti-U), where a × 50 objective lens was selected with NA of 0.6, using a halogen lamp and EMCCD detector (Andor Newton).

4.2.2.4 Photoluminescence (PL) and PL lifetime measurements

The substrates were coated with the perovskite nanoparticles as outlined in "*4.2.2.2 Preparation and coating of formamidinium lead iodide quantum dots ($FAPbI_3$ QD)"*. Immediately after the coating process, the samples were transferred to the imaging equipment and the measurements were carried out in ambient conditions. The PL mapping was conducted on a WITec Alpha 300 S Scanning Near-field Optical Microscope in confocal microscopy mode. A linearly polarized 532 nm CW laser with a power of 50 µW was focused on the sample through a 50× objective with a NA of 0.6. An integration time of 0.05-0.10 second was used. Typically, an area of 400 µm × 300 µm was recorded. The spectra were extracted from the same 3 positions on each array. During the analysis process, the resulting spectra was smoothed using the Savitzky-Golay filter to reduce noise. The time-resolved PL was collected on a Picoquant Microtime 200 TCSPC system coupled with an Olympus microscope in confocal configuration, with a 20× objective lens. The data was recorded and fitted with Picosharp software. A pulsed laser of 640 nm, with pulse duration of 70 *p*s was used to excite the sample, and the repetition rate was set to 40 MHz, with an average power of 1 µW. To collect the spectrally integrated PL (660-800 nm range), a Si single photon avalanche photodiode (APD) was used. The instrument response function (IRF) was obtained using the scattered excitation light from the sample, from which the instrument response time was determined (~240 *p*s). The PL spectra and PLQE were obtained by photo-exciting the samples in an integrating sphere,

using a Spectra-Physics 405 nm (100 mW, CW) diode laser, and measuring the absorption and photoluminescence using a calibrated Ocean Optics Flame-T and Flame-NIR spectrometer.

4.2.2.5 Numerical simulations and Purcell enhancement calculations

Far-field spectra and the near-field distributions were modelled using three-dimensional finite-difference time-domain (3D-FDTD) simulations with Ansys Lumerical FDTD Solutions R2.4 software. Elliptical structures were placed in a 436 nm × 436 nm × 1500 nm unit cell with a 4 nm × 4 nm × 4 nm mesh around them. The unit cell had a perfectly matched layer (PML) in the z direction and periodic boundary conditions in the *x* and *y* directions. The reflectance spectrum was recorded at normal incidence condition by a monitor placed above a plane wave source, with the polarization of the incident light wave set to be along the *x*- or *y*-axis. The refractive index (*n*) and extinction coefficient (*k*) values of Si were taken from previous measurements.[176] The optical properties of SiO_2 were selected from the software's material database from Palik.[288] To obtain the angle-dependent reflectance, a broadband fixed angle source technique (BFAST) plane wave was used to provide broadband simulations at a range of illumination angles. The Purcell factor calculation was carried out using the built-in calculation method of the software, using the ratio of the dipole emission power over the total emitted power. The domain was limited by the PML boundary conditions. The point dipole source was placed onto a 20×20 array of the nanoellipse pairs, at the area of the highest field enhancement of a nanoellipse in the middle of the array. The emission center was set to 755 nm, with a 100 nm span, and the simulation results were averaged from the orthogonal dipole orientations in the *x*-, *y*- and *z*-directions. Multipolar decomposition analysis was carried out by collaborators using COMSOL Multiphysics software, performing finite-element method (FEM) simulations. The details of the simulation setup and theory were shown in Supporting Information section S17 in the following reference paper.[289]

4.3 Results and discussion

To effectively modify the emission pathways of perovskite materials by coupling with a q-BIC mode, it is important to establish a surface design that enables precise control of their interaction. Recently, it was demonstrated that an array of symmetry broken amorphous Si (a-Si) nanoellipse pairs on quartz exhibit two q-BIC resonances when irradiated with linearly polarized light oscillating along the long axis of the ellipse pair, while polarized light along the short axis incudes one q-BIC resonance at a lower wavelength.[128] The distinctive response of the q-BIC modes to linearly polarized light makes this surface design ideal to explore its impact on the spectral characteristics of PQDs. Therefore, arrays of asymmetrical a-Si nanopillars of the same design were employed to generate q-BIC resonances, facilitating investigation of their effects on PQD spectral properties.

We begin by describing the structural and geometrical parameters of the arrays employed, as well as the fundamental optical properties of the system. Additionally, the underlying theory that explains the observed wavelength shift in emission is outlined. This is followed by a detailed investigation of the impact of array parameter variation and polarization tuning on the perovskite emission.

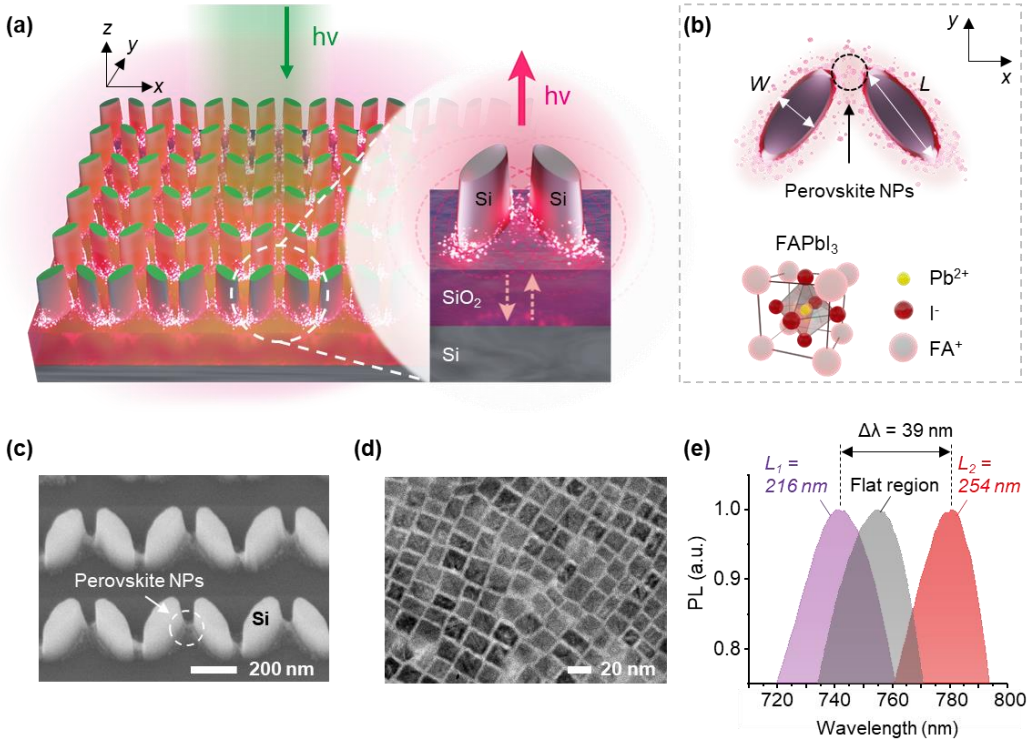

Figure 4.1. Design of quasi bound-states-in-the-continuum (q-BIC) resonance for engineering and controlling $FAPbI_3$ QD emissions. (a) Illustration of the silicon (Si) nanoellipse pair array, fabricated on top of a 300-nm-thick SiO_2 cavity on Si substrate and coated with $FAPbI_3$ QDs. (b) Top-down view of the nanoellipse pair, with the width (W) and length (L) annotated and an illustrative crystal structure of $FAPbI_3$. (c) Scanning electron micrograph (SEM) image of the perovskite-covered nanoellipse array, taken at a tilt angle of 30º. (d) Transmission electron microscope (TEM) image of the $FAPbI_3$ QDs. (e) Normalized PL spectra of $FAPbI_3$ QDs to demonstrate a tunable range of ~39 nm for the PL emission peak, using L_1 = 216 nm and L_2 = 256 nm nanoantenna arrays. All spectra were measured under the y-polarized pump laser excitation conditions.

Figure 4.1 shows the silicon (Si) antenna design which enables the engineering and shifting the emission wavelength of $FAPbI_3$ QDs via q-BIC resonances. It consists of an array of symmetry-broken amorphous Si nanoellipse pairs. The height of the Si nanostructures was fixed at 360 nm, with a pitch of 430 nm along the x-axis and 435 nm along the y-axis. We varied the antenna geometry, such that the lengths (L) of the ellipses spanned from 216 nm to 254 nm,

with the corresponding widths (*W*) varied from 79 nm to 103 nm, giving rise to optical modes within the red spectral region. Symmetry breaking was introduced by the rotation of the ellipse pair along the *x*-axis by 50º towards each other. To enhance the emission of the perovskite into the far-field, a 300-nm-thick SiO_2 cavity is incorporated into the design with Si as the backside reflector. Representative SEM images denoted with the array geometry parameters is demonstrated in Figure 4.2, with the corresponding average length and width values for each array listed in Table A2.1.

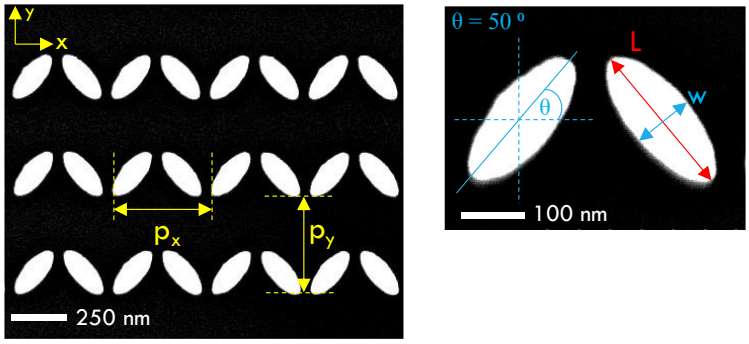

Figure 4.2. Representative SEM images of a nanoellipse array, showing the measured parameters extracted from each array, such as the length of the ellipse (*L*), width (*W*). The pitch in the *x*-direction (p_x) and *y*-direction (p_y) were fixed at 430 nm and 435 nm, respectively. The rotational angle (θ) was fixed at 50º.

For simplicity, the different arrays are specified by lengths only. To ensure effective interaction of between the q-BIC resonance and the perovskite, $FAPbI_3$ nanoparticles were chosen, which typically emit light within the red to near-IR spectral range. The $FAPbI_3$ nanoparticles were synthesized according to the method by Xue J. et al and were provided by collaborators.[10] Dissolved in toluene, the particles exhibit a high photoluminescence quantum efficiency (PLQE) of ca. 96% (see corresponding PL spectra used for the integration in Figure A2.1). Therefore, the particles have a high efficiency in converting absorbed photons into emitted photons upon excitation by an external light source. Prior to the deposition onto the surface,

the particles were separated by size using a centrifuge to remove any aggregates, followed by the deposition onto the antenna array by dip-coating method.[290,291]

The emission of the particles was recorded by mapping the PL signal on the sample surface at ambient conditions using a confocal microscope equipped with a linearly polarized 532 nm continuous wave (CW) laser. Each region was mapped by setting the polarization state of the pump laser alternately to *x*-polarized (with the electric field oscillating along the *x*-axis of the ellipse pair) and *y*-polarized (along the *y*-axis). The order of *x*- and *y*-polarized PL mapping was randomized to ensure that changes in the PL response were not due to laser-induced degradation of the perovskite. The mean peak position, intensity and FWHM were determined by taking measurements at three different points on the sample. As a reference, the PL emission of $FAPbI_3$ QDs was recorded on the flat region of the substrate. The optical reflectance of the substrate alone can be found in Figure A2.2.

The emission band was centred at ~755 nm on the flat region, close to the values typically reported for $FAPbI_3$ nanocubes,[292] and is within the range of the q-BIC resonance energies of the arrays under study (see detailed discussion later on). Figure 4.1(c) shows the scanning electron micrograph (SEM) image of the nanoantenna with $FAPbI_3$ nanoparticles, with the profile of the perovskite shown by high resolution transmission electron microscope (TEM) image on Figure 4.1(d). $FAPbI_3$ forms nanocubes with an average lateral size of 10–15 nm in length (size distribution can be found in Figure A2.3), enabling a good fit within the gaps between the Si structures, where the near-field effect is expected to be highest. The SEM imaging revealed that perovskite nanoparticles preferentially attach to and settle around the nanoellipse structures.

Figure 4.1(e) presents the range of the perovskite emission wavelength shift achieved under *y*-polarized laser conditions, as well as the emission at 755 nm on the flat region, shown for reference. This wide-ranging spectral control was enabled by coupling the excitonic states of the perovskite with the optical modes of the array – the latter of which is directly managed by tailoring the antenna geometry during the lithography process. For instance, when the perovskite is deposited on the array with L = 216 nm, the spectrum displays a blue-shifted PL emission at 741 nm, whereas on the array with larger nanoellipse size, L = 256 nm, the peak position redshifts to 780 nm. Therefore, the emission wavelength can be shifted to both higher and lower energies according to the energy of the q-BIC resonance the perovskite interacts with. The corresponding reflectance spectra of the arrays and the process which leads to the modified emission properties is illustrated in Figure 4.3.

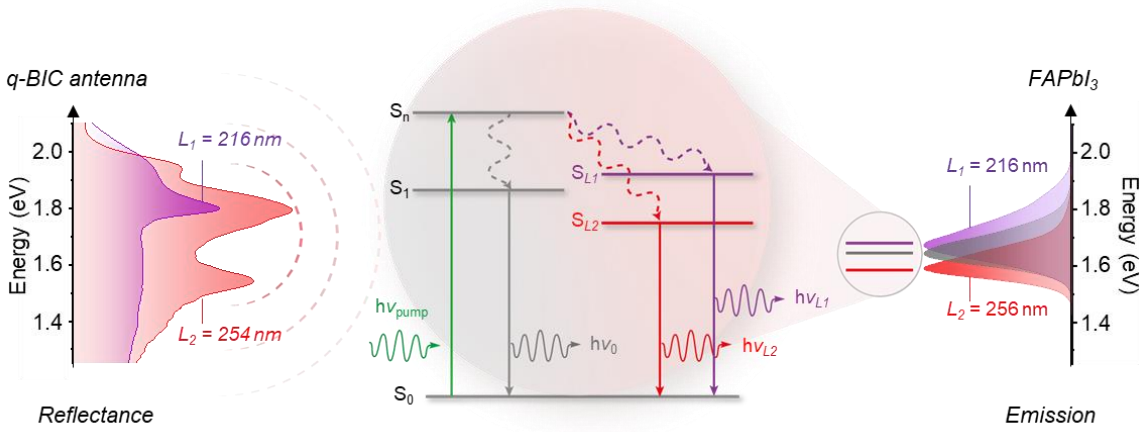

Figure 4.3. Schematic energy level diagram that depicts the interaction between the q-BIC resonance and the emission process of the $FAPbI_3$ QDs. The reflectance spectra of the arrays with L_1 and L_2 are shown on the left, with the corresponding PL emission on the flat region (without nanoantennae) and on the q-BIC antenna arrays shown on the right. The perovskite is pumped with the 532 nm CW laser. S_0, S_1, S_n denote the ground state, lowest energy excited state and nth excited state of the perovskite, respectively, while S_{L1} and S_{L2} denote the alternate energy levels provided by the Purcell effect (F_p) on the q-BIC nanoantenna arrays with L_1 and L_2.

On the left panel of Figure 4.3, the experimental reflectance spectrum of the short (L = 216 nm) array is presented, which exhibits a single q-BIC mode at 1.80 eV.[128] In contrast, the array with longer ellipses (L = 256 nm) reveals two distinct peaks at 1.54 eV and 1.79 eV that are attributed as q-BIC resonances. The appearance of the optical mode at the lower energy has a significant effect on the resulting PL response of the perovskite, which is demonstrated on the right panel. In the case of the L = 216 nm array, the PL emission shifts to 1.67 eV towards the high energy q-BIC resonance. On the other hand, when using the L = 256 nm array, there are two potential decay channels provided by the two q-BIC modes that exist within the system. Significantly, the perovskite preferentially couples to the lower energy resonance, thus leading to single emission band at 1.59 eV, closer to the low energy q-BIC resonance. The observed spectral shift of the emission wavelength originates from the Purcell effect (F_p), which refers to the coupling of the resonant q-BIC mode with the excitonic state of the perovskite. The interaction modifies the spontaneous emission rate of the system, creating an alternate radiative decay channel through the coupled state, where the PL emission wavelength shifts towards the resonance frequency of the coupled mode.[115,293]

4.3.1 Purcell enhancement of $FAPbI_3$ emission *via* q-BIC resonances

As discussed in Chapter 1, the coupling of an emitter to a resonant mode results in a modified radiative decay rate, and the degree of radiation enhancement can be quantified by the Purcell factor (F_p):[112]

$$F_p = \frac{3}{4\pi^2}\frac{Q}{V_{eff}}\left(\frac{\lambda}{n}\right)^3 \quad (1.12)$$

where Q is the quality factor of the resonance, V_{eff} is the mode volume, λ is the emission wavelength and n is the effective mode index.

First, the Purcell effect of the nanoantennas was investigated with L = 232 nm, where the resonant mode overlaps spectrally with the excitonic perovskite emission at ~755 nm. To achieve this, the measurements were performed under *y*-polarized conditions, as the symmetry-broken element of the nanoellipse design gives rise to a higher energy q-BIC mode under *x*-polarized light - leading to spectral mismatch and inefficient coupling, as discussed later on. For reference, the optical properties of the array under study in this section, excited using *x*-polarized light, can be found in Figure A2.4.

The resonant mode was analyzed by angle-resolved reflectance, measured using a back-focal-plane (BFP) microscope setup under *y*-polarized conditions and is presented on Figure 4.4(a).

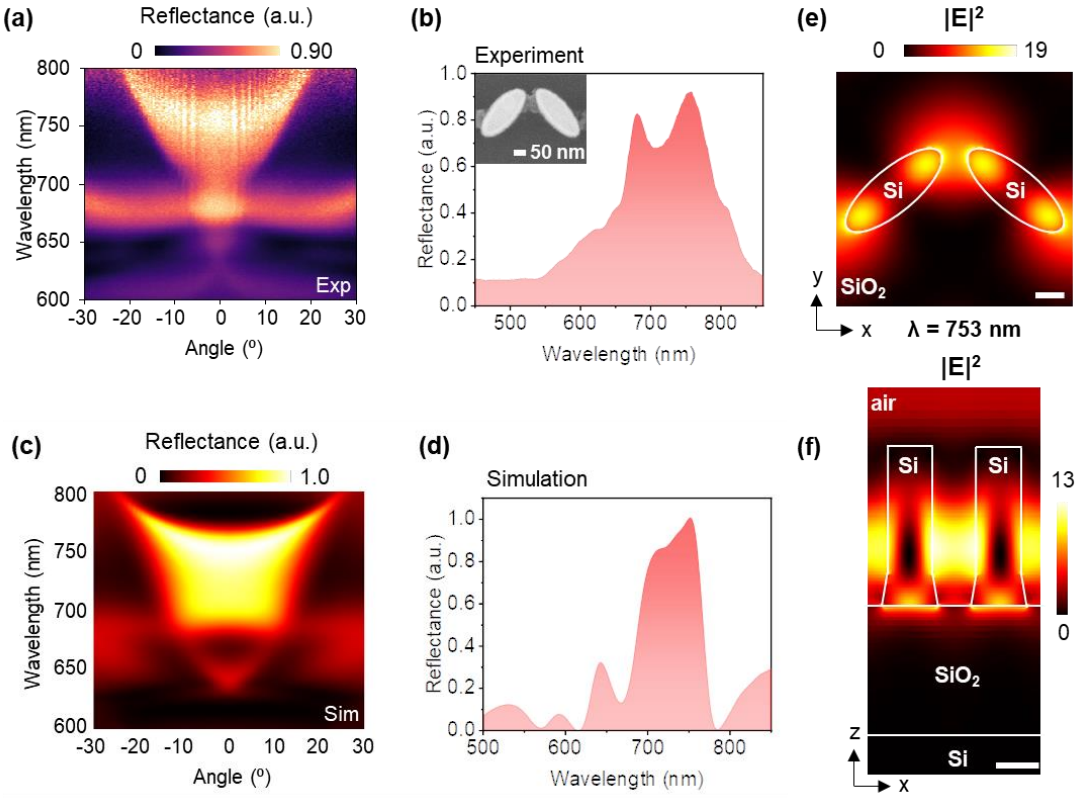

Figure 4.4. Purcell enhancement effect of the q-BIC antenna under *y*-polarization. (a) Back-focal-plane (BFP) image showing the experimental angular-resolved reflectance of an array with L = 232 nm and W = 93 nm under *y*-polarized incident condition and (b)

corresponding experimental reflectance spectra, taken from the cross-section from (a) at an incident angle of 0º. The inset shows an SEM image of the perovskite coated nanoantennas. (c) Simulated angular-resolved reflectance of an array with the same parameters under *y*-polarized conditions and (d) simulated reflectance spectra at the incident angle of 0º. (e) Spatial distribution of the electric field magnitude ($|\boldsymbol{E}|^2$) at λ = 753 nm for the array, obtained from FDTD simulations. The scale bar corresponds to 100 nm. (f) Corresponding electric field distribution at the cross-section (*z*-*x* plane) of the same nanoellipse pair (scale bar is 100 nm).

The experimental data shows a spectral band located at 753 nm at the Γ point, which varies little with the angle of the incident light. This feature is attributed to a q-BIC mode.[40] The experimental reflectance spectrum at 0º incident angle is presented on Figure 4.4(b). The angle-resolved data was found to agree well with the simulation obtained using finite-difference-time-domain (FDTD) calculations, shown in Figure 4.4(c) and (d), although the broadening of the experimental spectra is noted. In addition, the simulated reflectance shows a less separated and resolved higher energy q-BIC band, which is located at 681 nm in the experimental results. The discrepancy likely originates from small imperfections and differences in the nanostructure geometry compared to the computational setup. In particular, the walls of the Si nanopillars are not perfectly straight, but slightly angled towards the bottom due to the etching process.[128] While the simulation geometry is defined based on these angled structures, there may be slight variations within the physical array. Furthermore, the numerical aperture (NA) the objective used in the experiments was 0.60, which corresponds to the incident angle ranging from –36.9 degree to 36.9 degree, rather than being the ideal normal incidence condition in simulation. It is also noted that due to the overlap of the two q-BIC modes, the accurate determination of the *Q*-factor of these spectral features is difficult.

The electric field distribution $|\boldsymbol{E}|^2$ of the mode profile at λ = 753 nm is shown in Figure 4.4(e) from the top view of the nanopillar pair and the cross-section along the *x*-plane can be seen in

Figure 4.4(f). The simulation results demonstrate a significant field enhancement effect localized within and around the tips of the nanoellipses, where the majority of the perovskite nanoparticles is typically deposited. The corresponding charge distribution profiles are shown in Figure 4.5(a),(b).

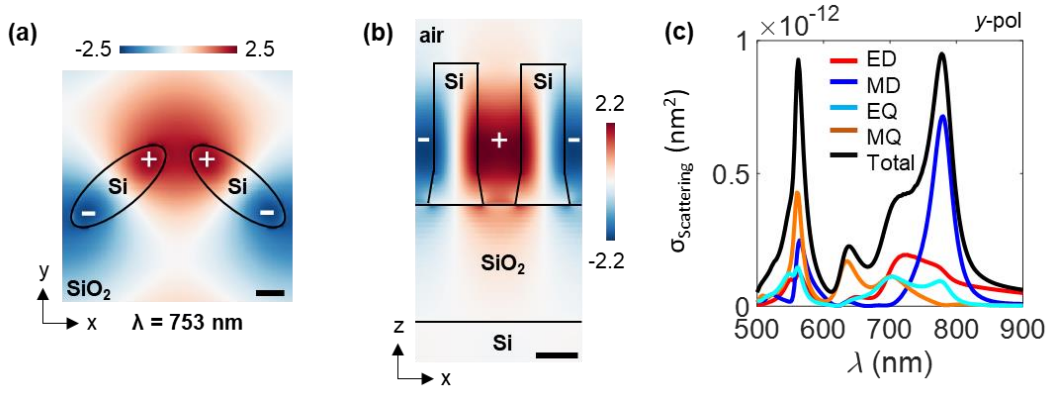

Figure 4.5. Spatial distribution profile of the E_z component of the resonant modes under *y*-polarized conditions for the array with L = 232 nm and W = 93 nm. (a) The mode pattern in the *y*-*x* plane. (b) Cross section through the ellipse pair in the *z*-*x* plane. The scale bars have lengths of 50 nm and 100 nm, respectively. (c) Multipolar decomposition of the scattering cross section of the array, showing the contributions of the electric dipole (ED), magnetic dipole (MD), electric quadrupole (EQ) and magnetic quadrupole (MQ) modes, as well as the total scattering spectrum.

To allow the identification of the individual multipole moments that contribute to the scattering behaviour of the array, multipolar mode decomposition calculations were performed (Figure 4.5(c)). By quantifying the contribution of each multipolar moment to the scattering cross-section, the dominance of specific multipolar modes in q-BIC resonances was assessed. The mode decomposition revealed that a strong magnetic dipole is manifested in the decomposition around the q-BIC peak, in agreement with the mode pattern distributions.

To investigate the Purcell effect of the q-BIC nanoarrays, F_p was calculated using FDTD by placing a point dipole source at the location of the highest field enhancement of the nanoellipse tip, which was found to be at the Si ellipse interface, ca. 5 nm above the surface of the SiO_2 layer. The dipole emission wavelength was set to 755 nm with a 100 nm span according to the experimental PL data, and F_p was obtained by averaging the results from the orthogonal dipole orientations.

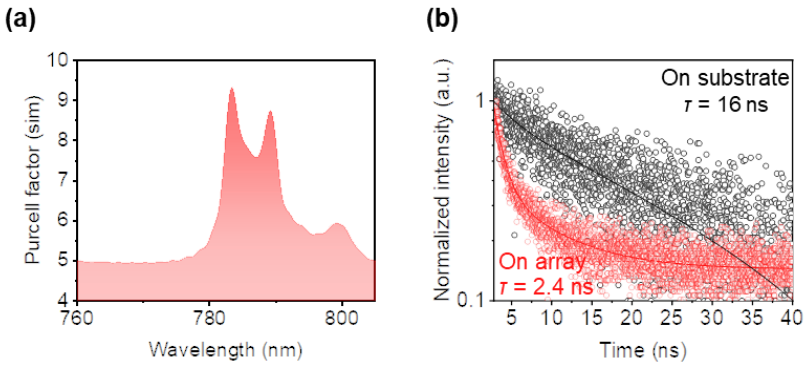

Figure 4.6. Purcell enhancement effect of the q-BIC antenna under *y*-polarization. (a) Simulated Purcell enhancement factor of the array with L = 232 nm and W = 93 nm under *y*-polarized incident condition, as a function of wavelength. (b) Experimental radiative decay rates of $FAPbI_3$ QDs recorded on the flat region of the sample and on an array with L = 230 nm.

Figure 4.6(a) shows that the Purcell factor increases sharply to a value of 9.3 at 783 nm, with another sharp peak present at 789 nm that has a value of 8.7. A small, broader feature can also be seen at 799 nm, with a Purcell factor of 5.9. The multiple peaks indicate that the emitter can couple into multiple optical modes of the nanostructure, with the highest enhancement of the radiative decay rate at the frequency closest to the lowest energy q-BIC resonance of the array, where the coupling interaction is the most efficient. According to Fermi's Golden Rule, F_p is directly related to the spectrally integrated Purcell enhancement ratio of γ / γ_{res}, where γ and γ_{res}

are the radiative decay rates of the emitter on the sample area without q-BIC resonances and within the resonant cavity (*i.e.*, the near-field region of the nanoantenna), respectively.[294]

To confirm the theoretical results, we performed PL lifetime measurements to obtain γ_{res} and γ, as shown on Figure 4.6(b). The perovskite nanoparticles were pumped using a 640 nm *y*-polarized pulsed femto-second (fs) laser at room temperature and the PL decay rate was determined by fitting the experimental data with the following exponential decay function:

$$y = A_1 e^{\left(-\frac{x}{t_1}\right)} + A_2 e^{\left(-\frac{x}{t_2}\right)} + y_0 \quad (4.1)$$

Where, A_1 and A_2 are the amplitudes, t_1 and t_2 are time constants and y_0 is the offset. The average lifetime (τ) was obtained via the following:

$$\tau = \frac{A_1 t_1 + A_2 t_2}{A_1 + A_2} \quad (4.2)$$

Table 3.1 summarises the decay parameters obtained from the measurements of arrays with lengths ranging from 216 ± 3 nm to 245 ± 4 nm, with the corresponding PL lifetime measurements and the reflectance spectra of the clean arrays shown in Figure A2.5, A2.6, respectively.

Sample	Lifetime (τ, ns)	A_1	t_1 (ns)	A_2	t_2 (ns)	y_0
IRF	0.24	46738.69	0.24	-	-	22.76
In toluene	12.68	1.36	1.65	1.07	26.70	-0.16
On the flat area	16.1	0.50	3.14	1.00	24.91	-0.10
***L* = 216 ± 3 nm**	2.63	48.19	7.33	153.71	1.16	28.14
***L* = 224 ± 4 nm**	2.75	48.00	7.56	162.27	1.33	28.27
***L* = 229 ± 3 nm**	2.11	46.91	5.91	165.20	1.03	26.98
***L* = 230 ± 3 nm**	2.42	40.14	6.31	123.75	1.16	26.96
***L* = 234 ± 5 nm**	3.31	43.43	7.14	76.24	1.12	27.38
***L* = 240 ± 4 nm**	2.83	47.74	6.83	108.86	1.08	27.77
***L* = 244 ± 3 nm**	2.98	41.36	7.40	106.37	1.26	27.96
***L* = 245 ± 4 nm**	3.09	46.54	8.39	144.47	1.38	28.63

Table 3.1. Extracted parameters of A_1, A_2, t_1, t_2, y_0 and τ from the PL lifetime decay measurements of $FAPbI_3$ in toluene, on the flat area of the substrate, on arrays with lengths varying from L = 216 ± 3 nm to L = 245 ± 4 nm. Parameters from the instrument response function (IRF) are shown as a reference.

The PL decay rate of $FAPbI_3$ on the flat region was determined to be 16.1 ns, close to the lifetime of the particles in toluene, and is ascribed to a combination of radiative and nonradiative exciton recombination mechanisms at this temperature.[292] Furthermore, the nanosecond scale suggests the presence of free excitons within the system.[295] Free excitons are formed from the promotion of an electron from the valence band to the conduction band. The excitons can travel around the material, resulting in higher chances of recombination and therefore possess shorter lifetimes compared to bound excitons. Thus, the energy of the PL emission is related to the bandgap of the perovskite. To measure γ_{res}, arrays were fabricated with nanoellipse lengths varied from L = 216 ± 3 nm to L = 245 ± 4 nm. It was found that the rate of spontaneous emission is enhanced on all arrays, with a reduced lifetime within the range of 2-3 ns, without correlation to the array geometry. This is not surprising, as the average nanoellipse size varied little across the different arrays. The array which exhibits the same

optical properties as the one discussed earlier (here, $L = 230 \pm 3$ nm) induced a 6.7-fold increment of the radiative decay rate (*i.e.*, EF_{Rad}) relative to the flat region, slightly lower than the theoretically calculated value. This radiative decay rate enhancement is ~2.3-fold larger than that achieved using hyperbolic metamaterials.[296]

We note that the detected PL intensity is influenced by the concentration of emitters within the sampling area, which may differ on the flat region and on the nanoarrays. Therefore, to obtain an accurate evaluation on the PL enhancement factor, periodic nanodisk arrays were fabricated by EBL that provide a similar platform for the perovskite distribution, without exhibiting resonant modes in the spectral region of interest (Fabrication methods are outlined under "*Si nanoarray fabrication*" in Chapter 5. The nanodisks have a diameter of 65 nm, pitch of 160 nm and height of 360 nm (see Figure 4.7).

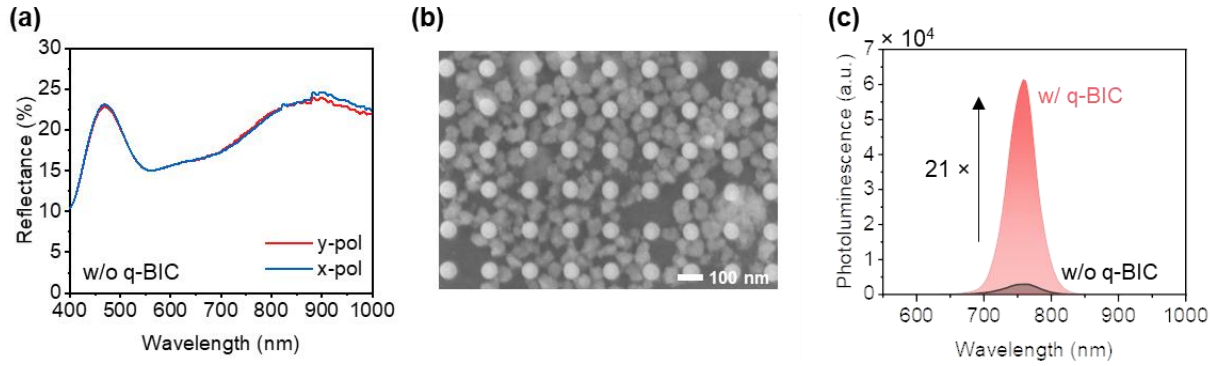

Figure 4.7. (a) Reflectance spectrum of the nanodisk array without optical modes in the spectral region of interest, fabricated as a reference to investigate the PL enhancement effect of the q-BIC resonant nanoarrays with q-BIC resonances. (b) SEM image of the nanodisk array coated with the perovskite nanoparticles. (c) The enhanced PL peak intensity of the perovskite on the array with $L = 232$ nm and $W = 93$ nm under *y*-polarized incident condition, compared to the PL response on a nanodisk array without q-BIC resonances.

As shown on Figure 4.7(c), the q-BIC nanoarrays promoted a 21-fold enhancement of the PL intensity under *y*-polarized excitation, relative to the arrays without resonant modes. This observed enhancement of 21-fold is ~3-times higher than the radiative decay enhancement factor. The additional enhancement mechanism is due to the enhanced pump laser absorption of the array, *i.e.*, EF_{Abs}, which can be analyzed via FDTD simulations. The total power absorption at 532 nm, the pump laser wavelength, was calculated and compared for a uniform film of perovskites on the substrate and on the q-BIC array. The electric field distribution of the nanopillars, as well as the flat substrate at 532 nm is shown in Figure A2.7, along with the corresponding reflectance spectrum. The contribution of the perovskite and the substrate/Si arrays alone to the total power absorption was determined and are summarised in Table 3.2.

Perovskite film on flat substrate

$A_{(NP)}$ ($\times 10^{-18}$ W)	$A_{(Sub)}$ ($\times 10^{-17}$ W)	$A_{(Total)}$ ($\times 10^{-17}$ W)	Perovskite contribution (%)	Substrate contribution (%)
8.54	1.14	2.00	42.9	57.1

Perovskite film on Si array

Conditions	$A_{(NP)}$ ($\times 10^{-17}$ W)	$A_{(Si)}$ ($\times 10^{-17}$ W)	$A_{(Total)}$ ($\times 10^{-16}$ W)	Perovskite contribution (%)	Si antenna contribution (%)	Enhancement factor
***y*-pol**	6.43	5.65	1.21	53.2	46.8	6.04
***x*-pol**	6.47	7.57	1.40	46.1	53.9	7.02

Table 3.2. Calculated power absorption values at $\lambda = 532$ nm under *x*- and *y*-polarized conditions. The total power absorption was calculated for a uniform film on the flat substrate (Si substrate with 300 nm with SiO_2 cavity layer) and for the Si array with $L = 232$ nm and $W = 93$ nm, with the perovskite layer at the base of the structures. The contribution of each component was calculated, showing the total power absorbed ($A_{(Total)}$), the power absorbed by the perovskite layer ($A_{(NP)}$), the flat substrate ($A_{(Sub)}$) and the Si nanostructures ($A_{(Si)}$).

According to the calculations, the EF_{Abs} is estimated to a ~6-fold, which explains the larger than expected PL intensity enhancement.

These findings therefore demonstrate the value of nanoantennas to achieve a non-invasive modification of the radiative decay rate of perovskites, enabling a significant improvement of the PL brightness.

4.3.2 Tunable PL emission via geometrical engineering of the array

Next, we investigated the degree of emission wavelength shift enabled by the engineering of the array geometry. The emission response of the perovskite is modulated by the coupled state with the q-BIC mode, which is directly related to the size of the nanoellipses. Figure 4.8(a),(b)

presents the evolution of the reflectance spectrum of arrays with increasing ellipse size under *x*- and *y*-polarized conditions. As expected, the increase in nanostructure size redshifts the q-BIC resonance wavelength. Furthermore, under *y*-polarized conditions, the resonance becomes more prominent and higher order modes emerge. The dashed line on the graphs represents the typical spectral position of the PL band of $FAPbI_3$ on the flat region, to illustrate the extent of spectral overlap between the two features.

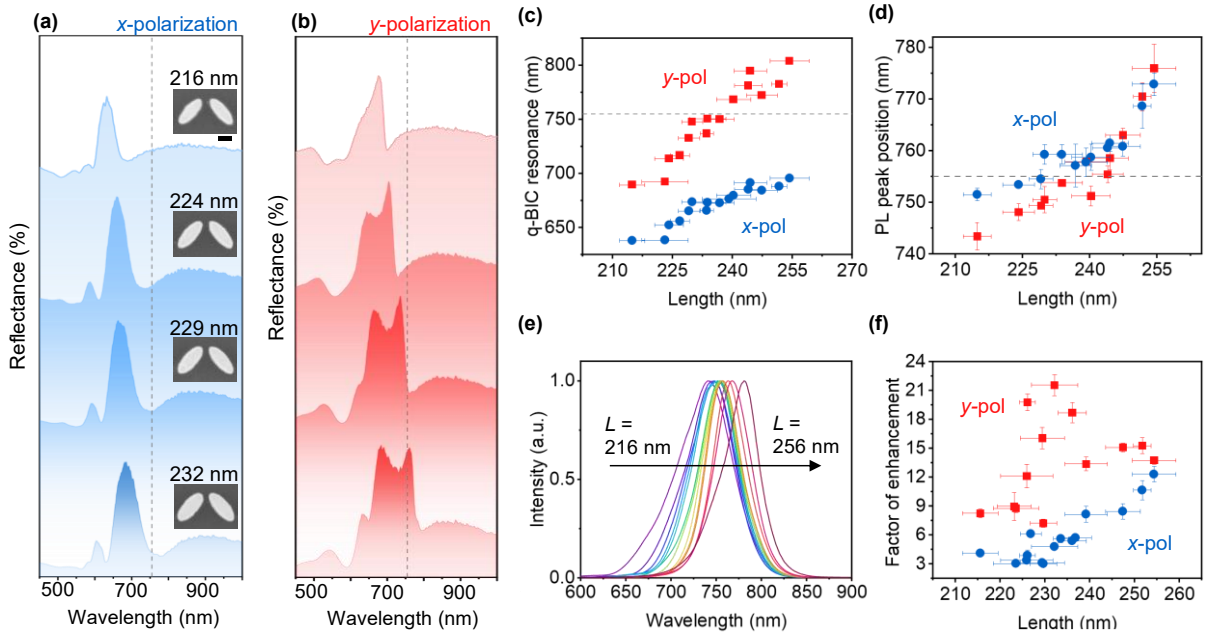

Figure 4.8. Control of the PL shift and brightness of perovskites via geometrical engineering of the array. Reflectance spectra of nanoarrays with different nanostructure sizes, with the corresponding SEM images of the nanoellipse pairs shown in the inset under (a) *x*-polarized and (b) *y*-polarized incident light. The dashed line represents the PL peak position of the perovskite on the flat area of the substrate on all graphs. (c) Spectral position of the q-BIC peak under *x*- and *y*-polarized conditions as a function of the nanoellipse lengths. For the *y*-polarized data, the lowest energy q-BIC peak positions are presented. (d) PL emission wavelength of the perovskite on arrays with varying nanostructure lengths, using *x*- and *y*-polarized laser excitation. (e) Demonstration of the PL band shift from the smallest geometry arrays (L = 216 nm) to the largest ones (L = 254 nm) under *y*-polarization. (f) Factor of enhancement of the PL intensity relative to that on the nanodisk arrays without q-BIC resonances, as a function of the nanoellipse size.

Figure 4.8(c) summarizes the size-dependent redshift of the q-BIC energy under both polarization states. Here, the wavelength of the lowest energy peak is presented from the *y*-polarized reflectance data. When L = 216 nm is increased to 256 nm, the optical mode redshifts from 690 nm to 804 nm under *y*-polarization, and from 638 nm to 696 nm under *x*-polarization. The polarization switching results in a significant difference in the range of 50-110 nm of the q-BIC spectral positions. Hence, when the arrays are excited using *x*-polarized laser light, the spectral overlap with the excitonic PL emission band is minimal or zero. Following the principles of the dyadic Green's function,[294] the perovskite emission characteristics change according to the properties of the resonant mode that the excitonic states couple with. This relationship between the Purcell factor and the emission wavelength shift was derived in detail in the work of H. P. Adl et al.[296] Consequently, the emission wavelength redshifts with increasing nanoellipse size and simultaneously exhibits a polarization-dependent PL band position. This phenomenon is shown in Figure 4.8(d), demonstrating a ~39 nm PL wavelength position shift under *y*-polarized excitation and a shorter range of ~19 nm under *x*-polarization. The representative normalized PL spectra for nanoellipse lengths ranging from 216 nm to 256 nm under *y*-polarized illumination displayed on Figure 4.8(e).

The nanoellipse size has a significant influence on the polarization-dependent PL emission, where smaller nanostructures, *i.e.*, higher energy q-BIC modes, result in larger differences. Here, the *y*-polarization induced q-BIC frequency is still close enough in energy for the perovskite excitons to couple to, thus introducing the alternate radiative decay channel closer to the energy of the coupled state. Moreover, the degree of spectral overlap between the excitonic emission wavelength and the resonant mode determines the strength of the Purcell enhancement effect of the array. Figure 4.8(f) presents the factor of enhancement of arrays with varying nanostructure sizes, illustrating that as the q-BIC resonance gets closer to full spectral

overlap, the factor of enhancement increases up to ~21-fold under *y*-polarization (*L* = ~226-236 nm). Further increase in the structure size results in a spectral mismatch which in turn decreases the enhancement factor to ~15. On the other hand, using *x*-polarized excitation on the same arrays, the achieved enhancement is only ~6-fold. However, this value increases continuously with increasing nanoellipse size owing to the more efficient coupling. In addition to the enhanced emission, the Purcell effect promotes a narrowing of the spectral FWHM linewidth, as shown in Figure 4.9, resulting from the more homogeneous emission at the resonant wavelength. The PL linewidth narrows by up to ~27% under *y*-polarization and ~19% for *x*-polarization.

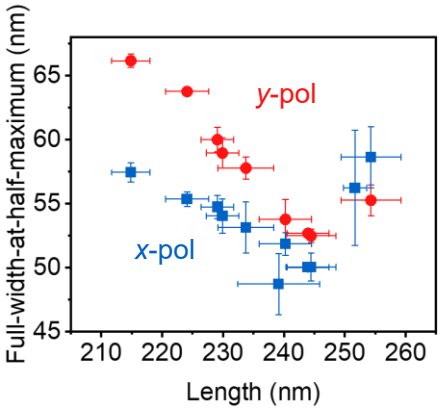

Figure 4.9. Full-width-at-half-maximum (FWHM) of the PL emission peak on nanoantennas with varying lengths under both *x*- and *y*-polarized conditions as a function of the nanoellipse lengths.

Lastly, the effect of the variation of the in-plane rotation angles of the nanopillar pair was examined. Since the q-BIC resonance originates from the symmetry-breaking element, it is expected that the *Q*-factor of the q-BIC mode would increase as the ellipses become near parallel to each other.[128] Figure 4.10(b),(c) shows the reflectance spectra of arrays with

L = 232 nm and W = 93 nm under both polarizations, as the in-plane rotational angle (θ) is varied from 36º to 63º.

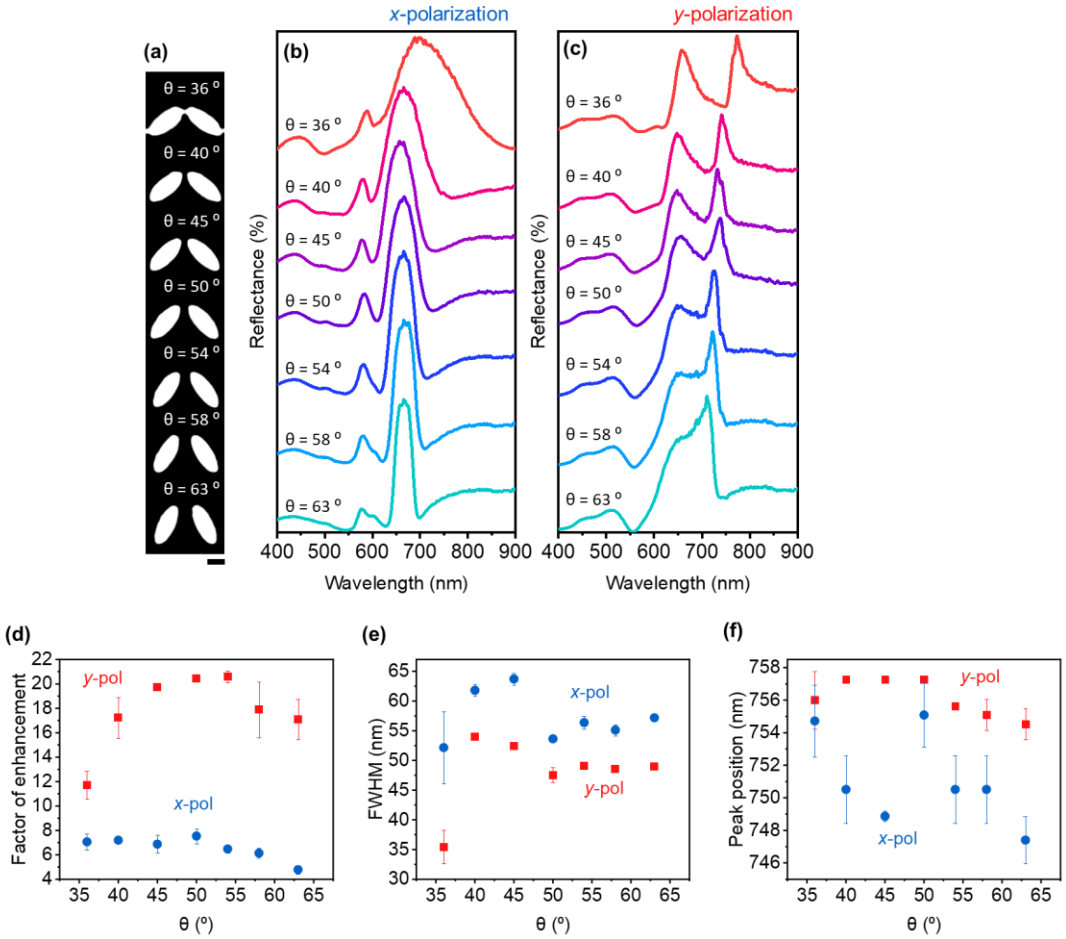

Figure 4.10. Variation of the in-plane tilt angle of the nanopillar pairs. (a) SEM images of the nanopillar pairs with different in-plane tilt angles (θ) in an array with ellipse length L = 232 nm and width W = 93 nm. Reflectance spectrum of the arrays under (b) x-polarized conditions and (c) under y-polarized conditions. (d) Corresponding enhancement factor of the PL intensity of perovskites as a function of the in-plane tilt angle (θ), under x- and y-polarized conditions. (e) Full-width-at-half-maximum (FWHM) and (f) peak positions of the PL peaks.

The increase of θ from 36º to 63º (i.e., rotation of the nanopillars from tilted to nearly parallel) results in the q-BIC band becoming narrower under x-polarized conditions. Meanwhile, under y-polarized conditions, when the tilt angle is decreased from 63º to 36º, the q-BIC band at 705

nm becomes more pronounced and separated in the reflectance spectrum. We investigated the effect on the enhancement factor of the perovskite QD emission intensity, the corresponding full width at-half maximum (FWHM) and the PL peak positions on arrays, under *x*- and *y*-polarized conditions, as a function of the nanopillar tilt-angle.

The enhancement factor was lowest (~12) at $\theta = 36^{o}$ under *y*-polarized excitation, which may be explained by the redshifted q-BIC peak not overlapping with the PL emission peak of the uncoupled perovskite. At other tilt angles, the enhancement factor showed little variation, and was in the range of ~17 to ~21. Similarly, *x*-polarized conditions showed low variation in the enhancement factors, ranging between 5-7. A significant drop was observed in the FWHM using $\theta = 36^{o}$ when using *y*-polarized excitation. This was attributed to a slightly asymmetrical PL peak, with one side of the peak being narrower. However, we did not observe a trend in the FWHM data. In addition, analysis of the PL peak positions showed little variation when using *y*-polarized excitation and significant scatter in the data when under *x*-polarization. As seen in the reflectance spectra, the variation of the tilt angle does not lead to significant shifting, narrowing or broadening of the q-BIC peaks, hence, there is less effect on the Purcell coupling.

Therefore, although the rotated geometries enabled q-BIC resonances with higher Q-factors, we did not observe a significant improvement or trend in the FWHM, enhancement or peak positions of the perovskite emission.

4.3.3 Polarization switchable perovskite PL emission wavelength

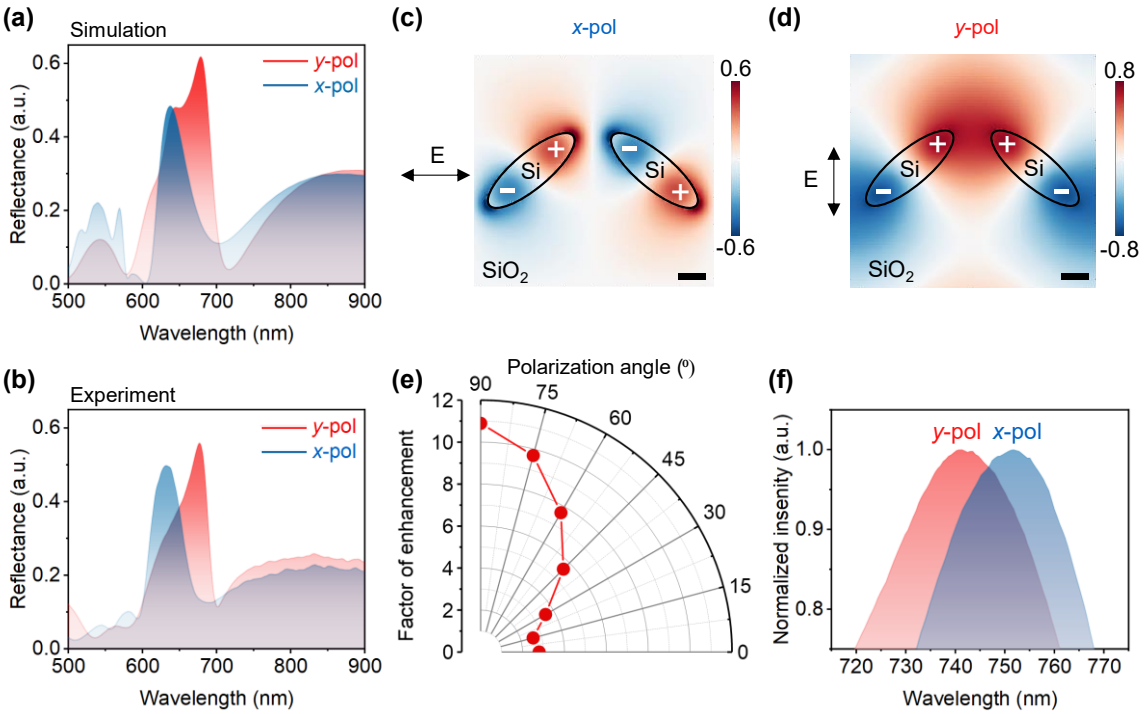

Figure 4.11. Polarization switchable perovskite PL emission wavelength. (a) Simulated and (b) experimental reflectance spectra of a nanoarray with L = 216 nm and W = 79 nm when illuminated with x- and y-polarized light. Spatial distribution profile of the E_z component of the resonant modes under (c) x- and (d) y-polarized conditions. Scale bar corresponds to 50 nm. (e) PL enhancement factor as a function of the polarization state of the excitation laser, changing from x-polarization (0º) to y-polarization (90º). (f) Normalized PL band of the perovskite coated array that demonstrates the emission wavelength shift under x- and y-polarized laser excitation.

To demonstrate the polarization switching of the emission wavelength, we selected the nanoarray with the shortest dimensions (L = 216 nm), which supports optical modes that are furthest in energy from the perovskite excitonic states. Figure 4.11(a),(b) shows the simulated and experimental reflectance spectra of the array when the polarization state of the light source is varied. The q-BIC resonances can be observed at 690 nm for y-polarized pump laser, and at 637 nm under x-polarized pump condition. The corresponding $\boldsymbol{E}_z$ component of the electric

field at the respective resonant wavelengths is shown in Figure 4.11(c),(d), presenting the distinct mode profiles under the two polarization conditions. Therefore, the emitters in the vicinity of the nanoantennas experience significantly different electromagnetic environments, which directly influences the Purcell effect under the given polarization. This difference can be observed as the polarization state of the incident laser light is varied in increments from *x*-polarization (0º) to *y*-polarization (90º), as shown in the polar plot in Figure 4.11(e), illustrating the gradual increase in the enhancement factor from 3 to 12. Most notably, the *y*-polarized laser excitation introduces a radiative decay channel that gives rise to an emission band at 741 nm, while switching to *x*-polarization, causes a redshift to 751 nm. The feature of switchable emission wavelengths, as well as the enhanced PL intensity, would be of particular interest in the design of single-photon emitter applications.[297] By trapping individual QD in the gap, one may realize efficient single-photon sources which emission is controlled by the antenna, which could mitigate the problems of spectral diffusion due to inhomogeneities during the material synthesis. In addition, the possibility of designing double resonances at both the pump laser frequency and emission wavelength could further enhance the efficiency of the system.[298]

4.4 Conclusions

In the work described in this Chapter, nanostructured Si optical antennas have been used to engineer the emission of $FAPbI_3$ via q-BIC resonances. By exploiting the variability of the q-BIC resonance energy, a tuning range of ~39 nm of the emission wavelength was achieved *via* the Purcell effect. Furthermore, it has been demonstrated that the q-BIC array facilitates switchable emission wavelengths of up to ~10 nm, as controlled by the polarization state of the

pump laser. Maximizing the coupling efficiency between the resonant mode and the perovskite excited state allows enhancement of the PL intensity by a factor of 21-fold using *y*-polarized conditions. When the Purcell interaction is maximised, the emission linewidth narrows by up to ~27% under *y*-polarization and ~19% for *x*-polarization. It was anticipated that the variation of the in-plane rotational angle of the Si nanopillars to achieve sharper q-BIC resonance peaks would enable further narrowing of the PL emission band. However, the variation did not influence the Purcell coupling. FDTD simulation of the optical properties of the arrays and the Purcell factor provided further insight into the underlying radiative decay rate enhancement. It was found that the arrays promote a 6.7-fold enhancement in the spontaneous radiative decay rate of the particles, with an additional ~6-fold enhancement in the pump laser absorption by the arrays. The presented work could pave the way for interesting optoelectronic applications, including wavelength-tunable single-photon sources and lasers.

Chapter 5. Achieving High Quality Factor Interband Nanoplasmonics in Ultraviolet Spectrum via Hybridization

5.1 Introduction

Interband plasmonics (IBPs), as supported by non-metals, semiconductors and topological insulators, have become a fast-emerging field in recent years.[134,299,300] Unlike classical plasmonic materials, such as gold and silver, where plasmon polaritons originate from the coupling between light and the oscillation of the free electron plasma, the plasmonic behaviour in IBPs is due to the interband transitions of bound electrons. As a result, *p*-block IBP materials, such as silicon, bismuth, gallium and arsenic, exhibit a strong plasmonic character in the UV and visible spectral range, while antimony displays this behaviour in the visible to NIR region.[134,299,301] These characteristics extend to their dichalcogenides and binary compounds, including antimony triselenide (Sb_2Se_3), antimony telluride (Sb_2Te_3), bismuth triselenide (Bi_2Te_3) and bismuth telluride (Bi_2Te_3).[302,303] Owing to their unique optical, physical and chemical properties, the use of these compounds can offer advantages over conventional plasmonic materials, and are currently being explored as materials for surface-enhanced spectroscopy,[304–306] thermoelectrics[307,308] and tuneable plasmonics.[309–311]

Despite their outstanding potential, leveraging the plasmonic nature of IBP materials has been challenging due to their intrinsically large damping losses (*i.e.*, extinction coefficient, *k*), which consequently leads to nanoplasmonic resonances with low *Q*-factors.[134] For example, Si nanodisk structures can support localized plasmon resonance with strong optical field enhancements in sub-10-nm gaps in the UV spectrum.[133] However, the *Q*-factor of the resonances is typically ~1. Generally, the *Q*-factor of currently known IBP materials does not

exceed ~3.[134] This problem severely limits their applications in optical sensors,[312] photodetectors[148,149] and other optoelectronic devices, which require sharp and sensitive resonances.[313–315] To fully utilise the extraordinary plasmonic properties of IBP materials, the *Q*-factor of the resonances could therefore be enhanced by exploring nanoantenna designs.[316–319]

In this chapter, the effect of mode hybridization on the Q-factors of IBP resonators is explored. It is demonstrated that the *Q*-factor can be improved by ~43-fold. A universal design generally applicable to the IBP materials is developed. The optical response is fine-tuned by controlling the interaction between the LSPR of the nanodisk and a photonic cavity modes. To achieve this, a Si nanodisk arrays on top of a SiO_2 cavity were fabricated, which exhibits plasmonic resonances within the deep UV region of ~4.6 eV. The observed *Q*-factors are higher than that reported for UV plasmonic Al nanodisks of a similar design.[155] Variation of the cavity thickness revealed the relationship between the degree-of-hybridisation and the resonance quality. Additionally, the role of dipolar and quadrupolar modes in controlling radiative losses was studied via finite-difference time-domain (FDTD) simulations and spectroscopic measurements. The sensitivity of the high-*Q* resonance to its local environment is demonstrated by depositing a UV-absorbing lignin-polyethylene glycol (lignin-PEG) co-polymer film over the plasmonic array. Lignin-PEG exhibits a strong absorption at ca. 4.54 eV, falling within the spectral range of the IBP resonances demonstrated in our work, thus facilitating effective interaction between these two materials. Our results indicate that mode hybridization leads to exceptionally high-quality resonances for IBP materials, therefore drastically improving the outlook for applications where narrow resonances are required.

5.2 Experimental

5.2.1 Materials

Acetone (HPLC grade, 99.8%), 2-Propanol (HPLC grade, ≥ 99.9%), toluene (anhydrous, 99.8%) and tetrahydrofuran (99%) were obtained from Sigma-Aldrich. Sodium hydroxide (≥ 97%) and sodium chloride (≥ 99.5%) were purchased from Fisher Scientific.

Silicon wafers with 100 nm, 200 nm or 300 nm thick SiO_2 layers and quartz substrates were purchased from Silicon Valley Microelectronics, Inc. Hydrogen silsesquioxane (XR-1541 E-beam resist) was purchased from Dow Corning. Chromium chips (99.5% trace metals basis) were obtained from Sigma-Aldrich.

5.2.2 Methods

5.2.2.1 Si nanoarray fabrication

Clean silicon wafers with 100 nm, 200 nm or 300 nm thick SiO_2 dielectric spacer layers were used as substrates. Thicker SiO_2 overlayers were achieved by additional SiO_2 growth using plasma-enhanced chemical vapour deposition (PE-CVD, Oxford Instruments Plasmalab System 380). The process was carried out using gases of SiH_4 at a flow rate of 7.5 sccm (standard cubic centimetres per minute) and N_2O at 20 sccm at 250 ºC and under a pressure of 4.0 mTorr. A DC power of 20 watts and coil power of 1000 watts were used. Next, the substrate with SiO_2 layer was used to grow a further layer of amorphous silicon (a-Si, thickness of 75 nm or 130 nm) on top using plasma-enhanced chemical vapour deposition (PE-CVD, Oxford Instruments Plasmalab System 380). The fabrication of reference arrays on quartz substrates was performed using the same experimental procedures. The a-Si film was grown using SiH_4 at a flow rate of 45 sccm and Ar at 30 sccm at 250 ºC and 8.0 mTorr pressure, with a DC power

of 50 watts and coil power of 30 watts. Next, the resulting samples were spin-coated at 5k round-per-minute (rpm) with 2% hydrogen silsesquioxane, followed directly by nanopatterning via electron beam lithography (EBL, Elionix ELS-7000). The EBL process was carried out using an electron acceleration voltage of 100 keV, beam current of 500 pA, and the exposure dose of 20,480 μC/cm^2 for arrays with disk diameters of 70 nm to 100 nm and 8,960 mC/cm^2 for diameters of 110 nm to 180 nm. Upon completion, the sample was transferred into a solution of NaOH/NaCl (1% wt./4% wt. in de-ionized water) for 60 seconds for development, followed by immersion in de-ionized water for 60 seconds. Then, the sample was rinsed by acetone, isopropyl alcohol (IPA) and dried by a continuous flow of N_2 for 1 minute. Following, the a-Si layer was etched (with over-etching of 15 nm) by inductively-coupled-plasma (ICP, Oxford Instruments Plasmalab System 100) using an ICP power of 300 watts, an RF power of 100 watts, Cl_2 flow rate of 22 sccm (standard-cubic-centimeters-per-minute), a process pressure of 5 mTorr, and a cooling temperature of 10 ^oC. Lastly, the samples were annealed using rapid thermal annealing (Jipelec, Jetfirst rapid thermal processing system) under nitrogen flow of 1500 sscm, a temperature ramp rate of 14.2 ºC/s over 60 s and annealed at 850 ºC for 120 s. Controlled cooling to room temperature over a period 300 s yielded the final arrays with crystalline silicon (c-Si) patterns.

5.2.2.2 Coating of lignin-poly(ethylene glycol) (lignin-PEG)

The lignin-PEG co-polymer was provided by collaborators. The synthesis procedure is outlined in the work by Yew et al.[320] The characterization of the resulting polymer can be found in Figure A3.1, as provided by the collaborators. For the coating of the nanoarray substrates, the lignin-PEG was dissolved in tetrahydrofuran (THF, 10 mL/mg). The samples were first treated using inductively-coupled plasma (Oxford Plasmalab System 80) at an O_2 flow rate of 50 sccm. The DC power used 100 watts, a coil power of 500 watts, a process pressure of 10 mTorr at

room temperature. Next, the samples were spin-coated with the lignin-PEG solution (10 mL/mg, THF). A film thicknesses of ~35 nm or ~55 nm were achieved using a spin-coating speed of 5k rpm and 2k rpm respectively.

5.2.2.3 Optical characterization

The optical constants of the lignin-modified poly(ethylene glycol) films were measured via spectroscopic ellipsometry at 50 º, 60 º and 70 º incident angles across the 190 nm to 320 nm spectral region. Optical reflectance measurements of the samples were taken using a CRAIC UV-VIS-NIR micro-spectrophotometer and a Zeiss Ultrafluar objective (×10 objective lens with a numerical aperture of 0.2), with a polarized broadband light source. Calibration for the absolute reflectance spectra was achieved using a NIST traceable calibration sample from CRAIC Technologies (http://www.microspectra.com/). The measurements were taken using an aperture size of 72 µm × 72 µm and integration time of 100 ms, where 50 measurements were averaged so as to reduce the measurement noise.

5.2.2.4 SEM imaging

The scanning electron microscope (SEM) images were taken with an electron acceleration voltage of 5 kV (Elionix, ESM-9000). Prior to the SEM imaging, the samples were coated with 5 nm of Cr using electron beam evaporation (Denton Explorer E-beam Evaporator) to reduce the anomalous contrast due to charging. A deposition rate of 1 Å/s at a pressure of 4×10^{-6} Torr was used for the Cr layer deposition.

5.2.2.5 Numerical simulations

Three-dimensional finite-difference time-domain (3D-FDTD) simulations were carried out to obtain the far field spectra and the near-field distributions using Lumerical FDTD Solutions

software. The simulated unit cell with a dimension of 200 nm × 200 nm × 1200 nm with perfectly matched layer (PML) for the *z* direction and periodic boundary conditions for the *x* and *y* directions at normal incidence condition. A plane wave source was used, with a monitor placed above the source to record the reflectance spectrum. The mesh size was set to be 2 nm × 2 nm × 2 nm. The material properties of Si were chosen based on the optical dielectric constants taken from previous measurements.[133] For the lignin-PEG film, the refractive index (*n*) and extinction coefficient (*k*) values obtained from the spectroscopic ellipsometry measurements were applied, while the optical dielectric constant of the SiO_2 cavity and Al were taken from the software's material database as adapted from Palik.[288] The electric, magnetic, total power absorption and charge field distributions were collected. To study the angle-dependent reflectance, a broadband fixed angle source technique (BFAST) plane wave was used to provide broadband simulations at a range of illumination angles. Multipolar decomposition analysis was carried out by collaborators using COMSOL Multiphysics software. The details of the simulation setup are outlined by Dong et al.[289]

5.3 Results and discussion

To exploit the attractive properties of Si in the field of UV plasmonics, the *Q*-factor of its IBP resonances must be improved. Achieving this requires the suppression of radiative losses within the system. Thus, the following section introduces the design of nanostructures and the underlying mechanisms that can address this requirement. These structures are intended to be capable of narrowing the plasmon band within the UV region via mode hybridization with a photonic waveguide.

Arrays of crystalline silicon (c-Si) nanodisks were fabricated on a SiO_2 dielectric spacer layer grown on a single Si substrate. The SiO_2 layer combined with the Si substrate forms a photonic

cavity, with the substrate serving as the back reflector. In this this configuration, the LSPR supported on the c-Si nanodisks interact with the cavity modes below them (Figure 5.1). These cavities are different from conventional Fabry-Perot type cavities that rely on two reflecting thin films. In the present case, a single mirror is employed and the nanodisk array serves as the "second mirror".

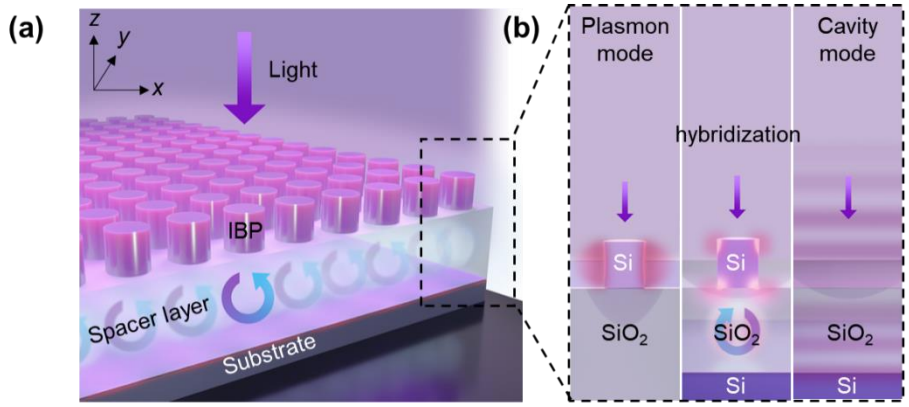

Figure 5.1. High-*Q* resonances of interband plasmonic materials achieved via hybridization. (a) Illustration depicting the surface design consisting of an array of interband plasmonic (IBP) nanodisks fabricated on top of a dielectric SiO_2 spacer layer and Si substrate as the back reflector. (b) Illustrative energy confinement effect resulting from the hybridization between the LSPR of the c-Si nanodisks and the cavity mode.

The properties of the hybridized state, including the linewidth of the resulting resonance band, are influenced by the degree of coupling between the cavity mode and the LSPR mode. Precise control of this interaction can be achieved by manipulating two key parameters: 1) the dielectric SiO_2 spacer layer thickness and 2) the geometric parameters of the disk array. These strategic adjustments enable the optimization of the optical characteristics of the arrays, and provides insight of the underlying mechanisms that give rise to it.

5.3.1 Influence of the SiO_2 cavity on the IBP resonance

The influence of the dielectric spacer layer was investigated by variation of its thickness. The experimental reflectance spectra of substrates with SiO_2 layer thicknesses of 100 nm, 200 nm and 300 nm are presented in Figure 5.2.

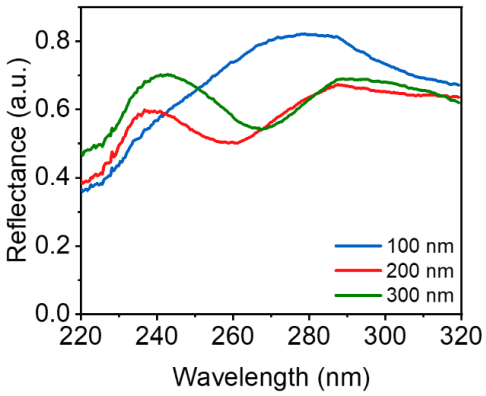

Figure 5.2. Experimental reflectance spectra of the Si substrate with 100 nm, 200 nm and 300 nm thick SiO_2 overlayers.

The bare substrates with 200 nm and 300 nm thick SiO_2 show broad low intensity dips in the reflectance spectrum at 260 nm and 268 nm, respectively. The substrate with 100 nm thick SiO_2 does not exhibit a resonance dip at this wavelength range. First, the optical properties of a conventional Fabry-Perot cavity system were investigated. The use of a Fabry-Perot cavity provides a simplified model to study the cavity mode formation as a function of the SiO_2 thickness. Using FDTD, the reflectance was recorded for the cavity where the nanodisk array is replaced with a 15 nm thick Al film, acting as a mirror (Figure 5.3).

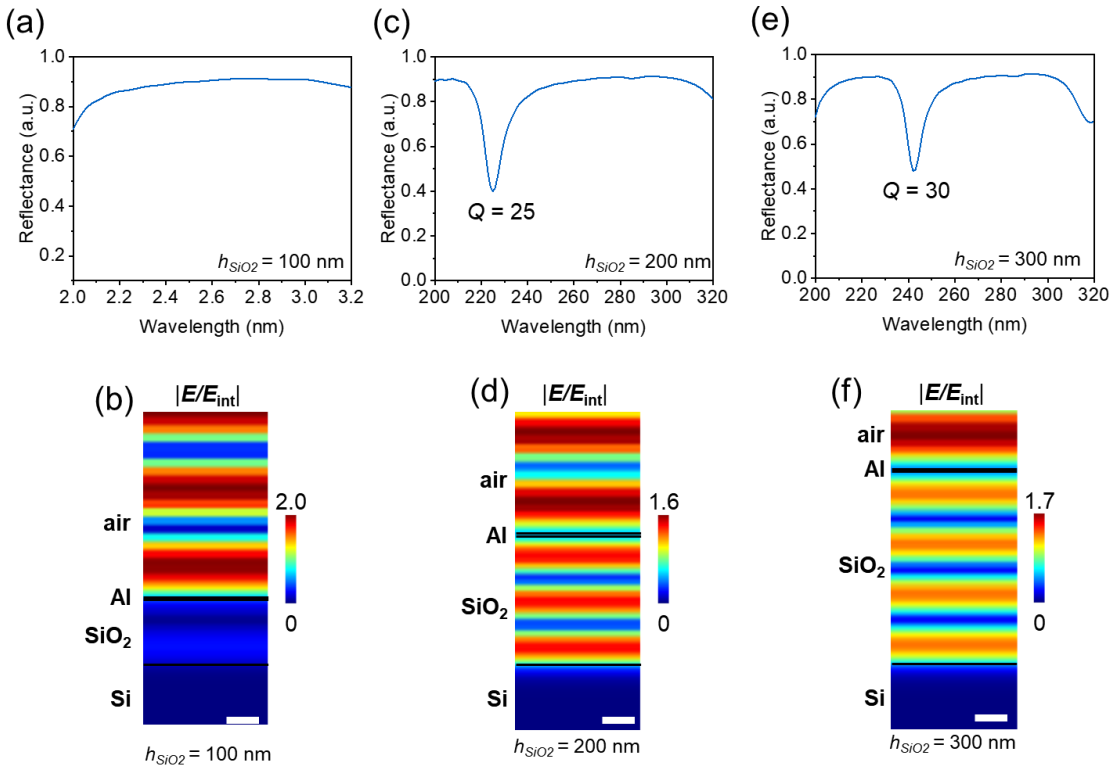

Figure 5.3. FDTD simulated reflectance spectra of a Si substrate with a SiO_2 layer and a 15 nm Al film on top, with a SiO_2 layer thickness of (a) 100 nm, (b) 200 nm and (c) 300 nm, with the *Q*-factor (*Q*) of the resonance dip displayed. Corresponding electric field $|\boldsymbol{E}/\boldsymbol{E}_{\text{int}}|$ intensity distribution at the resonance wavelength presented in (b), (d) and (f), respectively.

Al being a highly reflective material within the UV range, the simulated reflectance spectrum of this design shows a near total reflection when the SiO_2 layer is 100 nm thick. Increasing the cavity thickness to 200 nm leads to a dip in the reflection at 225 nm, attributed to Fabry-Perot resonances.[114] To extract the *Q*-factor from the reflectance data, the IBP dip was fitted with a Gaussian function. An example of the fitting is provided in Figure A3.2. The *Q*-factor of this dip was calculated to be 25. Further increase of the cavity height to 300 nm improves the *Q*-factor to 30 and redshifts the resonance to 243 nm. The simulated electric field $|\boldsymbol{E}/\boldsymbol{E}_{\text{int}}|$ intensity distributions at the resonant wavelengths show standing waves confined within the cavity, generated from the interference of the reflected waves. Thus, the theoretical results suggest that

the use of a Fabry-Perot cavity alone can provide a high *Q*-factor resonances in the UVC region. However, achieving these results experimentally is problematic as the Al layer needs to remain perfectly unoxidized, which is challenging under conventional experimental conditions. Nonetheless, the simulations of the conventional Fabry-Perot configuration show the nature of the mode confinement, which is characteristic to these cavity systems.

In contrast, the use of Si nanostructures leads to a significant difference in the reflectance properties. Furthermore, the adjustment of the geometrical features provides control over the optical properties. The variation of each of these parameters is discussed in the following sections. Using FDTD, the reflectance was simulated as a function of the cavity thickness for a c-Si antenna array with a height (h_{Si}) of 130 nm, disk diameter (d) of 130 nm and pitch length (p) of 200 nm, as shown in Figure 5.4(a). At the cavity thickness of 100 nm, 200 nm and 300 nm, the optical spectra of the arrays were obtained experimentally and theoretically. In addition, arrays were prepared on quartz (a continuous film of SiO_2), to demonstrate the optical response of the system in the absence of the cavity layer. The spatial distribution of the electric field $|\boldsymbol{E}/\boldsymbol{E}_{\text{int}}|$ mode patterns along the *x*-*z* plane at the resonance dip wavelength is provided next to the reflectance spectra. The mode pattern distribution from the *x*-*y* plane (parallel to the plane of the surface) can be found in Figure A3.3.

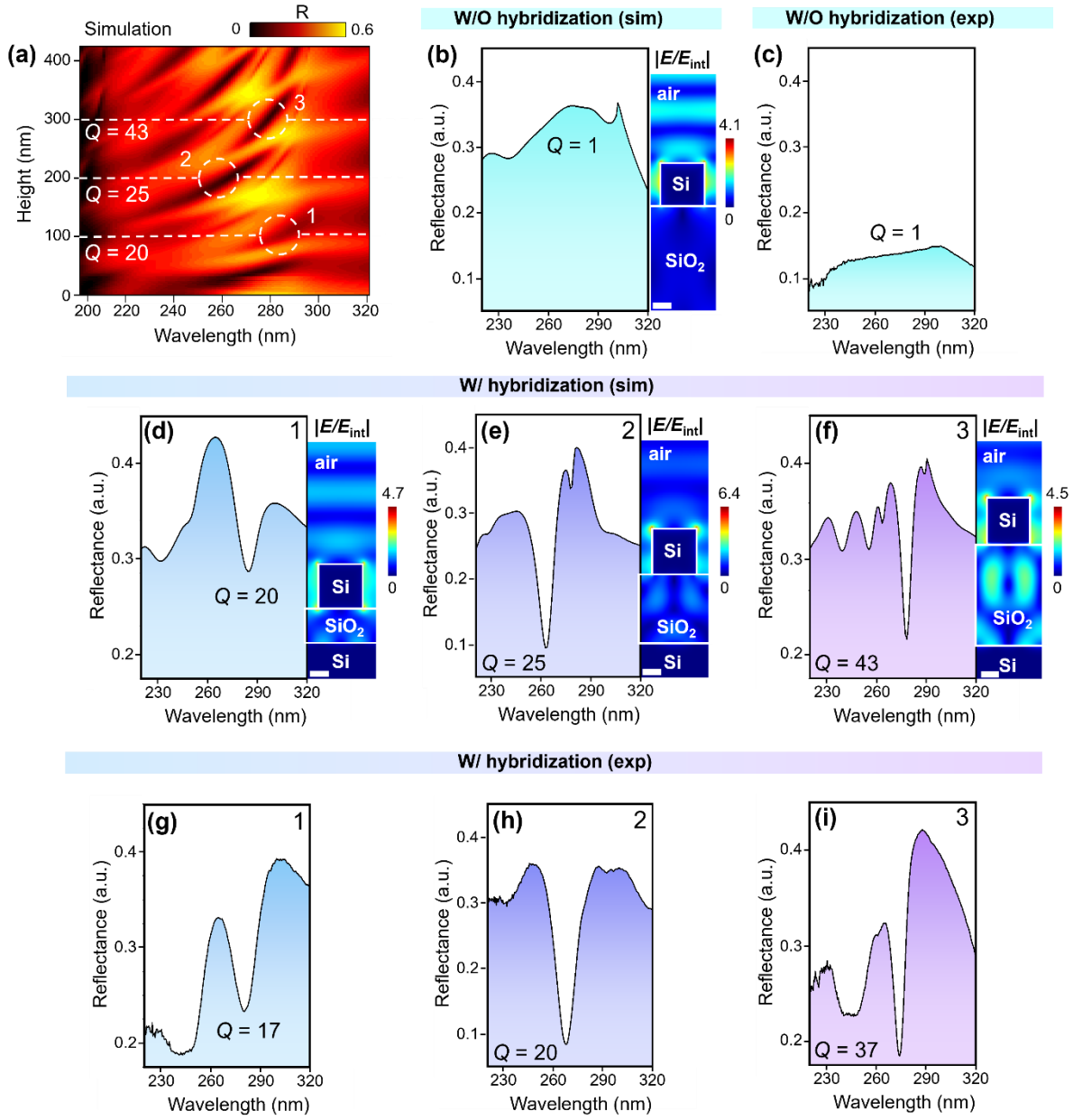

Figure 5.4. (a) FDTD simulation of the optical reflectance of a c-Si nanoarray (h_{Si} = 130 nm, d = 130 nm, p = 200 nm) as a function of the SiO_2 cavity thickness. (b) Simulated and (c) measured reflectance for nanoarrays with the same geometrical parameters on a quartz substrate. Simulated reflectance using (d) a 100-nm-thick SiO_2 spacer layer, (e) 200-nm spacer (f) a 300-nm spacer with (g)-(i) showing the corresponding experimental spectra, respectively. The simulated spatial distribution of the electric field $|\boldsymbol{E}/\boldsymbol{E}_{\text{int}}|$ at the resonance dip wavelength along the *x*-*z* plane (cross-section of the nanodisk) is presented next to the simulated reflectance results. The scale bar corresponds to 50 nm.

The c-Si nanoarrays were fabricated using EBL on Si substrates with 100 nm, 200 nm and 300 nm thick SiO_2 layers on top. When the Si nanoarrays are prepared on quartz, the simulated reflectance exhibits a broad feature spanning the 200 nm – 320 nm spectral region, with small dips observed at 237 nm and 297 nm. The broadness is attributed to non-radiative dissipation, which dampens the resonances and results in a low *Q*-factor of ~1.[133] The arrays fabricated on quartz in experiments displayed a similarly broad feature and low *Q*-factor of ~1. On the other hand, when the cavity thickness was increased to 100 nm, a more pronounced dip appeared at ~283 nm with a theoretical *Q*-factor of ~20, and an experimental Q-factor of ~17, indicating that the cavity mode is influencing the LSPR mode of the nanoantenna.

Increasing the cavity height to 200 nm increases its optical path length, which leads to the excitation of transverse cavity modes within the gap, as it could be seen in the conventional Fabry-Perot model system.[321] The increased confinement of light within the photonic cavity leads to a more pronounced resonance dip, with narrower FWHM. This can be observed in the simulated and experimental reflectance spectra in Figure 5.4(e),(h), respectively. Here, the plasmon dip is redshifted to 263 nm (theoretical) and 267 nm (experimental), with corresponding *Q*-factors of ~25 and 20, respectively. Notably, the FWHM of the resonances was the smallest when h_{SiO2} falls within the range of 295 nm to 315 nm. For instance, at the SiO_2 thickness of 300 nm, a pronounced plasmon dip is observed at ~278 nm in the theoretical results, with a *Q*-factor of 43. Experimentally, the redshifted resonance was centred at 274 nm, exhibiting a linewidth of ~7 nm with an improved *Q*-factor of 37. Further increasing the thickness of the dielectric slab, the cavity can support multiple higher order modes that interact with the LSPR mode, resulting in the formation of additional optical features. This can be observed on the simulated reflectance spectra above the 300 nm spacer thickness, where multiple bands emerge (Figure 5.4(a)).

These results confirm that the presence of the dielectric SiO_2 layer significantly influences the plasmonic behaviour of the IBP material. Examining the corresponding spatial distribution of the electric field $|\boldsymbol{E}/\boldsymbol{E}_{\text{int}}|$ mode patterns at the plasmon dip wavelength (provided next to the simulation results in Figure 5.4), illustrate the changes in the electric field confinement for these arrays. In particular, it is demonstrated that the increasing cavity thickness results in higher confinement of the electric field within the cavity and along the sides of the Si nanodisk, minimizing the radiation into the far-field. Notably, when the Si disk is placed on quartz, the nanodisk supports a dipole mode, similar to the mode distributions seen in conventional plasmonic nanostructures. However, introducing the 300 nm cavity modifies the mode pattern around the nanodisk. Here, the electric field is concentrated at the top and bottom areas of the nanodisk, representative of a quadrupolar mode. These findings and their impact on the overall optical response of the system are discussed in more detail later on.

In order to assign the spectral features in the reflectance spectrum, the angle-resolved reflectance of the array was calculated using 200 nm and 300 nm SiO_2 thicknesses. The bare substrate with the 300 nm SiO_2 layer is presented for reference (Figure 5.5).

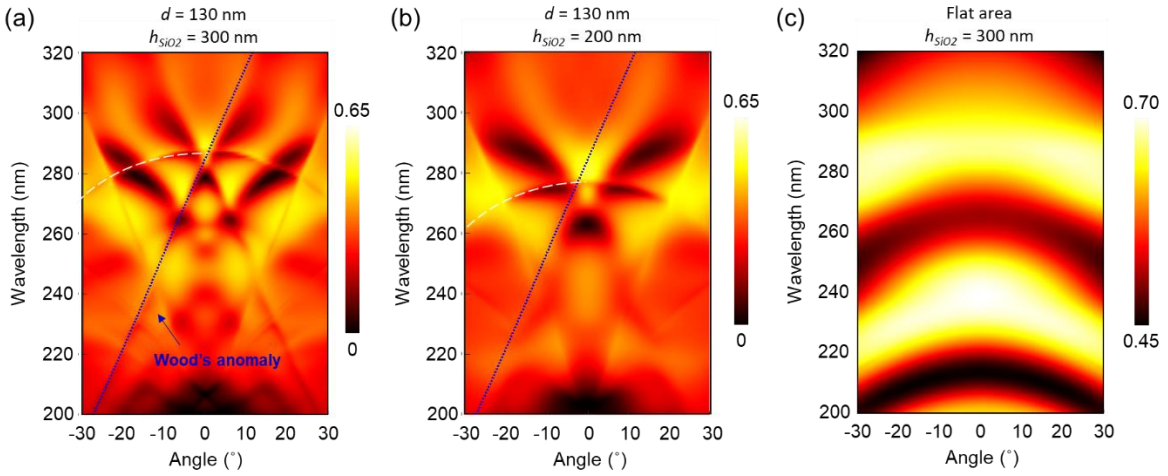

Figure 5.5. Simulated angle-resolved reflectance of arrays with h_{Si} = 130 nm, p = 200 nm, d = 130 nm and (a) SiO_2 cavity thicknesses of h_{SiO2} = 300 nm and (b) h_{SiO2} = 200 nm. (c) Shows the angle-resolved reflectance of the flat area without the nanoarrays when h_{SiO2} = 300 nm.

The straight lines marked in blue are attributed to first order Wood's anomaly diffraction patterns, arising from the periodicity of the array. These features do not change when the cavity thickness changes. Meanwhile, for the array with h_{SiO2} = 300 nm, the narrow feature, located at 289 nm at 0º incidence remains independent of the disk diameter but displays a blueshift with decreasing cavity thickness. This particular feature is associated with an interference phenomenon between the cavity and the Si nano-resonator. Notably, the dispersion plot did not show an avoided crossing pattern, indicating that the plasmon and cavity modes are not strongly coupled. Instead, it suggests that one of the modes is likely more dominant in the hybridized system. In addition, the complexity of the angle-resolved plot indicates that the optical properties are likely influenced by additional underlying interference mechanisms within the system. For instance, the interaction of the Si nanodisk with its mirror image could play a role in the observed sharpening of the IBP resonance dips. These mechanisms will be investigated in future work.

5.3.2 Geometrical parameter variation of the Si array

The spectral position of the plasmon dip (referring to the most pronounced dips in the reflectance spectra identified earlier) was found to be correlated with the pitch length of the arrays. This correlation was investigated for the arrays with h_{Si} = 130 nm, h_{SiO2} = 300 nm and d = 130 nm, as shown in the simulated and experimental results provided in Figure 5.6.

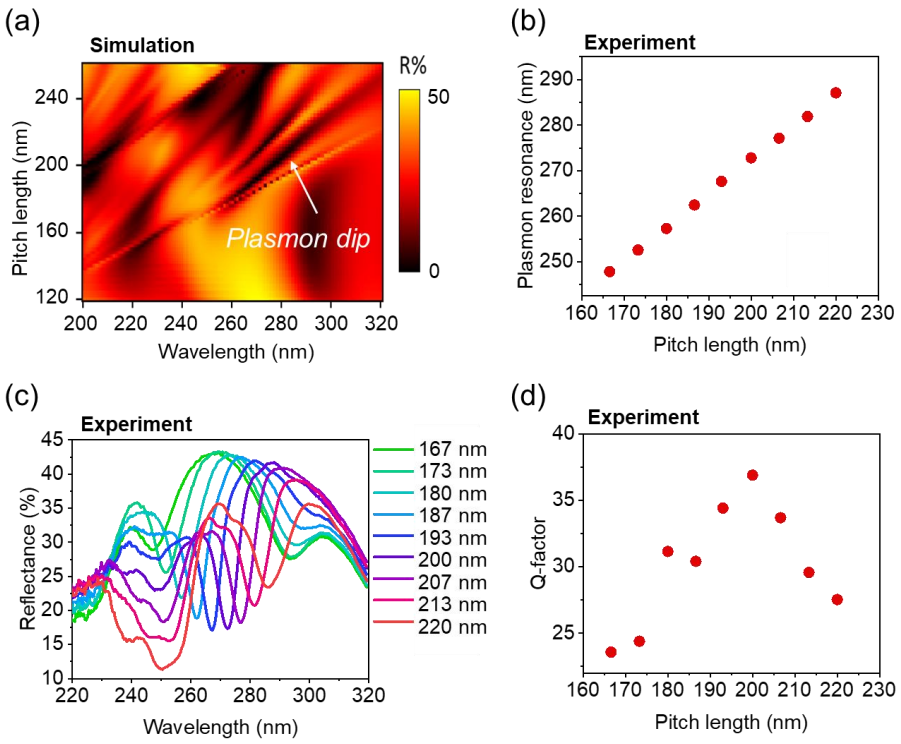

Figure 5.6. (a) Simulated reflectance spectra of the nanodisk array with h_{Si} = 130 nm, h_{SiO2} = 300 nm and d = 130 nm as a function of the pitch. (b) Experimental results of the spectral position of the plasmon resonance dip as a function of the pitch, extracted from the reflectance measurements, which is displayed in (c), and (d), the corresponding Q-factor of the resonance dips.

As previously discussed, pairing the 300 nm thick cavity with an array featuring h_{Si} = 130 nm, d = 130 nm and p = 200 nm yields a single prominent resonance band at 274 nm in the reflectance spectrum. The simulated reflectance in Figure 5.6(a) shows that when the distance

between the nanostructures is increased, the plasmon dip wavelength redshifts, concurrently impacting the resonance quality. This effect was investigated experimentally, using arrays fabricated with pitch ranging from 167 nm to 220 nm, while keeping h_{Si} = 130 nm, d = 130 nm and h_{SiO2} = 300 nm constant. The results are summarized in Figure 5.6(b), showing the experimental spectral position of the resonance dips, which demonstrated a good agreement with the simulated results. The corresponding experimental reflectance spectra of these arrays are shown in Figure 5.6(c), with the calculated *Q*-factors plotted in Figure 5.6(d).

The experimental data demonstrates that the shortest pitch length of 167 nm yields a broad dip centred at 248 nm in the deep UV region, with a *Q*-factor of 23. In this case, the high density of nanostructures on the surface impedes most of the incident light from coupling into the FP cavity and exciting the cavity modes. Increasing the distance between nanostructures allows a higher portion of light to enter the cavity and hybridize with the LSPR mode of the nanodisks. This results in a redshift of the plasmon band and an enhancement of the *Q*-factor. Consequently, when the pitch length is set to 200 nm, the *Q*-factor increases to 37, and the plasmon band redshifts into the UVC region at 273 nm. However, further increasing the pitch causes the *Q*-factor to decrease, as a significant portion of the energy can radiate out of the cavity. Hence, adjusting the pitch length of the array allows the tuning of the resonance spectral position within the UV range, although at the cost of affecting the *Q*-factor.

The relationship between the disk diameter and the *Q*-factor was also investigated, as shown in Figure 5.7. The pitch was maintained at a value of 200 nm, as it resulted in plasmon resonances with the narrowest FWHM. The parameters of h_{Si} = 130 nm and h_{SiO2} = 300 nm were fixed. Figure 5.7(a),(b) depict the simulated and experimental reflectance data, respectively, showcasing the results when the disk diameter is varied from 100 nm to 150 nm. The representative SEM images of the arrays are shown in Figure 5.7(c).

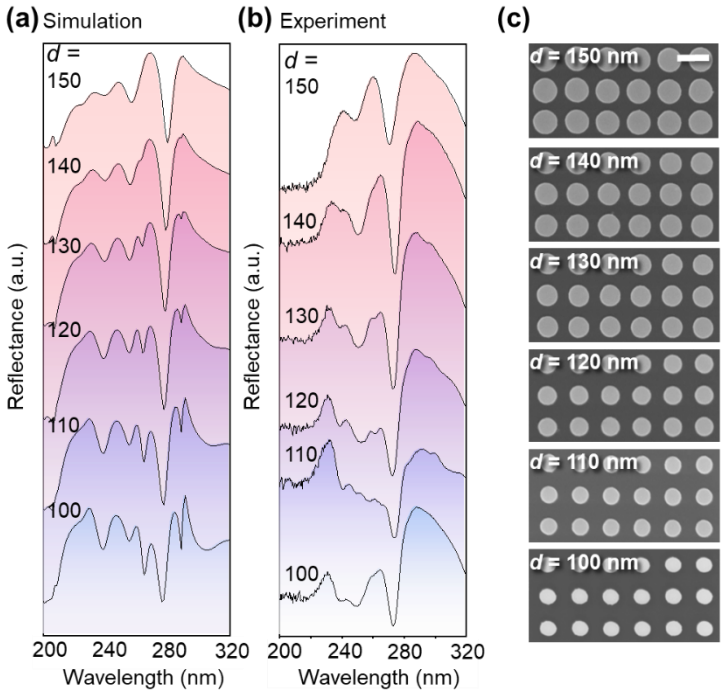

Figure 5.7. Theoretical and experimental characterization of Si nanodisk IBP arrays. (a) Simulated and (b) experimental reflectance spectra of Si nanoarrays with p = 200 nm, h_{Si} = 130 nm and h_{SiO2} = 300 nm, as the diameter (d) is varied from 100 nm to 150 nm. (c) Corresponding SEM images of the arrays, showcasing disks with diameters ranging from 100 nm to 150 nm. The scale bar corresponds to 100 nm.

Variation of the disk diameter showed little influence on the spectral position of the plasmon resonance dip, observed at ca. 273 nm. The same behaviour was observed at different pitch lengths, as shown in Figure A3.4. It is noted that the simulated reflectance exhibits better resolution of the features compared to the experimental results. This is due to the UV objective's numerical aperture of 0.20, which has an incident angle in the range of –11.5 º to 11.5 º, wider than the normal incidence condition used in simulation. Nevertheless, the resolution of the simulated reveals that reducing the disk diameter from 150 nm to 100 nm introduces multiple additional dips in the spectrum that gradually spread apart. These results

further suggest that the resonance dip is less influenced by the LSPR on the nanodisk, and is likely dominated by other components of the system.

To further investigate the origin of these resonances, a disk diameter of 100 nm was selected, with p = 200 nm, h_{Si} = 130 nm and h_{SiO2} = 300 nm. This array displayed the sharpest features in the simulated reflectance spectrum and a near-zero reflectance value at the resonance dip at 276 nm (Figure 5.8)

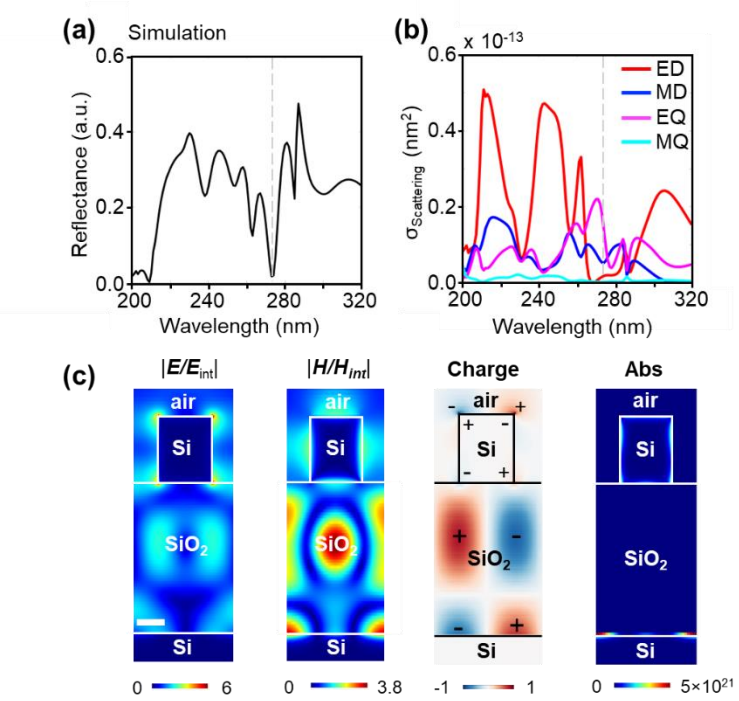

Figure 5.8. (a) Simulated reflectance spectra of the array with p = 200 nm, h_{Si} = 130 nm, h_{SiO2} = 300 nm and d = 100 nm, and (b) the corresponding multipolar decomposition of the scattering cross section ($\sigma_{scattering}$), showing the contribution of the electric dipole (*ED*), magnetic dipole (*MD*), electric quadrupole (*EQ*) and magnetic quadrupole (*MQ*) modes as a function of wavelength. (c) From left to right: simulated spatial distribution of the electric $|\boldsymbol{E}/\boldsymbol{E}_{int}|$ and magnetic $|\boldsymbol{H}/\boldsymbol{H}_{int}|$ fields, as well as the charge distribution and total power absorption (Abs) across the *x*-*z* plane of the disk of the same array, at 276 nm. The scale bar corresponds to 100 nm.

The theoretical reflectance intensity at the resonance dip at 276 nm was calculated to be 1.5%, under the normal incidence condition. However, the experimental measurements yielded a higher value of ~19%, likely due to the limitations of the UV objective used in experiments. To understand the origin of the low intensity band, the multipolar decomposition of the scattering cross-section was calculated. An electric quadrupole (*EQ*) was revealed that dominates the decomposition spectrum around the reflectance dip at 276 nm (Figure 5.8(b)). Analysis of the mode pattern distributions at this wavelength agreed well with the calculation results (Figure 5.8(c)). The spatial distribution of the electric field $|\boldsymbol{E}/\boldsymbol{E}_{\text{int}}|$ shows a hybridized mode pattern, where the electric field is localized at the top and bottom edges of the Si antenna surface, and confined within the cavity in a donut-like shape, distinct from the typically observed standing wave mode pattern in photonic cavities.[157] As expected, the $|\boldsymbol{H}/\boldsymbol{H}_{\text{int}}|$ intensity exhibits an opposing field distribution due to the interrelation of the electric and magnetic field vectors.[133] The charge density distribution pattern further supports the results obtained by the multipolar decomposition calculations, and provides an explanation for the near-zero reflectance observed. The top and bottom edges of the Si nanodisks show an *EQ* distribution, while the cavity confines strong opposing charges. Consequently, the opposing charges in both the Si disk and the cavity cancel each other, resulting in a nearly dark mode and minimal scattering into the far-field.

To investigate the absorption behaviour of the array, the distribution pattern of the total power absorption at this wavelength was also simulated. The results show that most of the absorption is localized along the walls of the Si disk (see Figure 5.8(c)). However, it was found that the absorption within the Si nanodisk is low, as also demonstrated by the simulated absorption spectrum of the array (Figure 5.9).

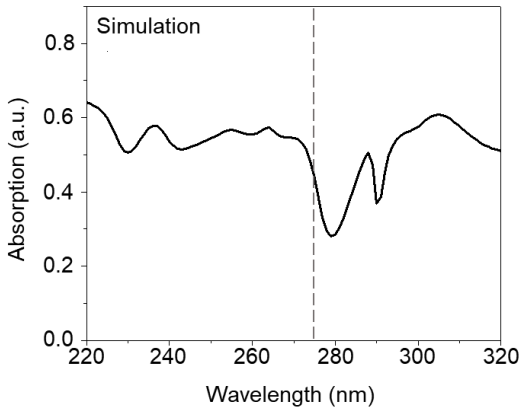

Figure 5.9. FDTD simulation of the absorption of an array with h_{Si} = 130 nm, p = 200 nm, d = 100 nm and h_{SiO2} = 300 nm. The dashed line corresponds to the wavelength of the reflectance dip for this array.

The absorption at the resonance wavelength of 273 nm has a value of ~0.5, which is lower than anticipated based on the reflectance results. This may be attributed to Si being a being a high loss material, thus a portion of the light may propagate away along the plane of the surface instead.[133]

5.3.3 Switching between narrow and broadband resonances

In the following section, the impact of varying the height of the Si disk examined. Specifically, the geometric parameters that facilitate the transition from sharp to broad reflectance bands are discussed.

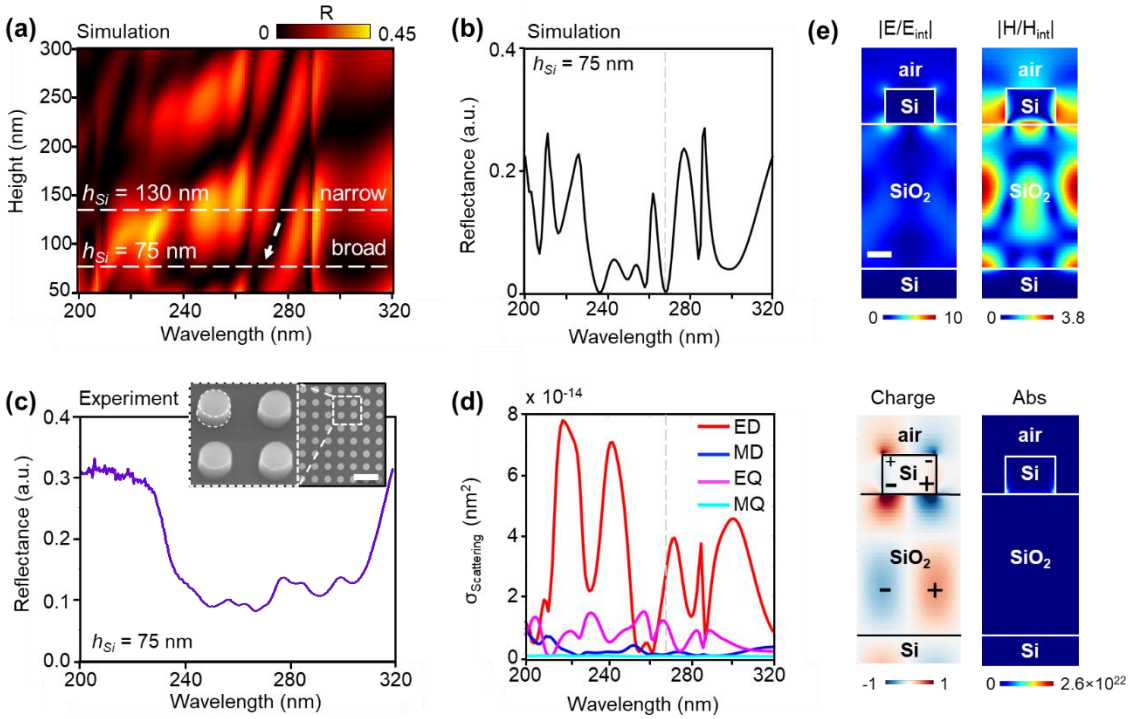

Figure 5.10. Transition from sharp to broad reflection band via geometry engineering. (a) Simulated reflectance of an array with d = 100 nm, p = 200 nm and h_{SiO2} = 300 nm, showing the narrowing and broadening of the resonance dip as a function of the Si nanostructure height. (b) Simulated reflectance spectra for the array with Si height of 75 nm, and (b) the corresponding experimental reflectance. The inset shows the SEM images of the array from the top and at a 30º tilt angle. The scale bar represents 250 nm. (d) Multipolar decomposition calculations of the scattering cross sections ($\sigma_{\text{scattering}}$) of the electric dipole (*ED*), magnetic dipole (*MD*), electric quadrupole (*EQ*) and magnetic quadrupole (*MQ*) modes. (e) The $|\boldsymbol{E}/\boldsymbol{E}_{\text{int}}|$ and $|\boldsymbol{H}/\boldsymbol{H}_{\text{int}}|$ field intensity distributions of the cross-section of the Si nanodisk, as well as the charge and total power absorption distribution across the *x*-*z* plane, at the excitation wavelength of 268 nm. The scale bar corresponds to 50 nm.

Figure 5.10(a) illustrates the simulated reflection as a function of the Si disk height for an array with d = 100 nm and p = 200 nm. As the disk height varies, the reflectance spectrum changes significantly. In particular, the bands transition from narrow to broad linewidths as the height is decreased from 130 nm to 75 nm, and from 250 nm to 170 nm. When the Si height is reduced

to 75 nm, several notable changes occur in the reflection spectrum (Figure 5.10(b)). The plasmonic feature is shifted to 268 nm, while the additional features become broader with reduced reflectance intensity. The experimental measurements were unable to provide the same resolution of these bands (Figure 5.10(c)). Nevertheless, the broad dip exhibits a significantly low reflection intensity of ~10 %, spanning the UV region from 235 nm to 310 nm.

To investigate the origin of these bands, multipolar decomposition of the scattering cross section was carried out. It was found that due to the smaller Si height, the electric dipole (*ED*) becomes the dominant mode in the scattering cross section, as shown in Figure 5.10(d). Examining the electric $|\boldsymbol{E}/\boldsymbol{E}_{\text{int}}|$ and magnetic field $|\boldsymbol{H}/\boldsymbol{H}_{\text{int}}|$ distribution patterns at 268 nm reveal that the electric field intensity is highest at the bottom edge of the nanodisk, with reduced field intensity within the cavity. However, the interaction between the cavity mode and the LSPR mode can still be observed. Consequently, the charge distribution image shows that a strong dipole manifests towards the bottom half of the Si nanodisk.

The intensity of the total power absorption was higher in regions where near-field enhancement occurs. However, the calculated absorption within the nanodisk was found to be low, as shown in the absorption spectrum in (Figure 5.11).

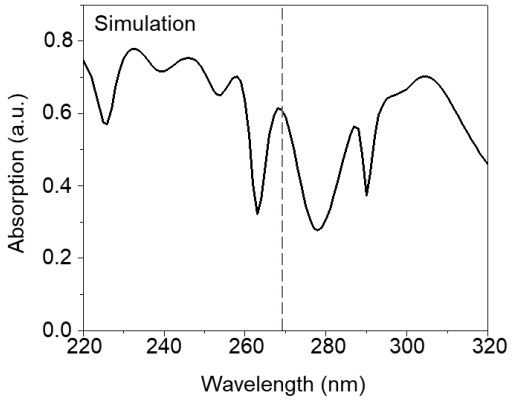

Figure 5.11. FDTD simulation of the absorption of an array with h_{Si} = 75 nm, p = 200 nm, d = 100 nm and h_{SiO2} = 300 nm. The dashed line corresponds to the wavelength of the reflectance dip for this array.

The total power absorption at the resonance wavelength of 268 nm was ca. 0.6, slightly higher than the results obtained from the arrays with a disk height of 130 nm, discussed previously. However, the overall absorption within the same UV range was higher.

5.3.4 Enhanced absorption capability of the array

To demonstrate the effect of using the high *Q*-factor Si arrays in combination with a UV-absorbing material, the arrays were coated with a lignin-modified polymer (Figure 5.12). The lignin copolymer (lignin-PEG, Figure 5.12(b)), was synthesized according to the method outlined by P. Y. M. Yew et al and was provided by collaborators.[320]

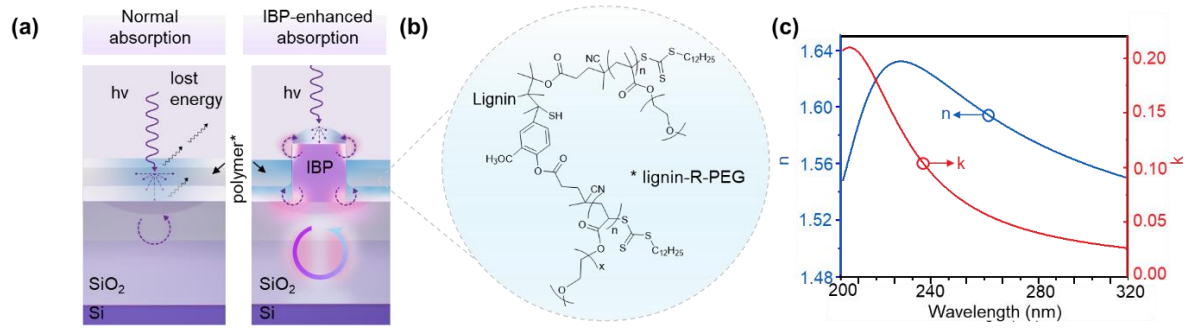

Figure 5.12. (a) Illustration of the absorption of incident light by the lignin-PEG polymer film on the flat surface and on top of the Si nanodisk array. (b) Chemical structure of the lignin-PEG polymer. (c) The refractive index (*n*) and extinction coefficient (*k*) of the lignin-PEG film, obtained from spectroscopic ellipsometry measurements.

Due to the network of aromatic rings in lignin, the polymer exhibits a strong absorption at ~273 nm, which coincides with the spectral position of the plasmon dip for the Si arrays with d = 130 nm, p = 200 nm and h_{SiO2} = 300 nm. Therefore, its optical properties make it suitable to study its interaction with the IBP resonances.

Prior to the deposition, the Si arrays were oxygen plasma treated, then spin-coated at different rotation speeds with a solution of lignin-PEG to achieve a range of polymer thicknesses on the surface. The film thickness was determined using spectroscopic ellipsometry measurements on the flat region of the substrate, and the refractive index (*n*) and extinction coefficient (*k*) were extracted from the fitting of the experimental spectra (Figure 5.12(c)).

In Figure 5.13 (a), the experimental optical reflectance results for the array with dimensions of p = 200 nm, h_{Si} = 130 nm and d = 130 nm is presented, before and after the deposition of a ~55 nm thick lignin-PEG film.

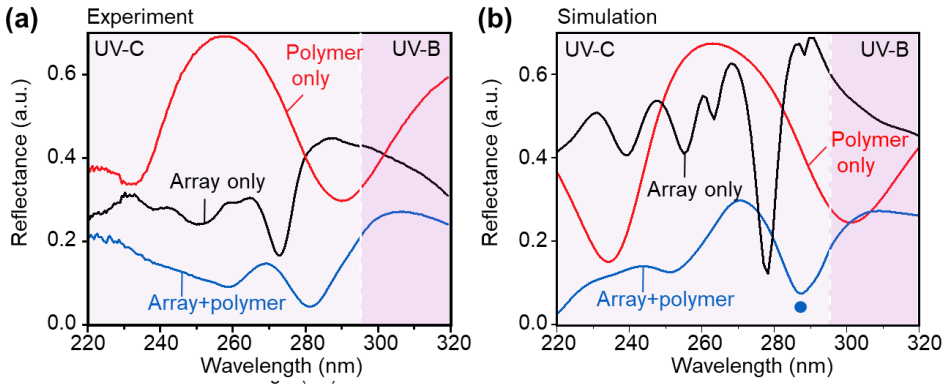

Figure 5.13. (a) Experimental and (b) simulated reflectance spectra of an array with d = 130 nm, p = 200 nm, h_{SiO2} = 300 nm and h_{Si} = 130 nm, with and without a 55 nm thick lignin-PEG films, as well as the spectrum of the polymer film alone on the flat substrate region.

The observed redshift and broadening of the plasmon dip indicate a weakly coupled interaction between the plasmon mode of the array and the excited state of the lignin-containing polymer. Most notably, the resonance band of the coupled system reaches near-zero reflectance values, significantly lower than those of the individual array or polymer films alone. On a clean array, 17% of the UV light is reflected back at the plasmon dip wavelength, while addition of 55 nm of lignin-PEG reduces this value to ~ 4%. Significantly, the introduction of nanoantenna results in the suppression of the UV light reflectance of the lignin-PEG polymer by 7.5-fold. To further analyse the optical properties of the polymer-coated arrays, FDTD simulations were performed based on the n and k values extracted from the ellipsometry measurements, as shown in Figure 5.13(b). Compared to the experimental results, the theoretical calculations showed a smaller change in the reflectance intensity following the addition of the polymer. Specifically, the intensity at the plasmon dip wavelength for the clean array was 9%, which was reduced to 5% after the introduction of the 55 nm lignin-PEG film.

Examining the spatial distribution of the mode pattern at 287 nm revealed a notable difference in the electric and magnetic field distributions after addition of the lignin copolymer film (Figure 5.14).

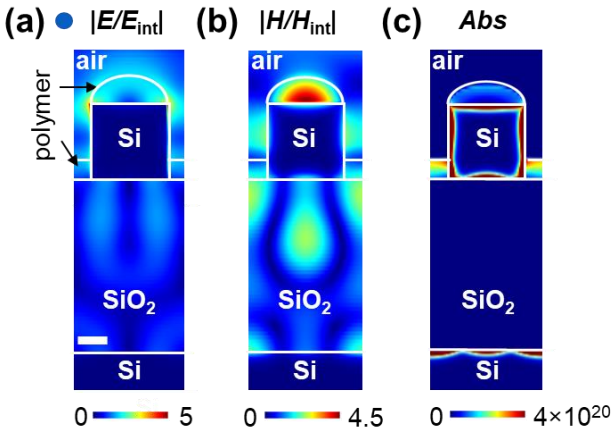

Figure 5.14. The simulated spatial distribution of the (a) electric field $|\boldsymbol{E}/\boldsymbol{E}_{int}|$ and (b) magnetic field $|\boldsymbol{H}/\boldsymbol{H}_{int}|$ intensity, as well as (c) the total power absorption distribution at the cross-section of the nanodisk with 55 nm lignin-PEG coating on top, at the wavelength of 287 nm for an array with d = 130 nm, p = 200 nm, h_{SiO2} = 300 nm and h_{Si} = 130 nm.

An increased total power absorption was observed within the polymer layer and at the edges of the nanodisk. Consequently, the overall absorption of the material was enhanced, accompanied by a decrease in the reflected light at the plasmon resonance. The effect of the reflectance reduction was observed experimentally using the arrays with diameters ranging from 100 nm to 150 nm after the coating process (Figure 5.15).

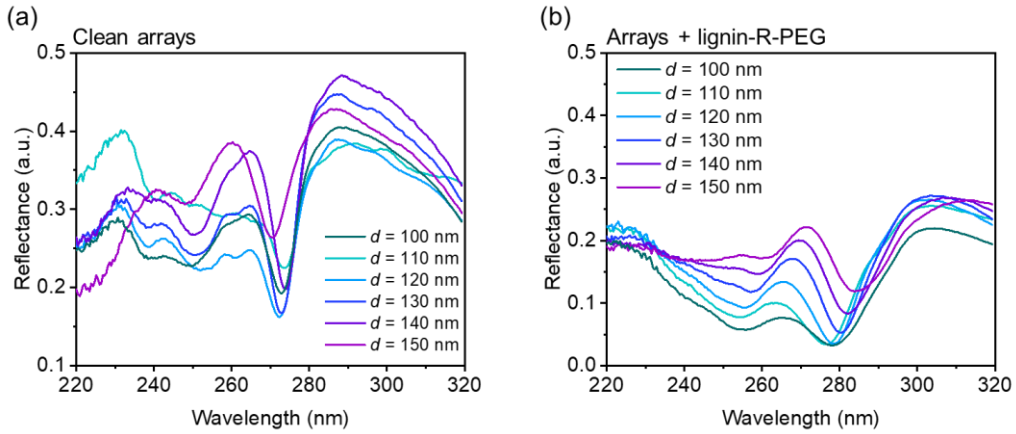

Figure 5.15. Experimental reflectance spectra of arrays with geometrical parameters of h_{Si} = 130 nm, p = 200 nm and h_{SiO2} = 300 nm, while varying the diameter from d = 100 nm to d = 150 nm when the surface is (a) clean, without any polymer added, and (b) after coating with 55 nm lignin-R-PEG.

However, when the nanodisk height is reduced to 75 nm, the coating of the arrays resulted in in the increase of the overall reflectance compared to the bare array. Figure 5.16 shows the experimental reflectance of the array with d = 100 nm, p = 200 nm, h_{SiO2} = 300 nm and h_{Si} = 75 nm before and after the coating with 55 nm lignin-PEG.

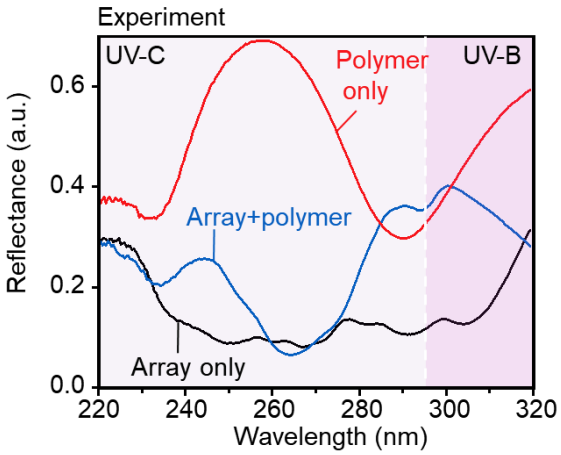

Figure 5.16. (a) Experimental reflectance spectra of an array with d = 100 nm, p = 200 nm, h_{SiO2} = 300 nm and h_{Si} = 75 nm, with and without a 55 nm thick lignin-PEG films, as well as the spectrum of the polymer film alone on the flat substrate region.

The reflectance within the UV region was higher after the coating process, with little change in the values around the resonant wavelength at ca. 268 nm. Therefore, absorption of these arrays with the lignin-PEG requires further investigation in future work.

Nonetheless, it was demonstrated that the quality of the plasmonic resonance can be significantly enhanced by leveraging the hybridization of plasmonic and cavity modes. Therefore, the use of Si nanostructures offer can similar plasmonic properties in the UV region as conventional plasmonic materials do in the visible region.

5.4 Conclusions

In conclusion, it was found that the combination of a SiO_2 cavity with a Si disk array enables the tunability of the plasmonic properties of the system due to the coupling between the LSPR modes and the cavity modes. The *Q*-factor of the plasmon resonance of nanoantenna can be significantly improved from ~1 to ~43 by variation of the cavity thickness. Additionally, the spectral position of the plasmon band can be fine-tuned by altering the pitch length between the nanostructures, while modifying the height of the disks allowed for switching between sharp and broad resonances, enabling near-zero reflectance values of ~ 4%. Using experimental measurements and FDTD simulations, the absorption enhancement capabilities of Si arrays coated with a UV-absorbing lignin-PEG polymer has been explored. The data revealed that the introduction of the Si nanoarray led to a stronger confinement of the electric field within the lignin-PEG layer. Consequently, this behaviour resulted in a reduction of the overall reflectance of the material by 7.5-fold. On the other hand, the absorption properties of the arrays are require further investigation in future work. Nonetheless, these results highlight the potential of Si nanodisk arrays as IBP materials. Moreover, Si nanodisk arrays of this nature

can potentially be utilized in UVC specific applications, such as investigations of germicidal mechanisms,[322,323] enhancement of light-absorption,[324,325] UV sensors or photodetectors.[326–329]

Conclusions and future work

In this thesis, the development of nanostructured materials that regulate light-matter interactions was discussed. In nature, light-harvesting complexes are organised by peptide scaffolds, which regulate efficient long-range transport of excitons. **Chapter 3** introduced the design of biomimetic materials inspired by pigment-protein complexes. Plexcitonic antenna complexes were synthesised, in which the scaffold is a surface-grafted PCysMA chain. To control the initiator concentration ($\chi_{Br(Au)}$) on gold surfaces, the initiator (DTBU) was co-adsorbed with an inert thiol (11-MUL) from solutions containing various ratios of the two adsorbates ($\chi_{Br(sol)}$). XPS studies showed the 11-MUL has a slight competitive advantage in the adsorption process due to its smaller size compared to the bulkier DTBU initiator disulfides. Thus, the observed relationship between $\chi_{Br(sol)}$ and $\chi_{Br(Au)}$ was non-linear. Nevertheless, the method was found to provide an effective way to regulate the density of the surface-grafter polymers. The variation of the polymerisation time and the grafting density allowed the synthesis of pCysMA brushes with controllable densities and thicknesses. The polymer height reached its maximum at the polymerisation time of 45 min, at which the thickness of a fully dense brush was 36 ± 5 nm, decreasing to 20 ± 3 nm for $\chi_{Br(Au)} = 0.47 \pm 0.11$. For $\chi_{Br(Au)} = 0.39 \pm 0.07$ and 0.26 ± 0.05 the film thicknesses were 8.5 ± 1 nm and 5.9 nm, respectively.

Subsequent to the polymerisation, the surface-grafted polymers were derivatised with Chl. Chlorophyll *a* was extracted from spinach and modified to contain an active ester functionality. The pigment was coupled to the PCysMA films via EDC/NHS coupling, and chemical state analysis of the systems was carried out using XPS characterisation. The XPS analysis showed that the Chl binding increases when the grafting density is $\chi_{Br(Au)} < 0.39 \pm 0.07$, with ca. 1 Chl for every 2.6 monomer units in the film. The films were characterised as a function of depth

using XPS depth profiling with Ar_{3000}^+ and Ar_{2000}^+ gas clusters. The analysis indicated that thin layers can be removed from the surface without altering the chemical state of the film. A correlation between the grafting density and the extent of pigment binding as a function of depth was revealed. In fully dense brushes, there was preferential binding towards the top layers of the brush. In contrast, the Chl concentration in reduced density films remains constant as a function of depth. The depth-profile analysis revealed that reduced density films could accommodate four times more Chl in comparison to fully dense brushes. This highlights that regulating the surface density allows control over Chl concentration onthe surface. To investigate the plasmon-exciton coupling capabilities of these systems, plexcitonic complexes were synthesized on plasmonic nanostructured gold surfaces. Examination of the extinction spectra demonstrated a direct correlation between the scaled coupling energy and the grafting density, thus confirming the results from the XPS analysis. When the grafting density was reduced, the concentration of excitons within the plasmon mode volume increased. Consequently, when the polymer density was reduced from $\chi_{Br(Au)}$ = 1.00 to 0.47 at 30 min polymerization time, the scaled coupling energy increased from ~0.1 eV to 0.46 eV. Therefore, the coupling energy could be controlled by adjusting the polymer grafting density. These studies highlight that the quantification of the extent of Chl functionalisation in the polymers using conventional XPS measurements is limited. XPS depth profiling, on the other hand, offers a more accurate analysis of the Chl concentration within the film volume. It is concluded that surface-grafted polymers enable the programmable organisation of pigments in three dimensions, thus providing a means to control plasmon-exciton coupling in these systems.

In future work, the use of alternative light-harvesting molecules could be explored. While Chl is a key component in photosynthesis, its synthetic modification typically results in low yields, limiting its scalability for applications. However, various commercially available dyes could be investigated as an alternative in these polymer systems, offering simpler synthetic routes.

For instance, rhodamine dyes exhibit a strong absorption around 550 nm. Spectrally tailoring the plasmonic surfaces to match the absorption of the dye could enable strong plasmon-exciton coupling.[330] Furthermore, the current approach that involves polymer growth from gold nanostructures on planar surfaces limits the available volume of the plasmon mode. Consequently, pigments located outside this region are unable to strongly couple with the LSPR and are underutilized within the system. The design principles presented here could be extended to plasmonic gold nanoparticles. Surface-grafted polymer brushes functionalized with dyes on plasmonic nanoparticles could yield materials that are suitable for spin-coating onto surfaces. The multilayers of nanoparticles would increase the available plasmon mode volume on the surface, potentially achieving extended plasmon-exciton coupling.

Chapter 4 focussed on addressing the challenges associated with the post-synthesis tuneability of the emission wavelength of perovskite nanoparticles. Existing methods in the literature involve invasive techniques, resulting in broad emission linewidths and reduced PL brightness. To address this issue, the chapter examined the use of a photonic nanostructure array to interact with perovskite excited states via the Purcell effect. Asymmetrical Si nanoellipse pair arrays were fabricated using EBL. The broken in-plane symmetry gave rise to polarization-controlled q-BIC resonances, which spectral position could be tuned from 690 nm to 804 nm under *y*-polarization, and from 638 nm to 696 nm under *x*-polarization, by variation of the nanoellipse size. $FAPbI_3$ perovskite nanoparticles with an emission at 755 nm were deposited on the arrays. It was found that the Purcell interaction can be regulated by the spectral overlap between the q-BIC resonance and the perovskite emission band by leveraging the variability of q-BIC resonance energy. Consequently, PL mapping measurements revealed that a PL tuning range of ~39 nm can be achieved. Furthermore, switchable emission wavelengths of up to 10 nm were observed by altering the polarization state of the pump laser. The maximum PL enhancement observed was 21-fold, accompanied by a reduction in emission linewidth by

~27% under *y*-polarization. Meanwhile, experimental and theoretical investigations of PL lifetime revealed a 6.7-fold enhancement of the spontaneous radiative decay rate. The discrepancy compared to PL mapping measurements was attributed to enhanced pump laser absorption by the arrays. In summary, this study demonstrated a non-invasive approach to modify perovskite emission properties in ambient conditions. The wavelength shift achieved was higher than the current state-of-the-art that relies on a similar principle,[296] with an added tunability element via the polarization state switching of the pump laser. These findings hold promise for various tuneable light-emission application, particularly in the design of wavelength-tunable single-photon sources.

These studies could be extended by improving the nanoantenna design in order to increase the Purcell factor. In the work presented here, the use of *y*-polarization conditions results in the excitation of two q-BIC resonances with overlapping bands in the reflectance spectrum. While this is useful to realise spectral bands in the red spectral region (and thus ensure overlap with the perovskite emission band), a better resolution of the individual q-BIC resonances could lead to an improvement of the maximum possible Purcell factor. Future work could focus on the development of a nanostructure design supporting single high *Q*-factor q-BIC resonances. Furthermore, polarization-dependent resonant modes that are further apart in energy could promote a higher separation of the potential radiative decay channels for the perovskite excited state. Studying these effects using a range of perovskite materials emitting at different wavelengths would allow a more comprehensive determination of the emission tuning capabilities of this design. For practical applications, the use of different surface coatings and encapsulation methods could be explored to avoid degradation of the perovskite material over time.

While Si nanoellipse pairs exhibit q-BIC resonances in the visible spectral range, employing an alternative Si nanostructure design allows for the realization of plasmonic resonances within the UV region due to strong interband transitions. IBP materials hold potential as promising candidates for applications in UV-plasmonic technologies. However, large intrinsic losses result in low *Q*-factors for their plasmonic resonances. **Chapter 5** focused on the fabrication of Si nanodisk arrays that support plasmonic resonances in the UV region with improved *Q*-factors. The Si nanodisk arrays were fabricated using EBL on Si substrates with a layer of SiO_2, with the cavity thickness ranging from 100 nm to 300 nm. The interaction between the LSPR mode on the Si nanodisk and the cavity modes were investigated using experimental and theoretical reflectance measurements. The arrays showed resonance dips in the reflectance ranging from ~270 nm to ~280 nm, depending on the thickness of the cavity. It was demonstrated that increasing the cavity height to 300 nm improves the *Q*-factor of the plasmonic feature from ~1 to ~43. FDTD studies of the mode pattern distributions revealed that the tunability of the plasmonic properties can be attributed to the coupling between the LSPR modes and the cavity modes. In addition, mode decomposition calculations of the scattering cross section revealed that arrays with p = 200 nm, h_{Si} = 130 nm, h_{SiO2} = 300 nm and d = 100 nm exhibit a strong electric quadrupole mode around the reflectance dip. The spectral position of the plasmon band was tuned by altering the pitch length between the nanostructures. Furthermore, the broadness of the resonance bands could be modified by variation of the nanodisk height. The arrays with disk height of 75 nm demonstrated a low reflection intensity of ~10 %, spanning from 235 nm to 310 nm. To investigate the combination of high *Q*-factor Si arrays with a UV-absorbing material, the arrays were coated with lignin-PEG polymer. Experimental measurement showed a 7.5-fold reduction of the reflectance intensity, while the FDTD results demonstrated a stronger confinement of the electric field within the lignin-PEG layer. However, the simulated total power absorption did not show a significant enhancement

in the absorptance spectra before and after the coating. Thus, the absorption mechanism of these arrays remains unclear and requires further investigation. In conclusion, it was demonstrated that the hybridisation between the LSPR modes on the nanodisk array and the SiO_2 cavity modes can significantly improve the *Q*-factor of the plasmon resonances within the UV region. These findings highlight the potential of Si as an IBP material, with potential possible applications in UV sensors and photodetectors.

The primary aim of this study was to design Si nanoarrays with improved *Q*-factors. While this goal was successfully achieved, the underlying mechanisms that enable the sharpening of the resonances require further investigation. In particular, since the Si substrate serves as a backside reflector for the cavity system, the mirror image of the nanodisk could potentially play an important role in the overall hybridisation process. Investigating the design with Al as the backside reflector, given its high reflectivity within the UV region, could yield valuable insights. Furthermore, the simulation of the absorption mechanisms of these arrays could be refined. While total power absorption has been calculated using FDTD, obtaining additional simulated data of the electric field intensity would enable the conversion of these results into absorption values. This approach would provide a more comprehensive understanding of the absorption behaviour of the arrays, particularly when combined with the UV-absorbing lignin-PEG material.

Appendix 1 - Chapter 3

DTBU					
Region	**Position**	**FWHM**	**Line shape**	**Area**	**% Atomic composition**
C1s	285	1.35	GL(30)	9343.58	78.72
C1s	286.9	1.35	GL(30)	1701.85	14.32
C1s	289.1	1.35	GL(30)	827.2	6.95
O1s	532.18	1.59	GL(30)	7063.33	76.02
O1s	533.58	1.59	GL(30)	2229.29	23.98
S2p	162.44	1.1	GL(30)	707.58	62.45
S2p	163.79	1.1	GL(30)	425.92	37.55

Table A1.1. XPS fitting details of a SAM of DTBU, presented in Figure 3.2(a).

11-MUL					
Region	**Position**	**FWHM**	**Line shape**	**Area**	**% Atomic composition**
C1s	285	1.26	GL(30)	21089.54	83.70
C1s	286.8	1.26	GL(30)	3380.42	13.43
C1s	288.4	1.26	GL(30)	722.35	2.87
O1s	533.0	1.55	GL(30)	9714.50	90.61
O1s	531.7	1.55	GL(30)	1006.54	9.39
S2p	162.2	0.84	GL(30)	1331.49	61.03
S2p	163.4	0.84	GL(30)	850.44	38.97

Table A1.2. XPS fitting details of a SAM of 11-MUL, presented in Figure 3.2(b).

DTBU + 11-MUL, $\chi_{Br(Au)}$ = 0.52					
Region	**Position**	**FWHM**	**Line shape**	**Area**	**% Atomic composition**
C1s	285	1.26	GL(30)	13335.88	84.87
C1s	286.8	1.26	GL(30)	1834.13	11.68
C1s	289.2	1.26	GL(30)	540.50	3.44

Table A1.3. XPS fitting details of a SAM of DTBU + 11-MUL, with $\chi_{Br(Au)}$ = 0.52, presented in Figure 3.2(c).

DTBU + 11-MUL, $\chi_{Br(Au)}$ = 0.40

Region	Position	FWHM	Line shape	Area	% Atomic composition
C 1s	285	1.19	GL(30)	14946.97	84.72
C 1s	286.72	1.19	GL(30)	1919.14	10.88
C 1s	288.66	1.19	GL(30)	773.98	4.39

Table A1.4. XPS fitting details of a SAM of DTBU + 11-MUL, with $\chi_{Br(Au)}$ = 0.40, presented in Figure 3.2(c).

DTBU + 11-MUL, $\chi_{Br(Au)}$ = 0.26

Region	Position	FWHM	Line shape	Area	% Atomic composition
C1s	285	1.23	GL(30)	22898.11	84.24
C1s	286.7	1.23	GL(30)	3795.67	13.97
C1s	289.1	1.23	GL(30)	484.00	1.78

Table A1.5. XPS fitting details of a SAM of DTBU + 11-MUL, with $\chi_{Br(Au)}$ = 0.26, presented in Figure 3.2(c).

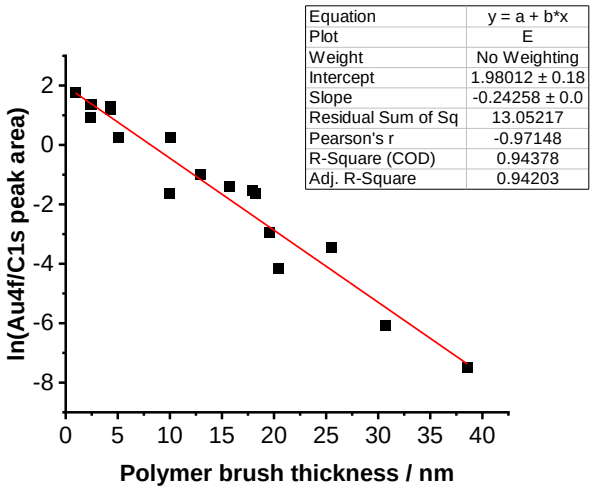

Figure A1.1. Calibration profile for dry thickness determination of full density brush films using XPS analysis. The natural logarithm of $Au4f_{7/2}$/C1s peak area ratio extracted from the high-resolution narrow spectra as a function of the polymer dry brush thickness determined by spectroscopic ellipsometry. The data was fitted with a straight line.

		Chl			
Region	**Position**	**FWHM**	**Line shape**	**Area**	**% Atomic composition**
Zn 2p	1045.11	3624.34	1.48	LA(1.4,2,2)	1.14
Zn 2p	1022.04	7195.4	1.48	LA(1.4,2,2)	2.29
O 1s	533.8	2649.51	1.89	GL(30)	5.17
O 1s	535.43	350.35	1.89	GL(30)	0.68
O 1s	532.43	2649.44	1.89	GL(30)	5.17
N 1s	398.49	2077.44	1.17	GL(30)	6.21
N 1s	400.42	141.82	1.17	GL(30)	0.42
N 1s	401.69	127.87	1.17	GL(30)	0.38
C 1s	285	12109.58	1.65	GL(30)	60.13
C 1s	286.69	1842.55	1.65	GL(30)	9.15
C 1s	288.01	929.7	1.65	GL(30)	4.62
C 1s	289.43	929.7	1.65	GL(30)	4.62

Table A1.6. XPS fitting details of a drop-casted *Chl* on a gold slide, for the corresponding high-resolution spectra shown in Figure 6(a).

11-MUL + Chl					
Region	**Position**	**FWHM**	**Line shape**	**Area**	**% Atomic composition**
O 1s	534.1	2302.87	1.61	GL(30)	2.27
O 1s	531.32	696.34	1.61	GL(30)	0.69
O 1s	532.69	6064.03	1.61	GL(30)	5.97
C 1s	285	24986.14	1.37	GL(30)	68.85
C 1s	286.7	2980.85	1.37	GL(30)	8.21
C 1s	289.5	1427.57	1.37	GL(30)	3.92
C 1s	287.98	1575.56	1.37	GL(30)	4.33
Zn2p	1021.88	1382.29	1.50	LA(1.4,2,2)	0.27
Zn2p	1044.94	706.95	1.50	LA(1.4,2,2)	0.13
N 1s	400.08	2049.56	1.23	GL(30)	3.18
N 1s	398.23	1405.2	1.23	GL(30)	2.19

Table A1.7. XPS fitting details of *Chl* functionalised 11-MUL, for the corresponding high-resolution spectra shown in Figure 6(b).

Appendix 2 - Chapter 4

L (nm)	StDev (nm)	*W* (nm)	StDev (nm)
216	4	79	5
223	6	69	3
224	5	75	4
225	6	77	1
226	2	85	4
227	2	76	7
229	5	81	2
230	3	79	3
232	6	89	2
234	2	77	1
236	3	97	2
237	4	85	3
239	7	93	5
247	4	101	6
252	2	104	8
254	5	103	4

Table A2.1. Extracted *L* and corresponding *W* parameters of the nanoellipses from SEM images, including the standard deviation (StDev) within the same array for each value.

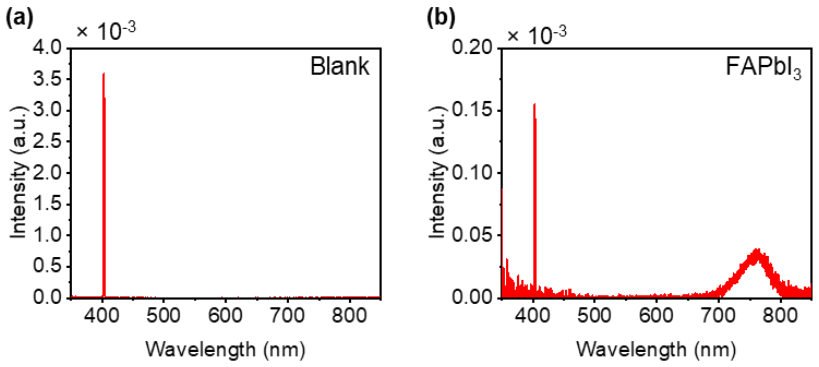

Figure A2.1. Photoluminescence measurements to derive the photoluminescence quantum efficiency (PLQE) of $FAPbI_3$ in toluene. An excitation wavelength of 405 nm was used to measure a (a) blank reference and (b) the $FAPbI_3$ solution in toluene in an integrating sphere. The PLQE was calculated by integration of the areas underneath the laser and the sample signal.

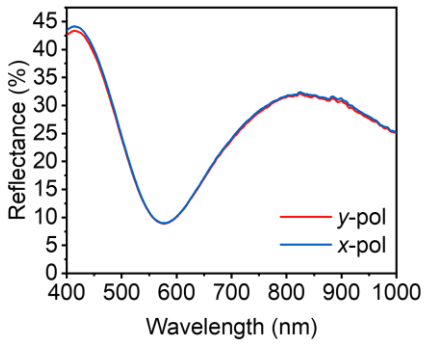

Figure A2.2. Reflectance spectrum of the flat area of the substrate with 300 nm SiO_2 overlayer, under *x*- and *y*-polarized light.

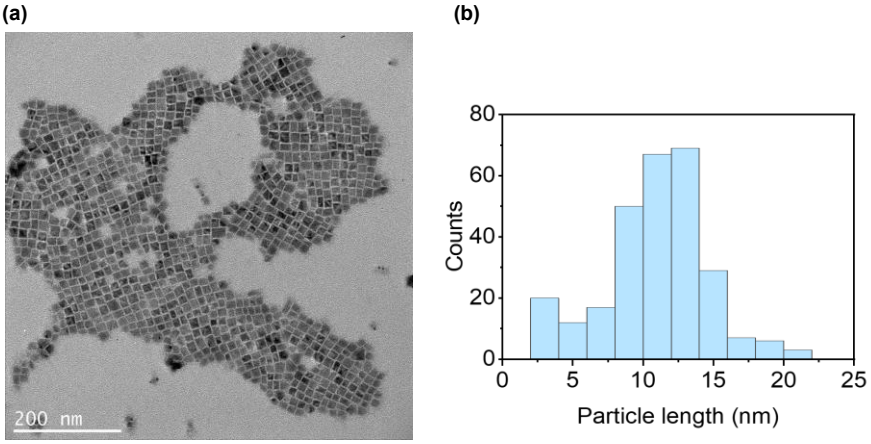

Figure A2.3. (a) Transmission electron microscope (TEM) image of formamidinium lead iodide ($FAPbI_3$) particles and (b) particle size distribution obtained from TEM images.

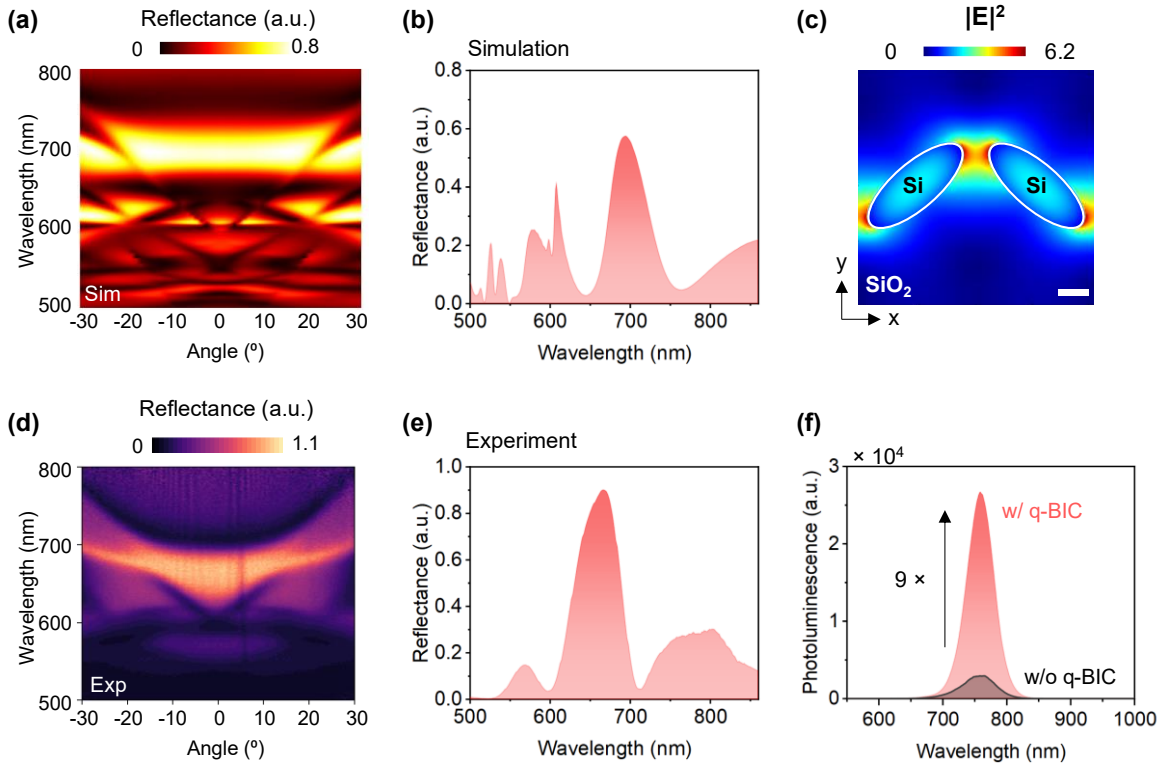

Figure A2.4. (a) Simulated angular-resolved reflectance of the array with L = 232 nm and W = 93 nm under x-polarized condition and corresponding. (b) The simulated reflectance spectra at the incident angle of 0º. (c) The electric field magnitude distribution ($|E|^2$) at λ = 693 nm for the nanoellipse pair. The scale bar corresponds to 50 nm. (d) Experimental angle-resolved reflectance of the same array with the (e) reflectance spectrum demonstrated at 0º incident angle x-polarized conditions. (f) Corresponding PL peaks of the perovskite on the nanoarray and on the reference nanodisk array without q-BIC resonances, excited with x-polarized laser.

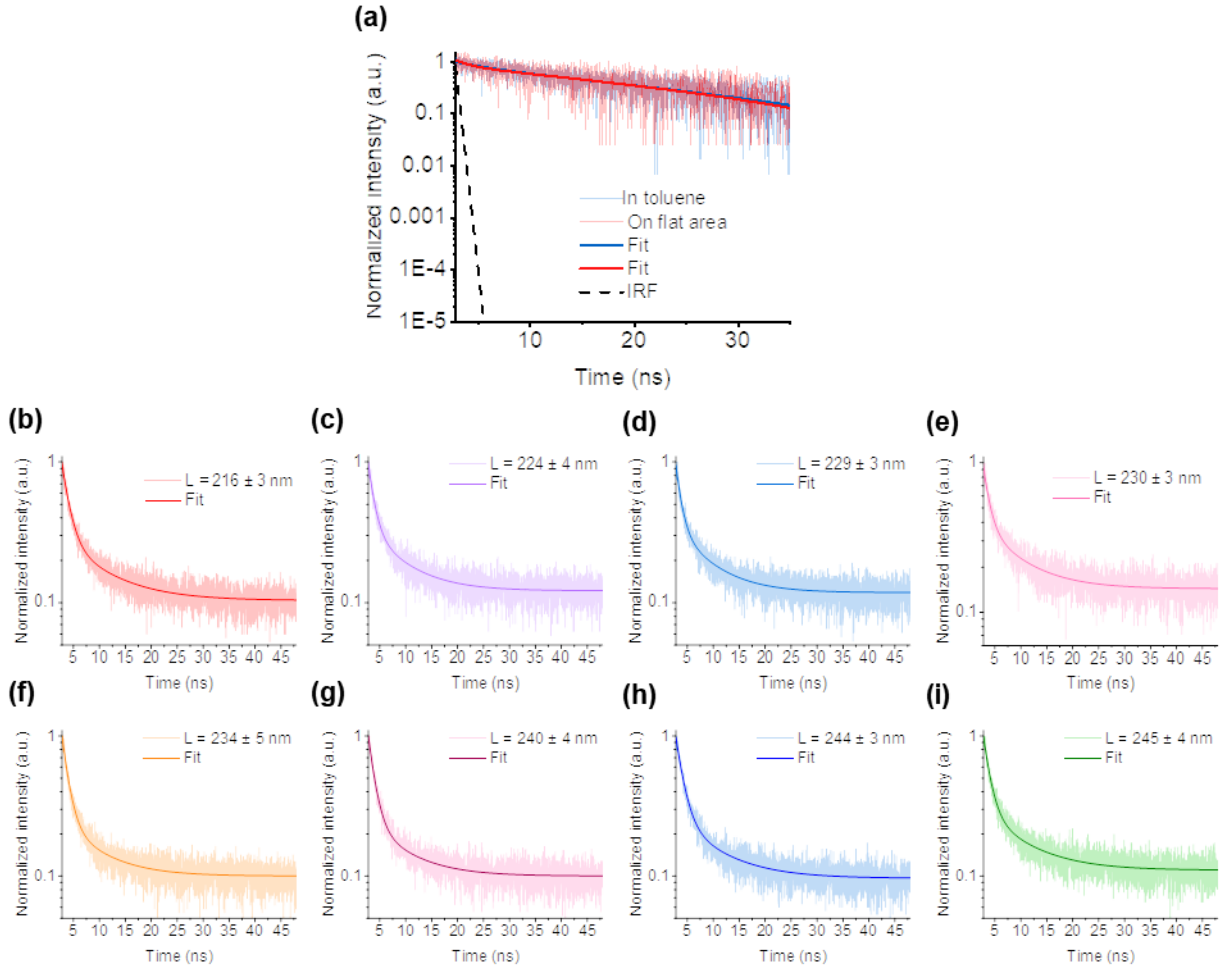

Figure A2.5. PL lifetime decay measurements of $FAPbI_3$ (a) in toluene and on the flat area of the substrate, along with the instrument response function (IRF), for reference. Spectra (b-i) shows the decay curves recorded on arrays with lengths varying from $L = 216 \pm 3$ nm to $L = 245 \pm 4$ nm.

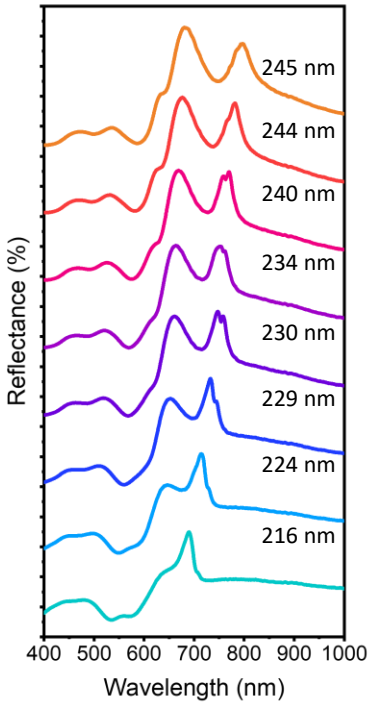

Figure A2.6. Experimental reflectance spectra of the arrays from the time-resolved PL study shown in Figure A2.6.

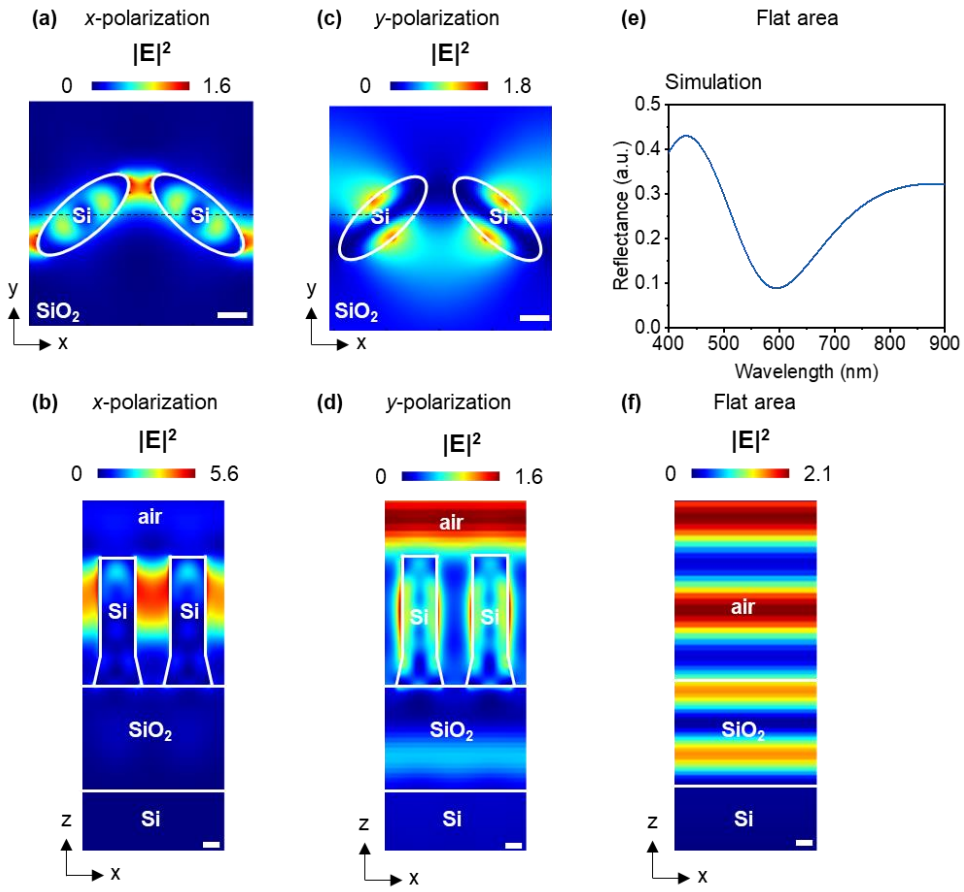

Figure A2.7. The simulated electric field magnitude distribution ($|\boldsymbol{E}|^2$) at λ = 532 nm for an array with nanoellipse pair parameters of L = 232 nm and W = 93 nm. (a) Top view of the nanoellipse pair under *x*-polarized light conditions, with the dashed line representing the cross-section that is shown in (b). (c) The top view of the same Si structures under *y*-polarized light and (d) their corresponding cross-section. (e) Simulated reflectance of the flat substrate area (results under *x*- and *y*-polarized conditions are identical) and (f) cross-section showing the distribution of the electric field magnitude ($|E|^2$) at λ = 532 nm. The scale bar corresponds to 50 nm.

Appendix 3 - Chapter 5

(a)

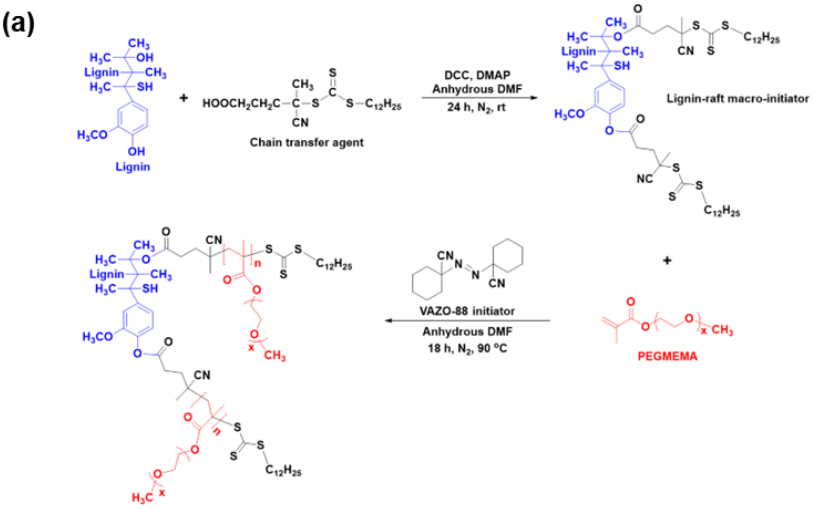

(b)

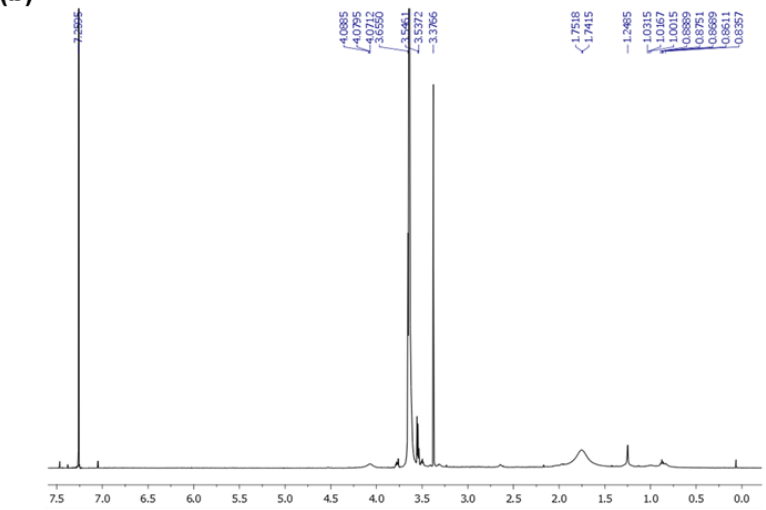

(c)

Polymers	Mn (kDa)	Mw (kDa)	Tg (°C)	Td (°C)	Particle size (nm)	PDI
Lignin-PEG950	4.5	4.7	-14	349	24	0.35

Figure A3.1. Characterization of lignin-poly(ethylene glycol) (lignin-PEG), as provided by collaborators. Further details can be found in the cited article.[320] (a) Reaction mechanism of the lignin-PEG synthesis. (b) 1H-NMR in $CDCl_3$ spectrum of lignin-PEG. Peaks attributed to lignin were detected at 3.85 ppm (methoxyl groups) and 6.85 ppm (phenyl rings). (c) Number average molecular weight (Mn), weight average molecular weight (Mw), glass transition (Tg) and thermal decomposition (Td) temperatures, particle size and the polydispersity index (PDI) of lignin-PEG.

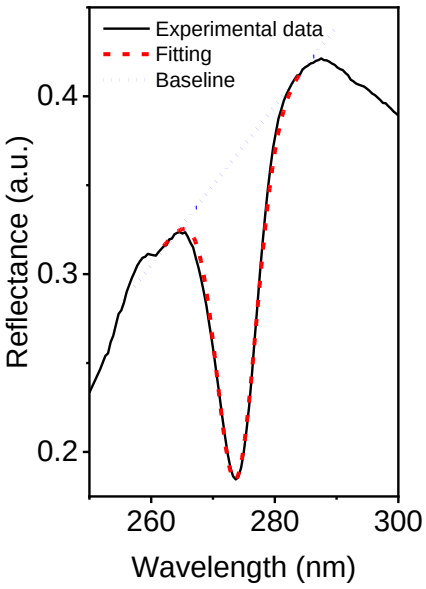

Figure A3.2. Experimental reflectance spectra for the nanodisk array with h_{Si} = 130 nm, d = 130 nm, p = 200 nm and SiO_2 layer thickness of 300 nm. The resonance dip was fitted by the standard Gaussian function by manually defining the background to connect each side of the spectral dip. A full-width-at-half-maximum of 7.4 nm was obtained with the peak maximum at 273.8 nm, which corresponds to a Q-factor of 37. The R^2 of the fitting is 0.998.

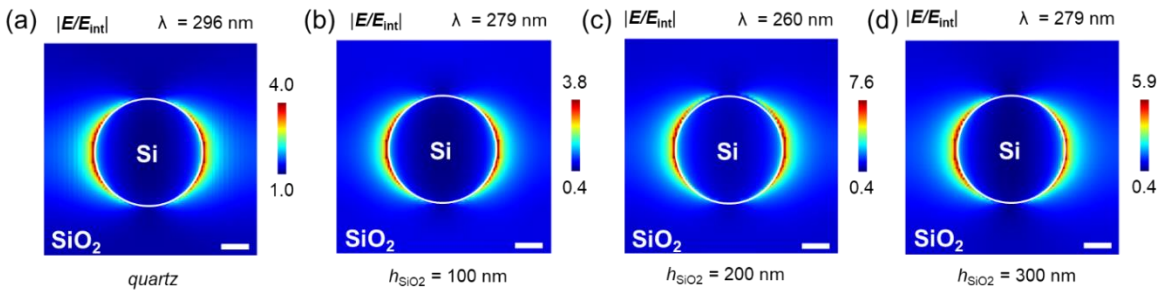

Figure A3.3. The simulated electric field magnitude distribution $|\boldsymbol{E/E_{int}}|$ from the x-y plane for c-Si nanoarrays (h_{Si} = 130 nm, d = 130 nm, p = 200 nm) on (a) quartz, (b) a 100 nm thick, (c) 200 nm and (d) 300 nm thick SiO_2 cavity. The wavelength of incident light is set to the resonance wavelength.

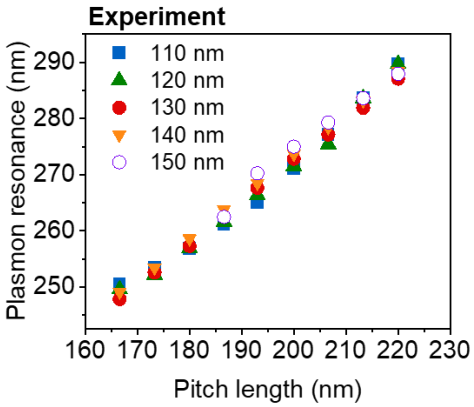

Figure A3.4. Experimental results of the spectral position of the plasmon resonance dip as a function of the pitch length for arrays with h_{Si} = 130 nm, h_{SiO2} = 300 nm and d = 130 nm and varying diameters from 110 nm to 150 nm, extracted from the reflectance measurements.

References

(1) Menzel, D. H. *Fundamental Formulas of Physics*; Menzel, D. H., Ed.; Dover Pubs: New York, 1960; Vol. 1.

(2) Andrews, D. L.; Allcock, P. *Fundamentals of Photonics and Physics*; Andrews, D. L., Ed.; John Wiley & Sons, Incorporated, 2015.

(3) Andrews, D. L.; Bradshaw, D. S. *Introduction to Photon Science and Technology*; SPIE, 2018. https://doi.org/10.1117/3.2503743.

(4) Schuller, J. A.; Barnard, E. S.; Cai, W.; Jun, Y. C.; White, J. S.; Brongersma, M. L. Plasmonics for Extreme Light Concentration and Manipulation. *Nature Materials*. Nature Publishing Group 2010, pp 193–204. https://doi.org/10.1038/nmat2630.

(5) Beliaev, L. Y.; Takayama, O.; Melentiev, P. N.; Lavrinenko, A. V. Photoluminescence Control by Hyperbolic Metamaterials and Metasurfaces: A Review. *Opto-Electronic Advances*. Chinese Academy of Sciences 2021. https://doi.org/10.29026/oea.2021.210031.

(6) Kravets, V. G.; Kabashin, A. V.; Barnes, W. L.; Grigorenko, A. N. Plasmonic Surface Lattice Resonances: A Review of Properties and Applications. *Chemical Reviews*. American Chemical Society June 27, 2018, pp 5912–5951. https://doi.org/10.1021/acs.chemrev.8b00243.

(7) Törmö, P.; Barnes, W. L. Strong Coupling between Surface Plasmon Polaritons and Emitters: A Review. *Reports on Progress in Physics*. Institute of Physics Publishing January 1, 2015. https://doi.org/10.1088/0034-4885/78/1/013901.

(8) Lu-Lin, Li, Eric Wei-Guang, D. Porphyrin-Sensitized Solar Cells. *Chem Soc Rev* **2013**, *42*, 291. https://doi.org/10.1039/c2cs35257e.

(9) Jiang, Q.; Zhao, Y.; Zhang, X.; Yang, X.; Chen, Y.; Chu, Z.; Ye, Q.; Li, X.; Yin, Z.; You, J. Surface Passivation of Perovskite Film for Efficient Solar Cells. *Nat Photonics* **2019**, *13* (7), 460–466. https://doi.org/10.1038/s41566-019-0398-2.

(10) Xue, J.; Lee, J. W.; Dai, Z.; Wang, R.; Nuryyeva, S.; Liao, M. E.; Chang, S. Y.; Meng, L.; Meng, D.; Sun, P.; Lin, O.; Goorsky, M. S.; Yang, Y. Surface Ligand Management for Stable FAPbI3 Perovskite Quantum Dot Solar Cells. *Joule* **2018**, *2* (9), 1866–1878. https://doi.org/10.1016/j.joule.2018.07.018.

(11) Khir, H.; Pandey, A. K.; Saidur, R.; Shakeel Ahmad, M.; Abd Rahim, N.; Dewika, M.; Samykano, M. Recent Advancements and Challenges in Flexible Low Temperature Dye Sensitised Solar Cells. *Sustainable Energy Technologies and Assessments*. Elsevier Ltd October 1, 2022. https://doi.org/10.1016/j.seta.2022.102745.

(12) Kozub, D. R.; Vakhshouri, K.; Kesava, S. V.; Wang, C.; Hexemer, A.; Gomez, E. D. Direct Measurements of Exciton Diffusion Length Limitations on Organic Solar Cell Performance. *Chemical Communications* **2012**, *48* (47), 5859–5861. https://doi.org/10.1039/c2cc31925j.

(13) Liu, H.; Gao, H.; Lin, J.; Hayat, T.; Alsaedi, A.; Tan, Z. Self-Assembled Bulk Heterojunctions from Integral Molecules with Nonconjugately Linked Donor and Acceptor Units for Photovoltaic Applications. *Sustainable Energy and Fuels*. Royal Society of Chemistry July 1, 2020, pp 3190–3210. https://doi.org/10.1039/d0se00206b.

(14) Blankenship, R. E. *Molecular Mechanisms of Photosynthesis*, 2nd ed.; 2014.

(15) F. Hohmann-Marriott, Martin, Blankenship E., R. Evolution of Photosynthesis. *Annu Rev Plant Biol* **2011**, *62*, 48. https://doi.org/10.1146/annurev-arplant-042110-103811.

(16) Ryan, A. A.; Senge, M. O. How Green Is Green Chemistry? Chlorophylls as a Bioresource from Biorefineries and Their Commercial Potential in Medicine and Photovoltaics. **2015**. https://doi.org/10.1039/c4pp00435c.
(17) H. Scheer. *Chlorophylls*; CRC Press, Boca Raton: USA, 1991.
(18) *Chlorophylls and Carotenoids: Measurement and Characterization by UV-VIS Spectroscopy*; 2001.
(19) Weiss, C. The Pi Electron Structure and Absorption Spectra of Chlorophylls in Solution. *J Mol Spectrosc* **1972**, *44* (1), 37–80. https://doi.org/10.1016/0022-2852(72)90192-0.
(20) Reimers, J. R.; Cai, Z.-L.; Kobayashi, R.; Rätsep, M.; Freiberg, A.; Krausz, E. Assignment of the Q-Bands of the Chlorophylls: Coherence Loss via Qx − Qy Mixing. *Sci Rep* **2013**, *3*, 2761.
(21) Hughes, J. L.; Conlon, B.; Wydrzynski, T.; Krausz, E. The Assignment of Q y (1,0) Vibrational Structure and Q x for Chlorophyll a. *Phys Procedia* **2011**, *00*, 0–000. https://doi.org/10.1016/j.phpro.2010.01.226.
(22) Law, C. J.; Roszak, A. W.; Southall, J.; Gardiner, A. T.; Isaacs, N. W.; Cogdell, R. J. The Structure and Function of Bacterial Light-Harvesting Complexes. *Mol Membr Biol* **2004**, *21* (3), 183–191. https://doi.org/10.1080/09687680410001697224.
(23) Scheuring, S.; Reiss-Husson, F.; Engel, A.; Rigaud, J. L.; Ranck, J. L. High-Resolution AFM Topographs of Rubrivivax Gelatinosus Light-Harvesting Complex LH2. *EMBO Journal* **2001**, *20* (12), 3029–3035. https://doi.org/10.1093/emboj/20.12.3029.
(24) Kumar, S.; Cartron, M. L.; Mullin, N.; Qian, P.; Leggett, G. J.; Hunter, C. N.; Hobbs, J. K. Direct Imaging of Protein Organization in an Intact Bacterial Organelle Using High-Resolution Atomic Force Microscopy. *ACS Nano* **2017**. https://doi.org/10.1021/acsnano.6b05647.
(25) Law, C. J.; Roszak, A. W.; Southall, J.; Gardiner, A. T.; Isaacs, N. W.; Cogdell, R. J. The Structure and Function of Bacterial Light-Harvesting Complexes. *Mol Membr Biol* **2004**, *21* (3), 183–191. https://doi.org/10.1080/09687680410001697224.
(26) Cogdell, R. J.; Gall, A.; Köhler, J. The Architecture and Function of the Light-Harvesting Apparatus of Purple Bacteria: From Single Molecules to in Vivo Membranes. *Quarterly Reviews of Biophysics*. 2006. https://doi.org/10.1017/S0033583506004434.
(27) Hu, X.; Damjanovic, A.; Ritz, T.; Schulten, K. Architecture and Mechanism Ofthe Light-Harvesting Apparatus of Purple Bacteria. *Proc Natl Acad Sci U S A* **1998**, *95* (11), 5935–5941.
(28) Papiz, M. Z.; Prince, S. M.; Howard, T.; Cogdell, R. J.; Isaacs, N. W. The Structure and Thermal Motion of the B800-850 LH2 Complex from Rps. Acidophila at 2.0 Å Resolution and 100 K: New Structural Features and Functionally Relevant Motions. *J Mol Biol* **2003**, *326* (5), 1523–1538. https://doi.org/10.1016/S0022-2836(03)00024-X.
(29) Harel, E.; Engel, G. S. Quantum Coherence Spectroscopy Reveals Complex Dynamics in Bacterial Light-Harvesting Complex 2 (LH2). *Proceedings of the National Academy of Sciences* **2012**. https://doi.org/10.1073/pnas.1110312109.
(30) Chen, Y.; Sun, M. Plexcitonics: Plasmon–Exciton Coupling for Enhancing Spectroscopy, Optical Chirality, and Nonlinearity. *Nanoscale* **2023**. https://doi.org/10.1039/d3nr01388j.
(31) Li, Y. *Plasmonic Optics: Theory and Applications*; SPIE, 2017.
(32) Gerard, D.; Gray, S. K. Aluminium Plasmonics. *J Phys D Appl Phys* **2015**, *48* (18). https://doi.org/10.1088/0022-3727/48/18/184001.

(33) Maidecchi, G.; Gonella, G.; Proietti Zaccaria, R.; Moroni, R.; Anghinolfi, L.; Giglia, A.; Nannarone, S.; Mattera, L.; Dai, H. L.; Canepa, M.; Bisio, F. Deep Ultraviolet Plasmon Resonance in Aluminum Nanoparticle Arrays. *ACS Nano* **2013**, *7* (7), 5834–5841. https://doi.org/10.1021/nn400918n.

(34) Kim, T.; Lee, C. H.; Joo, S. W.; Lee, K. Kinetics of Gold Nanoparticle Aggregation: Experiments and Modeling. *J Colloid Interface Sci* **2008**, *318* (2), 238–243. https://doi.org/10.1016/j.jcis.2007.10.029.

(35) Törmä, P.; Barnes, W. L. *Strong Coupling between Surface Plasmon Polaritons and Emitters*.

(36) Mejía-Salazar, J. R.; Oliveira, O. N. Plasmonic Biosensing. *Chem Rev* **2018**, *118* (20), 10617–10625. https://doi.org/10.1021/acs.chemrev.8b00359.

(37) Maier, S. A.; Brongersma, M. L.; Kik, P. G.; Meltzer, S.; Requicha, A. A. G.; Atwater, H. A. Plasmonics - A Route to Nanoscale Optical Devices. *Advanced Materials* **2001**, *13* (19), 1501–1505. https://doi.org/10.1002/1521-4095(200110)13:19<1501::AID-ADMA1501>3.0.CO;2-Z.

(38) Nie, S.; Emory, S. R. Probing Single Molecules and Single Nanoparticles by SERS. *Science (1979)* **1994**, *266* (5193), 1102–1106. https://doi.org/10.1126/science.266.5193.1961.

(39) Mandal, P. Application of Plasmonics in Solar Cell Efficiency Improvement: A Brief Review on Recent Progress. *Plasmonics*. Springer June 1, 2022, pp 1247–1267. https://doi.org/10.1007/s11468-022-01616-9.

(40) Cheng, Y. J.; Yang, S. H.; Hsu, C. S. Synthesis of Conjugated Polymers for Organic Solar Cell Applications. *Chem Rev* **2009**, *109* (11), 5868–5923. https://doi.org/10.1021/cr900182s.

(41) Jang, Y. H.; Jang, Y. J.; Kim, S.; Quan, L. N.; Chung, K.; Kim, D. H. Plasmonic Solar Cells: From Rational Design to Mechanism Overview. *Chem Rev* **2016**, *116* (24), 14982–15034. https://doi.org/10.1021/acs.chemrev.6b00302.

(42) Dang, X.; Qi, J.; Klug, M. T.; Chen, P. Y.; Yun, D. S.; Fang, N. X.; Hammond, P. T.; Belcher, A. M. Tunable Localized Surface Plasmon-Enabled Broadband Light-Harvesting Enhancement for High-Efficiency Panchromatic Dye-Sensitized Solar Cells. *Nano Lett* **2013**, *13* (2), 637–642. https://doi.org/10.1021/nl3043823.

(43) Malý, P.; Gruber, J. M.; Cogdell, R. J.; Mančal, T.; Van Grondelle, R. Ultrafast Energy Relaxation in Single Light-Harvesting Complexes. **2016**, *113* (11), 2934–2939. https://doi.org/10.1073/pnas.1522265113.

(44) Luo, Y.; Zhao, J. Plasmon-Exciton Interaction in Colloidally Fabricated Metal Nanoparticle-Quantum Emitter Nanostructures. *Nano Research*. Tsinghua University Press September 1, 2019, pp 2164–2171. https://doi.org/10.1007/s12274-019-2390-z.

(45) Liu, W.; Wang, Y.; Naylor, C. H.; Lee, B.; Zheng, B.; Liu, G.; Johnson, A. T. C.; Pan, A.; Agarwal, R. *Understanding the Different Exciton-Plasmon Coupling Regimes in Two-Dimensional Semiconductors Coupled with Plasmonic Lattices: A Combined Experimental and Unified Equations of Motion Approach*.

(46) Todisco, F.; De Giorgi, M.; Esposito, M.; De Marco, L.; Zizzari, A.; Bianco, M.; Dominici, L.; Ballarini, D.; Arima, V.; Gigli, G.; Sanvitto, D. Ultrastrong Plasmon-Exciton Coupling by Dynamic Molecular Aggregation. *ACS Photonics* **2018**, *5* (1), 143–150. https://doi.org/10.1021/acsphotonics.7b00554.

(47) Tsargorodska, A.; Cartron, M. L.; Vasilev, C.; Kodali, G.; Mass, O. A.; Baumberg, J. J.; Dutton, P. L.; Hunter, C. N.; Törmä, P.; Leggett, G. J. *Strong Coupling of Localized Surface Plasmons to Excitons in Light-Harvesting Complexes*.

(48) Lishchuk, A.; Csányi, E.; Darroch, B.; Wilson, C.; Nabok, A.; Leggett, G. J. Active Control of Strong Plasmon-Exciton Coupling in Biomimetic Pigment-Polymer

Antenna Complexes Grown by Surface-Initiated Polymerisation from Gold Nanostructures. *Chem Sci* **2022**, *13* (8), 2405–2417. https://doi.org/10.1039/d1sc05842h.

(49) Nan, F.; Ding, S. J.; Ma, L.; Cheng, Z. Q.; Zhong, Y. T.; Zhang, Y. F.; Qiu, Y. H.; Li, X.; Zhou, L.; Wang, Q. Q. Plasmon Resonance Energy Transfer and Plexcitonic Solar Cell. *Nanoscale* **2016**, *8* (32), 15071–15078. https://doi.org/10.1039/c6nr02633h.

(50) Barazzouk, S.; Hotchandani, S. Enhanced Charge Separation in Chlorophyll a Solar Cell by Gold Nanoparticles. *J Appl Phys* **2004**, *96* (12), 7744–7746. https://doi.org/10.1063/1.1811775.

(51) Patni, N.; G. Pillai, S.; Sharma, P. Effect of Using Betalain, Anthocyanin and Chlorophyll Dyes Together as a Sensitizer on Enhancing the Efficiency of Dye-Sensitized Solar Cell. *Int J Energy Res* **2020**, *44* (13), 10846–10859. https://doi.org/10.1002/er.5752.

(52) Furukawa, H.; Watanabe, T.; Kuroda, K. Immobilization of Chlorophyll Derivatives into Mesoporous Silica and Energy Transfer between the Chromophores in Mesopores. *Chemical Communications* **2001**, *1* (19), 2002–2003. https://doi.org/10.1039/b104959n.

(53) Kondo, M.; Nakamura, Y.; Fujii, K.; Nagata, M.; Suemori, Y.; Dewa, T.; Iida, K.; Gardiner, A. T.; Cogdell, R. J.; Nango, M. Self-Assembled Monolayer of Light-Harvesting Core Complexes from Photosynthetic Bacteria on a Gold Electrode Modified with Alkanethiols. *Biomacromolecules* **2007**, *8* (8), 2457–2463. https://doi.org/10.1021/bm070352z.

(54) Kondo, M.; Iida, K.; Dewa, T.; Tanaka, H.; Ogawa, T.; Nagashima, S.; Nagashima, K. V. P.; Shimada, K.; Hashimoto, H.; Gardiner, A. T.; Cogdell, R. J.; Nango, M. Photocurrent and Electronic Activities of Oriented-His-Tagged Photosynthetic Light-Harvesting/Reaction Center Core Complexes Assembled onto a Gold Electrode. *Biomacromolecules* **2012**, *13* (2), 432–438. https://doi.org/10.1021/bm201457s.

(55) Suemori, Y.; Nagata, M.; Nakamura, Y.; Nakagawa, K.; Okuda, A.; Inagaki, J. I.; Shinohara, K.; Ogawa, M.; Iida, K.; Dewa, T.; Yamashita, K.; Gardiner, A.; Cogdell, R. J.; Nango, M. Self-Assembled Monolayer of Light-Harvesting Core Complexes of Photosynthetic Bacteria on an Amino-Terminated ITO Electrode. *Photosynth Res* **2006**, *90* (1), 17–21. https://doi.org/10.1007/s11120-006-9101-9.

(56) Abrusci, A.; Stranks, S. D.; Docampo, P.; Yip, H. L.; Jen, A. K. Y.; Snaith, H. J. High-Performance Perovskite-Polymer Hybrid Solar Cells via Electronic Coupling with Fullerene Monolayers. *Nano Lett* **2013**, *13* (7), 3124–3128. https://doi.org/10.1021/nl401044q.

(57) Wang, B.; Li, N.; Yang, L.; Dall'agnese, C.; Jena, A. K.; Sasaki, S. I.; Miyasaka, T.; Tamiaki, H.; Wang, X. F. Chlorophyll Derivative-Sensitized TiO2Electron Transport Layer for Record Efficiency of Cs2AgBiBr6Double Perovskite Solar Cells. *J Am Chem Soc* **2021**, *143* (5), 2207–2211. https://doi.org/10.1021/jacs.0c12786.

(58) Lauterbach, R.; Liu, J.; Knoll, W.; Paulsen, H. Energy Transfer between Surface-Immobilized Light-Harvesting Chlorophyll a/b Complex (LHCII) Studied by Surface Plasmon Field-Enhanced Fluorescence Spectroscopy (SPFS). *Langmuir* **2010**, *26* (22), 17315–17321. https://doi.org/10.1021/la102525b.

(59) Lishchuk, A.; Vasilev, C.; Johnson, M. P.; Hunter, C. N.; Törmä, P.; Leggett, G. J. Turning the Challenge of Quantum Biology on Its Head: Biological Control of Quantum Optical Systems. *Faraday Discuss* **2019**. https://doi.org/10.1039/c8fd00241j.

(60) Matyjaszewski, K.; Hongchen, D.; Jakubowski, W.; Pietrasik, J.; Kusumo, A. Grafting from Surfaces for "Everyone": ARGET ATRP in the Presence of Air. *Langmuir* **2007**, *23* (8), 4528–4531. https://doi.org/10.1021/la063402e.

(61) Wang, J.; Karami, P.; Ataman, N. C.; Pioletti, D. P.; Steele, T. W. J.; Klok, H. A. Light-Activated, Bioadhesive, Poly(2-Hydroxyethyl Methacrylate) Brush Coatings. *Biomacromolecules* **2020**, *21* (1), 240–249. https://doi.org/10.1021/acs.biomac.9b01196.

(62) Tugulu, S.; Silacci, P.; Stergiopulos, N.; Klok, H. A. RGD-Functionalized Polymer Brushes as Substrates for the Integrin Specific Adhesion of Human Umbilical Vein Endothelial Cells. *Biomaterials* **2007**, *28* (16), 2536–2546. https://doi.org/10.1016/j.biomaterials.2007.02.006.

(63) Tugulu, S.; Arnold, A.; Sielaff, I.; Johnsson, K.; Klok, A. Protein-Functionalized Polymer Brushes. **2005**. https://doi.org/10.1021/bm050016n.

(64) Ma, H.; He, J.; Liu, X.; Gan, J.; Jin, G.; Zhou, J. Surface Initiated Polymerization from Substrates of Low Initiator Density and Its Applications in Biosensors. *ACS Appl Mater Interfaces* **2010**, *2* (11), 3223–3230. https://doi.org/10.1021/am1006832.

(65) Badoux, M.; Billing, M.; Klok, H.-A. Polymer Brush Interfaces for Protein Biosensing Prepared by Surface-Initiated Controlled Radical Polymerization. *Polym Chem* **2019**. https://doi.org/10.1039/c9py00163h.

(66) Bao, Z.; Bruening, M. L.; Baker, G. L. Control of the Density of Polymer Brushes Prepared by Surface-Initiated Atom Transfer Radical Polymerization. *Macromolecules* **2006**. https://doi.org/10.1021/ma060095a.

(67) Lillethorup, M.; Shimizu, K.; Plumeré, N.; Pedersen, S. U.; Daasbjerg, K. Surface-Attached Poly(Glycidyl Methacrylate) as a Versatile Platform for Creating Dual-Functional Polymer Brushes. *Macromolecules* **2014**, *47* (15), 5081–5088. https://doi.org/10.1021/ma500872b.

(68) Barbey, R.; Laporte, V.; Alnabulsi, S.; Klok, H. A. Postpolymerization Modification of Poly(Glycidyl Methacrylate) Brushes: An XPS Depth-Profiling Study. *Macromolecules* **2013**, *46* (15), 6151–6158. https://doi.org/10.1021/ma400819a.

(69) Szuwarzyński, M.; Wolski, K.; Pomorska, A.; Uchacz, T.; Gut, A.; Łapok, Ł.; Zapotoczny, S. Photoactive Surface-Grafted Polymer Brushes with Phthalocyanine Bridging Groups as an Advanced Architecture for Light-Harvesting. *Chemistry - A European Journal* **2017**, *23* (47), 11239–11243. https://doi.org/10.1002/chem.201702737.

(70) Dirani, A.; Laloyaux, X.; Fernandes, A. E.; Mathy, B.; Schicke, O.; Riant, O.; Nysten, B.; Jonas, A. M. Reversible Photomodulation of the Swelling of Poly(Oligo(Ethylene Glycol) Methacrylate) Thermoresponsive Polymer Brushes. *Macromolecules* **2012**, *45* (23), 9400–9408. https://doi.org/10.1021/ma302106c.

(71) Christau, S.; Möller, T.; Yenice, Z.; Genzer, J.; Von Klitzing, R. Brush/Gold Nanoparticle Hybrids: Effect of Grafting Density on the Particle Uptake and Distribution within Weak Polyelectrolyte Brushes. *Langmuir* **2014**, *30* (43), 13033–13041. https://doi.org/10.1021/la503432x.

(72) Zhang, Y.; Liu, J.; Wang, Z.; Xue, Y.; Ou, Q.; Polavarapu, L.; Zheng, J.; Qi, X.; Bao, Q. Synthesis, Properties, and Optical Applications of Low-Dimensional Perovskites. *Chemical Communications*. Royal Society of Chemistry 2016, pp 13637–13655. https://doi.org/10.1039/c6cc06425f.

(73) Wenk, H.-R.; Bulakh, A. G. (Andreĭ G. *Minerals : Their Constitution and Origin*; Cambridge University Press, 2004.

(74) Arya, S.; Mahajan, P.; Gupta, R.; Srivastava, R.; Tailor, N. kumar; Satapathi, S.; Sumathi, R. R.; Datt, R.; Gupta, V. A Comprehensive Review on Synthesis and Applications of Single Crystal Perovskite Halides. *Progress in Solid State Chemistry*. Elsevier Ltd December 1, 2020. https://doi.org/10.1016/j.progsolidstchem.2020.100286.

(75) Kojima, A.; Teshima, K.; Shirai, Y.; Miyasaka, T. Organometal Halide Perovskites as Visible-Light Sensitizers for Photovoltaic Cells. *J Am Chem Soc* **2009**, *131* (17), 6050–6051. https://doi.org/10.1021/ja809598r.

(76) Stranks, S. D.; Snaith, H. J. Metal-Halide Perovskites for Photovoltaic and Light-Emitting Devices. *Nature Nanotechnology*. Nature Publishing Group May 7, 2015, pp 391–402. https://doi.org/10.1038/nnano.2015.90.

(77) Adinolfi, V.; Peng, W.; Walters, G.; Bakr, O. M.; Sargent, E. H. The Electrical and Optical Properties of Organometal Halide Perovskites Relevant to Optoelectronic Performance. *Advanced Materials*. Wiley-VCH Verlag January 4, 2018. https://doi.org/10.1002/adma.201700764.

(78) Shamsi, J.; Urban, A. S.; Imran, M.; Trizio, L. De; Manna, L. Metal Halide Perovskite Nanocrystals: Synthesis, Post-SynthesisModifications, and Their Optical Properties. *Chem Rev* **2019**, *119*, 3296–3348. https://doi.org/10.1021/acs.chemrev.8b00644.

(79) Lee, M. M.; Teuscher, J.; Miyasaka, T.; Murakami, T. N.; Snaith, H. J. Efficient Hybrid Solar Cells Based on Meso-Superstructured Organometal Halide Perovskites. *Science (1979)* **2012**, *338* (6107), 640–643. https://doi.org/10.1126/science.1227193.

(80) Kim, H. S.; Lee, C. R.; Im, J. H.; Lee, K. B.; Moehl, T.; Marchioro, A.; Moon, S. J.; Humphry-Baker, R.; Yum, J. H.; Moser, J. E.; Grätzel, M.; Park, N. G. Lead Iodide Perovskite Sensitized All-Solid-State Submicron Thin Film Mesoscopic Solar Cell with Efficiency Exceeding 9%. *Sci Rep* **2012**, *2*. https://doi.org/10.1038/srep00591.

(81) Xing, G.; Mathews, N.; Sun, S.; Lim, S. S.; Lam, Y. M.; Grätzel, M.; Mhaisalkar, S.; Sum, T. C. Long-Range Balanced Electronand Hole-Transport Lengths in Organic-Inorganic CH3NH3PbI3. *Science (1979)* **2013**, *342* (6156), 344–347. https://doi.org/DOI: 10.1126/science.1243167.

(82) Fu, F.; Feurer, T.; Weiss, T. P.; Pisoni, S.; Avancini, E.; Andres, C.; Buecheler, S.; Tiwari, A. N. High-Efficiency Inverted Semi-Transparent Planar Perovskite Solar Cells in Substrate Configuration. *Nat Energy* **2017**, *2* (1). https://doi.org/10.1038/nenergy.2016.190.

(83) Cho, H.; Jeong, S.-H.; Park, M.-H.; Kim, Y.-H.; Wolf, C.; Lee, C.-L.; Hyuck Heo, J.; Sadhanala, A.; Myoung, N.; Yoo, S.; Im, S. H.; Friend, R. H.; Lee, T.-W. *Overcoming the Electroluminescence Efficiency Limitations of Perovskite Light-Emitting Diodes*. https://www.science.org.

(84) Smith, M. D.; Connor, B. A.; Karunadasa, H. I. Tuning the Luminescence of Layered Halide Perovskites. *Chemical Reviews*. American Chemical Society March 13, 2019, pp 3104–3139. https://doi.org/10.1021/acs.chemrev.8b00477.

(85) V. M. Goldschmidt. Die Gesetze Der Krystallochemie. *Naturwissenschaften* **1926**, *14*, 477.

(86) Li, C.; Lu, X.; Ding, W.; Feng, L.; Gao, Y.; Guo, Z. Formability of ABX 3 (X = F, Cl, Br, I) Halide Perovskites. *Acta Crystallogr B* **2008**, *64* (6), 702–707. https://doi.org/10.1107/S0108768108032734.

(87) Veldhuis, S. A.; Boix, P. P.; Yantara, N.; Li, M.; Sum, T. C.; Mathews, N.; Mhaisalkar, S. G. Perovskite Materials for Light-Emitting Diodes and Lasers. *Advanced Materials*. Wiley-VCH Verlag August 24, 2016, pp 6804–6834. https://doi.org/10.1002/adma.201600669.

(88) Borriello, I.; Cantele, G.; Ninno, D. Ab Initio Investigation of Hybrid Organic-Inorganic Perovskites Based on Tin Halides. *Phys Rev B Condens Matter Mater Phys* **2008**, *77* (23). https://doi.org/10.1103/PhysRevB.77.235214.

(89) Mosconi, E.; Amat, A.; Nazeeruddin, M. K.; Grätzel, M.; De Angelis, F. First-Principles Modeling of Mixed Halide Organometal Perovskites for Photovoltaic

Applications. *Journal of Physical Chemistry C* **2013**, *117* (27), 13902–13913. https://doi.org/10.1021/jp4048659.

(90) González-Carrero, S.; Galian, R. E.; Pérez-Prieto, J. Organometal Halide Perovskites: Bulk Low-Dimension Materials and Nanoparticles. *Particle and Particle Systems Characterization* **2015**, *32* (7), 709–720. https://doi.org/10.1002/ppsc.201400214.

(91) Smith, I. C.; Hoke, E. T.; Solis-Ibarra, D.; McGehee, M. D.; Karunadasa, H. I. A Layered Hybrid Perovskite Solar-Cell Absorber with Enhanced Moisture Stability. *Angewandte Chemie - International Edition* **2014**, *53* (42), 11232–11235. https://doi.org/10.1002/anie.201406466.

(92) Hong, X.; Ishihara, T.; Nurmikko, A. U. *Dielectric Confinement Eff'ect on Excitons in PbI4-Based Layered Semiconductors*; Vol. 45.

(93) Sun, S.; Lu, M.; Gao, X.; Shi, Z.; Bai, X.; Yu, W. W.; Zhang, Y. 0D Perovskites: Unique Properties, Synthesis, and Their Applications. *Advanced Science*. John Wiley and Sons Inc December 1, 2021. https://doi.org/10.1002/advs.202102689.

(94) Zhu, P.; Zhu, J. Low-Dimensional Metal Halide Perovskites and Related Optoelectronic Applications. *InfoMat* **2020**, *2* (2), 341–378. https://doi.org/10.1002/inf2.12086.

(95) Guhrenz, C.; Benad, A.; Ziegler, C.; Haubold, D.; Gaponik, N.; Eychmüller, A. Solid-State Anion Exchange Reactions for Color Tuning of CsPbX3 Perovskite Nanocrystals. *Chemistry of Materials* **2016**, *28* (24), 9033–9040. https://doi.org/10.1021/acs.chemmater.6b03980.

(96) Sheng, Y.; Zha, Y.; Feng, X.; Xing, F.; Di, Y.; Liu, C.; Zhang, X.; Gan, Z. Laser-Triggered Vapor-Phase Anion Exchange on All-Inorganic Perovskites for Multicolor Patterns and Microfabrications. *Adv Opt Mater* **2023**, *11* (4). https://doi.org/10.1002/adom.202202230.

(97) Akkerman, Q. A.; D'Innocenzo, V.; Accornero, S.; Scarpellini, A.; Petrozza, A.; Prato, M.; Manna, L. Tuning the Optical Properties of Cesium Lead Halide Perovskite Nanocrystals by Anion Exchange Reactions. *J Am Chem Soc* **2015**, *137* (32), 10276–10281. https://doi.org/10.1021/jacs.5b05602.

(98) Tiguntseva, E. Y.; Sadrieva, Z.; Stroganov, B. V.; Kapitonov, Y. V.; Komissarenko, F.; Haroldson, R.; Balachandran, B.; Hu, W.; Gu, Q.; Zakhidov, A. A.; Bogdanov, A.; Makarov, S. V. Enhanced Temperature-Tunable Narrow-Band Photoluminescence from Resonant Perovskite Nanograting. *Appl Surf Sci* **2019**, *473*, 419–424. https://doi.org/10.1016/j.apsusc.2018.12.084.

(99) Liu, S.; Sun, S.; Kwan Gan, C.; Granados del Águila, A.; Fang, Y.; Xing, J.; Thu Ha Do, T.; White, T. J.; Li, H.; Huang, W.; Xiong, Q. Manipulating Efficient Light Emission in Two-Dimensional Perovskite Crystals by Pressure-Induced Anisotropic Deformation. *Sci Adv* **2019**, *5*, eaav9445. https://doi.org/10.1126/sciadv.aav9445.

(100) Baranowski, M.; Plochocka, P. Excitons in Metal-Halide Perovskites. *Advanced Energy Materials*. Wiley-VCH Verlag July 1, 2020. https://doi.org/10.1002/aenm.201903659.

(101) Fu, M.; Tamarat, P.; Huang, H.; Even, J.; Rogach, A. L.; Lounis, B. Neutral and Charged Exciton Fine Structure in Single Lead Halide Perovskite Nanocrystals Revealed by Magneto-Optical Spectroscopy. *Nano Lett* **2017**, *17* (5), 2895–2901. https://doi.org/10.1021/acs.nanolett.7b00064.

(102) Becker, M. A.; Vaxenburg, R.; Nedelcu, G.; Sercel, P. C.; Shabaev, A.; Mehl, M. J.; Michopoulos, J. G.; Lambrakos, S. G.; Bernstein, N.; Lyons, J. L.; Stöferle, T.; Mahrt, R. F.; Kovalenko, M. V.; Norris, D. J.; Rainò, G.; Efros, A. L. Bright Triplet Excitons in Caesium Lead Halide Perovskites. *Nature* **2018**, *553* (7687), 189–193. https://doi.org/10.1038/nature25147.

(103) Ryu, H.; Park, D. Y.; McCall, K. M.; Byun, H. R.; Lee, Y.; Kim, T. J.; Jeong, M. S.; Kim, J.; Kanatzidis, M. G.; Jang, J. I. Static Rashba Effect by Surface Reconstruction and Photon Recycling in the Dynamic Indirect Gap of APbBr3(A = Cs, CH3NH3) Single Crystals. *J Am Chem Soc* **2020**, *142* (50), 21059–21067. https://doi.org/10.1021/jacs.0c09132.

(104) Li, Y.; He, S.; Luo, X.; Lu, X.; Wu, K. Strong Spin-Selective Optical Stark Effect in Lead Halide Perovskite Quantum Dots. *Journal of Physical Chemistry Letters* **2020**, *11* (9), 3594–3600. https://doi.org/10.1021/acs.jpclett.0c00879.

(105) Canneson, D.; Shornikova, E. V.; Yakovlev, D. R.; Rogge, T.; Mitioglu, A. A.; Ballottin, M. V.; Christianen, P. C. M.; Lhuillier, E.; Bayer, M.; Biadala, L. Negatively Charged and Dark Excitons in CsPbBr3 Perovskite Nanocrystals Revealed by High Magnetic Fields. *Nano Lett* **2017**, *17* (10), 6177–6183. https://doi.org/10.1021/acs.nanolett.7b02827.

(106) Lü, X.; Stoumpos, C.; Hu, Q.; Ma, X.; Zhang, D.; Guo, S.; Hoffman, J.; Bu, K.; Guo, X.; Wang, Y.; Ji, C.; Chen, H.; Xu, H.; Jia, Q.; Yang, W.; Kanatzidis, M. G.; Mao, H. K. Regulating Off-Centering Distortion Maximizes Photoluminescence in Halide Perovskites. *Natl Sci Rev* **2021**, *8* (9). https://doi.org/10.1093/nsr/nwaa288.

(107) Spirito, D.; Barra-Burillo, M.; Calavalle, F.; Manganelli, C. L.; Gobbi, M.; Hillenbrand, R.; Casanova, F.; Hueso, L. E.; Martín-García, B. Tailoring Photoluminescence by Strain-Engineering in Layered Perovskite Flakes. *Nano Lett* **2022**, *22* (10), 4153–4160. https://doi.org/10.1021/acs.nanolett.2c00909.

(108) Butler, R.; Burns, R.; Babaian, D.; Anderson, M. J.; Ullrich, C. A.; Morrell, M. V.; Xing, Y.; Lee, J.; Yu, P.; Guha, S. Weak Magnetic Field-Dependent Photoluminescence Properties of Lead Bromide Perovskites. *J Appl Phys* **2022**, *131* (12). https://doi.org/10.1063/5.0085947.

(109) Canneson, D.; Shornikova, E. V.; Yakovlev, D. R.; Rogge, T.; Mitioglu, A. A.; Ballottin, M. V.; Christianen, P. C. M.; Lhuillier, E.; Bayer, M.; Biadala, L. Negatively Charged and Dark Excitons in CsPbBr3 Perovskite Nanocrystals Revealed by High Magnetic Fields. *Nano Lett* **2017**, *17* (10), 6177–6183. https://doi.org/10.1021/acs.nanolett.7b02827.

(110) Purcell E., M. Proceedings of the American Physical Society. *Physical Review* **1946**, *69*, 674. https://doi.org/https://doi.org/10.1103/PhysRev.69.674.

(111) Martínez, E. D.; Prado, A.; González, M.; Anguiano, S.; Tosi, L.; Alarcón, L. S.; Pastoriza, H. Integrating Photoluminescent Nanomaterials with Photonic Nanostructures. *J Lumin* **2021**, *233*. https://doi.org/10.1016/j.jlumin.2020.117870.

(112) Krasnok, A. E.; Slobozhanyuk, A. P.; Simovski, C. R.; Tretyakov, S. A.; Poddubny, A. N.; Miroshnichenko, A. E.; Kivshar, Y. S.; Belov, P. A. An Antenna Model for the Purcell Effect. *Sci Rep* **2015**, *5*. https://doi.org/10.1038/srep12956.

(113) Adawi, A. M.; Cadby, A.; Connolly, L. G.; Hung, W. C.; Dean, R.; Tahraoui, A.; Fox, A. M.; Cullis, A. G.; Sanvitto, D.; Skolnick, M. S.; Lidzey, D. G. Spontaneous Emission Control in Micropillar Cavities Containing a Fluorescent Molecular Dye. *Advanced Materials* **2006**, *18* (6), 742–747. https://doi.org/10.1002/adma.200502099.

(114) Sorger, V. J.; Oulton, R. F.; Yao, J.; Bartal, G.; Zhang, X. Plasmonic Fabry-Pérot Nanocavity. *Nano Lett* **2009**, *9* (10), 3489–3493. https://doi.org/10.1021/nl901682n.

(115) Adl, H. P.; Gorji, S.; Habil, M. K.; Suárez, I.; Chirvony, V. S.; Gualdrón-Reyes, A. F.; Mora-Seró, I.; Valencia, L. M.; De La Mata, M.; Hernández-Saz, J.; Molina, S. I.; Zapata-Rodríguez, C. J.; Martínez-Pastor, J. P. Purcell Enhancement and Wavelength Shift of Emitted Light by CsPbI3Perovskite Nanocrystals Coupled to Hyperbolic Metamaterials. *ACS Photonics* **2020**, *7* (11), 3152–3160. https://doi.org/10.1021/acsphotonics.0c01219.

(116) Liu, T.; Yang, C.; Fan, Z.; Chen, X.; Chen, Z.; Su, Y.; Zhu, H.; Sun, F.; Jiang, T.; Zhu, W.; Shen, W.; He, J.; Zhu, H.; Liu, X.; Yang, Y. Spectral Narrowing and Enhancement of Directional Emission of Perovskite Light Emitting Diode by Microcavity. *Laser Photon Rev* **2022**, *16* (10). https://doi.org/10.1002/lpor.202200091.

(117) Wang, J.; Cao, R.; Da, P.; Wang, Y.; Hu, T.; Wu, L.; Lu, J.; Shen, X.; Xu, F.; Zheng, G.; Chen, Z. Purcell Effect in an Organic-Inorganic Halide Perovskite Semiconductor Microcavity System. *Appl Phys Lett* **2016**, *108* (2). https://doi.org/10.1063/1.4939724.

(118) Yang, Z.; Pelton, M.; Bodnarchuk, M. I.; Kovalenko, M. V.; Waks, E. Spontaneous Emission Enhancement of Colloidal Perovskite Nanocrystals by a Photonic Crystal Cavity. *Appl Phys Lett* **2017**, *111* (22). https://doi.org/10.1063/1.5000248.

(119) Li, H.; He, F.; Ji, C.; Zhu, W.; Xu, Y.; Zhang, W.; Meng, X.; Fang, X.; Ding, T. Purcell-Enhanced Spontaneous Emission from Perovskite Quantum Dots Coupled to Plasmonic Crystal. *Journal of Physical Chemistry C* **2019**, *123* (41), 25359–25365. https://doi.org/10.1021/acs.jpcc.9b06919.

(120) Yuan, S.; Zhang, X.; Cao, W.; Sheng, Y.; Liu, C.; Yu, L.; Di, Y.; Chen, Z.; Dong, L.; Gan, Z. Fluorescence Enhancement of Perovskite Nanocrystals Using Photonic Crystals. *J Mater Chem C Mater* **2021**, *9* (3), 908–915. https://doi.org/10.1039/d0tc05056c.

(121) Fu, Y.; Lakowicz, J. R. Modification of Single Molecule Fluorescence near Metallic Nanostructures. *Laser Photon Rev* **2009**, *3* (1–2), 221–232. https://doi.org/10.1002/lpor.200810035.

(122) Wu, Y.; Xu, J.; Poh, E. T.; Liang, L.; Liu, H.; Yang, J. K. W.; Qiu, C. W.; Vallée, R. A. L.; Liu, X. Upconversion Superburst with Sub-2 Ms Lifetime. *Nature Nanotechnology*. Nature Research December 1, 2019, pp 1110–1115. https://doi.org/10.1038/s41565-019-0560-5.

(123) Hsu, C. W.; Zhen, B.; Stone, A. D.; Joannopoulos, J. D.; Soljačić, M. *Bound States in the Continuum*.

(124) Hsu, C. W.; Zhen, B.; Stone, A. D.; Joannopoulos, J. D.; Soljacic, M. Bound States in the Continuum. *Nature Reviews Materials*. Nature Publishing Group July 19, 2016. https://doi.org/10.1038/natrevmats.2016.48.

(125) Lee, J.; Zhen, B.; Chua, S. L.; Qiu, W.; Joannopoulos, J. D.; Soljačić, M.; Shapira, O. Observation and Differentiation of Unique High-Q Optical Resonances near Zero Wave Vector in Macroscopic Photonic Crystal Slabs. *Phys Rev Lett* **2012**, *109* (6). https://doi.org/10.1103/PhysRevLett.109.067401.

(126) Liu, Z.; Xu, Y.; Lin, Y.; Xiang, J.; Feng, T.; Cao, Q.; Li, J.; Lan, S.; Liu, J. High- Q Quasibound States in the Continuum for Nonlinear Metasurfaces. *Phys Rev Lett* **2019**, *123* (25). https://doi.org/10.1103/PhysRevLett.123.253901.

(127) Dong, Z.; Mahfoud, Z.; Paniagua-Domínguez, R.; Wang, H.; Fernández-Domínguez, A. I.; Gorelik, S.; Ha, S. T.; Tjiptoharsono, F.; Kuznetsov, A. I.; Bosman, M.; Yang, J. K. W. *Photonic Bound-States-in-the-Continuum Observed with an Electron Nanoprobe*.

(128) Dong, Z.; Jin, L.; Daqiqeh Rezaei, S.; Wang, H.; Chen, Y.; Tjiptoharsono, F.; Ho, J.; Gorelik, S.; Jia Hong Ng, R.; Ruan, Q.; Qiu, C.-W.; W Yang, J. K. Schrödinger's Red Pixel by Quasi-Bound-States-in-the-Continuum. *Sci. Adv* **2022**, *8*, 4512.

(129) Zhu, L.; Yuan, S.; Zeng, C.; Xia, J. Manipulating Photoluminescence of Carbon G-Center in Silicon Metasurface with Optical Bound States in the Continuum. *Adv Opt Mater* **2020**, *8* (8). https://doi.org/10.1002/adom.201901830.

(130) Cao, S.; Jin, Y.; Dong, H.; Guo, T.; He, J.; He, S. Enhancing Single Photon Emission through Quasi-Bound States in the Continuum of Monolithic Hexagonal Boron Nitride Metasurface. *JPhys Materials* **2021**, *4* (3). https://doi.org/10.1088/2515-7639/abf3ce.

(131) Zhen, B.; Chua, S. L.; Lee, J.; Rodriguez, A. W.; Liang, X.; Johnson, S. G.; Joannopoulos, J. D.; Soljačić, M.; Shapira, O. Enabling Enhanced Emission and Low-Threshold Lasing of Organic Molecules Using Special Fano Resonances of Macroscopic Photonic Crystals. *Proc Natl Acad Sci U S A* **2013**, *110* (34), 13711–13716. https://doi.org/10.1073/pnas.1311866110.
(132) Staude, I.; Schilling, J. Metamaterial-Inspired Silicon Nanophotonics. *Nat Photonics* **2017**, *11* (5), 274–284. https://doi.org/10.1038/nphoton.2017.39.
(133) Dong, Z.; Wang, T.; Chi, X.; Ho, J.; Tserkezis, C.; Yap, S. L. K.; Rusydi, A.; Tjiptoharsono, F.; Thian, D.; Mortensen, N. A.; Yang, J. K. W. Ultraviolet Interband Plasmonics with Si Nanostructures. *Nano Lett* **2019**, *19* (11), 8040–8048. https://doi.org/10.1021/acs.nanolett.9b03243.
(134) Toudert, J.; Serna, R. Ultraviolet-Visible Interband Plasmonics with p-Block Elements. *Opt Mater Express* **2016**, *6* (7), 2434. https://doi.org/10.1364/ome.6.002434.
(135) Naik, G. V.; Shalaev, V. M.; Boltasseva, A. Alternative Plasmonic Materials: Beyond Gold and Silver. *Advanced Materials*. June 25, 2013, pp 3264–3294. https://doi.org/10.1002/adma.201205076.
(136) Song, K.; Mohseni, M.; Taghipour, F. Application of Ultraviolet Light-Emitting Diodes (UV-LEDs) for Water Disinfection: A Review. *Water Research*. Elsevier Ltd May 1, 2016, pp 341–349. https://doi.org/10.1016/j.watres.2016.03.003.
(137) Miller, S. L.; Linnes, J.; Luongo, J. Ultraviolet Germicidal Irradiation: Future Directions for Air Disinfection and Building Applications. In *Photochemistry and Photobiology*; 2013; Vol. 89, pp 777–781. https://doi.org/10.1111/php.12080.
(138) Kanellis, V. G. Ultraviolet Radiation Sensors: A Review. *Biophysical Reviews*. Springer December 1, 2019, pp 895–899. https://doi.org/10.1007/s12551-019-00556-9.
(139) Chen, X.; Leishman, M.; Bagnall, D.; Nasiri, N. Nanostructured Gas Sensors: From Air Quality and Environmental Monitoring to Healthcare and Medical Applications. *Nanomaterials*. MDPI AG August 1, 2021. https://doi.org/10.3390/nano11081927.
(140) Shaw, G. A.; Siegel, A. M.; Nischan, M. L. *Demonstration System and Applications for Compact Wireless Ultraviolet Communications*; 2003. http://proceedings.spiedigitallibrary.org/.
(141) Bigio, J. I.; Mourant, R. J. Ultraviolet and Visible Spectroscopies for Tissue Diagnostics: Fluorescence Spectroscopy and Elastic-Scattering. *Phys Med Biol* **1997**, *42*, 803.
(142) Zorić, I.; Zäch, M.; Kasemo, B.; Langhammer, C. Gold, Platinum, and Aluminum Nanodisk Plasmons: Material Independence, Subradiance, and Damping Mechanisms. *ACS Nano* **2011**, *5* (4), 2535–2546. https://doi.org/10.1021/nn102166t.
(143) J.H., W. Optical Properties of Rh, Pd, Ir, and Pt. *Physical Review* **1975**, *11* (4), 1416–1425.
(144) Toudert, J.; Serna, R.; Jiménez De Castro, M. Exploring the Optical Potential of Nano-Bismuth: Tunable Surface Plasmon Resonances in the near Ultraviolet-to-near Infrared Range. *Journal of Physical Chemistry C* **2012**, *116* (38), 20530–20539. https://doi.org/10.1021/jp3065882.
(145) Shekhar, P.; Pendharker, S.; Sahasrabudhe, H.; Vick, D.; Malac, M.; Rahman, R.; Jacob, Z. Extreme Ultraviolet Plasmonics and Cherenkov Radiation in Silicon. *Optica* **2018**, *5* (12), 1590. https://doi.org/10.1364/optica.5.001590.
(146) Deng, Y.; Wang, X.; Gong, Z.; Dong, K.; Lou, S.; Pégard, N.; Tom, K. B.; Yang, F.; You, Z.; Waller, L.; Yao, J. All-Silicon Broadband Ultraviolet Metasurfaces. *Advanced Materials* **2018**, *30* (38). https://doi.org/10.1002/adma.201802632.
(147) Zhao, D.; Lin, Z.; Zhu, W.; Lezec, H. J.; Xu, T.; Agrawal, A.; Zhang, C.; Huang, K. Recent Advances in Ultraviolet Nanophotonics: From Plasmonics and Metamaterials

to Metasurfaces. *Nanophotonics*. De Gruyter Open Ltd July 1, 2021, pp 2283–2308. https://doi.org/10.1515/nanoph-2021-0083.
(148) Berini, P. Surface Plasmon Photodetectors and Their Applications. *Laser and Photonics Reviews*. March 2014, pp 197–220. https://doi.org/10.1002/lpor.201300019.
(149) Lin, K. Te; Lin, H.; Jia, B. Plasmonic Nanostructures in Photodetection, Energy Conversion and Beyond. *Nanophotonics*. De Gruyter Open Ltd September 1, 2020, pp 3135–3163. https://doi.org/10.1515/nanoph-2020-0104.
(150) Ropers, C.; Park, D. J.; Stibenz, G.; Steinmeyer, G.; Kim, J.; Kim, D. S.; Lienau, C. Femtosecond Light Transmission and Subradiant Damping in Plasmonic Crystals. *Phys Rev Lett* **2005**, *94* (11). https://doi.org/10.1103/PhysRevLett.94.113901.
(151) Wang, B.; Yu, P.; Wang, W.; Zhang, X.; Kuo, H. C.; Xu, H.; Wang, Z. M. High-Q Plasmonic Resonances: Fundamentals and Applications. *Advanced Optical Materials*. John Wiley and Sons Inc April 1, 2021. https://doi.org/10.1002/adom.202001520.
(152) Okazaki, S.; Ito, T. Pushing the Limits of Lithography. *Nature* **2000**, *406*.
(153) West, P. R.; Ishii, S.; Naik, G. V.; Emani, N. K.; Shalaev, V. M.; Boltasseva, A. Searching for Better Plasmonic Materials. *Laser and Photonics Reviews*. November 2010, pp 795–808. https://doi.org/10.1002/lpor.200900055.
(154) Shopa, M.; Kolwas, K.; Derkachova, A.; Derkachov, G. Dipole and Quadrupole Surface Plasmon Resonance Contributions in Formation of Near-Field Images of a Gold Nanosphere. **2010**. https://doi.org/10.2478/s11772−010−0047−2.
(155) Zhu, X.; Imran Hossain, G. M.; George, M.; Farhang, A.; Cicek, A.; Yanik, A. A. Beyond Noble Metals: High Q-Factor Aluminum Nanoplasmonics. *ACS Photonics* **2020**, *7* (2), 416–424. https://doi.org/10.1021/acsphotonics.9b01368.
(156) Liu, J. N.; Huang, Q.; Liu, K. K.; Singamaneni, S.; Cunningham, B. T. Nanoantenna-Microcavity Hybrids with Highly Cooperative Plasmonic-Photonic Coupling. *Nano Lett* **2017**, *17* (12), 7569–7577. https://doi.org/10.1021/acs.nanolett.7b03519.
(157) Jiang, M. M.; Zhao, B.; Chen, H. Y.; Zhao, D. X.; Shan, C. X.; Shen, D. Z. Plasmon-Enhanced Ultraviolet Photoluminescence from the Hybrid Plasmonic Fabry-Perot Microcavity of Ag/ZnO Microwires. *Nanoscale* **2014**, *6* (3), 1354–1361. https://doi.org/10.1039/c3nr05119f.
(158) Han, Y.; Yang, J.; He, X.; Huang, J.; Zhang, J.; Chen, D.; Zhang, Z. High Quality Factor Electromagnetically Induced Transparency-like Effect in Coupled Guided-Mode Resonant Systems. *Opt Express* **2019**, *27* (5), 7712. https://doi.org/10.1364/oe.27.007712.
(159) Liu, Y. C.; Li, B. B.; Xiao, Y. F. Electromagnetically Induced Transparency in Optical Microcavities. *Nanophotonics*. Walter de Gruyter GmbH August 28, 2017, pp 789–811. https://doi.org/10.1515/nanoph-2016-0168.
(160) Zhang, S.; Genov, D. A.; Wang, Y.; Liu, M.; Zhang, X. Plasmon-Induced Transparency in Metamaterials. *Phys Rev Lett* **2008**, *101* (4). https://doi.org/10.1103/PhysRevLett.101.047401.
(161) Wang, J.; Yuan, B.; Fan, C.; He, J.; Ding, P.; Xue, Q.; Liang, E. A Novel Planar Metamaterial Design for Electromagnetically Induced Transparency and Slow Light. *Opt Express* **2013**, *21* (21), 25159. https://doi.org/10.1364/oe.21.025159.
(162) Tompkins, H. G.; Irene, E. A. *Handbook of Ellipsometry*; William Andrew Publishing, 2005. https://doi.org/10.1515/arh-2005-0022.
(163) Negara, C. *Fast Polarization State Detection by Division-of-Amplitude in a Simple Configuration Setup*; 2016. https://www.researchgate.net/publication/332859509.
(164) Muller, R. H. *Principles of Ellipsometry*; 1971.

(165) Hajati, S.; Tougaard, S. XPS for Non-Destructive Depth Profiling and 3D Imaging of Surface Nanostructures. *Analytical and Bioanalytical Chemistry*. April 2010, pp 2741–2755. https://doi.org/10.1007/s00216-009-3401-9.
(166) Delcorte, A.; Delmez, V.; Dupont-Gillain, C.; Lauzin, C.; Jefford, H.; Chundak, M.; Poleunis, C.; Moshkunov, K. Large Cluster Ions: Soft Local Probes and Tools for Organic and Bio Surfaces. *Physical Chemistry Chemical Physics*. Royal Society of Chemistry August 21, 2020, pp 17427–17447. https://doi.org/10.1039/d0cp02398a.
(167) Yamada, I.; Matsuo, J.; Toyoda, N.; Aoki, T.; Seki, T. Progress and Applications of Cluster Ion Beam Technology. *Curr Opin Solid State Mater Sci* **2015**, *19* (1), 12–18. https://doi.org/10.1016/j.cossms.2014.11.002.
(168) Giessibl, F. J. *Advances in Atomic Force Microscopy*.
(169) McCoy, D. E.; Shneidman, A. V.; Davis, A. L.; Aizenberg, J. Finite-Difference Time-Domain (FDTD) Optical Simulations: A Primer for the Life Sciences and Bio-Inspired Engineering. *Micron*. Elsevier Ltd December 1, 2021. https://doi.org/10.1016/j.micron.2021.103160.
(170) Taflove, A. *Review of the Formulation and Applications of the Finite-Difference Time-Domain Method for Numerical Modeling of Electromagnetic Wave Interactions with Arbitrary Structures*; 1988; Vol. 10.
(171) Bratton, D.; Yang, D.; Dai, J.; Ober, C. K. Recent Progress in High Resolution Lithography. *Polymers for Advanced Technologies*. February 2006, pp 94–103. https://doi.org/10.1002/pat.662.
(172) Museau, M.; Masclet, C.; Tichkiewitch, S. Integrated Design of MEMS: Aiming at Manufacturability. *International Journal on Interactive Design and Manufacturing (IJIDeM)* **2007**, *1* (3), 127–134. https://doi.org/10.1007/s12008-007-0017-1.
(173) Xia, D.; Ku, Z.; Lee, S. C.; Brueck, S. R. J. Nanostructures and Functional Materials Fabricated by Interferometric Lithography. *Advanced Materials*. January 11, 2011, pp 147–179. https://doi.org/10.1002/adma.201001856.
(174) Tsargorodska, A.; El Zubir, O.; Darroch, B.; Cartron, M. L.; Basova, T.; Hunter, C. N.; Nabok, A. V.; Leggett, G. J. Fast, Simple, Combinatorial Routes to the Fabrication of Reusable, Plasmonically Active Gold Nanostructures by Interferometric Lithography of Self-Assembled Monolayers. *ACS Nano* **2014**. https://doi.org/10.1021/nn5014319.
(175) Tsargorodska, A.; El Zubir, O.; Darroch, B.; Cartron, M. L.; Basova, T.; Hunter, C. N.; Nabok, A. V.; Leggett, G. J. Fast, Simple, Combinatorial Routes to the Fabrication of Reusable, Plasmonically Active Gold Nanostructures by Interferometric Lithography of Self-Assembled Monolayers. *ACS Nano* **2014**, *8* (8), 7858–7869. https://doi.org/10.1021/nn5014319.
(176) Dong, Z.; Wang, T.; Chi, X.; Ho, J.; Tserkezis, C.; Yap, S. L. K.; Rusydi, A.; Tjiptoharsono, F.; Thian, D.; Mortensen, N. A.; Yang, J. K. W. Ultraviolet Interband Plasmonics with Si Nanostructures. *Nano Lett* **2019**, *19* (11), 8040–8048. https://doi.org/10.1021/acs.nanolett.9b03243.
(177) Odobel, F.; Pellegrin, Y.; Warnan, J. Bio-Inspired Artificial Light-Harvesting Antennas for Enhancement of Solar Energy Capture in Dye-Sensitized Solar Cells. *Energy and Environmental Science*. July 2013, pp 2041–2052. https://doi.org/10.1039/c3ee24229c.
(178) Springer, J. W.; Parkes-Loach, P. S.; Reddy, K. R.; Krayer, M.; Jiao, J.; Lee, G. M.; Niedzwiedzki, D. M.; Harris, M. A.; Kirmaier, C.; Bocian, D. F.; Lindsey, J. S.; Holten, D.; Loach, P. A. Biohybrid Photosynthetic Antenna Complexes for Enhanced Light-Harvesting. *J Am Chem Soc* **2012**, *134* (10), 4589–4599. https://doi.org/10.1021/ja207390y.

(179) Ning, Y.; Jin, G. Q.; Zhang, J. L. Porpholactone Chemistry: An Emerging Approach to Bioinspired Photosensitizers with Tunable Near-Infrared Photophysical Properties. *Acc Chem Res* **2019**, *52* (9), 2620–2633. https://doi.org/10.1021/acs.accounts.9b00119.
(180) Brédas, J. L.; Sargent, E. H.; Scholes, G. D. Photovoltaic Concepts Inspired by Coherence Effects in Photosynthetic Systems. *Nature Materials*. Nature Publishing Group December 20, 2016, pp 35–44. https://doi.org/10.1038/nmat4767.
(181) Balaban, T. S. Tailoring Porphyrins and Chlorins for Self-Assembly in Biomimetic Artificial Antenna Systems. *Accounts of Chemical Research*. August 2005, pp 612–623. https://doi.org/10.1021/ar040211z.
(182) Gust, D.; Moore, T. A.; Moore, A. L. Mimicking Photosynthetic Solar Energy Transduction. *Acc Chem Res* **2001**, *34* (1), 40–48. https://doi.org/10.1021/ar9801301.
(183) Gust, D.; Moore, T. A.; Moore, A. L. Solar Fuels via Artificial Photosynthesis. *Acc Chem Res* **2009**, *42* (12), 1890–1898. https://doi.org/10.1021/ar900209b.
(184) Sun, J.; Zhang, J.; Zhang, M.; Antonietti, M.; Fu, X.; Wang, X. Bioinspired Hollow Semiconductor Nanospheres as Photosynthetic Nanoparticles. *Nat Commun* **2012**, *3*. https://doi.org/10.1038/ncomms2152.
(185) Mubeen, S.; Lee, J.; Singh, N.; Krämer, S.; Stucky, G. D.; Moskovits, M. An Autonomous Photosynthetic Device in Which All Charge Carriers Derive from Surface Plasmons. *Nat Nanotechnol* **2013**, *8* (4), 247–251. https://doi.org/10.1038/nnano.2013.18.
(186) Proppe, A. H.; Li, Y. C.; Aspuru-Guzik, A.; Berlinguette, C. P.; Chang, C. J.; Cogdell, R.; Doyle, A. G.; Flick, J.; Gabor, N. M.; van Grondelle, R.; Hammes-Schiffer, S.; Jaffer, S. A.; Kelley, S. O.; Leclerc, M.; Leo, K.; Mallouk, T. E.; Narang, P.; Schlau-Cohen, G. S.; Scholes, G. D.; Vojvodic, A.; Yam, V. W. W.; Yang, J. Y.; Sargent, E. H. Bioinspiration in Light Harvesting and Catalysis. *Nature Reviews Materials*. Nature Research November 1, 2020, pp 828–846. https://doi.org/10.1038/s41578-020-0222-0.
(187) Zhang, T.; Lin, W. Metal-Organic Frameworks for Artificial Photosynthesis and Photocatalysis. *Chemical Society Reviews*. Royal Society of Chemistry August 21, 2014, pp 5982–5993. https://doi.org/10.1039/c4cs00103f.
(188) Hollauf, M.; Trimmel, G.; Knall, A. C. Dye-Functionalized Polymers via Ring Opening Metathesis Polymerization: Principal Routes and Applications. *Monatshefte fur Chemie*. Springer-Verlag Wien July 13, 2015, pp 1063–1080. https://doi.org/10.1007/s00706-015-1493-9.
(189) Ciardelli, F.; Ruggeri, G.; Pucci, A. Dye-Containing Polymers: Methods for Preparation of Mechanochromic Materials. *Chem Soc Rev* **2013**, *42* (3), 857–870. https://doi.org/10.1039/c2cs35414d.
(190) Breul, A. M.; Hager, M. D.; Schubert, U. S. Fluorescent Monomers as Building Blocks for Dye Labeled Polymers: Synthesis and Application in Energy Conversion, Biolabeling and Sensors. *Chem Soc Rev* **2013**, *42* (12), 5366–5407. https://doi.org/10.1039/c3cs35478d.
(191) Wang, C.; Yan, Q.; Liu, H. B.; Zhou, X. H.; Xiao, S. J. Different EDC/NHS Activation Mechanisms between PAA and PMAA Brushes and the Following Amidation Reactions. *Langmuir* **2011**, *27* (19), 12058–12068. https://doi.org/10.1021/la202267p.
(192) Yan, Q.; Zheng, H. N.; Jiang, C.; Li, K.; Xiao, S. J. EDC/NHS Activation Mechanism of Polymethacrylic Acid: Anhydride versus NHS-Ester. *RSC Adv* **2015**, *5* (86), 69939–69947. https://doi.org/10.1039/c5ra13844b.
(193) Perdih, P.; Čebašek, S.; Možir, A.; Žagar, E. Post-Polymerization Modification of Poly(L-Glutamic Acid) with D -(+)-Glucosamine. *Molecules* **2014**, *19* (12), 19751–19768. https://doi.org/10.3390/molecules191219751.

(194) Lillethorup, M.; Shimizu, K.; Plumeré, N.; Pedersen, S. U.; Daasbjerg, K. Surface-Attached Poly(Glycidyl Methacrylate) as a Versatile Platform for Creating Dual-Functional Polymer Brushes. *Macromolecules* **2014**, *47* (15), 5081–5088. https://doi.org/10.1021/ma500872b.
(195) Fairbanks, B. D.; Love, D. M.; Bowman, C. N. Efficient Polymer-Polymer Conjugation via Thiol-Ene Click Reaction. *Macromolecular Chemistry and Physics*. Wiley-VCH Verlag September 1, 2017. https://doi.org/10.1002/macp.201700073.
(196) Neri-Cruz, C. E.; Teixeira, F. M. E.; Gautrot, J. E. A Guide to Functionalisation and Bioconjugation Strategies to Surface-Initiated Polymer Brushes. *Chemical Communications* **2023**. https://doi.org/10.1039/d3cc01082a.
(197) Degirmenci, A.; Yeter Bas, G.; Sanyal, R.; Sanyal, A. "clickable" Polymer Brush Interfaces: Tailoring Monovalent to Multivalent Ligand Display for Protein Immobilization and Sensing. *Bioconjug Chem* **2022**, *33* (9), 1672–1684. https://doi.org/10.1021/acs.bioconjchem.2c00298.
(198) Gevrek, T. N.; Degirmenci, A.; Sanyal, R.; Klok, H. A.; Sanyal, A. Succinimidyl Carbonate-Based Amine-Reactive Polymer Brushes: Facile Fabrication of Functional Interfaces. *ACS Appl Polym Mater* **2021**, *3* (5), 2507–2517. https://doi.org/10.1021/acsapm.1c00107.
(199) Schüwer, N.; Geue, T.; Hinestrosa, J. P.; Klok, H. A. Neutron Reflectivity Study on the Postpolymerization Modification of Poly(2-Hydroxyethyl Methacrylate) Brushes. *Macromolecules* **2011**, *44* (17), 6868–6874. https://doi.org/10.1021/ma201069d.
(200) Zoppe, J. O.; Ataman, N. C.; Mocny, P.; Wang, J.; Moraes, J.; Klok, H. A. Surface-Initiated Controlled Radical Polymerization: State-of-the-Art, Opportunities, and Challenges in Surface and Interface Engineering with Polymer Brushes. *Chem Rev* **2017**, *117* (3), 1105–1318. https://doi.org/10.1021/acs.chemrev.6b00314.
(201) Conard, T.; Vandervorst, W.; Bergmaier, A.; Kimura, K. Thin Layer Composition Profiling with Angular Resolved X-Ray Photoemission Spectroscopy: Factors Affecting Quantitative Results. *Journal of Vacuum Science & Technology A: Vacuum, Surfaces, and Films* **2012**, *30* (3), 031509. https://doi.org/10.1116/1.4704603.
(202) Hofstetter, Y. J.; Vaynzof, Y. Quantifying the Damage Induced by X-Ray Photoelectron Spectroscopy Depth Profiling of Organic Conjugated Polymers. *ACS Appl Polym Mater* **2019**, *1* (6), 1372–1381. https://doi.org/10.1021/acsapm.9b00148.
(203) Holländer, A.; Haupt, M.; Oehr, C. On Depth Profiling of Polymers by Argon Ion Sputtering. *Plasma Processes and Polymers*. November 22, 2007, pp 773–776. https://doi.org/10.1002/ppap.200700092.
(204) Bernasik, A.; Haberko, J.; Marzec, M. M.; Rysz, J.; Łużny, W.; Budkowski, A. Chemical Stability of Polymers under Argon Gas Cluster Ion Beam and X-Ray Irradiation. *Journal of Vacuum Science & Technology B, Nanotechnology and Microelectronics: Materials, Processing, Measurement, and Phenomena* **2016**, *34* (3), 030604. https://doi.org/10.1116/1.4943951.
(205) Nobuta, T.; Ogawa, T. Depth Profile XPS Analysis of Polymeric Materials by C60+ Ion Sputtering. *J Mater Sci* **2009**, *44* (7), 1800–1812. https://doi.org/10.1007/s10853-009-3274-5.
(206) Barbey, R.; Laporte, V.; Alnabulsi, S.; Klok, H. A. Postpolymerization Modification of Poly(Glycidyl Methacrylate) Brushes: An XPS Depth-Profiling Study. *Macromolecules* **2013**, *46* (15), 6151–6158. https://doi.org/10.1021/ma400819a.
(207) Vorobii, M.; Pop-Georgievski, O.; de los Santos Pereira, A.; Kostina, N. Y.; Jezorek, R.; Sedláková, Z.; Percec, V.; Rodriguez-Emmenegger, C. Grafting of Functional Methacrylate Polymer Brushes by Photoinduced SET-LRP. *Polym Chem* **2016**, *7* (45), 6934–6945. https://doi.org/10.1039/c6py01730d.

(208) Karagiovanaki, S.; Koutsioubas, A.; Spiliopoulos, N.; Anastassopoulos, D. L.; Vradis, A. A.; Toprakcioglu, C.; Siokou, A. E. Adsorption of Block Copolymers in Nanoporous Alumina. *J Polym Sci B Polym Phys* **2010**, *48* (14), 1676–1682. https://doi.org/10.1002/polb.21972.
(209) Gilbert, J. B.; Luo, M.; Shelton, C. K.; Rubner, M. F.; Cohen, R. E.; Epps, T. H. Determination of Lithium-Ion Distributions in Nanostructured Block Polymer Electrolyte Thin Films by X-Ray Photoelectron Spectroscopy Depth Profiling. *ACS Nano* **2015**, *9* (1), 512–520. https://doi.org/10.1021/nn505744r.
(210) Schmitt, S. K.; Trebatoski, D. J.; Krutty, J. D.; Xie, A. W.; Rollins, B.; Murphy, W. L.; Gopalan, P. Peptide Conjugation to a Polymer Coating via Native Chemical Ligation of Azlactones for Cell Culture. *Biomacromolecules* **2016**, *17* (3), 1040–1047. https://doi.org/10.1021/acs.biomac.5b01682.
(211) Varol, H. S.; Sánchez, M. A.; Lu, H.; Baio, J. E.; Malm, C.; Encinas, N.; Mermet-Guyennet, M. R. B.; Martzel, N.; Bonn, D.; Bonn, M.; Weidner, T.; Backus, E. H. G.; Parekh, S. H. Multiscale Effects of Interfacial Polymer Confinement in Silica Nanocomposites. *Macromolecules* **2015**, *48* (21), 7929–7937. https://doi.org/10.1021/acs.macromol.5b01111.
(212) Taketa, T. B.; dos Santos, D. M.; Fiamingo, A.; Vaz, J. M.; Beppu, M. M.; Campana-Filho, S. P.; Cohen, R. E.; Rubner, M. F. Investigation of the Internal Chemical Composition of Chitosan-Based LbL Films by Depth-Profiling X-Ray Photoelectron Spectroscopy (XPS) Analysis. *Langmuir* **2018**, *34* (4), 1429–1440. https://doi.org/10.1021/acs.langmuir.7b04104.
(213) Reese, C. M.; Thompson, B. J.; Logan, P. K.; Stafford, C. M.; Blanton, M.; Patton, D. L. Sequential and One-Pot Post-Polymerization Modification Reactions of Thiolactone-Containing Polymer Brushes. *Polym Chem* **2019**, *10* (36), 4935–4943. https://doi.org/10.1039/c9py01123d.
(214) Odobel, F.; Pellegrin, Y.; Warnan, J. Bio-Inspired Artificial Light-Harvesting Antennas for Enhancement of Solar Energy Capture in Dye-Sensitized Solar Cells. *Energy and Environmental Science*. July 2013, pp 2041–2052. https://doi.org/10.1039/c3ee24229c.
(215) Fang, Z.; Ito, A.; Stuart, A. C.; Luo, H.; Chen, Z.; Vinodgopal, K.; You, W.; Meyer, T. J.; Taylor, D. K. Soluble Reduced Graphene Oxide Sheets Grafted with Polypyridylruthenium- Derivatized Polystyrene Brushes as Light Harvesting Antenna for Photovoltaic Applications. *ACS Nano* **2013**, *7* (9), 7992–8002. https://doi.org/10.1021/nn403079z.
(216) Szuwarzyński, M.; Wolski, K.; Pomorska, A.; Uchacz, T.; Gut, A.; Łapok, Ł.; Zapotoczny, S. Photoactive Surface-Grafted Polymer Brushes with Phthalocyanine Bridging Groups as an Advanced Architecture for Light-Harvesting. *Chemistry - A European Journal* **2017**, *23* (47), 11239–11243. https://doi.org/10.1002/chem.201702737.
(217) Badiei, Y. M.; Annon, O.; Maldonado, C.; Delgado, E.; Nguyen, C.; Rivera, C.; Li, C.; Ortega, A. F. Single-Site Molecular Ruthenium(II) Water-Oxidation Catalysts Grafted into a Polymer-Modified Surface for Improved Stability and Efficiency. *ChemElectroChem* **2023**, *10* (7). https://doi.org/10.1002/celc.202300028.
(218) Cedeno, D.; Krawicz, A.; Doak, P.; Yu, M.; Neaton, J. B.; Moore, G. F. Using Molecular Design to Control the Performance of Hydrogen-Producing Polymer-Brush-Modified Photocathodes. *Journal of Physical Chemistry Letters* **2014**, *5* (18), 3222–3226. https://doi.org/10.1021/jz5016394.

(219) Gsänger, M.; Bialas, D.; Huang, L.; Stolte, M.; Würthner, F. Organic Semiconductors Based on Dyes and Color Pigments. *Advanced Materials*. Wiley-VCH Verlag May 18, 2016, pp 3615–3645. https://doi.org/10.1002/adma.201505440.
(220) Beiler, A. M.; Khusnutdinova, D.; Jacob, S. I.; Moore, G. F. Chemistry at the Interface: Polymer-Functionalized GaP Semiconductors for Solar Hydrogen Production. *Ind Eng Chem Res* **2016**, *55* (18), 5306–5314. https://doi.org/10.1021/acs.iecr.6b00478.
(221) Beaujuge, P. M.; Reynolds, J. R. Color Control in π-Conjugated Organic Polymers for Use in Electrochromic Devices. *Chem Rev* **2010**, *110* (1), 268–320. https://doi.org/10.1021/cr900129a.
(222) Ohno, K.; Mizuta, Y. Structural Color Materials Using Polymer-Brush-Decorated Hybrid Particles. *ACS Appl Polym Mater* **2020**, *2* (2), 368–375. https://doi.org/10.1021/acsapm.9b00839.
(223) Alswieleh, A. M.; Cheng, N.; Canton, I.; Ustbas, B.; Xue, X.; Ladmiral, V.; Xia, S.; Ducker, R. E.; Zubir, O. el; Cartron, M. L.; Hunter, C. N.; Leggett, G. J.; Armes, S. P. Zwitterionic Poly(Amino Acid Methacrylate) Brushes. **2014**. https://doi.org/10.1021/ja503400r.
(224) Nelson, K. E.; Gamble, L.; Jung, L. S.; Boeckl, M. S.; Naeemi, E.; Golledge, S. L.; Sasaki, T.; Castner, D. G.; Campbell, C. T.; Stayton, P. S. Surface Characterization of Mixed Self-Assembled Monolayers Designed for Streptavidin Immobilization. *Langmuir* **2001**, *17* (9), 2807–2816. https://doi.org/10.1021/la001111e.
(225) Kang, J. F.; Liao, S.; Jordan, R.; Ulman, A. *Mixed Self-Assembled Monolayers of Rigid Biphenyl Thiols: Impact of Solvent and Dipole Moment*; 1998. https://pubs.acs.org/sharingguidelines.
(226) Chen, S.; Li, L.; Boozer, C. L.; Jiang, S. Controlled Chemical and Structural Properties of Mixed Self-Assembled Monolayers by Coadsorption of Symmetric and Asymmetric Bisulfides on Au(111). *Journal of Physical Chemistry B* **2001**, *105* (15), 2975–2980. https://doi.org/10.1021/jp0040650.
(227) Lacour, V.; Moumanis, K.; Hassen, W. M.; Elie-Caille, C.; Leblois, T.; Dubowski, J. J. Formation Kinetics of Mixed Self-Assembled Monolayers of Alkanethiols on GaAs(100). *Langmuir* **2019**, *35* (13), 4415–4427. https://doi.org/10.1021/acs.langmuir.7b00929.
(228) Bain, C. D.; Biebuyck, H. A.; Whitesides, G. M. *Comparison of Self-Assembled Monolayers on Gold: Coadsorption of Thiols and Disulfidesr*; 1989; Vol. 5.
(229) Moon, J. H.; La, Y. H.; Shim, J. Y.; Hong, B. J.; Kim, K. J.; Kang, T. H.; Kim, B.; Kang, H.; Park, J. W. Selective Cleavage of the Carbon-Halide Bond in Substituted Benzaldimine Monolayers by Synchrotron Soft X-Ray: Anomalously Large Cleavage Rate of the Carbon-Bromide Bond. *Langmuir* **2000**, *16* (6), 2981–2984. https://doi.org/10.1021/la991061h.
(230) Brittain, W. J.; Minko, S. A Structural Definition of Polymer Brushes. *J Polym Sci A Polym Chem* **2007**, *45* (16), 3505–3512. https://doi.org/10.1002/pola.22180.
(231) Dukes, D.; Li, Y.; Lewis, S.; Benicewicz, B.; Schadler, L.; Kumar, S. K. Conformational Transitions of Spherical Polymer Brushes: Synthesis, Characterization, and Theory. *Macromolecules* **2010**, *43* (3), 1564–1570. https://doi.org/10.1021/ma901228t.
(232) Wu, T.; Efimenko, K.; Genzer, J. Combinatorial Study of the Mushroom-to-Brush Crossover in Surface Anchored Polyacrylamide. *J Am Chem Soc* **2002**, *124* (32), 9394–9395. https://doi.org/10.1021/ja027412n.
(233) Li, M.; Jiang, S.; Simon, J.; Paßlick, D.; Frey, M. L.; Wagner, M.; Mailander, V.; Crespy, D.; Landfester, K. Brush Conformation of Polyethylene Glycol Determines the

Stealth Effect of Nanocarriers in the Low Protein Adsorption Regime. *Nano Lett* **2021**, *21* (4), 1591–1598. https://doi.org/10.1021/acs.nanolett.0c03756.
(234) High Resolution XPS of Organic Polymers: The Scienta ESCA300 Database (Beamson, G.; Briggs, D.). *J Chem Educ* **1993**, *70* (1), A25. https://doi.org/10.1021/ed070pA25.5.
(235) Bourg, M. C.; Badia, A.; Bruce Lennox, R. Gold-Sulfur Bonding in 2D and 3D Self-Assembled Monolayers: XPS Characterization. *Journal of Physical Chemistry B* **2000**, *104* (28), 6562–6567. https://doi.org/10.1021/jp9935337.
(236) D. Briggs; M. P. Seah. *Practical Surface Analysis, Auger and X-Ray Photoelectron Spectroscopy*; Wiley, 1990; Vol. 1.
(237) Jung, L. S.; Campbell, C. T. Sticking Probabilities in Adsorption of Alkanethiols from Liquid Ethanol Solution onto Gold. *Journal of Physical Chemistry B* **2000**, *104* (47), 11168–11178. https://doi.org/10.1021/jp001649t.
(238) Zhang, Z.; Moxey, M.; Alswieleh, A.; Morse, A. J.; Lewis, A. L.; Geoghegan, M.; Leggett, G. J. Effect of Salt on Phosphorylcholine-Based Zwitterionic Polymer Brushes. *Langmuir* **2016**, *32* (20), 5048–5057. https://doi.org/10.1021/acs.langmuir.6b00763.
(239) Tolba, S. A.; Xia, W. Molecular Insights into the Hydration of Zwitterionic Polymers. *Mol Syst Des Eng* **2023**. https://doi.org/10.1039/d3me00020f.
(240) Spampinato, V.; Ceccone, G.; Giordani, S. Surface Analysis of Zinc-Porphyrin Functionalized Carbon Nano-Onions. *Biointerphases* **2015**, *10* (1), 019006. https://doi.org/10.1116/1.4907726.
(241) Spitaleri, L.; Gangemi, C. M. A.; Purrello, R.; Nicotra, G.; Sfrazzetto, G. T.; Casella, G.; Casarin, M.; Gulino, A. Covalently Conjugated Gold–Porphyrin Nanostructures. *Nanomaterials* **2020**, *10* (9), 1–19. https://doi.org/10.3390/nano10091644.
(242) Hutt, D. A.; Leggett, G. J. *Influence of Adsorbate Ordering on Rates of UV Photooxidation of Self-Assembled Monolayers*; 1996. https://pubs.acs.org/sharingguidelines.
(243) Johnson, A.; Madsen, J.; Chapman, P.; Alswieleh, A.; Al-Jaf, O.; Bao, P.; Hurley, C. R.; Cartron, M. L.; Evans, S. D.; Hobbs, J. K.; Hunter, C. N.; Armes, S. P.; Leggett, G. J. Micrometre and Nanometre Scale Patterning of Binary Polymer Brushes, Supported Lipid Bilayers and Proteins. *Chem Sci* **2017**, *8* (6), 4517–4526. https://doi.org/10.1039/c7sc00289k.
(244) Aden, B.; Kite, C. M.; Hopkins, B. W.; Zetterberg, A.; Lokitz, B. S.; Ankner, J. F.; Kilbey, S. M. Assessing Chemical Transformation of Reactive, Interfacial Thin Films Made of End-Tethered Poly(2-Vinyl-4,4-Dimethyl Azlactone) (PVDMA) Chains. *Macromolecules* **2017**, *50* (2), 618–630. https://doi.org/10.1021/acs.macromol.6b01999.
(245) Schüwer, N.; Geue, T.; Hinestrosa, J. P.; Klok, H. A. Neutron Reflectivity Study on the Postpolymerization Modification of Poly(2-Hydroxyethyl Methacrylate) Brushes. *Macromolecules* **2011**, *44* (17), 6868–6874. https://doi.org/10.1021/ma201069d.
(246) Luo, D.; Li, X.; Dumont, A.; Yu, H.; Lu, Z. H. Recent Progress on Perovskite Surfaces and Interfaces in Optoelectronic Devices. *Advanced Materials*. John Wiley and Sons Inc July 1, 2021. https://doi.org/10.1002/adma.202006004.
(247) Kovalenko, M. V; Protesescu, L.; Bodnarchuk, M. I. Properties and Potential Optoelectronic Applications of Lead Halide Perovskite Nanocrystals. *Science (1979)* **2017**, *358*, 2023.
(248) Polavarapu, L.; Nickel, B.; Feldmann, J.; Urban, A. S. Advances in Quantum-Confined Perovskite Nanocrystals for Optoelectronics. *Adv Energy Mater* **2017**, *7* (16). https://doi.org/10.1002/aenm.201700267.

(249) Fu, Y.; Zhu, H.; Chen, J.; Hautzinger, M. P.; Zhu, X. Y.; Jin, S. Metal Halide Perovskite Nanostructures for Optoelectronic Applications and the Study of Physical Properties. *Nature Reviews Materials*. Nature Publishing Group March 1, 2019, pp 169–188. https://doi.org/10.1038/s41578-019-0080-9.
(250) Sutherland, B. R.; Sargent, E. H. Perovskite Photonic Sources. *Nature Photonics*. Nature Publishing Group May 1, 2016, pp 295–302. https://doi.org/10.1038/nphoton.2016.62.
(251) Van Le, Q.; Jang, H. W.; Kim, S. Y. Recent Advances toward High-Efficiency Halide Perovskite Light-Emitting Diodes: Review and Perspective. *Small Methods* **2018**, *2* (10), 1700419. https://doi.org/10.1002/smtd.201700419.
(252) Wang, K.; Xing, G.; Song, Q.; Xiao, S. Micro- and Nanostructured Lead Halide Perovskites: From Materials to Integrations and Devices. *Advanced Materials*. Wiley-VCH Verlag February 1, 2021. https://doi.org/10.1002/adma.202000306.
(253) Akkerman, Q. A.; Rainò, G.; Kovalenko, M. V.; Manna, L. Genesis, Challenges and Opportunities for Colloidal Lead Halide Perovskite Nanocrystals. *Nat Mater* **2018**, *17* (5), 394–405. https://doi.org/10.1038/s41563-018-0018-4.
(254) Huang, H.; Polavarapu, L.; Sichert, J. A.; Susha, A. S.; Urban, A. S.; Rogach, A. L. Colloidal Lead Halide Perovskite Nanocrystals: Synthesis, Optical Properties and Applications. *NPG Asia Materials*. Nature Research 2016. https://doi.org/10.1038/am.2016.167.
(255) Zhang, J.; Zhang, S.; Zhang, Y.; Al-Hartomy, O. A.; Wageh, S.; Al-Sehemi, A. G.; Hao, Y.; Gao, L.; Wang, H.; Zhang, H. Colloidal Quantum Dots: Synthesis, Composition, Structure, and Emerging Optoelectronic Applications. *Laser and Photonics Reviews*. John Wiley and Sons Inc March 1, 2022. https://doi.org/10.1002/lpor.202200551.
(256) Yang, D.; Zhao, B.; Yang, T.; Lai, R.; Lan, D.; Friend, R. H.; Di, D. Toward Stable and Efficient Perovskite Light-Emitting Diodes. *Advanced Functional Materials*. John Wiley and Sons Inc February 1, 2022. https://doi.org/10.1002/adfm.202109495.
(257) Liu, X. K.; Xu, W.; Bai, S.; Jin, Y.; Wang, J.; Friend, R. H.; Gao, F. Metal Halide Perovskites for Light-Emitting Diodes. *Nature Materials*. Nature Research January 1, 2021, pp 10–21. https://doi.org/10.1038/s41563-020-0784-7.
(258) Song, J.; Li, J.; Li, X.; Xu, L.; Dong, Y.; Zeng, H. Quantum Dot Light-Emitting Diodes Based on Inorganic Perovskite Cesium Lead Halides (CsPbX3). *Advanced Materials* **2015**, *27* (44), 7162–7167. https://doi.org/10.1002/adma.201502567.
(259) Li, C.; Wang, H.; Wang, F.; Li, T.; Xu, M.; Wang, H.; Wang, Z.; Zhan, X.; Hu, W.; Shen, L. Ultrafast and Broadband Photodetectors Based on a Perovskite/Organic Bulk Heterojunction for Large-Dynamic-Range Imaging. *Light Sci Appl* **2020**, *9* (1). https://doi.org/10.1038/s41377-020-0264-5.
(260) Lu, X.; Li, J.; Zhang, Y.; Han, Z.; He, Z.; Zou, Y.; Xu, X. Recent Progress on Perovskite Photodetectors for Narrowband Detection. *Adv Photonics Res* **2022**, *3* (5), 2100335. https://doi.org/10.1002/adpr.202100335.
(261) Fang, Y.; Dong, Q.; Shao, Y.; Yuan, Y.; Huang, J. Highly Narrowband Perovskite Single-Crystal Photodetectors Enabled by Surface-Charge Recombination. *Nat Photonics* **2015**, *9* (10), 679–686. https://doi.org/10.1038/nphoton.2015.156.
(262) Hu, F.; Zhang, H.; Sun, C.; Yin, C.; Lv, B.; Zhang, C.; Yu, W. W.; Wang, X.; Zhang, Y.; Xiao, M. Superior Optical Properties of Perovskite Nanocrystals as Single Photon Emitters. *ACS Nano* **2015**, *9* (12), 12410–12416. https://doi.org/10.1021/acsnano.5b05769.

(263) Jia, Y.; Kerner, R. A.; Grede, A. J.; Rand, B. P.; Giebink, N. C. Continuous-Wave Lasing in an Organic-Inorganic Lead Halide Perovskite Semiconductor. *Nat Photonics* **2017**, *11* (12), 784–788. https://doi.org/10.1038/s41566-017-0047-6.

(264) Liu, A.; Guan, G.; Chai, X.; Feng, N.; Lu, M.; Bai, X.; Zhang, Y. Metal Halide Perovskites toward Electrically Pumped Lasers. *Laser and Photonics Reviews*. John Wiley and Sons Inc October 1, 2022. https://doi.org/10.1002/lpor.202200189.

(265) Steele, J. A.; Puech, P.; Monserrat, B.; Wu, B.; Yang, R. X.; Kirchartz, T.; Yuan, H.; Fleury, G.; Giovanni, D.; Fron, E.; Keshavarz, M.; Debroye, E.; Zhou, G.; Sum, T. C.; Walsh, A.; Hofkens, J.; Roeffaers, M. B. J. Role of Electron-Phonon Coupling in the Thermal Evolution of Bulk Rashba-Like Spin-Split Lead Halide Perovskites Exhibiting Dual-Band Photoluminescence. *ACS Energy Lett* **2019**, *4* (9), 2205–2212. https://doi.org/10.1021/acsenergylett.9b01427.

(266) Dong, Z.; Mahfoud, Z.; Paniagua-Domínguez, R.; Wang, H.; Fernández-Domínguez, A. I.; Gorelik, S.; Ha, S. T.; Tjiptoharsono, F.; Kuznetsov, A. I.; Bosman, M.; Yang, J. K. W. Nanoscale Mapping of Optically Inaccessible Bound-States-in-the-Continuum. *Light Sci Appl* **2022**, *11* (1). https://doi.org/10.1038/s41377-021-00707-2.

(267) Kruk, S. S.; Wang, L.; Sain, B.; Dong, Z.; Yang, J.; Zentgraf, T.; Kivshar, Y. Asymmetric Parametric Generation of Images with Nonlinear Dielectric Metasurfaces. *Nat Photonics* **2022**, *16* (8), 561–565. https://doi.org/10.1038/s41566-022-01018-7.

(268) Kuznetsov, A. I.; Miroshnichenko, A. E.; Brongersma, M. L.; Kivshar, Y. S.; Luk'yanchuk, B. Optically Resonant Dielectric Nanostructures. *Science*. American Association for the Advancement of Science November 18, 2016. https://doi.org/10.1126/science.aag2472.

(269) Koshelev, K.; Lepeshov, S.; Liu, M.; Bogdanov, A.; Kivshar, Y. Asymmetric Metasurfaces with High- Q Resonances Governed by Bound States in the Continuum. *Phys Rev Lett* **2018**, *121* (19). https://doi.org/10.1103/PhysRevLett.121.193903.

(270) Tiguntseva, E. Y.; Zograf, G. P.; Komissarenko, F. E.; Zuev, D. A.; Zakhidov, A. A.; Makarov, S. V.; Kivshar, Y. S. Light-Emitting Halide Perovskite Nanoantennas. *Nano Lett* **2018**, *18* (2), 1185–1190. https://doi.org/10.1021/acs.nanolett.7b04727.

(271) Tiguntseva, E. Y.; Zograf, G. P.; Komissarenko, F. E.; Zuev, D. A.; Zakhidov, A. A.; Makarov, S. V.; Kivshar, Y. S. Light-Emitting Halide Perovskite Nanoantennas. *Nano Lett* **2018**, *18* (2), 1185–1190. https://doi.org/10.1021/acs.nanolett.7b04727.

(272) Gholipour, B.; Adamo, G.; Cortecchia, D.; Krishnamoorthy, H. N. S.; Birowosuto, M. D.; Zheludev, N. I.; Soci, C. Organometallic Perovskite Metasurfaces. *Advanced Materials* **2017**, *29* (9). https://doi.org/10.1002/adma.201604268.

(273) Carreño, J. M.; Passarelli, N.; Otero-Martínez, C.; Polavarapu, L.; Pérez, L. A.; Reparaz, J. S.; Alonso, M. I.; Mihi, A. Enhanced Photoluminescence of Cesium Lead Halide Perovskites by Quasi-3D Photonic Crystals. *Adv Opt Mater* **2022**, *10* (3). https://doi.org/10.1002/adom.202101324.

(274) Fan, Y.; Wang, Y.; Zhang, N.; Sun, W.; Gao, Y.; Qiu, C. W.; Song, Q.; Xiao, S. Resonance-Enhanced Three-Photon Luminesce via Lead Halide Perovskite Metasurfaces for Optical Encoding. *Nat Commun* **2019**, *10* (1). https://doi.org/10.1038/s41467-019-10090-7.

(275) Klein, M.; Wang, Y.; Tian, J.; Ha, S. T.; Paniagua-Domínguez, R.; Kuznetsov, A. I.; Adamo, G.; Soci, C. Polarization-Tunable Perovskite Light-Emitting Metatransistor. *Advanced Materials* **2023**, *35* (1). https://doi.org/10.1002/adma.202207317.

(276) Tian, J.; Adamo, G.; Liu, H.; Klein, M.; Han, S.; Liu, H.; Soci, C. Optical Rashba Effect in a Light-Emitting Perovskite Metasurface. *Advanced Materials* **2022**, *34* (12). https://doi.org/10.1002/adma.202109157.

(277) Chen, Y.; Feng, J.; Huang, Y.; Chen, W.; Su, R.; Ghosh, S.; Hou, Y.; Xiong, Q.; Qiu, C. W. Compact Spin-Valley-Locked Perovskite Emission. *Nat Mater* **2023**. https://doi.org/10.1038/s41563-023-01531-2.
(278) Mendoza-Carreño, J.; Molet, P.; Otero-Martínez, C.; Alonso, M. I.; Polavarapu, L.; Mihi, A. Nanoimprinted 2D-Chiral Perovskite Nanocrystal Metasurfaces for Circularly Polarized Photoluminescence. *Advanced Materials* **2023**. https://doi.org/10.1002/adma.202210477.
(279) Dong, Z.; Mahfoud, Z.; Paniagua-Domínguez, R.; Wang, H.; Fernández-Domínguez, A. I.; Gorelik, S.; Ha, S. T.; Tjiptoharsono, F.; Kuznetsov, A. I.; Bosman, M.; Yang, J. K. W. Nanoscale Mapping of Optically Inaccessible Bound-States-in-the-Continuum. *Light Sci Appl* **2022**, *11* (1). https://doi.org/10.1038/s41377-021-00707-2.
(280) Purcell, E. M. Spontaneous Emission Probabilities at Radio Frequencies. *Physical Review* **1946**, *69*, 681–681. https://doi.org/doi:10.1007/978-1-4615-1963-8_40.
(281) Colom, R.; Binkowski, F.; Betz, F.; Kivshar, Y.; Burger, S. Enhanced Purcell Factor for Nanoantennas Supporting Interfering Resonances. *Phys Rev Res* **2022**, *4* (2). https://doi.org/10.1103/PhysRevResearch.4.023189.
(282) Jung, C.; Kim, G.; Jeong, M.; Jang, J.; Dong, Z.; Badloe, T.; Yang, J. K. W.; Rho, J. Metasurface-Driven Optically Variable Devices. *Chemical Reviews*. American Chemical Society November 10, 2021, pp 13013–13050. https://doi.org/10.1021/acs.chemrev.1c00294.
(283) Wang, K.; Xing, G.; Song, Q.; Xiao, S. Micro- and Nanostructured Lead Halide Perovskites: From Materials to Integrations and Devices. *Advanced Materials*. Wiley-VCH Verlag February 1, 2021. https://doi.org/10.1002/adma.202000306.
(284) Zhang, C.; Xiao, S.; Wang, Y.; Gao, Y.; Fan, Y.; Huang, C.; Zhang, N.; Yang, W.; Song, Q. Lead Halide Perovskite-Based Dynamic Metasurfaces. *Laser Photon Rev* **2019**, *13* (7). https://doi.org/10.1002/lpor.201900079.
(285) Ren, A.; Wang, H.; Zhang, W.; Wu, J.; Wang, Z.; Penty, R. V.; White, I. H. Emerging Light-Emitting Diodes for next-Generation Data Communications. *Nature Electronics*. Nature Research August 1, 2021, pp 559–572. https://doi.org/10.1038/s41928-021-00624-7.
(286) Wang, K.; Wang, S.; Xiao, S.; Song, Q. Recent Advances in Perovskite Micro- and Nanolasers. *Advanced Optical Materials*. Wiley-VCH Verlag September 18, 2018. https://doi.org/10.1002/adom.201800278.
(287) Ren, A.; Wang, H.; Zhang, W.; Wu, J.; Wang, Z.; Penty, R. V.; White, I. H. Emerging Light-Emitting Diodes for next-Generation Data Communications. *Nature Electronics*. Nature Research August 1, 2021, pp 559–572. https://doi.org/10.1038/s41928-021-00624-7.
(288) Palik, E. D. *Handbook of Optical Constants of Solids*; Academic Press : San Diego, 1998.
(289) Dong, Z.; Ho, J.; Yu, Y. F.; Fu, Y. H.; Paniagua-Dominguez, R.; Wang, S.; Kuznetsov, A. I.; Yang, J. K. W. Printing beyond SRGB Color Gamut by Mimicking Silicon Nanostructures in Free-Space. *Nano Lett* **2017**, *17* (12), 7620–7628. https://doi.org/10.1021/acs.nanolett.7b03613.
(290) Xu, J.; Dong, Z.; Asbahi, M.; Wu, Y.; Wang, H.; Liang, L.; Ng, R. J. H.; Liu, H.; Vallée, R. A. L.; Yang, J. K. W.; Liu, X. Multiphoton Upconversion Enhanced by Deep Subwavelength Near-Field Confinement. *Nano Lett* **2021**, *21* (7), 3044–3051. https://doi.org/10.1021/acs.nanolett.1c00232.
(291) Dong, Z.; Asbahi, M.; Lin, J.; Zhu, D.; Wang, Y. M.; Hippalgaonkar, K.; Chu, H. S.; Goh, W. P.; Wang, F.; Huang, Z.; Yang, J. K. W. Second-Harmonic Generation from Sub-5 Nm Gaps by Directed Self-Assembly of Nanoparticles onto Template-Stripped

Gold Substrates. *Nano Lett* **2015**, *15* (9), 5976–5981. https://doi.org/10.1021/acs.nanolett.5b02109.
(292) Fu, M.; Tamarat, P.; Trebbia, J. B.; Bodnarchuk, M. I.; Kovalenko, M. V.; Even, J.; Lounis, B. Unraveling Exciton–Phonon Coupling in Individual FAPbI3 Nanocrystals Emitting near-Infrared Single Photons. *Nat Commun* **2018**, *9* (1). https://doi.org/10.1038/s41467-018-05876-0.
(293) Hider, M. H.; Leung, P. T. Frequency Shifts of Molecules at Rough Metal Surfaces. *Phys Rev B* **1991**, *44*, 15–1991.
(294) Novotny, L.; Hecht, B. *Principles of Nano-Optics*; Cambridge University Press: Cambridge, 2006.
(295) Fang, H. H.; Wang, F.; Adjokatse, S.; Zhao, N.; Even, J.; Loi, M. A. Photoexcitation Dynamics in Solution-Processed Formamidinium Lead Iodide Perovskite Thin Films for Solar Cell Applications. *Light Sci Appl* **2016**, *5*. https://doi.org/10.1038/lsa.2016.56.
(296) Adl, H. P.; Gorji, S.; Habil, M. K.; Suárez, I.; Chirvony, V. S.; Gualdrón-Reyes, A. F.; Mora-Seró, I.; Valencia, L. M.; De La Mata, M.; Hernández-Saz, J.; Molina, S. I.; Zapata-Rodríguez, C. J.; Martínez-Pastor, J. P. Purcell Enhancement and Wavelength Shift of Emitted Light by CsPbI3Perovskite Nanocrystals Coupled to Hyperbolic Metamaterials. *ACS Photonics* **2020**, *7* (11), 3152–3160. https://doi.org/10.1021/acsphotonics.0c01219.
(297) Couteau, C.; Barz, S.; Durt, T.; Gerrits, T.; Huwer, J.; Prevedel, R.; Rarity, J.; Shields, A.; Weihs, G. Applications of Single Photons to Quantum Communication and Computing. *Nature Reviews Physics*. Springer Nature June 1, 2023. https://doi.org/10.1038/s42254-023-00583-2.
(298) Hu, C. Le; Perevalov, V. I.; Cheng, C. F.; Hua, T. P.; Liu, A. W.; Sun, Y. R.; Tan, Y.; Wang, J.; Hu, S. M. Optical-Optical Double-Resonance Absorption Spectroscopy of Molecules with Kilohertz Accuracy. *Journal of Physical Chemistry Letters* **2020**, *11* (18), 7843–7848. https://doi.org/10.1021/acs.jpclett.0c02136.
(299) Toudert, J.; Serna, R. Interband Transitions in Semi-Metals, Semiconductors, and Topological Insulators: A New Driving Force for Plasmonics and Nanophotonics [Invited]. *Opt Mater Express* **2017**, *7* (7), 2299. https://doi.org/10.1364/ome.7.002299.
(300) Agarwal, A.; Vitiello, M. S.; Viti, L.; Cupolillo, A.; Politano, A. Plasmonics with Two-Dimensional Semiconductors: From Basic Research to Technological Applications. *Nanoscale*. Royal Society of Chemistry May 21, 2018, pp 8938–8946. https://doi.org/10.1039/c8nr01395k.
(301) Toudert, J.; Serna, R. *Interband Plasmonics with P-Block Elements*.
(302) Toudert, J.; Serna, R.; Camps, I.; Wojcik, J.; Mascher, P.; Rebollar, E.; Ezquerra, T. A. Unveiling the Far Infrared-to-Ultraviolet Optical Properties of Bismuth for Applications in Plasmonics and Nanophotonics. *Journal of Physical Chemistry C* **2017**, *121* (6), 3511–3521. https://doi.org/10.1021/acs.jpcc.6b10331.
(303) McMahon, J. M.; Schatz, G. C.; Gray, S. K. Plasmonics in the Ultraviolet with the Poor Metals Al, Ga, In, Sn, Tl, Pb, and Bi. *Physical Chemistry Chemical Physics* **2013**, *15* (15), 5415–5423. https://doi.org/10.1039/c3cp43856b.
(304) Camden, J. P.; Dieringer, J. A.; Zhao, J.; Van Duyne, R. P. Controlled Plasmonic Nanostructures for Surface-Enhanced Spectroscopy and Sensing. *Acc Chem Res* **2008**, *41* (12), 1653–1661. https://doi.org/10.1021/ar800041s.
(305) Chowdhury, M. H.; Ray, K.; Gray, S. K.; Pond, J.; Lakowicz, J. R. Aluminum Nanoparticles as Substrates for Metal-Enhanced Fluorescence in the Ultraviolet for the Label-Free Detection of Biomolecules. *Anal Chem* **2009**, *81* (4), 1397–1403. https://doi.org/10.1021/ac802118s.

(306) Jha, S. K.; Ahmed, Z.; Agio, M.; Ekinci, Y.; Löffler, J. F. Deep-UV Surface-Enhanced Resonance Raman Scattering of Adenine on Aluminum Nanoparticle Arrays. *J Am Chem Soc* **2012**, *134* (4), 1966–1969. https://doi.org/10.1021/ja210446w.
(307) Heremans, J. P.; Cava, R. J.; Samarth, N. Tetradymites as Thermoelectrics and Topological Insulators. *Nature Reviews Materials*. Nature Publishing Group September 5, 2017. https://doi.org/10.1038/natrevmats.2017.49.
(308) Poudel, B.; Qing, H.; Yi, M.; Yucheng, L.; Austin, M.; Bo, Y.; Yan, X.; Wang, D.; Muto, A.; Vashaee, D.; Chen, X.; Liu, J.; Dresselhaus S., M.; Chen, G.; Ren, Z. High-Thermoelectric Performance of Nanostructured Bismuth Antimony Telluride Bulk Alloys. *Science (1979)* **2008**, *320* (5876), 630–638. https://doi.org/10.1126/science.1155140.
(309) Tao, A.; Sinsermsuksakul, P.; Yang, P. Tunable Plasmonic Lattices of Silver Nanocrystals. *Nat Nanotechnol* **2007**, *2* (7), 435–440. https://doi.org/10.1038/nnano.2007.189.
(310) Todorov, R.; Hristova-Vasileva, T.; Katrova, V.; Atanasova, A. Silver and Gold Containing Compounds of P-Block Elements As Perspective Materials for UV Plasmonics. *ACS Omega*. American Chemical Society April 25, 2022. https://doi.org/10.1021/acsomega.2c05943.
(311) Piccinotti, D.; Gholipour, B.; Yao, J.; MacDonald, K. F.; Hayden, B. E.; Zheludev, N. I. Stoichiometric Engineering of Chalcogenide Semiconductor Alloys for Nanophotonic Applications. *Advanced Materials* **2019**, *31* (14). https://doi.org/10.1002/adma.201807083.
(312) Li, M.; Cushing, S. K.; Wu, N. Plasmon-Enhanced Optical Sensors: A Review. *Analyst*. Royal Society of Chemistry January 21, 2015, pp 386–406. https://doi.org/10.1039/c4an01079e.
(313) Zhu, X.; Imran Hossain, G. M.; George, M.; Farhang, A.; Cicek, A.; Yanik, A. A. Beyond Noble Metals: High Q-Factor Aluminum Nanoplasmonics. *ACS Photonics* **2020**, *7* (2), 416–424. https://doi.org/10.1021/acsphotonics.9b01368.
(314) Chorsi, H. T.; Lee, Y.; Alù, A.; Zhang, J. X. J. Tunable Plasmonic Substrates with Ultrahigh Q-Factor Resonances. *Sci Rep* **2017**, *7* (1). https://doi.org/10.1038/s41598-017-16288-3.
(315) West, P. R.; Ishii, S.; Naik, G. V.; Emani, N. K.; Shalaev, V. M.; Boltasseva, A. Searching for Better Plasmonic Materials. *Laser and Photonics Reviews*. November 2010, pp 795–808. https://doi.org/10.1002/lpor.200900055.
(316) Artar, A.; Yanik, A. A.; Altug, H. Fabry-Ṕerot Nanocavities in Multilayered Plasmonic Crystals for Enhanced Biosensing. *Appl Phys Lett* **2009**, *95* (5). https://doi.org/10.1063/1.3202391.
(317) Ameling, R.; Langguth, L.; Hentschel, M.; Mesch, M.; Braun, P. V.; Giessen, H. Cavity-Enhanced Localized Plasmon Resonance Sensing. *Appl Phys Lett* **2010**, *97* (25). https://doi.org/10.1063/1.3530795.
(318) Ciracì, C.; Hill, R. T.; Mock, J. J.; Urzhumov, Y.; Fernández-Domínguez, A. I.; Maier, S. A.; Pendry, J. B.; Chilkoti, A.; Smith, D. R. Probing the Ultimate Limits of Plasmonic Enhancement. *Science (1979)* **2012**, *337* (6098), 1072–1074. https://doi.org/10.1126/science.1224823.
(319) Bahramipanah, M.; Dutta-Gupta, S.; Abasahl, B.; Martin, O. J. F. Cavity-Coupled Plasmonic Device with Enhanced Sensitivity and Figure-of-Merit. *ACS Nano* **2015**, *9* (7), 7621–7633. https://doi.org/10.1021/acsnano.5b02977.
(320) Yew, P. Y. M.; Zhu, D. D.; Lin, Q. Y.; Jiang, L.; Chee, P. L.; Leong, H. S.; Dong, Z.; Guo, X. D.; Kai, D.; Loh, X. J. Synergistic UV Protection Effects of the Lignin

Nanodiamond Complex. *Mater Today Chem* **2021**, *22*. https://doi.org/10.1016/j.mtchem.2021.100574.

(321) Olmon, R. L.; Krenz, P. M.; Jones, A. C.; Boreman, G. D.; Raschke, M. B. Near-Field Imaging of Optical Antenna in the Mid-Infrared. *Optical Society of America* **2008**, *16* (25), 20295–20305.

(322) Reinhard, B. M. Plasmonic Enhancement Strategies for Light-Driven Microbe Inactivation. *Journal of Physical Chemistry C*. American Chemical Society February 10, 2022, pp 2325–2335. https://doi.org/10.1021/acs.jpcc.1c09951.

(323) Kunz, J. N.; Voronine, D. V.; Lu, W.; Liege, Z.; Lee, H. W. H.; Zhang, Z.; Scully, M. O. Aluminum Plasmonic Nanoshielding in Ultraviolet Inactivation of Bacteria. *Sci Rep* **2017**, *7* (1). https://doi.org/10.1038/s41598-017-08593-8.

(324) Zhou, N.; López-Puente, V.; Wang, Q.; Polavarapu, L.; Pastoriza-Santos, I.; Xu, Q. H. Plasmon-Enhanced Light Harvesting: Applications in Enhanced Photocatalysis, Photodynamic Therapy and Photovoltaics. *RSC Advances*. Royal Society of Chemistry 2015, pp 29076–29097. https://doi.org/10.1039/c5ra01819f.

(325) An, C.; Wang, S.; Sun, Y.; Zhang, Q.; Zhang, J.; Wang, C.; Fang, J. Plasmonic Silver Incorporated Silver Halides for Efficient Photocatalysis. *Journal of Materials Chemistry A*. Royal Society of Chemistry 2016, pp 4336–4352. https://doi.org/10.1039/c5ta07719b.

(326) Anker N., J.; Hall W., P.; Lyandres, O.; Shah C. Nilam; Zhao, J.; Duyne P. Van, R. Biosensing with Plasmonic Nanosensors. *Nat Mater* **2008**, *7*, 443–453.

(327) Zhao, D.; Lin, Z.; Zhu, W.; Lezec, H. J.; Xu, T.; Agrawal, A.; Zhang, C.; Huang, K. Recent Advances in Ultraviolet Nanophotonics: From Plasmonics and Metamaterials to Metasurfaces. *Nanophotonics*. De Gruyter Open Ltd July 1, 2021, pp 2283–2308. https://doi.org/10.1515/nanoph-2021-0083.

(328) Qu, Y.; Bai, Y.; Aba, T.; Ullah, H.; Abudukelimu, A.; Huang, J.; Gou, T.; Li, J.; Zhang, Z. Chiral Near-Fields Induced by Plasmonic Chiral Conic Nanoshell Metallic Nanostructure for Sensitive Biomolecule Detection. *Journal of Physical Chemistry C* **2020**, *124* (25), 13912–13919. https://doi.org/10.1021/acs.jpcc.0c03523.

(329) Ho, J.; Dong, Z.; Sheng Leong, H.; Zhang, J.; Tjiptoharsono, F.; Daqiqeh Rezaei, S.; Choon Hwa Goh, K.; Wu, M.; Li, S.; Chee, J.; Pei Yu Wong, C.; Kuznetsov, A. I.; W Yang, J. K. *Miniaturizing Color-Sensitive Photodetectors via Hybrid Nanoantennas toward Submicrometer Dimensions*; 2022. https://www.science.org.

(330) Li, X.; Zhou, L.; Hao, Z.; Wang, Q. Q. Plasmon–Exciton Coupling in Complex Systems. *Advanced Optical Materials*. Wiley-VCH Verlag September 18, 2018. https://doi.org/10.1002/adom.201800275.